uOttawa

L'Université canadienne
Canada's university

FACULTÉ DES ÉTUDES SUPÉRIEURES ET POSTOCTORALES

uOttawa

L'Université canadienne
Canada's university

FACULTY OF GRADUATE AND POSDOCTORAL STUDIES

Bryan Orendorff
AUTEUR DE LA THÈSE / AUTHOR OF THESIS

M.A.Sc. (Civil Engineering)
GRADE / DEGREE

School of Information Technology and Engineering
FACULTÉ, ÉCOLE, DÉPARTEMENT / FACULTY, SCHOOL, DEPARTMENT

An Experimental Study of Embankment Dam Breaching

TITRE DE LA THÈSE / TITLE OF THESIS

Joan Nistor
DIRECTEUR (DIRECTRICE) DE LA THÈSE / THESIS SUPERVISOR

C. Rennie
CO-DIRECTEUR (CO-DIRECTRICE) DE LA THÈSE / THESIS CO-SUPERVISOR

EXAMINATEURS (EXAMINATRICES) DE LA THÈSE / THESIS EXAMINERS

O. Seidou

S. Vanapalli

P. Simms

Gary W. Slater
Le Doyen de la Faculté des études supérieures et postdoctorales / Dean of the Faculty of Graduate and Postdoctoral Studies

An Experimental Study of Embankment Dam Breaching

Bryan D. E. Orendorff

Submitted under the supervision of
Dr. Ioan Nistor
Dr. Colin Rennie

In partial fulfillment of the requirements
for the degree of
Master of Applied Science in Civil Engineering

Department of Civil Engineering
University of Ottawa
September, 2009

Your file Votre référence
ISBN: 978-0-494-61200-2
Our file Notre référence
ISBN: 978-0-494-61200-2

PREFACE

Why is it we do these things? I have often thought about why I decided to accept the challenge of this study and for the longest time I could not see the answer. Initially, it looked like such a risk, but I did it anyways. I suppose, the reason is different for everyone, just as everyone themselves is different, but for me, I felt compelled to do it.

While others may hopefully one day see this work as some significant contribution, to me it is far more important than a few pieces of paper. To me, this work represents the desire and the will for someone to explore, to seek out answers to some of the mysteries that surround us, and to come closer to the truth of who we are. It is this journey which is everything, and a journey is never about the destination. It is about all the steps you took along the way, and who was there walking with you.

Like most journeys, this one was not made alone. I wish to thank the entire research team including the summer research students Sihame Mimid and Pierre Moreels from France, and Philippe St. Germain from the University of Ottawa, senior technical officer Mark Lapointe, PhD candidate Mahmoud Al-Riffai from the University of Ottawa, and research supervisors Dr. Colin Rennie and Dr. Ioan Nistor without whom none of this would have been possible. I also wish to thank the Chemical, Biological, Radiological-Nuclear, and Explosives Research and Technology Initiative (CRTI) who so graciously funded the project and the McCormick Rankin Corporation for their continued personal patronage. I wish to thank my family, and in particular my father, for their continued support throughout the entire process. May everyone be so fortunate as to have such quality people journey with them.

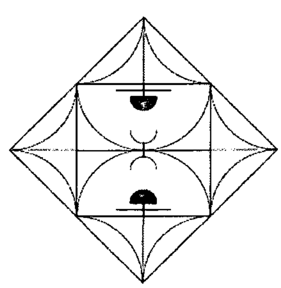

EXECUTIVE SUMMARY

There are thousands of embankment dams around the world which represent a significant economic and ecological risk should any of them fail. In previous failure events such as the Baldwin Hills Reservoir near Los Angeles which failed in 1964, destroying 277 homes and killing five people and causing $73 million in property damage. Other failures include the Buffalo Creek coal tailings dam in West Virginia which failed in 1972, killing 125 people, injuring over 1000 more and leaving thousands homeless and the Teton Dam in Idaho which failed in 1976 killing 14 people and causing over $1 billion in damages, and the recent Situ Gintung Lake Dam near Jakarta, Indonesia which failed March 26, 2009 killing almost 100 people.

The goal of this study is to provide the experimental basis for a new numerical dam breach model which will help to address many of the shortcomings identified in the literature which are due primarily to lack of knowledge. Shortcomings have been identified in the existing models in the areas of breach initiation, breach location, breach morphology, hydraulics of flow over an embankment, sediment transport equations, geo-mechanics of the breach, and modeling composite embankments. For example, it has been said that there is an uncertainty of about 50% which can be expected from estimates of peak discharge for the existing numerical models (Franca and Almeida, 2004).

To address the existing limitations, two embankment test series were developed. The first series of tests was conducted in a smaller flume in which compaction was varied. These tests shed light on the effects of compaction as well as the effects of side walls in testing and some of the effects that unsaturated soils and slope stability have on the breach process. The second series of tests was conducted in a larger flume with varying initial breach geometry as well as varying the filtration characteristics of the embankment. These tests demonstrate the role of initial breach geometry in dam breach mechanics and also help with understanding the importance of slope stability and unsaturated soil mechanics. One of these runs also included a clay core to study the effects of composite construction. These two test series were supported by data obtained by a series of geotechnical investigations as well as a series of erosion characteristics tests which were both conducted using the dam construction materials.

From these test series, the following conclusions have been drawn:

i. A four phase breach process is proposed based on quantitative analysis of breach morphology.

ii. Initial breach geometry does not appear to have any effect on the peak breach outflow.
iii. The density of the embankment plays an important role in determining the shape of the outflow hydrograph as well as the peak flow.
iv. The breach is widest at the downstream toe of the embankment and smallest at the crest, but widens again upstream of the crest.
v. The slope failure mode does not appear to have any impact on breach characteristics.
vi. Tailwater conditions have a notable effect on breach morphology and reservoir volume also appears to have an important effect on sediment deposition characteristics.

It should be noted that these conclusions have not been drawn for the purposes of improving dam construction techniques. Rather, they are useful for developing a more advanced numerical breach model in the hope of improving the accuracy of risk assessments in downstream flood zones. A new set of criteria could then be developed to define the new flood elevations and improve warning times for people who may be at risk.

TABLE OF CONTENTS

LIST OF TABLES

TABLE OF FIGURES

LIST OF SYMBOLS

A, area, [m^2]
b, weir crest width, [m]
c, undrained cohesion, [kPa]
c', effective cohesion, [kPa]
C, clay content, [%]
C_e, erosion rate constant, [FF]
C_w, weir coefficient, [FF]
D, apparent crater diameter, [m]
d, charge depth, [m]
d_s, particle size, [mm]
D_{50}, mean sediment grain size, [mm]
D_r, crater diameter, [m]
E, total erosion, [kg/m^2/s]
e, void ratio, [ND]
Fr, Froude number, [ND]
g, gravity constant, [m/s^2]
G_s, specific gravity of the soil, [ND]
H, hydraulic head, [m]
i, hydraulic gradient, [ND]
I_p, plasticity index, [ND]
i_s, positive impulse, [N·s]
K_b, Manning-Strickler coefficient of roughness for the bed region, [ND]
K_r, Manning-Strickler coefficient of bed roughness assoc. with skin friction, [ND]
k_e, empirical erosion constant, [FF]
k, coefficient of permeability, [m/s]
n, erosion rate exponential constant, [FF]
P_b, moist bulk density, [kg/m^3]
ρ_f, density of eroding water, [kg/m^3]
$p(t)$, pressure function with respect to time, [kPa]
p_o, ambient temperature, [kPa]
p_s, peak overpressure, [kPa]
Q, flow, [m^3/s]
q^*, dimensionless volume bedload transport rate per unit width, [ND]
q_w, volume discharge per unit width, [m^2/s]
q_w', corrected volume discharge per unit width, [m^2/s]

R, range from blast centre, [m]

Re, Reynolds number, [ND]

Re_*, non-dimensional Reynolds stress, [ND]

S, channel slope, [ND]

ΔS, salinity difference, [ND]

t, time, [s]

t'_b, fluctuation time of turbulence burst, [s]

T_s, duration of the positive blast phase, [ms]

u, mean streamwise velocity, [m/s]

u_*, shear velocity, [m/s]

u_b, near-bed time averaged velocity, [m/s]

u'_b, near-bed velocity fluctuation, [m/s]

v, velocity, [m/s]

W, equivalent TNT charge weight, [kg]

w, water content, [%]

w_{LL}, liquid limit, [%]

w_{PL}, plastic limit, [%]

Z, scaled distance, [ND]

β, empirical breach constant, [ND]

γ_d, dry unit weight, [kN/m^3]

γ_s, unit weight of soil particles, [kN/m^3]

γ_w, unit weight of water, [kN/m^3]

κ, von Karman constant, [ND]

u_w, pore water pressure, [kPa]

u_a, pore air pressure, [kPa]

ν, kinematic viscosity, [m^2/s]

ϕ, angle of internal friction, [degrees]

ϕ', effective angle of internal friction, [degrees]

ϕ^b, angle indicating rate of increase in shear strength relative to matric suction, [degrees]

ρ_s, soil density, [kg/m^3]

ρ_w, water density, [kg/m^3]

σ, normal stress, [kPa]

$\tau_\circ$, shear stress, [Pa]

τ_*, non-dimensional shear stress, [ND]

$\tau_\circ$, bed shear stress, [Pa]

τ_c,	critical shear stress, [Pa]

ND refers to non-dimensional units
FF refers to "force fit" units derived from empirical equations which can change depending on the application

1.0 INTRODUCTION

Dams are some of the most impressive and beneficial structures ever constructed. In early times, dams were constructed of large mounds of earth to block rivers, providing water and irrigation to nearby towns and fields. Since those early days, designs have been refined to include concrete spillways for flood control, cores of impervious clay, and the ability to generate electricity, thanks largely to the development of soil mechanics and geotechnical engineering (Foster *et al.*, 2000). Today, some of the largest dams in the world and some of the tallest structures are earth embankments. The United States Committee on Large Dams (USCOLD) estimates that nearly 80% of all large dams currently in operation in the United States are embankment dams (USCOLD, 1975). In the mid-twentieth century in the United States alone, about 11,000 flood control and multipurpose dams were constructed with assistance from the United States government (Caldwell, 1999). Given the cheaper cost often associated with earth dam construction in developing countries, this percentage is likely higher on a global scale. But, for as long as these dams have stood, there has been the threat of failure and the inherent risks to people, land, and property downstream from the flood wave.

In most countries, the risk of failure is greater now that much of the existing dam infrastructure is nearing the end of its service life. Compounding the service life concern is the increase in urban development that now surrounds many aging dam sites causing increases in runoff which, in turn, increases the risks of dam failure. Increased flow due to development is thought to be the leading cause of the March 26, 2009 failure of the Situ Gintung Lake Dam near Jakarta in Indonesia which killed almost 100 people after heavy rains caused the dam to fail (BBC, 2009; Jakarta Post, 2009).

In the latter half of the twentieth century, several major embankment dams failed. The Baldwin Hills Reservoir near Los Angeles failed in 1964, destroying 277 homes and killing 5 people after discharging 1 million m^3 of water from the reservoir and causing an additional 73 million CAD (12M USD in 1971) in property damage (Hamilton and Meehan, 1971). The Buffalo Creek coal tailings dam in West Virginia failed in 1972, killing 125 people, injuring over 1000 more and leaving thousands homeless after discharging 0.5 million m^3 of water (Wikipedia, 2009). The Teton Dam in Idaho failed in 1976 and is considered one of the most well known dam failures in the world; 14 people were killed and over $1 billion in damages were caused (Solava and Delatte, 1995). Due to these failures, United States government agencies such as the Bureau of Reclamation (USBR) and the Army Corps of Engineers (USACE) seriously re-evaluated their dam hazard and risk classification systems and began to develop predictive numerical models for dam breaching (Hahn *et al.*, 2000). Between 1985 and 1994, there have been more than 400 dam failures in the United States alone (Graham, 1998).

Dam failures do not always result in loss of life, however, as many have been constructed far away from populated centers. Massive ecological damage is also possible. When the Aznalcòllar tailings pond dam in Spain failed in 1998, a great quantity of toxic material spilled out into the river system, causing devastating ecological damage which threatened a nearby national park (Coleman *et al.*, 2002). Similarly, when the Opuha Dam in New Zealand failed in 1997 while it was under construction, it caused significant economic and environmental damage (Coleman *et al.*, 2002).

Not all dams that fail are of anthropic origin. Landslide dams, formed by large slope failures often the result of earthquakes, are some of the largest dams in the world (Fread, 1988). Following the eruption of Mount St. Helens in 1980, landslides and other debris poured into the valleys, blocking the existing drainage paths and creating a number of new lakes such as Castle Lake and Coldwater Lake (USGS, 2005). These newly formed natural embankments are in turn at risk of failure. The Tunawaea landslide dam in New Zealand failed in 1992 and caused relatively minor damage (Webby and Jennings, 1994).

The computer models developed for predicting the effects of dam breaching were aimed at quantifying the risk associated with the flood wave resulting from a dam breach. While there was a heavy focus on determining the peak flow of the flood wave, there was also focus on the time to peak flow for the breach. Analysis of several high fatality embankment dam failures from around the world showed that the average number of fatalities is 19 times greater when there is inadequate or no warning (Costa, 1985), indicating that the time to peak for the breach is a key parameter that requires accurate prediction. Other cases were studied by Brown and Graham (1988) and it was determined that loss of life can vary from 0.02 percent of the population at risk when the warning time is 90 minutes to 50% of the population at risk when the warning time is 15 minutes or less. More generally, the potential for loss of life after a dam failure is heavily dependent on the warning time available to evacuate the population at risk (DeKay and McClelland, 1993; USBR, 1999). Additionally, Hamilton and Meehan (1971) report that the Baldwin Hills Reservoir would likely have killed far more than 5 people had not a worker on the dam given warnings to the nearby community.

In order to help quantify the risk of dam failure for communities near embankment dams, the United States National Weather Service (NWS) released its Dam Break Flood Forecasting Model (DAMBRK) in 1981 which helps predict the characteristics of the dam break flood wave. In 1983, the NWS released a simplified version of the program

(SMPDBK) which was intended for more general use. In 1988, they released BREACH and in 1993 they released FLDWAV. With the exception of BREACH, these models focus their computational effort on routing the breach hydrograph rather than the breach formation process (Wahl, 1998) and are not considered to be physically-based models.

However, researchers have shown that the embankment breach parameters are very sensitive and that there is a great deal of uncertainty in predicting them (Wahl, 2004). Singh and Snorrason (1984) and Petraschek and Sydler (1984) examined breach parameters using the DAMBRK model and determined that discharge, flood levels, and time to peak change significantly with the breach width and breach formation time. The above models also often require the user to make assumptions for which there is little guidance (Morris and Hassan, 2002). In general, there is an uncertainty of about 50% which can be expected for the estimate of maximum discharge between the existing models (Franca and Almeida, 2004).

Morris and Hassan (2002) conducted a review of a number of physically-based breach models (Table 1.1), comparing the manner in which parameters such as breach morphology, flow calculation, sediment transport, and side slope failures are determined. This review identified a number of deficiencies in each model. Further reviews of the existing models revealed weaknesses within the modeling process itself (Mohammed *et al.*, 2002) including lack of knowledge of data in the following areas:

- *Breach initiation*: to date, mostly associated with piping, but focused on the need to develop early warning systems where possible.
- *Breach location*: most models use a centerline breach. However, what about those, such as in the case of the Teton dam, for which the breach occurred near a relatively non-erodible rock wall?
- *Data for model calibration and verification*: very few breach events have been well recorded and documented, so most models have been calibrated to events that do not necessarily represent very well the limitations of the model (for example, a model that uses a centerline breach but which is calibrated to the Teton Dam failure).
- *Breach morphology*: many models assume a certain empirical approach of progressive breach morphology which is not normally consistent with the results obtained when combining existing flow and sediment transport equations.
- *Hydraulics of flow over an embankment*: many models use hydraulic equations that do not necessarily apply to such flows, such as small channel slopes or using the one-dimensional St. Venant equations, as simplifications.

Table 1.1: Comparison and Assessment of Physically-based Breach Prediction Models (Morris and Hassan, 2002)

Model	Breach Morphology	Flow Calculation	Sediment Transport	Geo-mechanics of Breach Side Slopes	Limitations and Deficiencies
Christofano (1965)	Trapezoidal, with constant bottom width	Broad crested weir formula	Christofano empirical formula	None	- Constant breach bottom width and shape - No lateral erosion mechanism - No slope stability mechanism - Unrealistic erosion relation
Harris-Wagner (1967)	Parabolic, with top width = 3.75 depth	Broad crested weir formula	Schoklitsch formula	None	- Constant sediment concentration - No slope stability mechanism - User input breach slope
BRDAM (1977)	Parabolic, with 45° side slopes	Broad crested weir formula	Schoklitsch formula	Failure of top wedge above pipe specified by user	- Constant sediment concentration - No slope stability mechanism - No lateral erosion mechanism - User input time for pipe failure
Ponce-Tsivoglu (1981)	Top width flow rate relation	St. Venant equations	Exner equation with Meyer-Peter-Muller	None	- No slope stability mechanism - Use of the regime concept - No lateral erosion after peak flow
Lou (1981)	Most effective stable section (cosine curve shape)	St. Venant equations	1.Christofano empirical formula 2. Duboy and Einstein formula 3. Lou's formula	None	- No slope stability mechanisms - No lateral erosion after peak flow - Empirical formula to compute the erosion - Inappropriate method to model the breach growth
Nogueira (1984)	Effective shear stress section (cosine curve shape)	St. Venant equations	Exner equation with Meyer-Peter-Muller	None	- No slope stability mechanisms - No lateral erosion after peak flow - Empirical formula to compute the erosion - Inappropriate method to model the breach growth
Flood Levee Breaches (1987)	Rectangular breach shape above water level, trapezoidal below	Critical flow equation	Sediment transport rate estimated assuming energy slope consumed only in sediment transport	None	- Uniform erosion of the breach - No slope stability mechanism
BEED (1987)	Trapezoidal	Broad crested weir formula	Einstein-Brown	Breach side slope stability	- Uniform erosion of the breach - Incompatible computation method - Inaccurate slope stability analysis

Table 1.1 (continued)

Model	Breach Morphology	Flow Calculation	Sediment Transport	Geo-mechanics of Breach Side Slopes	Limitations and Deficiencies
NWS BREACH (1988)	Rectangular and trapezoidal	Broad crested weir formula	Smart Method	Breach side slope stability and top wedge failure	- Uniform erosion of the breach - Incompatible computation method - Inaccurate slope stability analysis - Simplified modeling of the failure of composite embankments
SITES (1998)	3 stage failure: cover failure, headcut formation, headcut erosion	Flow-stage rating curve	For stages 1 and 2, a detachment model was used. For stage 3, an energy dissipater equation was used	Spillway exit channel stability	- Does not model complete embankment failure process - Empirical coefficient to compute erosion
NCP BREACH (1998)	Parabolic	Empirical formula	Empirical formula	None	- Empirical formula based on small scale models - No slope stability mechanism
EDBREACH (1998)	Trapezoidal	Broad crested weir formula	Meyer-Peter-Muller	Top wedge failure during piping	- Uniform erosion of the breach - Inaccurate slope stability analysis
BRES (1998)	5 stages of failure	Broad crested weir formula	Several transport formulae	None	- No slope stability mechanism - Incomplete computation method
DEICH N1/N2 (1998)	Diffusion approach	Shallow water equations	Several transport formulae	None	- Parabolic breach shape - No slope stability mechanism - Unrealistic modeling of the vertical and lateral erosion
Renard and Rupro (1998)	Uniform erosion of the pipe	Orifice equation	Meyer-Peter-Muller	Failure of material above the pipe	- Unrealistic modeling of failure of material above the pipe - No slope stability mechanism

- *Sediment transport equations*: Most sediment transport equations show exceptional variability from one another and were derived for flow types vastly different than what is characterizing a breach, giving rise to the idea that they may not be applicable to breach mechanics.
- *Geo-mechanics of the breach*: Most existing models do not consider the geotechnical aspects of the embankment as they focus on the hydraulic equations instead, yet slope stability seems to have a significant role in breach mechanics.
- *Modeling composite embankments*: Most existing models have been designed for homogenous embankments, even though most dams are constructed with selective layering of materials which often include impervious cores and/or slope protection.

From this list of limitations, Mohammed *et al.* (2002), recommend some key areas of potential research, including a realistic representation of breach development during the breaching process, a more accurate analysis of the breach side slope stability process, and a methodology to model the failure of composite embankments. This study endeavors to provide input, in the form of experimental results, to all of the above points as well as to provide input into a new numerical breach model which will hopefully address at least some of the above listed concerns of the previous breach models.

These limitations have prompted the need for more realistic breach models. In 1998, the European Commission funded the Concerted Action on Dam Break Modelling (CADAM) project which ran from 1998 until 2000 with the goals of defining the current state-of-the-art for modeling and with the purpose of producing a guidance document for dam break modeling best practices (CADAM, 2000). CADAM presented 31 conclusions in their final report. Some of the conclusions which are most relevant to this study are presented below.

- (8) The accuracy of dambreak models should not be compared to normal river models as flow conditions are far more complex and data to validate the models is limited.
- (11) It is impossible, within the scope of CADAM, to identify a single best model or type of model for any or all dambreak conditions. A more detailed analysis of data and model performance is required.
- (13) Our current ability to predict the location and rate of breach growth is limited.
- (19) Breach growth mechanisms for river banks appear to differ from those for embankment dams.

- (22) Research is required to determine whether existing or modified morphological river models are appropriate to simulate sediment transport under dambreak conditions.

In 2001, in order to address the conclusions of the CADAM project, the Investigation of Extreme Flood Processes and Uncertainty (IMPACT) project was initiated. As part of the IMPACT study, five large scale embankments were tested in the field and twenty-two 1:10 scale embankments were tested in laboratory conditions. The final technical report was released in January, 2005. The embankment construction methods and materials are discussed in greater detail in Section 2.3 of this thesis. To date, the final results from the numerical modeling have yet to be released. However, the study did put forth several valuable practice guidelines which are summarized below.

- *Breach modeling*: A range of breach models were assessed and it was determined that the NWS BREACH model is now obsolete in its approach as newer models have improved capabilities and are more reliable in comparison. This author notes, however, that the NWS BREACH model is easy to obtain, whereas other models are not, making it still the preference for many end users.
- *Flood propagation modeling*: Limitations in modeling are found to be constrained by the accuracy of the data provided for the models, modeling assumptions, and computing power, rather than mathematical approaches. Research is needed to clarify modeling roughness values for extreme flow conditions.
- *Sediment movement*: Sediment transport has a significant effect on the depth of flood water and on the wave propagation rate. Further research into this area is required to advance knowledge and modeling ability.

In 2000, HR Wallingford released HR BREACH, a new physically-based dam breach model. The IMPACT study has the goal to improve upon this model. Further, it was concluded that the scope of the IMPACT project was insufficient to fully establish a method for assessing modeling uncertainty and that this limitation would be addressed by the European Commission's FLOODsite project (IMPACT, 2005). Al-Riffai *et al.* (2007) compared the results of this model with that of the NWS BREACH model and found that the HR BREACH model showed greater sensitivity to input parameters and that NWS BREACH showed no variability for certain input parameters such as the mean particle diameter, believed to be a controlling parameter for sediment transport equations. The authors concluded that the HR BREACH model was more reliable for those reasons.

Nistor and Rennie (2005) also commented that there have been recent concerns regarding the security of infrastructure from terrorist attack and that there has been virtually no research into dam breaching as a result of explosive blast. Moreover, there has been no examination of the effects of any initial breach geometry in the dam breaching process.

1.1 Objectives, Outline and Novelty of Current Study

The objective of this study is to advance the current state-of-the-art by conducting a series of laboratory tests on homogeneous and composite embankments, with the aim of creating the foundation for a new numerical model for dam breaching. A review of the existing literature, presented in Section 2 of this thesis shows that there are limitations in our knowledge of breach initiation and initial breach geometry. Many researchers have used varying initial ways of initiating breaches, but what effect that variance has on other breach parameters is still unknown.

This study will address the following questions and concerns arising from the existing literature, as further described in Section 2.

- To determine the effects of varying initial breach geometry in order to include uncontrolled breaches over a flat crest as well as breaches induced by a potential terrorist attack;
- To determine the effects of compaction on non-cohesive embankment breaching;
- To determine what effects breaching against a side wall may have on the experimental process;
- To determine how great an impact unsaturated soil mechanics has on dam breach morphology;
- To determine if previously unexamined characteristics such as the tailwater condition and reservoir volume are important parameters in dam breaching; and
- To conduct a breach test on a composite dam containing a clay core.

Some of the above points are also discussed in the collaborative effort of Al-Riffai *et al* (2009). Also, new technologies have become more readily available since many of the earlier physical model tests have been conducted. Applications such as the geographic information system (GIS) and video analysis may prove useful in adding detail to the breaching process so as to aid in determining some of the subaqueous breach characteristics.
In order to address the above points, two embankment test series were developed. The first was a series of tests conducted in a smaller flume in which compaction was varied.

These tests shed light on the effects of compaction as well as the effects of side walls in testing and some of the effects that unsaturated soils and slope stability have on the breach process. This test series is also discussed in the collaborative effort of Al-Riffai *et* al (2009). The second series of tests were conducted in a larger flume with varying initial breach geometry as well as varying the filtration characteristics of the embankment. These tests show the role of initial breach geometry in dam breach mechanics and also help to examine the importance of slope stability and unsaturated soil mechanics. One of these runs also included a clay core to study the effects of composite construction. These two test series were supported by data obtained by a series of geotechnical investigations as well as a series of erosion characteristics tests which were both conducted using the dam construction materials.

The review of existing literature in Section 2 and provides the context and scope for this study. The review gives a brief introduction to scaling and embankment failure mechanics and delves into greater detail with a summary of previous experimental studies with special attention being paid to the initial breach geometries which those studies used as well as the construction methods utilized for their embankments. A brief review on erosion rates and sediment transport are also included which focuses primarily on the characteristic differences of sands in clays in response to hydraulic forces as well as an overview of the transport formulae which previous researchers have used in their studies and numerical analyses. Also included is a short overview on the geotechnical aspects which are important in dam breaching in order to explain the mechanics behind the geotechnical investigations which were conducted in this study. The section concludes with a review of blast effects and the formation of craters. This portion of the review is included as one of the driving forces behind this study is the relatively new aspect of acts of terrorism being committed on dams and the associated risks associated with such an act.

Section 3 explains the methodology behind the four independent test series (geotechnical, erosion, compaction, and large flume) as well as the experimental setup and/or standards used for each test. Section 4 examines the detailed explanation of the methodology and procedures used for the analytical portion of the study which includes an explanation of how the breach outflow hydrographs were generated.

Section 5 presents the results for each of the four test series as well as the accompanying analysis which helps to explain in greater detail the meaning of the figures and tables which have been included. Section 6 summarizes and discusses the results and analysis and prepares the conclusions to be drawn in response to the compelling questions of this study. The conclusions of the study and proposed future work are summarized in Sections 7 and 8 respectively.

In Sections 2, 3, 5 and 6, each of the four test series has been given one subsection which is independent of the other subsections to reflect the independent nature of each of the test series. As such, this document is designed so it can be read for each test series independently by reading the appropriate subsections rather than reading the entire document.

2.0 LITERATURE REVIEW

The field of experimental embankment dam breaching is truly multi-disciplinary. While the acting forces on the embankment are largely hydraulic, the structure itself is made of earth which has its design roots based in a separate engineering discipline. As such, any investigation into the field of earth dams must have both a hydraulic and a geotechnical component in order to examine the forces acting on the structure as well as the structure's response to those forces. This review of the existing literature provides an overview of the geotechnical characteristics which are involved in the experimental process for dam breaching as well as a more specific background into the work which has been performed with regards to earth dam breaching. Also included is a review on literature dealing with erosion and sediment transport phenomena as they pertain to breach characteristics.

This review is limited to mostly experimental works and does not delve deeply into the many papers which have been published on numerical analysis and computer modeling of dam breaching. While these papers have value in showing what equations are employed by the end users of the experimental data, for the purposes of this review most of those papers have not been mentioned here. Also, the geotechnical review is limited to an overview of geotechnical concepts as they pertain to the tests which were conducted for the present study.

This review will provide the theoretical and experimental background for the current dam breaching experiments and will clearly define the novelty of this work and how it can fit in with the greater body of existing literature.

2.1 Scaling

Scaling is an important aspect of any laboratory experiment. Without proper scaling, the results obtained in the experiment cannot be easily verified for their applicability to works at the prototype scale. In many cases of hydraulic experiments, similitude is based on Froude number, which gives the relative importance of inertial forces acting on a fluid particle to the weight of the particle (Munson *et al.*, 1990). Scaling according to Froude number therefore is designed to keep similar balance between inertial and gravitational forces in the model as in the prototype and is generally applied in cases where gravitational forces are dominant, which is to say most flows with a free surface.

Scaling by factors other than Froude number, shown in Equation 2.1, is also possible, of course, for situations where forces other than gravity dominate the system. For example, Reynolds number scaling is used in situations where viscous forces dominate and Weber number scaling is used for situation where surface tension forces dominate. Dam breaching is dominated by gravity forces and hence Froude scaling was adopted for this study.

$$Fr = \frac{V}{\sqrt{2g}} \qquad [2.1]$$

V = velocity

g = gravity constant

While Froude scaling will take care of the acting and resisting forces in the system, the sediment composing the embankment must also be scaled. Sediment is scaled based on non-dimensional shear stress, shown in Equation 2.2, and non-dimensional Reynolds stress, shown in Equation 2.3, as determined by the Shields curve. Generally, however, the sediment scales similarly to the length scale of the model.

$$\tau_* = \frac{\tau_\circ}{(\gamma_s - \gamma_w)d_s} \qquad [2.2]$$

$$\mathrm{Re}_* = \frac{u_* d_s}{\nu} \qquad [2.3]$$

$\tau_\circ$ = applied shear stress

γ_s = specific weight of the sediment

γ_w = specific weight of water

d_s = sediment grain size

u_* = shear velocity

ν = kinematic viscosity

For this study, the scale was chosen to be 1:100. Given that the prototype embankment would be composed largely of sand, the model sediment should be approximately 1% the diameter of the prototype sediment. If the prototype sediment has a median grain size of 1.0 mm (typical medium sand), the median grain size of the model sediment would be 10 μm (typical silt). However, most silts will exhibit cohesive forces which, unlike sand, will resist the applied gravitational forces. In a Froude-scaled model, cohesion scales with the linear model scale. In this case, therefore, any cohesive forces found in the model should be multiplied 100 times for the prototype, whereas the prototype will not have any cohesion due to the lack of cohesion in sand. Therefore, the use of silt in model construction would not be appropriate because the modeled cohesive forces would be vastly overstated.

Given the problems associated with the scale of the model, the scaling limitations should be immediately noted.

2.2 Embankment Failure Mechanisms

Lecointe (1998) presents three modes of failure for an earth embankment: overtopping, piping, and macro-instability. Overtopping occurs when the water level in the reservoir surpasses the crest of the dam and spills over to the downstream side. Piping can be called an internal erosion failure and occurs where material from the inner body of the dam is transported away by forces due to seepage flow. Macro-instability is a sliding failure of the embankment and occurs when there is a lack of shear strength to hold the embankment together which generates what is effectively a landslide. Lecointe also mentions micro-instability as a type of failure, but describes it more as a cause for either piping or macro-instability.

Piping can be further subdivided into embankment failures, foundation failures, and embankment-foundation failures (Foster *et al.*, 1998). Of all the piping failures, 50% have been identified as embankment failures, 40% have been identified as foundation failures, and 10% have been identified as composite embankment-foundation failures where, generally, the pipe builds up in the foundation and emerges in the embankment (Fell *et al.*, 2003). Figure 2.1 shows the processes of piping.

Apart from subdividing piping failures based on their location, they can also be subdivided by definition (Richards and Reddy, 2007). For example, Terzaghi (1939) presented a piping failure model as backwards erosion, while Lane (1934) presented a model for internal erosion. While very similar in process, internal erosion occurs because of pre-existing faults in the material and is expressed as a tractive load (Richards and Reddy, 2007).

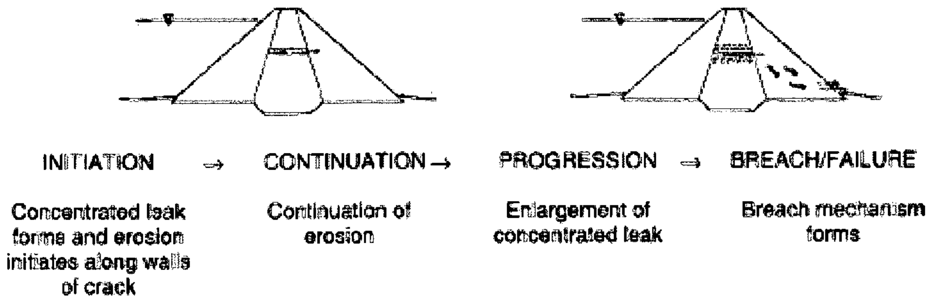

Figure 2.1: Model for Development of Failure by Internal Erosion and Piping (Fell *et al.*, 2003).

For the purposes of this study, however, only the overtopping failure mode is being examined. The overtopping flow regime is shown in Figure 2.2. Overtopping is generally initiated by upstream flooding of the reservoir where the water level behind the dam rises higher than the crest and spills over the downstream side. The flow passes from a generally subcritical flow regime on the upstream side to a supercritical flow regime on the downstream side due to the sudden increase in slope. Often, equations for flow over a broad crested weir, as shown in Equation 2.4, are used to describe this process.

$$Q = C_w b H^{1.5} \quad [2.4]$$

H is the head over the weir and b is the width of the weir crest. The coefficient C_w is normally idealized as 1.7, but in practicality has a range of values. For example, Prasuhn (1992) suggests a value of 1.84.

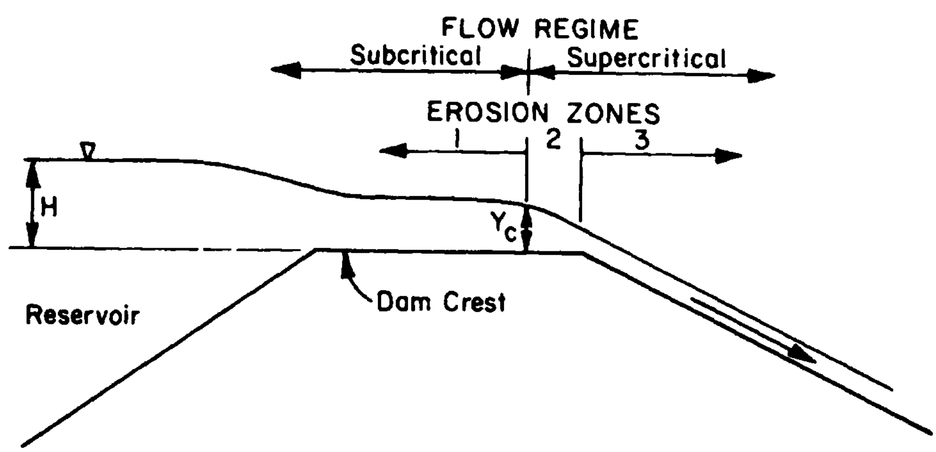

Figure 2.2: Flow and Erosion Regimes in Embankment Overtopping (Powledge *et al.*, 1989).

Overtopping can also be initiated by wave action as shown in Figure 2.3. In this case, the flow regime is the same as in Figure 2.2, but overtopping can initiate before the water elevation in the reservoir (still water level) reaches the elevation of the dam crest due to the wave height and wind setup.

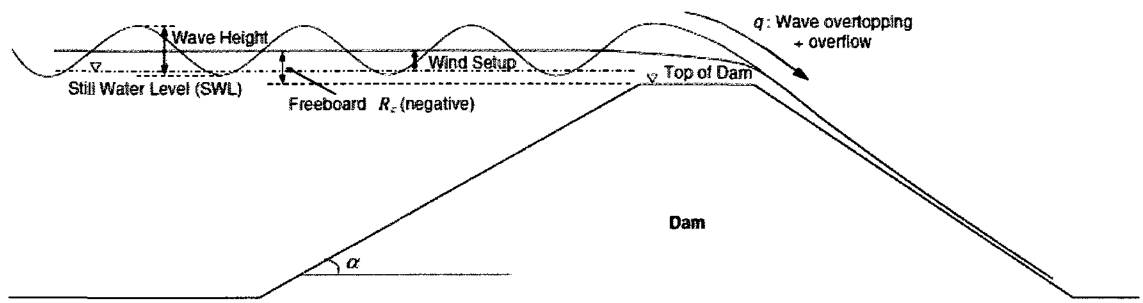

Figure 2.3: Schematic Figure of the Combination of Wave Overtopping and Overflow (Wang and Bowles, 2006)

There is, however, a difference between an overtopping failure and a breach failure. While a wave might break on the crest of an embankment and scour the downstream face of the dam, it does not mean that the dam will breach and fail. But the differences between these two types of failure are somewhat muddied. Wahl (2004) describes two phases: (1) an initiation phase and (2) a breach development phase. The initiation phase ends "when a breach has reached the point at which the volume in the reservoir is compromised and failure becomes imminent." The development phase ends simply when the breach stops getting larger. Visser (1998) describes a five stage process of breach erosion in sand dikes. However, it can be argued that the first stage begins once significant erosion has already begun and therefore the stages really represent a breakdown of the breach development phase define by Wahl (2004). Visser also used a notably large pilot channel in his experiments which makes defining initial breach stages more difficult.

Given the absence of detailed failure definitions, this study has set out to define its own. These failure definitions apply only to overtopping failures. First, an inundation failure takes place where flood waters and waves have spilled onto the crest of the dam, but where there has been no spilling onto the downstream face. This type of failure may cause a roadway on the embankment to be closed, but will not cause any damage to the dam itself. Once water has spilled over onto the downstream face, an overtopping failure has been initiated. In certain cases where the protection on the downstream embankment is suitably strong or where the overtopping flow is suitably weak, an overtopping failure may not initially cause any damage to the embankment. Therefore, an overtopping failure has the potential to be subdivided. Using the definition proposed by Wahl (2004) as a guideline, a breach failure will be defined as the point at which erosion will cataclysmically persist even if no further inflow were to be added to the system. It is one of the goals of this study to help define that point of no return.

In the case of inundation and overtopping failures, the one must follow the other, and both must have occurred before a breach failure. If either inundation or overtopping ceases to progress, a breach failure can be avoided.

2.3 Previous Experimental Studies

There have been more than 325 embankment tests since the 19^{th} century (Wahl, 2007). These tests have sought to vary a number of different parameters including material gradation, upstream and downstream slope, size, crest width, etc. From these tests, numerous numerical models have been derived. These tests are summarized in Table 2.1. It should be noted that the tests shown in Table 2.1 include tests of piping failures in addition to overtopping failures.

A subset of the tests shown in Table 2.1 is shown in greater detail in Table 2.2. The sources shown in Table 2.2 are discussed in greater detail below. Construction methods for those embankments as well as breach initiation are discussed in Sections 2.3.1 and 2.3.2 respectively.

Table 2.1: Laboratory Breach Tests (Wahl *et al.*, 2007)

Organization	Test Description	Dates	No. of Tests
Washington State U.	Fuse plug breach – models	1959	10
Washington State U.	Fuse plug breach – field scale	1959	1
Washington State U.	Fuse plug breach – sectional	1959	2
U. of Windsor	Fuse plug breach – models	1978	N/A
China – fuse plugs	Fuse plug breach – field scale	1970s - 1982	>50
Bureau of Reclamation	Fuse plug breach – model	1985	8
Tech. U. of Graz	Overtopping breach failure of various configurations of rockfill dams	1982	22
China – rockfill dams	Rockfill dam breach – lab scale	N/A	6-8
USDOT-FHWA	Highway embankment overtopping	1982 - 1986	35
USDOT-FHWA	Evaluate embankment damage and protection	1985 – 1988	57
USDOT-FHWA	Evaluate articulated concrete block systems	1988 – 1989	17
USBR	Embankment dam overtopping	Mid 1980s	9
U. of Colorado	Centrifuge testing – feasibility	1983	2
U. of Colorado	Prototype test	1983	1
Colorado State U.	Overtopping breach failure	1991	2
USDA-ARS-HERU	Erosion in cohesive bare-earth and steep channel	Late 1990s	4
USDA-ARS-HERU	Overtopping breach – cohesive soil	1999 – 2001	7
USDA-ARS-HERU	Breach widening – cohesive soil	2003	3
IMPACT	Lab-scale overtopping breach – non-cohesive	N/A	9
IMPACT	Lab-scale overtopping breach – cohesive	N/A	8
IMPACT	Piping initiation and development	N/A	5
IMPACT	Large scale tests of overtopping	2002 – 2003	5
Norway – field tests	Through-flow and breaching of rockfill dams	2002	2
Norway – lab tests	Through-flow and overtopping of rockfill dams	2002 - 2003	23
Delft U. of Tech.	Breaching of sand dikes	1994, 1996	5
U of Birmingham	Qualitative evaluation of overtopping breach	1998	2
Brno U. of Tech.	Overtopping breach – non-cohesive	Before 2000	1
U. of Auckland	Overtopping breach – non-cohesive	Late 1990s	9
Tech. U. of Lisbon	Overtopping breach – rockfill	2001	22
St. Petersburg State Tech. U.	Overtopping breach – non-cohesive	2003?	4
Thailand	Overtopping breach – non-cohesive	2001	4
South Africa	Overtopping breach – non-cohesive	Before 2005	24
École Poly. de Montreal	Overtopping breach – moraine	Before 2005	1

Table 2.2: Previous Experimental Studies

Paper	Visser, 1998	Mohamed *et al.*, 1999	Hahn *et al.*, 2000 (Outdoor Flume)	Hahn *et al.*, 2000 (Full-Scale)	Tingsanchali and Chinnarasri, 2001	Franca and Almeida, 2002	Coleman *et al.*, 2002	IMPACT, 2005 (Norway)	IMPACT, 2005 (Wallingford)	Davies *et al.*, 2007
Number of Tests	1	3	2	3	11	1	3	3	17	2
Material	Sand	Sand	Silty sand	Silty sand and lean clay	Sand	Gravel	Sand	Silty clay, rockfill with moraine, sand	Sand and silty clay	Sand with gravel
D_{50} (µm)	88	300-500	NA	Varied	520 and 860	18900	500, 900 and 1600	Varied	Varied	NA
Crest Height (mm)	150	300	900	2300	800	500	300	4500, 5000, and 6000	450, 500, and 600	650
Crest Width (mm)	200	200,300, and 500	NA	NA	300	200	65	NA	NA	NA
U/S Slope (H:V)	2 to 1	1 to 1	3 to 1	3 to 1	3 to 1	1 to 1.5	2.7 to 1	2 to 1 or less	2 to 1 or less	Varied
D/S Slope (H:V)	4 to 1	1 to 1	3 to 1	3 to 1	Varied	1 to 1.5	2.7 to 1	2 to 1 or less	2 to 1 or less	Varied
Scale	NA	NA	NA	NA	NA	NA	NA	1 to 1	1 to 10	1 to 130
Inflow (L/s)	Varied	NA	Varied	About 1000	Constant within test but varying between tests	39	Varied (stopped at certain intervals)	NA	NA	3
Reservoir (m3)	NA	NA	NA	NA	About 14	2.7	NA	NA	Varied, but all >100	0.7

Table 2.2 (continued)

Paper	**Visser, 1998**	**Mohamed *et al.*, 1999**	**Hahn *et al.*, 2000 (Outdoor Flume)**	**Hahn *et al.*, 2000 (Full-Scale)**	**Tingsanchali and Chinnarasri, 2001**	**Franca and Almeida, 2002**	**Coleman *et al.*, 2002**	**IMPACT, 2005 (Norway)**	**IMPACT, 2005 (Wallingford)**	**Davies *et al.*, 2007**
Tailwater Condition	Channel continuation	Channel continuation	Channel continuation	Another embankment downstream	Channel continuation	Channel continuation	Free overfall	Channel continuation	Channel continuation with free overflow immediately downstream	Another embankment downstream
Notes	Simulating dike breaching, not dam breaching	Why sand of varying D_{50}? Very steep slopes	Conducted point gauge measurements of breach channel during test	Scale of embankment not the same as per outdoor flume tests	More of a bedform erosion test than a breach test	Single test conducted for rockfill dam with impervious upstream layer	Included toe drain, breach initiated at side wall	Large scale testing on Norwegian fjord	Tests meant to simulate Norway tests	Designed to replicate a landslide dam failure

Table 2.2 shows a great deal of variation not only between the different embankment testing programs but also in the level of detail reported and the focus of the various experimental studies. It should be noted that the indicators in Table 2.2 were selected on the basis of comparison for the physical modeling of earth embankments rather than the core set of variables which would be used for numerical analysis, such as the angle of internal friction, shear strength, and erodibility functions. They represent only the information required to physically make an attempt at duplicating the experiments. For the above studies, Table 2.3 summarizes the parameters which were varied between tests.

An item of concern with regard to the experimental programs listed above is the complete lack of uniformity they have with respect to the inflow characteristics and the reservoir size. While most do not report the size of the reservoir, many use a highly varied inflow, more often than not to achieve a constant reservoir elevation. However, it has been shown quite clearly breach morphology is sensitive to inflow characteristics (Froehlich, 1995; Wang and Bowles, 2006).

Table 2.3: Test Program Variable

Study	Parameter(s) Varied
Visser, 1998	None.
Mohamed *et al.*, 1999	Crest width (and gradation, though possibly not intentionally).
Hahn *et al.*, 2000 (Outdoor Flume)	None.
Hahn *et al.*, 2000 (Full Scale)	Gradation and soil type.
Tingsanchali and Chinnarasri, 2001	Downstream slope, gradation, and initial head over the crest of the dam.
Franca and Almeida, 2002	None.
Coleman *et al.*, 2002	Gradation.
IMPACT, 2005 (Norway)	Soil type, crest height, upstream and downstream slope.
IMPACT, 2005 (Wallingford)	Soil type, crest height, upstream and downstream slope.
Davies *et al.*, 2007	Upstream and downstream slope.

The experiment by Visser (1998) was designed to examine the failure mode of a dike breached by overtopping. The main assumption of the investigation is that the core of the dike is composed largely of sand and therefore the clay surface covered in grass does not significantly affect the breaching process. The purpose of the experiment was to help calibrate a mathematical model based on a five stage breach process. The breach process as described by Visser is shown in Figure 2.4.

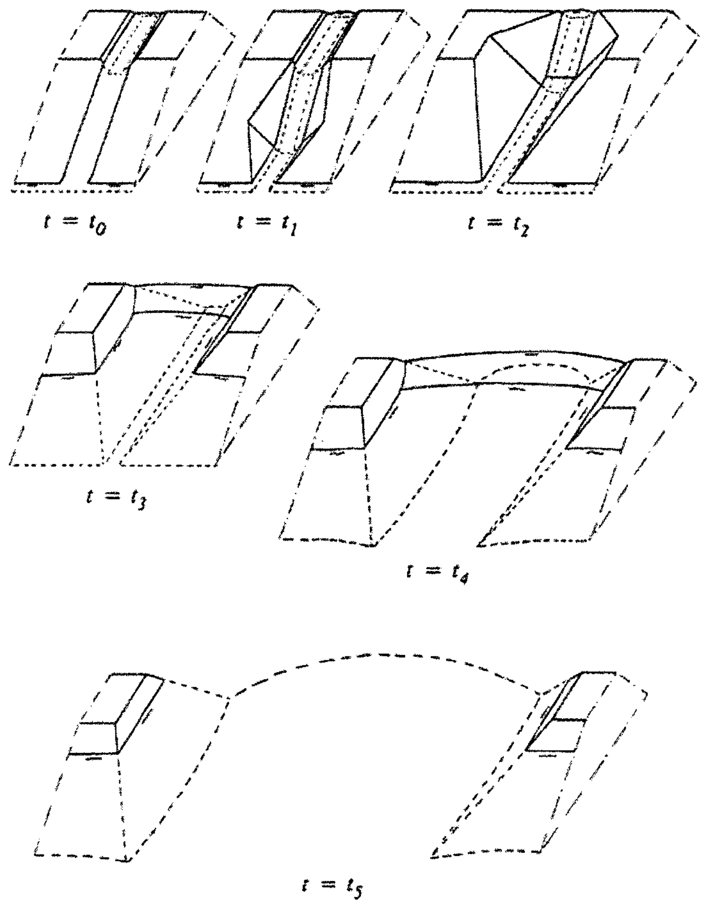

Figure 2.4: Process of Breach Growth in a Sand Dike (Visser 1998)

Visser describes the process generally as follows: from t_0 to t_3 the breach cuts itself into the dike, while at t_4 tailwater effects start to affect flow, and at t_5 the dike stops widening and flow is subcritical throughout the entire breach area. It is interesting to note that the Visser model shows a fairly constant breach width at the downstream end of the breach channel from t_0 to t_3. In this case, the breach widens starting near the middle of the embankment and progresses upstream and only once the crest has been fully washed away at t_3 does the downstream toe of the embankment start to undergo significant erosion. It should also be noted that Visser describes most of the discharge occurring during stages IV and V (from t_3 to t_5).

Erosion in the vertical direction is shown in Figure 2.5. In this case, the angle of the downstream slope increases from β_o to β_1 as erosion progresses. β_1 is described simply as a limiting erosion angle and the suggestion is given that it could be equal to the angle of internal friction, φ. As with the lateral erosion characteristics, most initial mass erosion takes place near the center of the embankment and, as such, β on the upper half of the embankment reaches β_1 more quickly.

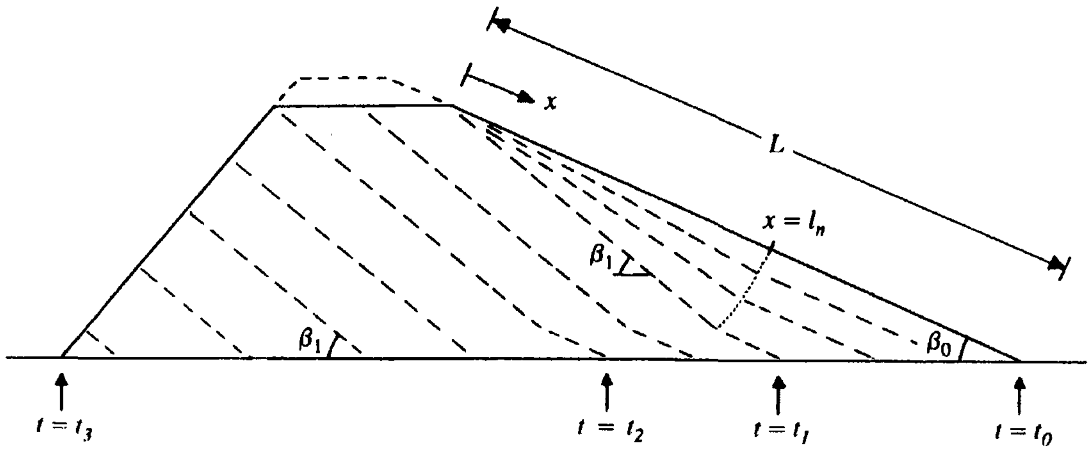

Figure 2.5: Vertical Erosion Characteristics (Visser, 1998)

In addition to the mathematical model, Visser plotted the breach width against time for both the laboratory experiment as well as a larger scale experiment conducted in the Zwin Channel tidal outlet, as shown in Figure 2.6. The time stamps corresponding to stages described in Figure 2.4 are also shown. In both cases, there is a lag where the breach does not widen (presumably, this constant width is the width of the pilot channel). Also, with respect to the figure from the lab test, there is a lack of smoothness, presumably due to sudden breach widening due to slope failures which may be more dramatically measured at the smaller scale.

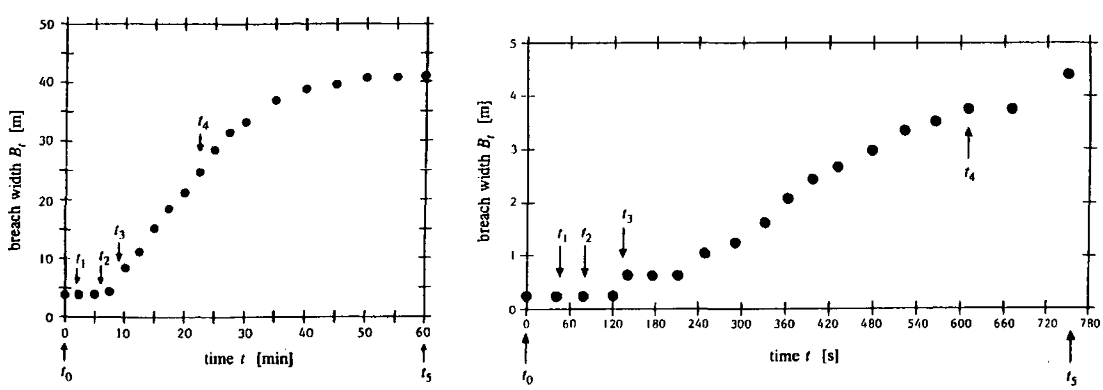

Figure 2.6: Increase of Breach Width in the field (left) and laboratory (right) (Visser, 1998)

The study by Mohamed *et al.* (1999) involved three tests which were largely used to develop a better understanding of breach mechanics. This seemingly casual approach to physically modeling embankment breaches is evidenced by the used of very steep 1:1 slopes on both the upstream and downstream sides. Even when constructing rock embankments, such a slope is not recommended.

Like Visser in Figure 2.4, Mohamed *et al.* found that the erosion of the breach side slope was not constant. One key difference, however, was that they found that the maximum breach width occurred at the bottom of the breach and that the minimum breach width was found at the crest. Also, they determined that the breach side slope erosion was due to a combination of continuous erosion, as well as slope instability and that the breach width at the crest grew significantly larger due to those slopes failures.

It is strange, however, that the tests by Mohamed *et al.* apparently used different sands from one test to another as shown by the variance in D_{50} (300μm-500μm) they reported. They also did not publish much in the way of experimental data beyond a qualitative high level overview. In fact, the present study conducted a similarly high level overview experiment in our experimental program just for interest's sake, as explained in Section 6.3. This lack of published data makes the contributions of this paper to the field of physical dam breaching rather limited.

The study by Hahn *et al.* (2000) involved a flume test series as well as a large scale test series. For the flume tests, the experiments were conducted outdoors with a fairly common setup as shown in Figure 2.7. This portion of their study focused mainly on qualitative observations of erosion characteristics of fine, mildly cohesive sediment (c = 1.4 kPa). A point gauge was installed on a carriage in order to take measurements of the water surface as well as the breach profile during the test.

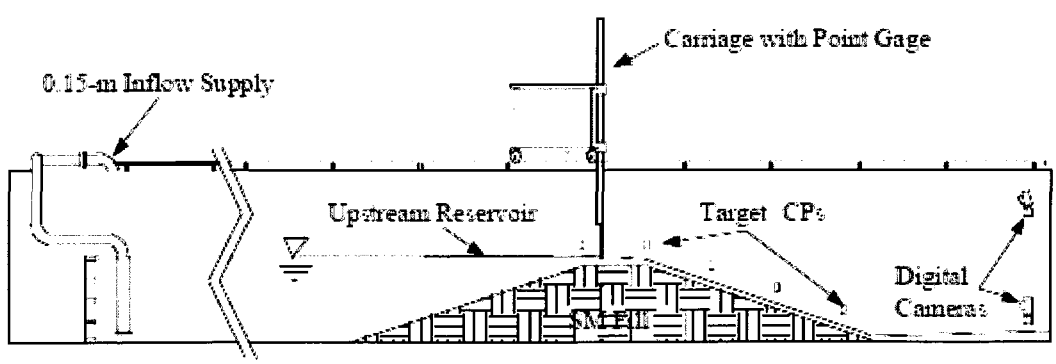

Figure 2.7: Cross-section of Typical Flume Embankment Overtopping Test Setup (Hahn *et al.*, 2000)

While taking measurements during the test might seem like adding an unnecessary bias to the results, it should be noted that erosion of cohesive sediment takes place much more slowly than erosion of non-cohesive sediment, which would reduce the potential for bias in the overall results. Unfortunately, the authors reported very little on these flume tests. Digital cameras were also utilized for this test and were set to take photos every 1 to 3 minutes. While these photos were taken to help augment the quality of the analysis at a later date, no follow-up paper where the photos might have been used was found.

Hahn *et al.* also conducted a series of large scale tests where the characteristics of breaches in cohesive soil were observed. With respect to the soil they used for the testing, it should be noted that it was highly variable between the three tests. The angles of internal friction, φ, varied from 13.3° to 26.5°, the cohesive strength, c, varied from 0.8 kPa to 10.3 kPa, and some samples did not have a measurable plasticity index, I_p. In addition, for the large scale tests, jet erosion tests were conducted according to ASTM D5852-95 to determine the erodibility of the soil. Jet erosion tests are described in more detail in Section 2.4.

The qualitative observations did show a difference in the erosion characteristics for cohesive sediment, however, as described in Figure 2.8. In Stage B, striations are formed on the downstream side which then formed into steps in Stage C. The steps gradually become a single step in Stage D which migrates upstream until the breach progresses to the upstream toe in Stage F. This process is known as headcut erosion and is the same process described by Al Qaser (1991).

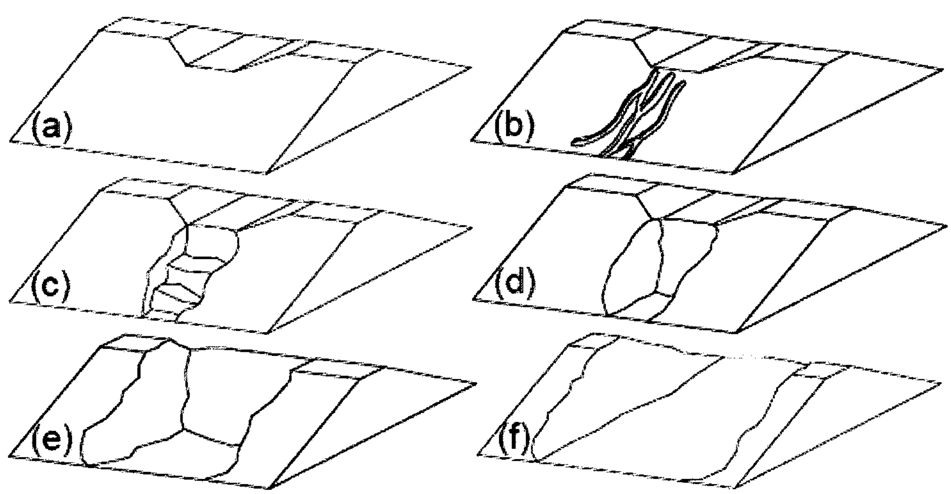

Figure 2.8: General Breach Stages for Cohesive Sediment (Hahn *et al.*, 2000)

Tingsanchali and Chinnarasri (2001) constructed a one-dimensional numerical model for dam breaching and calibrated it using a series of laboratory tests as well as a case study from the Buffalo Creek dam failure. They note that one of the main shortfalls of the existing literature is that there is "no readily available sediment transport formula for calculating erosion of dam surface due to overtopping discharge [for supercritical flow]." In their experiments, they fixed the height and crest width of the dam and varied the downstream slope as well as the initial head over the crest and the sand used for construction.

Interestingly, in order to calculate the shear stress initially applied to the embankment, the authors first constructed embankments out of plywood and glued sand to them to simulate the correct roughness. These runs enabled a Manning's roughness coefficient to be determined for each sand. It should be noted that, in the FLDWAV model designed by Fread (1998), there is a variation with depth of the Manning's coefficient. This variation suggests that during the course of the breach the roughness value might change.

Because the experiments were only used as calibration for a numerical model, little is known about the differences that were determined in the breach characteristics due to changes in downstream slope or grain size. The authors instead focused their efforts on the changes that occur in the sensitivity analysis of their model.

Franca and Almeida (2002) conducted their experiment using a rockfill dam. It is interesting to note that for rockfill dams, due to the larger grain size, proper scaling of the embankment is actually possible using Froude scaling. The authors found that the failure mechanism is very different from that of non-cohesive sands and cohesive sediment as determined by Visser (1998) and Hahn *et al.* (2000) respectively. The outflow hydrograph contains a number of seemingly random peaks which occur as slopes fail. Initially, there is a small breach which, after being sustained for a few minutes, continues to cause damage to the embankment and results in a second peak of similar flow.

It should be noted that the embankment experienced damaging effects due to seepage before the pilot channel was reached and the breach started to form. This weakening of the slopes of the embankment could have contributed to the irregularity of the breach outflow peaks and the duality of the breach formation.

The final configuration of the breach was also different than that seen in earthfill embankments. The authors in this case chose to relate the final breach configuration to the height of the dam. The breach top width was approximately 2.25 times the dam height and the average breach width was 1.70 times the dam height. Only the top 80% of the dam was eroded away. They found that the lateral slope was slightly smaller than the angle of repose. However, there were also some areas where the side slope was nearly vertical.

Coleman *et al.* (2002) had the unique idea of halting the breach erosion process at different times during the breach in order to take surface measurements of the eroded dam. The experiments were also unique in that they positioned their embankment right at the edge of their stilling basin so that there would be no tailwater effects and possibly no hydraulic jump due to the free overfall. This positioning does not seem to be due to any technical breach consideration but rather seems to be a limitation of the size of their flume which was only 12 m long, of which nearly 1.7 m was the base of the embankment.

The authors also used an overflow side channel spillway so that a constant head was generated at the embankment crest. The level of the reservoir just downstream of the side channel spillway was monitored using a water-level probe. With this addition, despite the small size of their flume, they were able to simulate the effects from an infinitely large reservoir.

In order to stop the breaching process, the authors used a flap gate positioned at the upstream toe of the embankment which could be raised quickly to stop the breach. The embankment was then measured using an electronic surface profile measurement system. The three-dimensional rendering of the breach can be seen in Figure 2.9 with the downstream direction to the right.

Contrary to Visser's (1998) analysis, the largest breach width occurred at the crest and the smallest breach width occurred at the toe of the embankment. Also, at the upstream end of the breach channel, the profile cut into the embankment was curved around the back of the breach, indicating that the breach flow funneled into the breach channel. While this curved pattern is clearly visible at time 113s, it becomes much less apparent afterwards (Figure 2.9). It should be noted that the boundary next to the breach was in fact a glass wall which was installed for profile viewing.

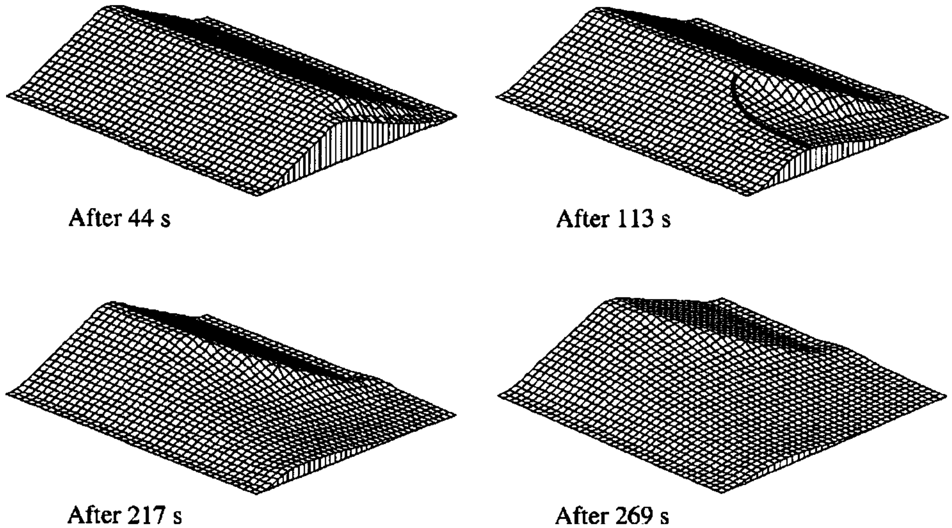

Figure 2.9: Breach Development for Coarse Sand Embankment (Coleman *et al.*, 2002)

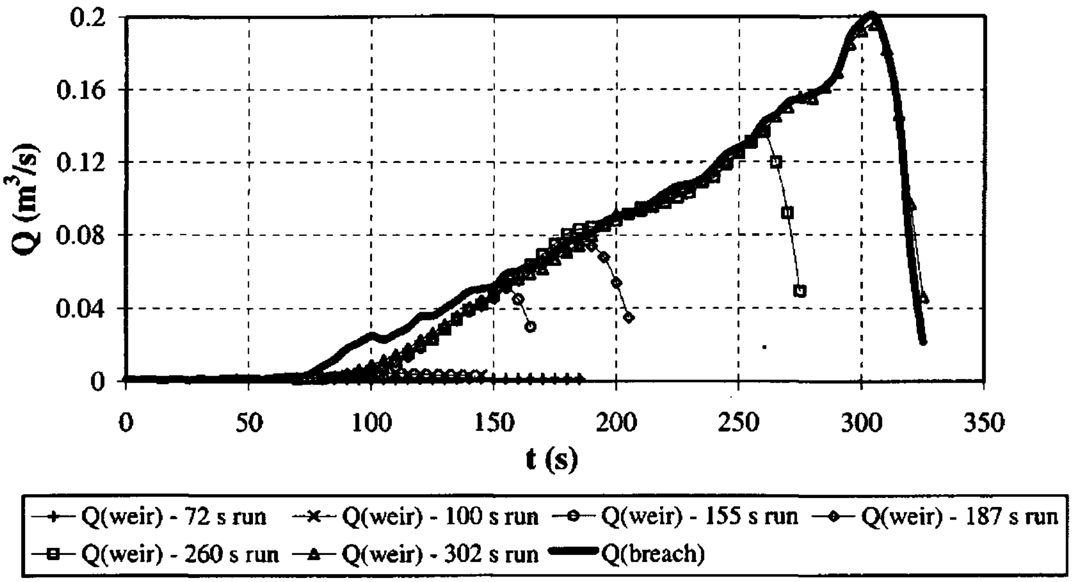

Figure 2.10: Flow Rates for Medium Sand Embankment (Coleman *et al.*, 2002)

Figure 2.10 shows that there was excellent duplicability within these experiments. Even with 6 separate tests stopped at different times during the breach, each successive test generally follows the same breach outflow path.

The experiments conducted by the IMPACT (2005) study are summarized by Morris *et al.* (2007). The study was comprised mainly of five large field tests accompanied by 22 supporting laboratory tests of which most tested overtopping failures, but some were devoted to piping failures. For the large scale tests, they used movement sensors to determine the phases of breach development and also used digital camera and video to monitor the downstream face of the dam upon which had been painted a grid for special coordinate determination.

They determined that flow through the breach channel is controlled by a curved weir at the upstream end of the breach channel, much as was found in the experiments of Coleman *et al.* (2002). This weir section can be seen in Figure 2.11. They also determined that once a breach is more fully formed that there is minimal sediment transport through the middle of the breach channel and that lateral erosion dominates as shown in Figure 2.12 where the muddy areas indicate greater transport. Therefore, they determined that sediment transport cannot be uniform across the entire beach section as some models suggest.

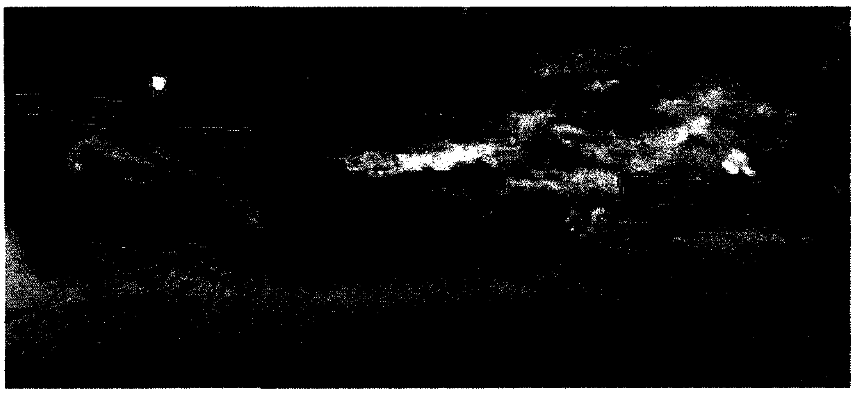

Figure 2.11: Weir Control Section (Morris *et al.*, 2007)

Figure 2.12: Lateral Erosion of Embankments (Morris *et al.*, 2007)

They also confirmed that the headcutting process described by Hahn *et al.* (2000) occurs for both the large scale tests and the laboratory tests. They also showed in the laboratory tests that the degree of compaction can affect the headcut erosion process. They found that by decreasing the level of compaction by half, the headcut erosion rate increased by 160%. The results from the IMPACT study have not as yet been completed and, as such, many of the details of the analysis are not yet available for review.

Davies *et al.* (2007) conducted laboratory experiments on the breaching of landslide dams. While many experimental setups have been conducted in straight, rectangular flumes with a null slope, Davies *et al.* sought to model actual landslide dams with as great a degree of physical accuracy as possible. While the detailed topography could not be modeled at 1:130 scale, the side slopes were modeled as a V shape to reflect the slopes of the valley.

However, the landslide was composed largely of cohesive sediment with a cohesive strength of 20 kPa. While at 1:130 scale, the model cohesion would only need to be 0.15 kPa. Such an internal force is effectively nil. However, by using non-cohesive sediment to represent the landslide dam, Davies *et al.* were not able to reproduce headcut erosion as would be expected of that type of sediment. There were also issues with accurately scaling the reservoir of the dam for which they attributed their underestimation in outflow duration compared to their case study. Nevertheless, they claimed to achieve good estimates with respect to the peak discharge.

2.3.1 Method of Construction

There are few papers available that specifically describe the method of construction of embankments constructed for breach testing as shown in Table 2.4. Many do not reference the unit weight of their material or the height of the lifts used in the compaction process and none make mention of the method of compaction.

With a lack of information as presented in Table 2.4, it is not possible to duplicate the experimental results. Moreover, it has been shown that for cohesive material there is a significant difference in the rate of breach formation (Morris *et al.*, 2007). This study will endeavor to determine what the effects of compaction are on non-cohesive embankment breaching.

For some of the test programs, we can assume that the density of the material, and hence its compaction, were high based on the slopes which were achieved. In the Mohammed *et al.* (1999) study, 1:1 slopes could only have been maintained with sand if compaction energy was high. If the dam were simply constructed of loose, dry material, it would not be able to hold a slope beyond the angle of repose. In addition to the factors listed in Table 2.4, water content, too, plays a key role in determining the density of the embankment as well as the maximum slope which can be achieved after compaction.

A more complete review of geotechnical characteristics as they pertain to embankment dams and breaching can be found in Section 2.5.

Table 2.4: Methods of Construction

Paper	Compaction Method	Lift Height (mm)	Standard Proctor Density (%)	Unit Weight (kN/m3)	Notes
Visser, 1998	NA	NA	NA	NA	No information available on construction methods
Mohamed *et al.*, 1999	NA	NA	NA	NA	Suspect high Proctor density if 1:1 slopes were maintained
Hahn *et al.*, 2000 (Outdoor)	NA	NA	NA	16.7-17.7	Unit weights are maximum density from Proctor tests
Hahn *et al.*, 2000 (Full-Scale)	NA	130	94	17.2-17.6	Unit weights are maximum density from Proctor tests
Tingsanchali and Chinnarasri, 2001	NA	50	NA	NA	Moisture supplied by spraying – uncertain to what water content
Franca and Almeida, 2002	NA	NA	NA	NA	No information available on construction methods
Coleman *et al.*, 2002	NA	NA	NA	25.7	Each embankment compacted to the same degree
IMPACT, 2005 (Norway)	NA	NA	NA	NA	No information available on construction methods
IMPACT, 2005 (Wallingford)	NA	NA	NA	NA	Suspect high Proctor density if steep slopes were maintained
Davies *et al.*, 2007	NA	NA	NA	NA	No information available on construction methods

2.3.2 Breach Initiation

As shown in Table 2.5, there is no uniformity which can be determined in how previous studies have initiated the overtopping breach of the earth dams. In many cases, a notch is the favoured mechanism, but not in all cases. Moreover, while a notch or pilot channel may represent an easier way of experimentally modeling a breach, it is not an accurate way. This lack of uniformity urges the compelling question of this document which is to know what effect can be expected from these variations.

There are generally three ways in which previous studies initiated their breaches: notches, pilot channel, and uniform flooding. Notches vary in size and shape though most researchers seem to favour a trapezoidal shape. Notches are simply cuts in the crest which terminate at a known elevation on the embankment. Conversely, a pilot channel incorporates a notch at the crest but also continues the shape along the downstream slope to the toe of the dam so as to create both the initial breach at the crest and the initial breach channel along the downstream slope.

Tingsanchali and Chinnarasri (2001) are unique in that their initiation involves initiating an overtopping failure with a known head over the crest. They used a plate to back up the reservoir to the desired elevation using an electronic meter to measure the water surface elevation and then released a uniform head across the top of the entire embankment. While innovative and suited to their search for supercritical flow characteristics, it is also the most unrealistic manner of initiating a breach. In fact, it becomes not so much an embankment breach test as it becomes a test of supercritical flow parameters as, due to the roughly uniform overtopping characteristics, lateral erosion will be minimal, especially when compared with vertical erosion.

Table 2.5: Breach Initiation Mechanisms

Paper	Initiation Method	Shape	Dimensions (mm)	Notes
Visser, 1998	Pilot channel	Rectangular	100 wide and 30 deep	Pilot channel cut next to glass wall
Mohamed *et al.*, 1999	Notch	NA	NA	-
Hahn *et al.*, 2000 (Outdoor)	Notch	Trapezoidal	150 high x 900 wide base, 3:1 side slopes	-
Hahn *et al.*, 2000 (Full-Scale)	Notch	Trapezoidal	460 high x 1830 wide base, 3:1 side slopes	-
Tingsanchali and Chinnarasri, 2001	Uniform over top width	NA	30 and 50 above dam crest	Not a realistic initiation mechanism
Franca and Almeida, 2002	Notch	NA	200 wide	-
Coleman *et al.*, 2002	Pilot channel	Triangular	20 deep	Pilot channel cut next to glass wall
IMPACT, 2005 (Norway)	NA	NA	NA	No information available on breach initiation
IMPACT, 2005 (Wallingford)	notch	NA	NA	-
Davies *et al.*, 2007	NA	NA	NA	No information available on breach initiation

Both Visser (1998) and Coleman *et al.* (2002) placed their pilot channel next to a glass wall at the side of the their flumes in order to both maximize the lateral erosion potential for their facility and make the breach process more visible to cameras and video equipment. While this placement may be convenient for visual measurement purposes, the friction effects from the side wall are presumed to be different than what would normally be seen in the centerline of a breach channel and one must wonder on the effect this friction change has on breach morphology. This study will endeavor to show the effects of the side wall.

Hahn *et al.* (2000) conducted two test series using smaller scale flume tests as well as larger scale tests. For the flume tests, the notches they used 900 mm wide and 150 mm high with 3:1 side slopes. When scaled against the height of their embankment, the notches are 1:1 wide and 1:6 high. The notches used for the large scale tests were 1830 mm wide by 460 mm high. When scaled against the height of their embankment, the notches are approximately 4:5 wide and 1:5 high, again with 3:1 side slopes. This difference is puzzling and is the primary reason that the two test series were separated for the tabular analysis.

2.4 Erosion Rates and Sediment Transport

Generally, sediment can be classified as either cohesive sediment or non-cohesive sediment. Non-cohesive sediments are generally larger diameter sediments such as sands and gravels which are arranged as individual grains normally composed mostly of silica (quartz). The strength or erodibility of these sediments is considered to be mainly a function of the physical properties of the particles such as size, shape, density, porosity, and fall velocity (Zhu *et al.*, 2008). Cohesive sediments are composed of fine particles, such as silts and clays, which have a more complex mineralogy consisting generally of aluminum silicates. These sediments derive most of their strengths from electro-chemical cohesive bonds between the particles. However, it has been found that a soil can exhibit cohesive properties if it is made up of as little as 10% cohesive material (Bui, 2000).

Due to the differences in how non-cohesive and cohesive sediments derive their strength, the manner in which each type of sediment is eroded and is transported downstream also differs. Much of the existing literature has been conducted on non-cohesive sediments. The physics of cohesive sediment erosion and transport is so complex that the understanding and modeling of these processes is still limited (Zhu *et al.*, 2008). Moreover, much of the research into cohesive sediment transport has been conducted for coastal applications. However, it has been found that sediment transport parameters differ based on the salinity of the transporting fluid (Kelly and Gularte, 1981; Debnath *et al.*, 2007), meaning it is difficult to apply coastal studies to fresh water streams and reservoirs where most dams are located.

Erosion rate is defined generally as the mass of sediment removed from an area over a given time, expressed in kg/m^2/s. Sediment transport is defined as the mass which travels across the unit width of a plane (such as a river cross-section) over a given time, expressed in kg/m/s. While the mechanics of moving sediment particles is similar for both of these concepts, they are still quite different, especially with regards to how sediment transport focuses on both the entrainment and deposition characteristics of the sediment while erosion considers only entrainment and removal of sediment. Given that sediment transport equations are designed to consider deposition and a long upstream source of sediment, it is unclear if they can or should be used for the purposes of modeling dam breaches.

Generally, sediment movement takes place once the shear stress, τ, on the sediment surface (normally a river or creek bed in most literature sources) exceeds a certain limiting value referred to as the critical shear stress, τ_c. This incipient motion condition is generally derived using a stress balance. Shields (1936) expressed incipient motion as a curved relationship between dimensionless shear stress, τ_*, and boundary particle Reynolds number, Re_*, as shown in Figure 2.13. The parameter u_* in the boundary Reynolds number is defined as $u_* = \sqrt{\tau / \rho_w}$. The Shields curve is derived for uniform sediment which is largely made up of quartz and, as such, its applicability to finer sediments is debated (Hanson and Simon, 2001).

There are two types of sediment loading which can occur in a watercourse: bed load and suspended load. Bed load represents the mass of particles that are transported at the bed surface, while suspended load represents the mass of particles which have been entrained by the fluid. Generally, the concentration of sediment will be highest near the eroded surface (most often the bed) and will decrease exponentially with distance away from that surface.

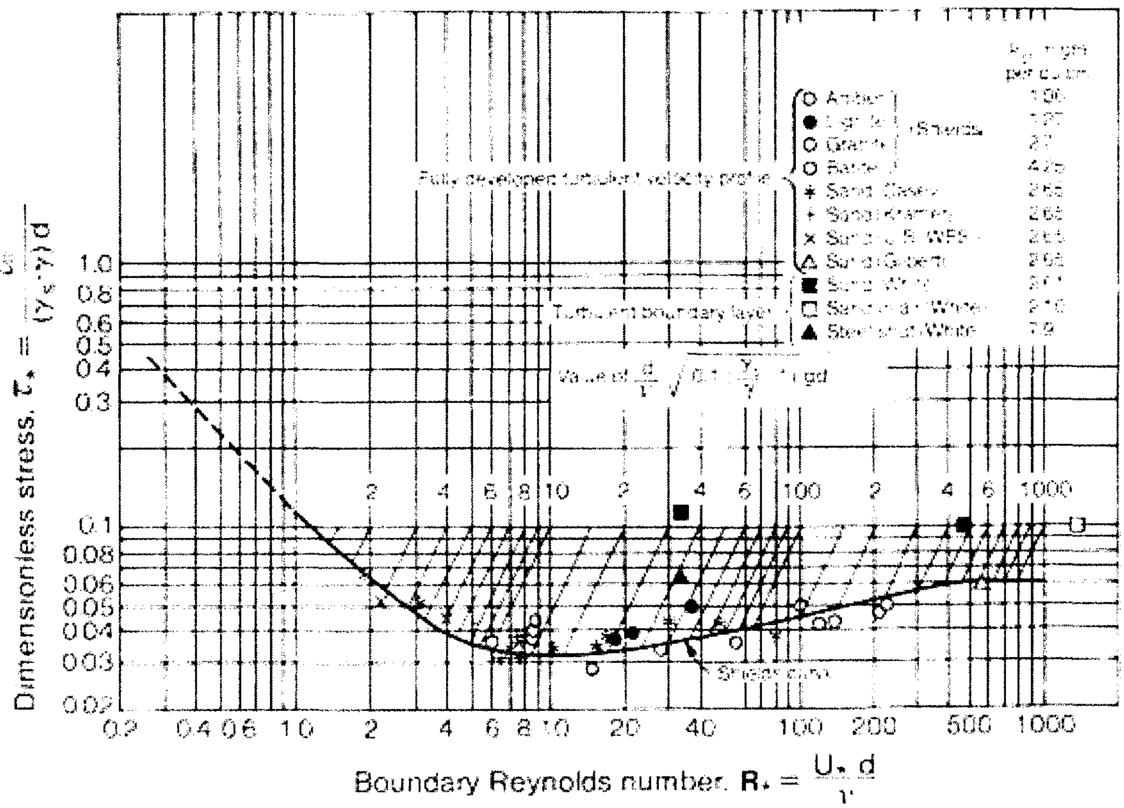

Figure 2.13: Shields Curve (Shields, 1936, reproduced from Prasuhn, 1992)

Experimentally, sediment transport rates can be measured in a number of ways including, but not limited to, physical sampling, acoustics, particle tracers, and scour monitors. Physical sampling can be conducted with devices such as the Helley-Smith (Helley and Smith, 1971) which is a device which can be lowered onto a surface to sample the bedload transport, or a device that is permanently installed on the bed such as a pit trap (Reid *et al.*, 1980). Other physical sampling devices such as a Delft fish or a Delft-Nile Sampler (Van Rijn, 1993) can be used to obtain the suspended load portion of total sediment transport.

Wan and Fell (2004) list several experimental methods for determining the erodibility of soils: flume tests, jet erosion tests, rotating cylinder tests, soil dispersion tests, hole or crack tests, and erosion function apparatus. Each of these methods is described in greater detail below. Hanson and Hunt (2007) comment that the most dependable method is to use a large open channel flow test with the soil of interest forming the entire bed, though this method is often not possible due to cost and space constraints.

Flume tests, such as those conducted by Gibbs (1962) and Kandiah and Arulanandan (1974) are designed to measure erosion in channelized environments such as canals.

Sekine and Iizuka (2000) used a 4.0 m long flume with a 0.1 m x 0.1 m rectangular cross section for their tests with a sample which was 0.5 m long and 30 mm high, spanning the width of the flume. Flow was passed over the test section and velocity measurements were taken so that shear stresses could be extrapolated to the bed using the log law. Measurements of the bed elevation were also taken to obtain the depth of erosion with respect to time for different average velocities. They found that erosion rate is not constant as shown in Figure 2.14. Debnath *et al.* (2007) used an *in-situ* variation of this type of test which is discussed in more detail in Section 2.4.2.

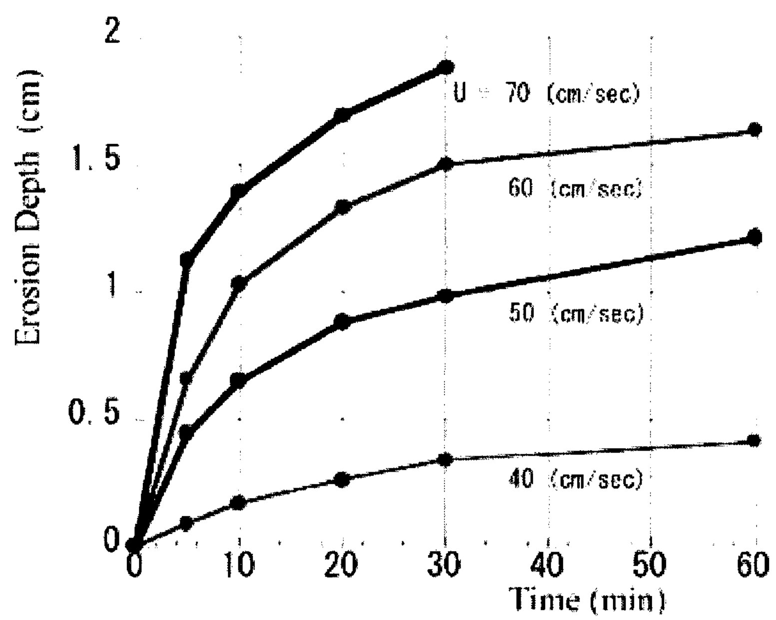

Figure 2.14: Time Variation of Erosion Depth (Sekine and Iizuka, 2000)

Jet erosion tests such as the one proposed by Hanson and Hunt (2007) are designed to simulate water plunging over a vertical face as is often the case with the headcut erosion formation in cohesive soils. This test involves compacting the soil in a standard mold and then submerging it in a small tank. Erosion is initiated by jet flow from an above orifice with a static head that plunges down against the submerged soil sample. Scour depth is measured at given time intervals in order to determine the rate of erosion. It is important to note that this test can be used in the field to test *in situ* samples as well as in the laboratory to test compacted samples.

Rotating cylinder tests such as those conducted by Chapuis and Gatien (1986) are designed to study the relationship between erosion characteristics and soil properties. With this type of test, the properties of the soil can be more easily controlled. The principle of the test is to use annular flow between two concentric cylinders to induce shear stress and erosion. The inner cylinder is stationary and holds the often remolded soil sample while the outer cylinder rotates and shear stress is generated at the soil surface due to the torque required to hold the soil sample in place (Chapuis and Gatien, 1986).

Soil dispersivity tests such as the pinhole dispersion test do not truly measure erosion as much as they measure the likelihood of initiation of erosion (Wan and Fell, 2004). Hole or crack tests, such as the slot erosion test and hole erosion test, shown by Wan and Fell (2002), are designed to simulate the initiation of piping failures in embankments. The hole erosion test is conducted by compacting the soil sample in a standard Proctor mold and then drilling a 6mm longitudinal hole through the soil sample. A known head of water is applied to the drilled hole which causes it to widen with time due to the applied shear stress. The erosion rate is then a function of how quickly the hole widens.

An erosion function apparatus such as the one constructed by Briaud *et al.* (2001) is designed to measure erosion rates around hydraulic structures such as bridge piers. These apparati involve pushing a soil sample so that the top 1mm of the sample is exposed to the flow of a pressurized pipe at a given velocity. The time it takes to erode that 1mm of sample material is measured and then the velocity is increased and the next 1mm of the sample is pushed into the flow. This process is designed to measure the vertical erosion rate of the soil in mm/hr rather than the mass erosion rate (though it can be used for such a purpose).

Given that this study is not intent on measuring pier effects, piping, initiation of erosion, or headcut erosion, only a flume study was considered to be appropriate for this test series. It should also be noted that sediment transport often infers the movement of non-cohesive sediment whereas erosion rate commonly infers the movement of cohesive sediment.

2.4.1 Non-cohesive Sediment

Different numerical breach models use different sediment transport equations. The NWS BREACH model by Fread (1988), for example, uses the Meyer-Peter-Mueller (MPM) method as modified by Smart (1984) to calculate sediment transport during the breach process. Other breach models use different sediment transport models including empirical formulations based on their experimental work, as shown in Table 1.1. Some models use multiple methods such as Wang and Bowles (2006), which uses a method by Chen and

Anderson (1987) to determine erosion rate and then uses the Smart method to determine the transport capacity of the overtopping flow. Given that many used the MPM formula, it is discussed below.

Meyer-Peter and Mueller (1948) developed a widely used empirical sediment transport method for slopes ranging from 0.04 to 2.0% based on data from experiments conducted over sixteen years. The formulation is presented below. "The data pertain to both sediment of uniform size and size mixtures, various values of sediment specific gravity, and cases both with and without the presence of bedforms" (Wong and Parker, 2006).

$$q^* = 8\left[\frac{q'_w}{q_w}\left(\frac{K_b}{K_r}\right)^{1.5}\tau_* - 0.047\right]^{1.5} \qquad [2.5]$$

In Equation 2.5, q^* is the dimensionless volume bedload transport rate per unit width. It should be noted that 0.047 is the common value for the critical dimensionless shear stress for quartz based mixed-size sediments such as sand. The parameter q_w is the volume discharge per unit width, q_w' is the volume discharge per unit width after a correction factor has been applied for side wall effects, K_b is the Manning-Strickler coefficient of roughness for the bed region and K_r is the Manning-Strickler coefficient of bed roughness associated with skin friction only.

Tingsanchali and Chinnarasri (2001) determined that the best existing numerical model to use for sediment transport purposes was the Smart method. Smart (1984) presented a modification of the Meyer-Peter and Muller equation for use in steep channels with slopes between 3 and 25% (4:1 slope). The equation was developed because it was determined that the Meyer-Peter Muller equation underestimates transport for slopes greater than 3%. The data were generated using a tilting flume which was 6.0 m long and 0.2 m wide. Sediment was supplied using a hopper and the sediment feed rate was monitored until it came to equilibrium and was determined to be the sediment capacity of the channel at a particular slope. It should be noted that for some materials, the entire bed started to fail in a slide with slopes 20% and higher and these results were not included in the formulation of the equation below. The sediment size to which the equation best applies is greater than 400μm.

$$q^* = 4\left[\left(\frac{D_{90}}{D_{20}}\right)^{0.2} S^{0.6}\frac{u}{u_*}\tau_*^{\ 0.5}\left(\tau_* - \tau_{cr}\right)\right] \qquad [2.6]$$

S is the channel slope, u is the means channel velocity and u_* is the shear velocity.

2.4.2 Cohesive Sediment

While the erosion characteristics of non-cohesive sediments such as sands can be said to be generally well understood, the erosion characteristics of cohesive sediments like clays are much more complex. In addition to the forces of gravity which act on the fluid as well as the bed material there are internal electrochemical and biological forces within a clay which cause it to bind to itself and have much greater resistance to the shear stress imposed by the fluid flowing overtop of it. These electrochemical and biological processes are in turn affected by a great multitude of factors including water content, water salinity, suction, and mineralogy.

Given that dams are generally rather large, building prototypes for testing is often not economically feasible. Therefore, scaling methods are used in order to create a simulation at a smaller, lab scale. However, while Froude scaling is possible for non-cohesive sediment up to a certain extent, it is virtually impossible for cohesive sediment due to the chemical bonds which bind the material together. Studies have shown that the application of Shields' diagram to cohesive soils underestimates τ_c and therefore significantly overestimates the amount of erosion (Hanson and Simon 2001). In general, it is thought that the easiest way to scale such sediment is to scale the gravitational forces, which is to say conduct the experiment in a centrifuge or on a different planet. For obvious reasons, these methods are not truly feasible.

Generally, erosion of cohesive sediment has two components: mass erosion and surface erosion. Mass erosion is the process whereby flocs or aggregates (simply a large clump of particles attached together) break off from the bed and get pushed downstream. This process is likened to bed load. Surface erosion is the process by which individual particles are entrained in the flow and are transported downstream. This process is likened to suspended load.

It is currently uncertain how many factors affect the erosion of cohesive soils and how great an impact these factors have on the two erosion processes. Berlamont *et al.* (1993) proposed a list of twenty-eight parameters for the characterization of cohesive sediments. Heinzen (1976) proposed that the following factors are the most significant in cohesive sediment erosion: clay percentage (the amount of sediment which is clay, not to be confused with clay fraction which is often associated with the percent fines), chemical composition of the pore fluid, presence of organic matter or other cementing agents, grain-size distribution, thixotropy and stress history of the soil matrix or streambank, and temperature, pH, and water content of the soil matrix. Mostafa *et al.* (2008) proposed the following relationship for erosion resistance, τ_R with emphasis on the moist bulk density, ρ_b.

$$\tau_R = f\left(\Delta S, C, \rho_b, D_{50}, w, w_{LL}, w_{PL}, g, \rho_w, \rho_f, u_b, u'_b, t'_b\right) \qquad [2.7]$$

ΔS = salinity difference
C = clay content
P_b = moist bulk density
D_{50} = mean sediment size
w = water content
w_{LL} = liquid limit
w_{PL} = plastic limit
ρ_w = density of clear water
ρ_f = density of eroding water
u_b = near-bed time averaged velocity
u'_b = near-bed velocity fluctuation
t'_b = fluctuation time of turbulence burst

However, Briaud *et al.* (2001) did not observe much correlation between the parameters representing erodibility and the soil properties mentioned above. Instead, they found a better correlation between initial erodibility and critical shear stress. So, while the process of erosion itself is very complex, there is even disagreement about whether flow characteristics or sediment characteristics play the more dominant role in cohesive sediment erosion.

There is also no truly general form for an erosion rate equation. While separate equations can be constructed for each of the two components of erosion (mass erosion and surface erosion), it is more common to express erosion rate as a simple undivided summation of the two components. It is also easier to measure this total erosion rate in experiments. Many researchers have attempted to use the following general form for the erosion rate equation:

$$E = C_e\left(\tau - \tau_c\right)^n \qquad [2.8]$$

In Equation 2.8, C_e is an empirically calculated coefficient, as is the exponential factor, n. The parameter τ is the shear stress on the bed and τ_c is the critical shear stress of the sediment. Debnath *et al.* (2007) made some subtle additions to the equation that make C_e and τ_c both functions of depth relative to the bed elevation. Aberle *et al.* (2003) made note that their experiments showed a distinct increase in shear strength with the depth of the bed material and attributed this phenomenon to support the hypothesis of depth limiting erosion. Bui (2000) also notes that this addition is appropriate because cohesive bed material in streams is eroded layer-by-layer and that each layer has different properties due to the manner in which cohesive beds are formed over time. Banasiak and Verhoeven (2006) support this claim by showing that consolidation plays a key role in the erosion resistance of cohesive soils and that the physical characteristics of the sediment and the biogenic activity are stratified. Banasiak and Verhoeven (2006) also suggest that Equation 2.8 can be modified by omitting τ_c if sufficient spatial and temporal averages of the shear stress values are used.

Debnath *et al.* (2007) suggest an exponential relationship is more appropriate than a power relationship and use the very general form in Equation 2.9 where C_e and k_e are experimentally derived coefficients.

$$E = C_e e^{-k_e t} \qquad [2.9]$$

Equation 2.9 does not include the excess shear stress, as Equation 2.8 does, and is more suitable for the *in situ* experimental tests which have been conducted by Debnath *et al.*, because *in situ* measurements of the critical bed shear are difficult to make. For the purposes of this study, Equation 2.8 will be used. It is important to note, however, that the jet erosion tests and soil dispersion tests examined in Section 2.4 assume a linear relationship ($n = 0$) between erodibility and excess shear stress.

2.5 Geotechnical Considerations

In the following section, a basic review of soil mechanics is provided, which will provide insight to the thesis objectives and experimental procedures.

Soil can be generally divided into 4 groups based on particle size gradation: gravel, sand, silt, and clay. Anything larger than gravel is considered to be rock, and not soil. Gravels and sands are larger particles that can be seen individually with the naked eye (i.e. >0.075 mm) and are typically considered to be non-cohesive as they have no internal electrochemical bonds which bind individual particles together. Instead, they obtain much of their strength from internal friction between the particles in the soil matrix. Silts and clay, called fine sediments, are much smaller and derive much of their strength from electrochemical bonds rather than internal friction which is generally weaker than that of sands and gravels largely due to the orientation of the fine particles. Soil is generally considered to be a three phase system or matrix comprised of soil solids, water, and air. In unsaturated soils, a fourth phase called the contractile skin which represents the air-water interface is sometimes also considered (Fredlund and Morgenstern, 1977).

While hydraulic forces may be acting to destroy an embankment, resistance forces from the soil such as shear strength are also present. In order to make a proper risk assessment for the failure of an embankment dam, both the acting forces (hydraulic) and resisting forces (geotechnical) must be considered in detail. It is generally considered that the three main parameters which help to define the engineering behaviour of a soil are permeability, shear strength, and volume change (Vanapalli, 2008).

Much can be known about those three parameters by simply classifying the soil. Classification of coarse grained soils like sands and gravels is done by gradation or particle size. Particle size distribution is determined by sieving the soil with a number of standard sieves and is then applied to the Unified Soil Classification System (USCS) which was proposed by Casagrande in 1942 and is standardized using ASTM D-2487. A soil is considered to be well-graded if there is little uniformity in the gradation. A soil is considered to be poorly graded is there is a high degree of uniformity, which means there are many particles of similar size which make up the soil matrix. Well-graded soils are less permeable, have higher shear strength, and exhibit less volume change than poorly graded soils, which makes them much more desirable construction materials.

While sieves are appropriate for coarse soils, they are not as desirable for fine soils. Instead, a hydrometer is used to estimate the gradation of fine soils. A hydrometer uses Stokes law to indirectly estimate particle sizes under the assumption that they are spherical. Stokes law assumes that the density of the soil suspension decreases with time as the particles settle out of suspension (Vanapalli, 2006). Hydrometer analysis is performed using ASTM D-422. However, as the hydrometer test is only generally good to use as an estimate of soil gradation for fine grained soils, other means of classification have been made for these soil types.

The nature of a soil can be divided into four states based on moisture content: solid, semi-solid, plastic, and liquid (Das, 2002). Atterberg limits are the characteristics used under USCS to classify fine grained soils using those states. They are easily determined characteristics which define the liquid limit and plastic limit values of a fine-grained soil. Both are somewhat arbitrarily determined values. The liquid limit is the moisture content at which the soil acts more like a liquid than it does like a plastic substance. The plastic limit is the water content at which the soil begins to act more like a semi-solid. Liquid limit and plastic limit tests are governed by ASTM D-4318. It should be noted that fine grained soils are much more variable than coarse grained soils and, as such, the classification system adopted for them are not as useful in estimating the soil strength characteristics.

One of the geotechnical characteristics most used for hydraulic analysis is the specific gravity of the soil particles. Specific gravity, G_s, is the ratio of the unit weight of a given material to the unit weight of water. Common values for G_s of soils range between 2.6 and 2.9 (Das, 2002). In many cases for sand, the specific gravity for quartz (2.65) is simply assumed given that, most often, quartz makes up the vast majority of a soil matrix of sand.

Permeability is one of the three most important geotechnical characteristics and is related to the continuity and the tortuosity of the liquid phase in the soil matrix (Vanapalli, 2008). Following Bernoulli's equation, the total head at a point in water under motion can be given by the sum of the pressure, velocity, and elevation heads according to Equation 2.10.

$$h = \frac{u_w}{\gamma_w} + \frac{v^2}{2g} + Z \qquad [2.10]$$

In the case of soils, the velocity through the soil medium is very small and so the velocity head can be neglected (Vanapalli, 2008). Darcy's law builds on the Bernoulli Equation to express flow through a soil medium, as shown in Equation 2.11.

$$Q = kiA \qquad [2.11]$$

In this equation, i is the hydraulic gradient, A is the surface area, and k is the coefficient of permeability. In most situations, the area subjected to flow is well known, but a permeability test was developed to determine the coefficient of permeability for a given soil using a known flow and hydraulic gradient. For coarse grained soils, it is important to maintain a constant head above the soil sample as sands and gravels are rather rapidly draining soils. The constant head permeability test follows ASTM D-2434.

The coefficient of permeability is considered to be a function of void ratio (for saturated soils), as well as the degree of saturation and water content in unsaturated soils because flow can be visualized to take place only through the pore space filled with water

(Vanapalli, 2008). Thus, an unsaturated soil is less permeable than a saturated soil. The majority of an earth embankment is unsaturated.

Shear resistance is what gives soil strength. In a saturated soil, it is a function of the cohesive forces present as well as the internal friction resistance of the soil. The effective shear stress equation was defined by Terzaghi (1939), as shown in Equation 2.12.

$$\tau = c' + (\sigma - u_w)\tan\phi' \qquad [2.12]$$

c' = effective cohesion

σ = normal stress

u_w = pore water pressure

φ' = effective angle of internal friction

In most coarse grained soils, there is no effective cohesive element and so shear strength is derived from the internal friction alone. To determine the failure envelope of a given soil, a soil sample is sheared at different effective normal stresses. Unsurprisingly, as greater normal stress is applied, internal friction and shear resistance is increased, much the same way as putting more pressure on a smooth surface will help stop an object from sliding. A direct shear test conducted according to ASTM D-3080 is a good way to determine the effective shear stress parameters for coarse grained soils.

For unsaturated soils, the internal friction is a function of both the applied net normal stress as shown in Equation 2.11 as well as matric suction. Matric suction is a stress state variable which describes the free energy state of soil water that can be measured in terms of the partial vapour pressure of the soil water and the partial pressure of the pore-water vapour (Vanapalli, 2008). It is also commonly referred to as the negative pore water pressure and is often associated with the capillary phenomenon arising from the surface tension of water. Fredlund *et al.* (1978) proposed a modification to Terzaghi's equation which took into account both stress state variables, as shown in Equation 2.13.

$$\tau = c' + (\sigma - u_a)\tan\phi' + (\sigma - u_w)\tan\phi^b \qquad [2.13]$$

u_a = pore air pressure

φ^b = angle indicating the rate of increase in shear strength relative to matric suction

Both the angle of internal friction and the coefficient of permeability are a function of the density of the soil and how compact it is. The more compact the soil, the less permeable it is and the more resistant to shear it is. Hence, compaction is used as an effective means of constructing geotechnically stable foundations and slopes. Physically, compaction reduces the number of voids in the soil matrix and brings individual soil particles closer together. This process reduces the amount of water that can fill the voids and increases the infiltration path length which reduces permeability. Furthermore, the closer proximity of the individual particles causes more inter-particle contact and thus increases the internal friction.

Typically, the dry density of soil gradually increases up to a particular water content. This density is commonly referred to as the maximum dry density and the corresponding moisture content is termed the optimum moisture content (Vanapalli, 2006). This change in density relative to water content is due to the changes in orientation of soil particles at different moisture contents. Dry unit weight can be defined using Equation 2.14.

$$\gamma_d = \frac{G_s \gamma_w}{1+e} \qquad [2.14]$$

G_s = specific gravity of the soil
e = void ratio

The Standard Proctor test conducted following ASTM D-698 tests the density of a soil at a number of different water contents in order to determine the optimum moisture content for compaction. While the standard test uses a specific compaction effort of 594 kN·m/m^3, the test can be varied for a variety of compaction efforts. Equation 2.15 shows the formula for determining the energy of compaction (Das, 2002).

$$E = \frac{\text{Number of Blows per Layer} \times \text{Number of Layers} \times \text{Weight of the Hammer} \times \text{Hammer Drop Height}}{\text{Volume of Mold}} \qquad [2.15]$$

Another method of determining the density of soil is by conducting a sand cone test. The sand cone test is an *in-situ* test which can easily be conducted in the field, though unfortunately, it is a destructive test. The test involves digging out a hole in the soil and then filling it with a known mass of sand which has a known density in order to find the volume of the hole. All the material taken from the hole is then dried and weighed to obtain the dry unit weight of the excavated material. The sand cone test follows ASTM D-1556.

2.6 Blast Effects and Craters

An explosion is a phenomenon resulting from a sudden release of energy from sources such as gunpowder, pressurized steam, or even wheat flour dust. The release is sudden and happens so rapidly there is a local accumulation of energy at the site of the explosion. The accumulated energy is then suddenly dissipated in various ways including blast waves, propulsion (whether bomb fragments or rocket propulsion) and various forms of radiation (Kinney and Graham, 1985).

The size of an explosion (its yield) is defined by the amount of energy which is released (in units such as Joules or British Thermal Units), expressed using a scale which is relative to the energy released by a given weight of Trinitrotoluene (TNT). Customarily, the explosive power of a material is expressed as a percentage of the weight, and thereby explosive power, of TNT. Table 2.6 is a reproduction from the Blast Resistant Structures Design Manual (1986) produced by the Naval Facilities Engineering Command in the Unites States and shows some common explosives and their TNT equivalence.

A common explosive, ammonium nitrate fuel oil (ANFO, also commonly called a fertilizer bomb) is not represented on the table below but is worth noting given how often it is referred to as an explosive source which can be used by civilians. It has a TNT equivalence of 0.87 (Braimah, 2007). It should be noted, however, that the values presented in Table 2.6 are not universally recognized and that changes in those values (and the one cited for ANFO above) can change depending on the source used to reference TNT equivalence.

When an explosive is detonated, a blast wave is formed. Figure 2.15 shows a typical pressure-time profile for a blast wave detonated in free air. It is characterized by an abrupt pressure increase at the shock front followed by a quasi-exponential decay back to ambient pressure and a negative pressure phase in which the pressure is less than ambient (Ambrosini *et al.*, 2002).

Table 2.6: TNT Equivalences (NAVFAC, 1986)

Explosive Material	TNT Equivalent Weight [1]
Baratol	0.525
Boraticol	0.283
BTF	1.198
Composition B	1.092
Composition C-4	1.129
Cyclotol 75/25	1.115
DATB/DATNB	0.893
DIPAM	0.959
DNPA	0.752
EDNP	0.874
FEFO	1.149
HMX	1.042
HNAB	1.044
HHS	1.009
LX-01	1.222
LX-02-1	1.009
LX-04	1.007
LX-07	1.058
LX-08	1.406
LX-09-1	1.136
LX-10-0	1.101
LX-11-0	0.874
LX-14	1.119
NG	1.136
NQ	0.750
OCTOL 70/30	1.113
PBX-9007	1.108
PBX-9010	1.044
PBX-9011	1.087
PBX-9205	1.137
PBX-9404	1.108
PBX-9407	1.136
PBX-9501	1.129
Pentolite 50/50	1.085
PETIN	1.169
RDX	1.149
TETRYL	1.071
TNT	1.000

[1] Values are based on calculated heats of detonation

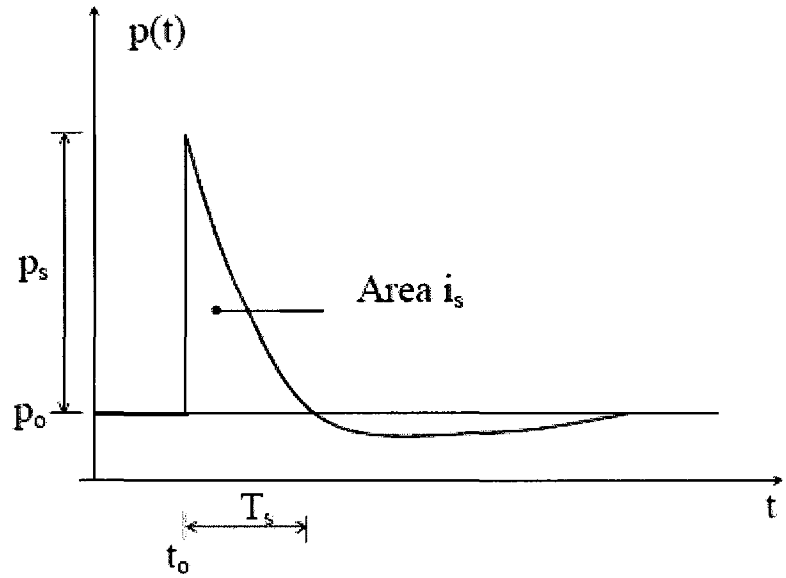

Figure 2.15: Pressure- Time Relationship in Free Air Burst

In Figure 2.15, p_o is the ambient temperature (normally atmospheric), p_s is the peak overpressure, T_s is the duration of the positive phase and i_s is the positive impulse. This relationship is often described using the Friedlander equation which has the form:

$$p(t) = p_S\left[1-\frac{t}{T_S}\right]\exp\left(-\frac{bt}{T_S}\right) \qquad [2.16]$$

Due to safety and expenditure concerns, there are only a select number of locations in a given country where explosives testing can be conducted. Even in these locations, it is often only small charges which can be used for the purposes of experimentation, though it is large blasts which are examined during the design process and during investigations. As such, most researchers use the Hopkinson's Scaling Law (also called the Hopkinson-Cranz Scaling Law) which gives the following relationship:

$$Z = \frac{R}{W^{1/3}} \qquad [2.17]$$

Z is the scaled distance, R is the range (m) from the blast centre to the target and W is the equivalent charge weight of TNT (kg). The relationship states that if an explosive with a charge mass W_1 is detonated at a range R_1 from a recording station, the explosive with a charge mass W_2 can be calculated for a distance R_2 provided that the explosives are of the same type and atmospheric conditions are the same at the times of detonation. It should be noted, however, that other scaling laws do exist (such as the Sachs Scaling Law), though Hopkinson's Law is most often used (Braimah, 2007).

2.6.1 Craters

A cavity is always formed during a blast regardless of whether or not the origin of the explosive is above the ground level (up to a certain limit after which little impact is seen on the ground) or below the ground level (up to a certain limit after which the cavity is located completely underground and is called a camouflet). Most public research into crater formation has been done for explosions originating underground (mostly in the mining sector). There is also a substantial amount of information which has been collected on crater formation by government sources. This research is classified and shared only within specific government agencies. Figure 2.16 shows a generic model of a crater.

Research focus into the impact of explosions has been directed more towards understanding explosions generated from below ground level. The mechanism associated with the formation of craters is complex. Errors of 10% are expected and errors of as much as 30% to 40% are common. The most important variables for crater formation are the charge weight, *W*, and *d*, the depth of the charge relative to the ground. Crater radius and apparent depth increase as *d* increases until a certain limit value after which they decrease rapidly (Bull and Woodford, 1998).

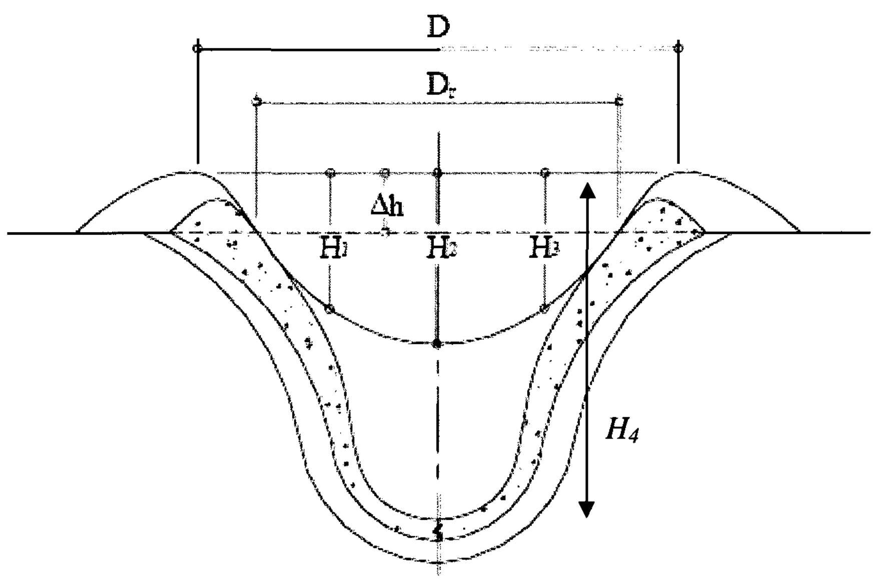

Figure 2.16: General Crater Dimensions (Ambrosini *et al.*, 2002)

The parameters are defined as follows:

D_r: Crater diameter
D: Apparent crater diameter
H_2: Apparent crater depth
Δh: Height of ejecta
H_4: True crater depth

The dimension H_4 was added to the figure for the purposes of denoting the actual crater depth.

Given that the size of the crater changes with the depth of embedment of the charge (for a given charge weight), one can expect to see different crater shapes as the depth changes. Figure 2.17 shows a number of different crater shapes for different depths of explosion. Figure 2.17 (a to d) describe surface blasts, shallow blasts, optimum depth blasts, and deep burial blasts. As noted by Bull and Woodford (1998), the crater depths and radii do reach a maximum at the optimal burial depth (as does the volume of the apparent crater). However, it is worth noting that the true crater depth continues to increase with depth and that there is simply more fall back.

Pokrovskyi and Tshernygovskyi (1967) suggested the following formula for the crater radius, $D_r/2$ [m]:

$$D_r = 2d\sqrt{\left[\sqrt{\left(\frac{4W}{k_3 d^3(1+Bd)}\right)}-1\right]} \qquad [2.18]$$

where: d is the charge depth [m];
W is the charge weight [kg TNT];
B is a factor dependent on the type of explosive [m^{-1}]; and
k_3 is a coefficient dependent on the type of soil or rock [kg/m^3].

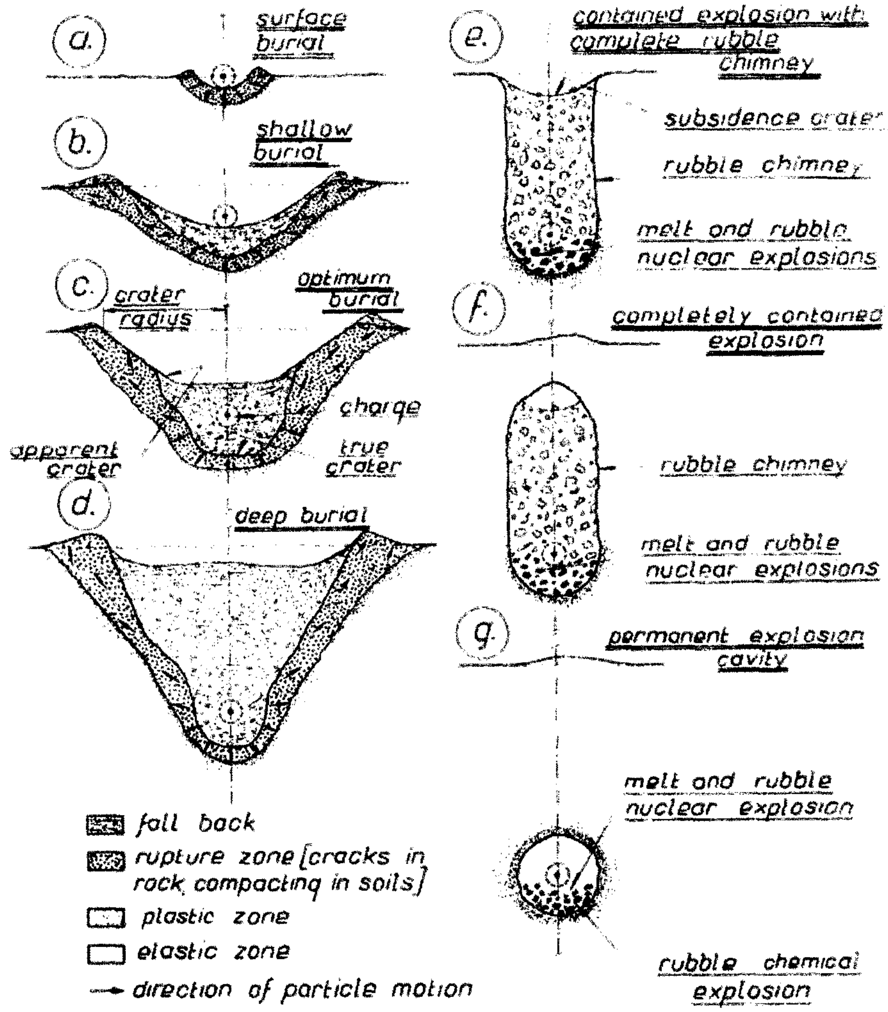

Figure 2.17: Explosion Craters for Various Depths of Charge Burial (Henrych, 1979)

The apparent depth of the crater, H_2, is also defined as

$$H_2 = \frac{H_v}{1 + 0.013d^{2/3}} \qquad [2.19]$$

where $H_v = w[(2n\text{-}1)/3]$ (soil, medium-brisance explosive)
$H_v = 0.25\, D_r$ (soil, high-brisance explosive)
$H_v = 0.1\, D_r + 0.6w$ (rocks) (Henrych, 1979)

Baker *et al.* (1983) presented a dimensional analysis to model the crater formation. They chose six parameters to determine the problem:

1. Charge mass, W [kg TNT];
2. Depth of the explosive charge, d [m];
3. Apparent crater radius, $R = D/2$ [m];
4. Soil density, ρ [kg/m^3];
5. A soil strength parameter, σ; and
6. A gravitational effects parameter, K.

After a dimensional analysis and many empirical observations, the following functional relation was obtained (Baker *et al.*, 1991)

$$\frac{R}{d} = f\left(\frac{W^{7/24}}{\sigma^{1/6}K^{1/8}d}\right) \qquad [2.20]$$

where R/d is the scaled radius of the crater. It is noted, however, that experimental conditions are better controlled for $W^{7/24}/d > 0.3$. It can be deduced that the specific weight, γ, is the best measure for K and that ρc^2 is the best measure for σ, where c is the seismic velocity in the soil. If experimental results for different types of soils are plotted in a R/d vs. $\dfrac{W^{7/24}}{\rho^{7/24}c^{1/3}g^{1/8}d}$ graph, there is very little variability in the results (Ambrosini *et al.*, 2002).

2.6.2 Explosions at Ground Level

Much research has been conducted for explosions originating below ground level and only a limited number of studies have been directed towards explosions at ground level (Ambrosini *et al.*, 2002). Lately, this research has been given priority due to the risks associated with various activities and the number of explosions which are set off every year and which originate at ground level (normally with a mind to cause damage to human targets rather than cause craters).

Ground level explosions are considered to encompass explosive devices which have a centre of blast radius located at the ground level (meaning they are idealized as half submerged in soil and d = 0), explosive devices which are sitting on the earth surface (where d is negative yet close to 0) and explosive devices which are located about 1 m in the air (d = -1) which is considered to be an accurate representation of an explosive device which has been mounted in a truck or a car which is often used by terrorists as a means of attack.

The crater developed by an explosion originating at ground level is not different in its definition than the crater formed by an underground explosion. The shape of the crater and the mechanics of its formation, however, are significantly different. The mechanism for the development of the crater is more complex when the explosion originates at ground level because it is related to the dynamic properties of air, soil, and the soil-air interface.

However, even for explosions originating at ground level, the following relationship still applies:

$$L = C\,W^{\alpha} \qquad [2.21]$$

L is any linear dimension of the crater, C is a constant based on experimental results, and α is a coefficient depending upon if gravitational effects can be neglected or not and in many cases is expressed as 1/3 (Ambrosini *et al.*, 2002).

Kinney and Graham (1985) present the results of a study that examined about 200 chemical explosions of rather large magnitude which originated at ground level and used the above scaling analysis. Though there was a variation of the coefficient, C, of about 30%, they presented the following equation:

$$D = 0.8W^{1/3} \qquad [2.22]$$

However, upon examination of this equation, it was determined that Kinney and Graham (1985) do not substantiate this formula with a source or even a study name. Therefore, it is difficult to determine the exact range of charges which were studied and the manner in which they were studied in order to conduct a thorough review of the data and results. Kinney and Graham (1985) also state that the average depth for the craters is about one quarter of the diameter but that the exact result depends on the soil type. Again, however, the specifics of the data are hidden and what the authors actually mean by soil type having an effect on the depth of the crater is lost as the factor does not enter into the presented equation.

Ambrosini *et al.* (2002) used experimentally based approach to propose an equation for estimating crater diameter based on charge weight, W, and the depth, d, of the charge relative to the ground ($d < 0$ is above the ground surface). They used charges between 1 kg and 10 kg TNT and detonated them at different heights (including below ground in order to establish a base line to established literature) and measured the crater dimensions. The experimental results yielded the following equations to determine the diameter, D, and depth, H_2, of a crater:

$$\log\left(\frac{D}{2|d|}\right) = 1.241\log\left(\frac{W^{1/3}}{|d|}\right) - 0.818 \qquad [2.23]$$

$$D/H_2 = 5.78 + 5.05|d| \qquad [2.24]$$

The experiment was restricted to heights of blasts lower than 1 m but this restriction is in line with the definition of an explosion originating at ground level.

Ambrosini *et al.* (2002) examined crater formation and dimensions for blasts up to 500 kg TNT. While achieving a mean difference of 6.4% with their experimental results for 1 to 10 kg TNT explosives and a mean difference of 1% with the experimental result of a greater charge, they arrived at the following formulae for crater diameters, similar to the form of Equation 2.21:

$$D = 0.42W^{1/3} \qquad [2.25]$$

$$D = 0.61W^{1/3} \qquad [2.26]$$

The diameters are described for charges sitting on the surface and charges located with their blast centre in line with the soil surface, respectively as shown in Figure 2.18. These formulae represent a notable difference from that which was proposed by Kinney and Graham (1985), yet reaffirm that the empirical laws previously defined are still applicable for the prediction of apparent crater diameter.

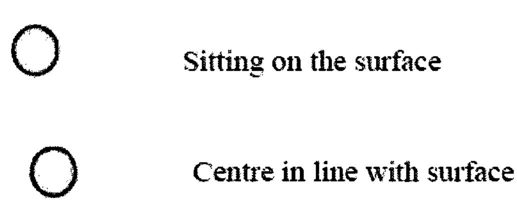

Figure 2.18: Charge Locations (Ambrosini *et al.*, 2003)

Ambrosini *et al.* (2006) refined the existing model from 2002 by taking into account soil factors such as the shear modulus, *G*, the mass density of the soil, the hydro tensile limit, and the yield stress of the soil. Rather than use the actual values at the site (which may have changed since the experiment was conducted), they were varied and each one considered in order to find the value which best fit the experimental results.

Figure 2.19 shows an experimental blast for a charge situated 1 m above the surface and Figure 2.20 shows an experimental blast for a charge located at the surface. It can be seen that the results shown in Figure 2.17 (d) seem to be fairly accurate in describing the phenomenon.

Figure 2.19: Experimental Blast Crater (Ambrosini *et al.*, 2002)

Figure 2.20: Surface Blast (Ambrosini *et al.*, 2002)

The following equations were proposed to model the diameter of craters from surface blasts sitting on the surface ($d < 0$) and where $d = 0$ respectively:

$$D = 0.51W^{1/3} \quad [2.27]$$

$$D = 0.65W^{1/3} \quad [2.28]$$

These equations form a consequential change from the previous formulae. The authors do not give any reason for this change and we can only assume that it can be attributed to refinements in the model. It is interesting to note, however, that the new formulae are more similar to the equation originally presented by Kinney and Graham.

After varying the properties of the soil, it was determined that for the charge weights which had been examined, the elastic properties as well as the yield and failure limit had no impact on the crater diameter. This result demonstrates that the above equations can be applied to any type of soil (Ambrosini, 2006).

It was also determined that, as the weight of the charge increases, so does the depth of the crater, regardless of the diameter, though the ratio D/H still does not get as low as when it is on the ground. Rather, the distance the charge is elevated above the ground becomes less of a factor when the charge weight is larger (Ambrosini *et al.*, 2007).

3.0 METHODOLOGY AND EXPERIMENTAL SETUP

Given the multifaceted nature of dam breaching, in the present work, numerous tests in addition to the dam breaching tests were conducted to determine the properties of the materials used in the embankment construction. Geotechnical tests included gradation, Atterburg limits, and shear strength. The soil erodibility parameters were also studied from flume tests.

In addition to determining the soil characteristics, there were a number of different elements to the test program that required examination. In all, there were three main areas of experimental interest in breach characteristics studied in this thesis: effects of compaction, effects of initial breach geometry, and the effects of composite (clay core) construction. The effects of compaction were also discussed in the collaborative effort of Al-Riffai *et al* (2009). This section describes the experimental setup and methodology for each of the test series.

All tests were conducted at the University of Ottawa. Geotechnical tests were conducted in the Geotechnical Laboratory while dam breaching tests were conducted in the Hydraulics Laboratory. Two different flumes were used for the experiments: a tilting flume and a large flume.

3.1 Geotechnical Tests

For this study, a number of tests were conducted to determine the geotechnical properties of the soils used in the experiments. Two sands and one clay were used. Both Sand I and Sand II were obtained from the Burnside Quarry, just south of Ottawa. While they were taken from the same pile of sand, they were taken at two different times of the year and as such were excavated from two different locations in the quarry. While the hope was that the two sands would have similar gradations, they were different enough to be considered two different sources. The clay was taken from a deep road excavation in the Sandy Hill area of Ottawa. The depth of excavation was approximately 3 m beneath the existing top of road grade.

The material used for the construction of the drains in the embankments was common fine gravel used to prevent slipping on icy driveways and walkways and was obtained at a Home Depot store. The filter medium used between Sand II and the drain was pre-graded fine filter sand purchased at Merkley Supply.

The properties of the soils used in the study were determined following procedures outlined in the University of Ottawa Department of Civil Engineering Laboratory Manual. These test procedures are based on ASTM standards. Table 3.1 shows the tests conducted and the ASTM standards which were followed.

Table 3.1: Geotechnical Tests

Test Conducted	ASTM Standard
Sieve Analysis	D-2487
Hydrometer Analysis	D-422
Atterberg Limits	D-4318
Specific Gravity	D-792
Permeability	D-2434
Direct Shear	D-3080
Standard Proctor	D-698
Sand Cone	D-1556

Sieve Analyses were conducted numerous times for all materials used in the construction of embankments. Other tests were only conducted for Sand I. Sand II was considered to be similar to Sand I so that values other than gradation determined for Sand I were also used for Sand II. The clay was not tested using the sieve analysis, permeability, shear, or sand cone tests.

3.2 Erosion Rate and Critical Shear Tests

The experimental program consisted of six erosion tests for sand and six erosion tests for clay in addition to preliminary tests conducted to determine the feasibility of the experimental procedure and to determine the critical shear stress of both the non-cohesive and cohesive sediment. A test section was setup in the downstream portion of the tilting flume. Initially, the test section was 300 mm long in the streamwise direction, but the time for erosion of this size of test section was deemed to take too long, so it was shortened. In order to minimize the head loss effects from the test section, the bed was made a maximum of 10 mm high. During the initial tests, this bed height did not induce a hydraulic jump except at high velocity flows with relatively shallow depths.

In order to simulate similar roughness in the flume as there is in the test section the steel floor of the flume was roughened by applying a mixture of sand and paint. In order to achieve sufficient depth of flow so as to allow for a multiple of measurements and to avoid the potential for a hydraulic jump, the gate at the downstream end of the flume was raised. Figure 3.1 shows a view of the experimental setup. The flume used for the experiments is 12.2 m long by 0.381 m wide by 0.60 m deep. The test section was 0.221 m long, measured the full width of the flume, and was 0.01 m high. The slope of the flume was nil, though there were localized grade changes (both positive and negative) at some locations in the flume.

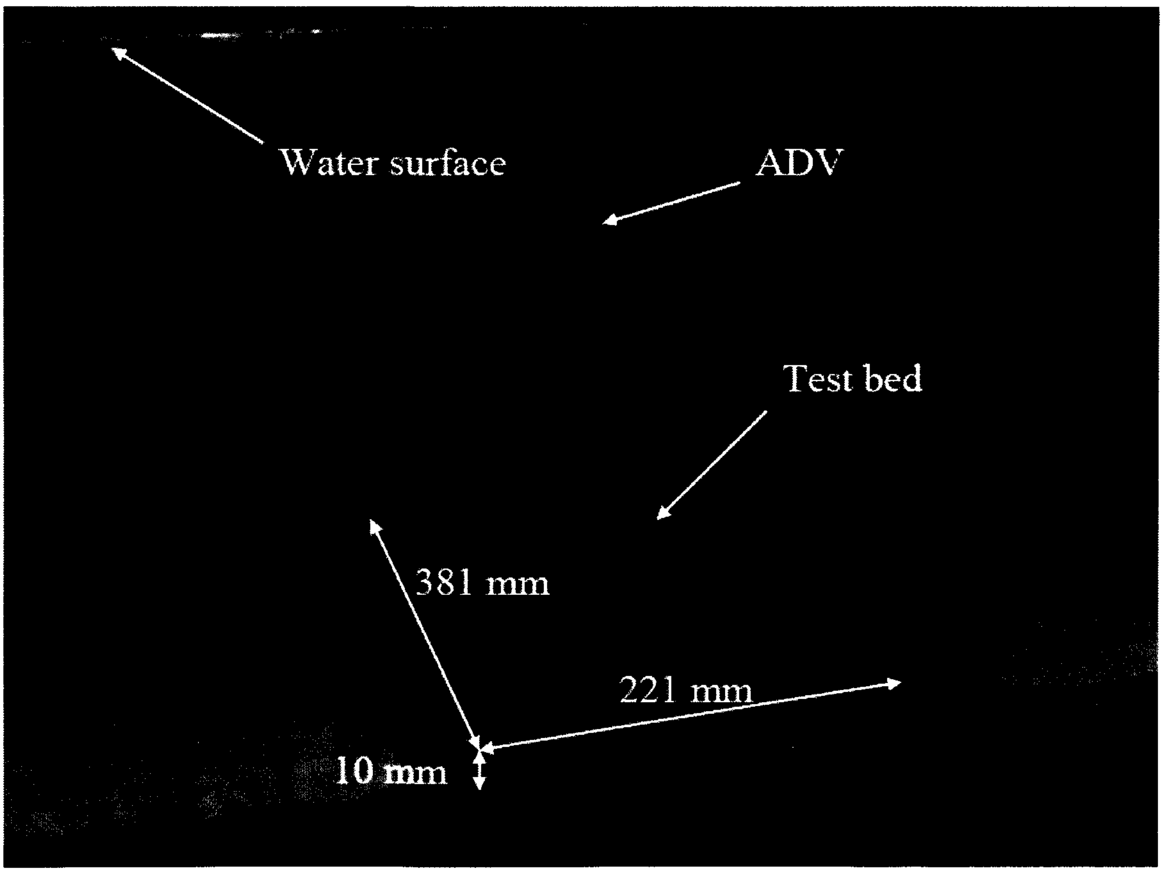

Figure 3.1: Experimental Setup (Sand Bed)

3.2.1 Sand Tests

The sand used for the tests was acquired from the Burnside quarry in the south end of Ottawa. The properties of the sand are presented in Table 3.2. It should be noted that the specific gravity of the sand was measured to be 2.75 (as opposed to the common value of 2.65 for sand/quartz) due to the large natural iron content in the local sand. The angle of internal friction determined from the direct shear test was equal to 36°.

Table 3.2: Sand Properties for Erosion Tests

Material	D_{10} (μm)	D_{50} (μm)	D_{90} (μm)
Sand II	110	220	410

The sand was dried over a period of a few days and was placed loosely in the test section. As such, the loose, dry density of the sand was deemed to be applicable when determining the density of the sand in the test section.

In order to ensure the size of the test section was maintained between tests, small forms 10 mm high were placed at the upstream and downstream ends of the section between which the sand could be placed. However, only the upstream test section boundary was defined. On the downstream side, the test section was made deliberately longer so that the downstream edge of the test boundary could maintain a height of 10 mm. While this change was not critical, it did allow the shape of the sand test section to be more similar to that of the clay test section which was able to maintain a 10 mm height at the downstream boundary. Once the sand was placed in the test section, the forms were removed and the sand was allowed to settle to its natural angle of repose on the upstream and downstream ends of the test section. While ramps were considered to help ease the flow over the test section, they were not used for the sand because of the concern that they would cause too much turbulence around the sand and affect the results. Therefore, the physical sand test section extended beyond that of the clay, though the observed and measured test section remained of the same dimensions.

3.2.2 Clay Tests

The clay used for the tests is a Champlain Sea clay which was obtained from the area of Sandy Hill in Ottawa. The properties of the clay are shown in Table 3.3. In its original state (various size lumps with some small rocks), the clay is difficult to form to fit the desired test section dimensions and, moreover, is quite rough and somewhat brittle. As such, it was remolded by drying it out and crushing it. The clay was then mixed with tap water to the desired water content which was in excess of the liquid limit for ease of fitting to the test section.

Table 3.3: Clay Properties for Erosion Tests

D_{50}	**Clay Fraction**	**Liquid Limit**	**Plastic Limit**	G_s
4.5 μm	95 %	32%	20%	2.76

It should be noted that the clay cannot have what could be called uniform water content. This non-uniformity can be attributed to the nature of the clay itself and how it absorbs moisture. It was noticed that, almost instantaneously, clumps in the clay would begin to form when water was added. While some areas of the clay absorbed as much water as they could, other areas seemed relatively dry. The look and feel of the mixing process can most closely be compared to the mixing of batter. While the lumps likely could have been fully removed from the clay, this removal would likely require a great amount of mixing to the point where the properties of the clay might be affected.

It should also be noted that at the center of most of the lumps of clay, a particle of sand could be found. This finding lends credence to the idea that sand content plays a role in the erosion process as it seems to alter fundamentally the composition of the mixture even at very small sand contents.

Once the clay was mixed, samples were taken to confirm the water content of the mixture and then the clay was placed into the test section. Given that no immediate confirmation of water content could be made for each sample (typically, clay samples took 48 hours to dry in the oven), the water contents vary slightly from test to test. Thus the feel of the clay was essential to estimating the water content so as to ensure it was similar to previous tests.

The test section was bounded on the upstream and downstream ends by small painted steel ramps with approximately 5:1 slopes which were also used as forms for the test section. Using the ramps as an elevation guide, the clay bed was planed down to the required elevation (10mm). It should be noted that this planning process effectively shears the top layer of the clay, changing the surface properties slightly. This change is unavoidable, however, as the otherwise the surface would not be smooth and roughness related issues would be identified instead as the clay was very sticky.

While consolidation is an important parameter in the erosion rate of clay, in these tests it remained a relatively uncontrolled parameter. Placement of the clay was conducted in a similar manner from one test to another but it is impossible to say that the consolidation practice and the final void ratio of the clay test section was the same for all the tests.

3.2.3 Experimental Procedures

In order to take a sufficient number of point velocity measurements with an Acoustic Doppler Velocimeter (ADV) above the bed, the flow depth needed to be increased by raising the gate at the downstream end of the flume. ADVs are well explained by Voulgaris and Trowbridege (1998) and Rennie and Hay (2009). The height of the gate varied from test to test, as did the flow through the flume, but these variables enabled a change of applied shear stress to the bed.

Tests were started by slowly filling up the flume from both the upstream and the downstream ends. This process meant that no undue stress was applied to the bed during impounding and as such the test bed could be kept smooth. After impounding, flow was slowly increased until incipient motion was reached. Incipient motion was determined visually by watching for the point at which a few particles along the surface of the test section were moving. Then, flow was increased suddenly so that motion was achieved quickly at a desired flow. It should be noted that it took about 2 minutes for the flow in the flume to come to equilibrium after which measurements of velocity and water depth could be accurately made.

Flow depths were taken at four points along the length of the flume using a physical point gauge with precision of 0.1 mm. Measurements were taken at 1.0 m, 6.2 m, 7.2 m, and 10.0 m from the upstream gate. The test bed started at 6.58 m from the upstream gate and the ADV was placed at 6.7 m at the centerline of the flume, near the middle of the test section. Figure 3.2 shows the test setup. Measurements from the ADV were taken at a rate of 50 Hz over 30s starting at the greatest depth and then working higher. Starting measurements near the bed meant that there would be less error in the near bed results as the erosion would be less notable early in the run.

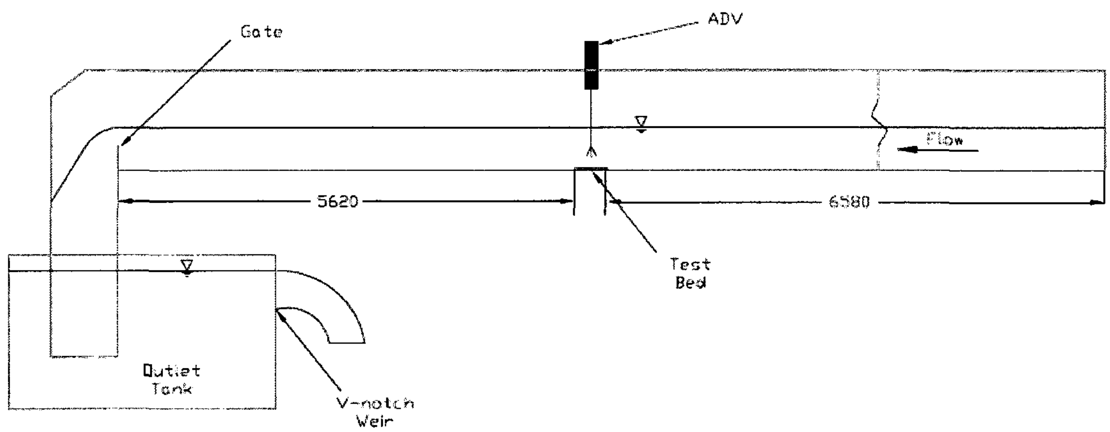

Figure 3.2: Experimental Setup for Erosion Tests
(dimensions in mm)

The tests were run generally until vertical erosion progressed to the bottom of the flume (10 mm). However, some tests for the sand eroded very quickly before all the ADV measurements could be taken. These tests ran until the measurements were finished and then the test was stopped. Tests were terminated by rapidly reducing the inflow to the flume and then opening up the drain in the flume inlet tank to drain the water from the flume. Care was taken to drain slowly so as not to cause any consequential sediment transport during this process. Once the upstream end of the flume had drained, the gate was lowered and the downstream end was then drained.

Once the flume had been fully drained, the remaining sediment in the test section was removed to be dried and weighed. It should be noted that full removal of all sediment from the test section was not possible due to the rough nature of the bed and the small and wet nature of the remaining material. In the case of the clay, the remaining sediment was mostly a thin layer of highly fluid mud.

Flow in the flume was determined using a V-notch weir at the outlet of the flume. The weir coefficient was assumed to be 1.38 which is common for a 90° notch (Prasuhn, 1992). The weir coefficient was not verified for experimental testing, but as all results from this portion of the test series are to be compared only to each other, any error associated with this assumption has been deemed to be inconsequential.

3.3 Compaction Tests

In order to determine the effects compaction has on breach characteristics, a series of tests were conducted in the tilting flume where only the compaction effort was varied. The tilting flume is 12.2 m long and 0.381 m wide and the upstream toe of the embankments were placed at 9.22 m. The schematic for the experimental setup is shown in Figure 3.3.

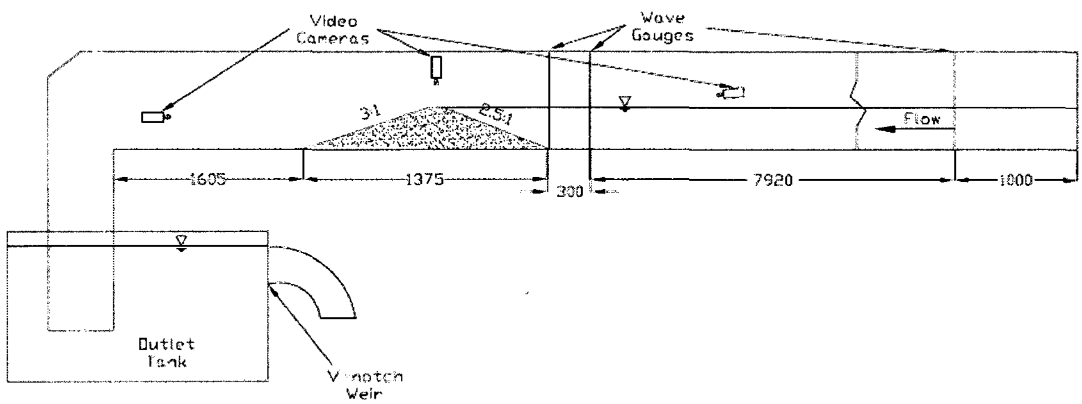

Figure 3.3: Experimental Setup for Compaction Tests
(dimensions in mm)

The embankments were constructed 250 mm high with an 80 mm crest width, 3:1 downstream slope, and 2.5:1 upstream slope. The slope of the flume was nil and the floor of the flume was smooth. The sand used for the tests was acquired from the Burnside quarry in the south end of Ottawa. The properties of the sand are presented in Table 3.4. It should be noted that the specific gravity of the sand was measured to be 2.75 (as opposed to the common value of 2.65 for sand/quartz) due to the large natural iron content in the local sand. The angle of internal friction was determined to be 36°.

Table 3.4: Sand Properties for Compaction Tests

Material	D_{10} (μm)	D_{50} (μm)	D_{90} (μm)
Sand I	90	140	220

Compaction of the embankment took place in 5 lifts of 50 mm each. For the first few trial tests, compaction of the lifts was unconfined and was conducted at the natural water content of the sand. However, upon completing *in situ* density tests on the embankment to confirm the predicted density, it was determined that not only was the target density not being reached but also that the density was less than the loose, dry density of the sand which was determined to be 1420 kg/m^3. This improbable phenomenon was checked numerous times and was eventually determined to be due inefficiencies in the compaction process as well as due to the water content at which compaction was taking place. For the case of the sand used in the experiments, compacting at the natural water content produced both the least sand density possible as well as the most highly variable. As such, further tests were conducted with sand which was mixed to a near-optimum water content and formwork was added to the construction apparatus in order to attempt to minimize inefficiencies in the compaction process. Figures 3.4 and 3.5 show the construction process.

Compaction was done by hand using a tamper composed of a steel plate welded to a steel rod which was dropped from a known elevation above the compacted surface using a movable rig pictured in Figure 3.4. The mass of the compactor was 8.7 kg and was dropped evenly over the surface for each lift. However, it should be noted that overlap in the compaction method did occur which necessitated an averaging of the total compaction energy over the entire lift. Total compaction energy varies from lift to lift owing to the difference in surface area for each lift. For each lift, a number of series of blows was applied in order to achieve compaction: 5 blows from 50 mm high, 5 blows from 100 mm high, 10 blows from 100 mm high, and 20 blows from 100 mm high.

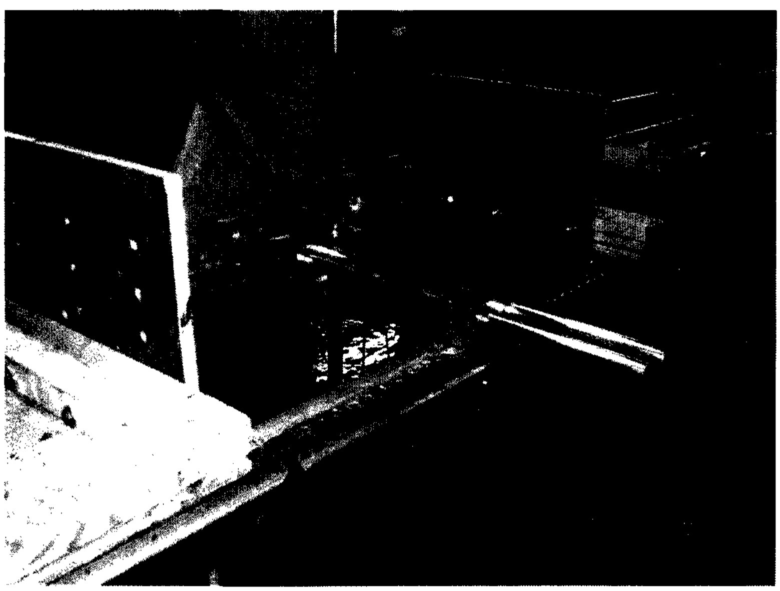

Figure 3.4: Construction of Embankment

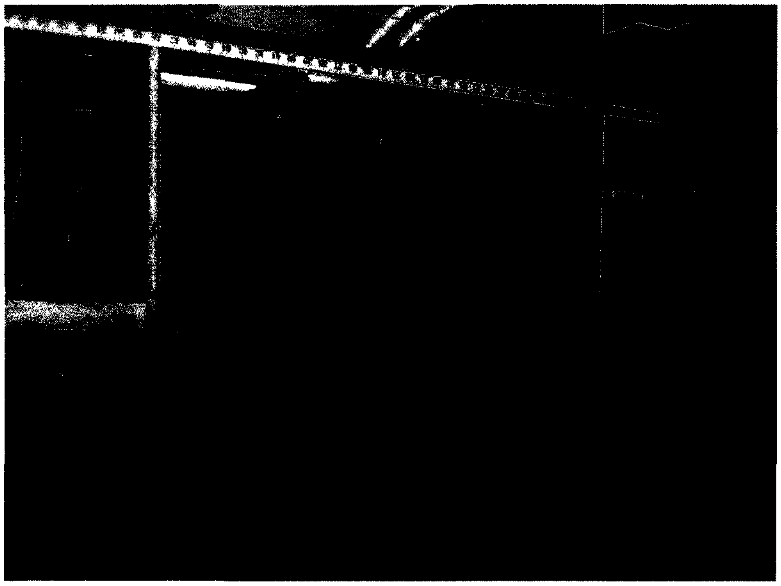

Figure 3.5: Construction of Embankment - Side View

For each lift, soil samples were taken prior to compaction to confirm the water content at which compaction took place. After compaction, the embankment was shaped in order to achieve the proper upstream and downstream slopes. Shaping was done using a trowel as well as a spirit level in order to ensure the uniformity of the slope as well as embankment outlines drawn on the flume side walls to use as guides. Once the slopes were shaped, gridlines were applied to the embankment using a chalk line. Gridlines were also applied to the glass side wall of the flume. The gridlines measured 40 mm x 40 mm. A completed embankment can be seen in Figure 3.6. Each breach was initiated using a V-notch with 1:1 side slopes and 20 mm depth located at the centerline of the flume.

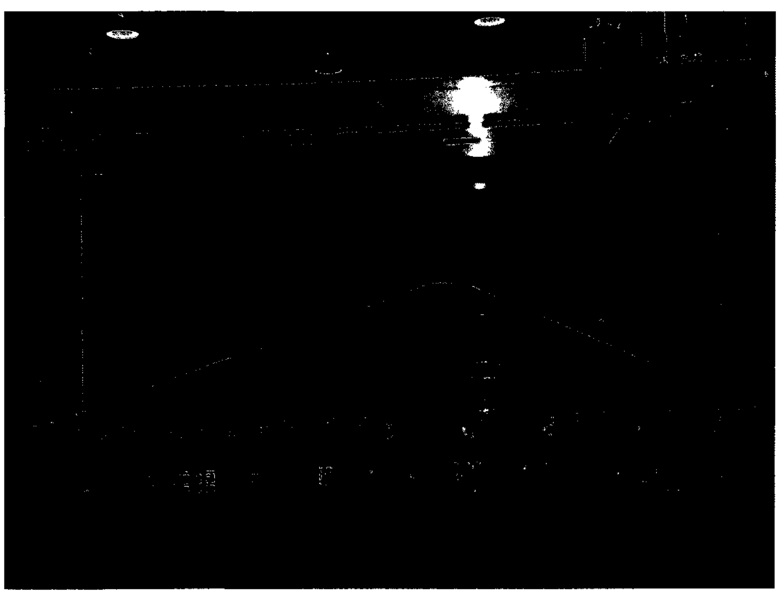

Figure 3.6: Embankment Dam in Tilting Flume

The embankment shown in Figure 3.6 is one of the preliminary embankments which was constructed using the natural water content of the sand. Due to the low initial water content of the embankment, the seepage can be seen at the upstream toe. In later tests, this progression of seepage could not be seen without the use of dyes and piezometers. It was also a test where one ADV was used immediately upstream of the dam crest and another was used downstream in the hope of capturing velocities from the flood wave. From this test is was determined that the range of data which could be determined from the ADVs was quite minimal as in the early stages of the breach there was no measurable velocity at the sampling locations and the time at which useable samples could be taken had a very short duration. This limitation arose in part because the ADV sample volume is 5 cm below the ADV probe tip, and the ADV probe tip must be fully submerged. As such, the ADVs were not used in subsequent embankment tests and surface tracers were instead used as a means of measuring velocities.

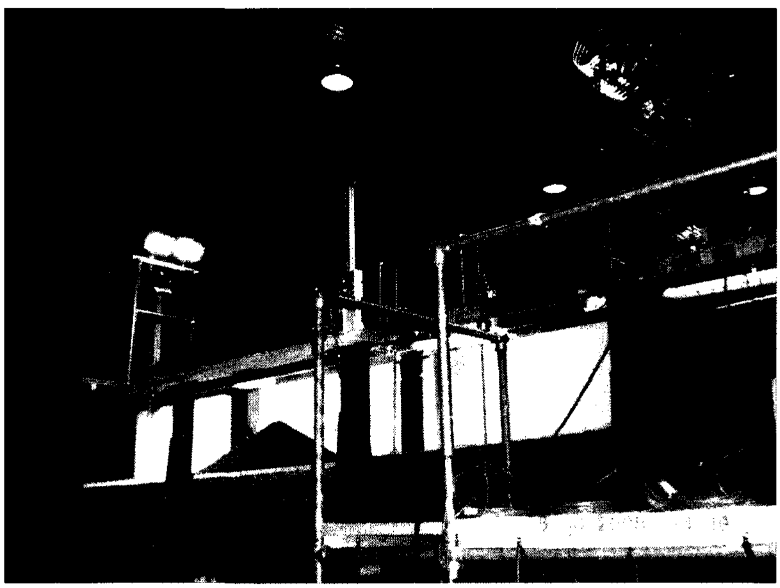

Figure 3.7: Experiment Setup for Tilting Flume

Two rigs were set up above the flume: one upstream and one downstream as shown in Figure 3.7. Two lights were placed at the top of each rig to brighten the flume for ease of filming. These rigs also housed arms that reached down and held digital video cameras in place for the upstream and downstream camera angles. Not pictured is a third rig which was situated above the crest of the dam from which a video camera was placed for the vertical view from above the crest. A fourth video camera and another light stand were set up to the side of the flume for a side view, as shown in Figure 3.8. Therefore, video cameras were used to capture an upstream view, a downstream view, a top view, and a side view for all tests in this portion of the test program. The video camera types varied between the tests as they were often borrowed from the University of Ottawa Multimedia Centre but had minimum specifications of 410, 000 pixels and a shutter speed of 30 Hz.

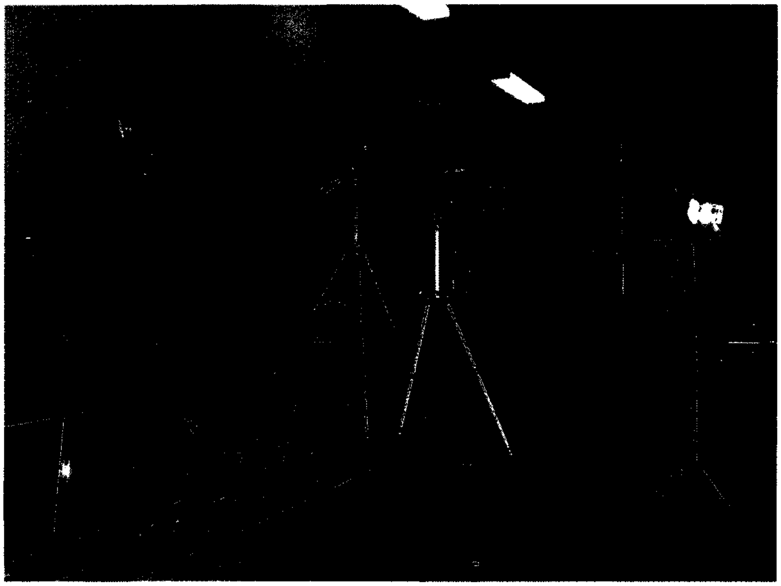

Figure 3.8: Side View Camera and Lighting Setup

Also pictured in Figure 3.7 are two of the four WG-50 capacitance wave gauges which were used for each test. Each gauge measures the electrical resistance between two nodes. This resistance changes based on the type of fluid medium it is in contact with (in the case of this study, water and air). The gauges are calibrated using a linear calibration of voltage vs. water depth. During testing, they are further checked to make sure that the calibration is yielding the appropriate water elevation. This check is conducted using a point gauge on a calm surface in the reservoir behind the embankment just prior to testing. Wave gauges were set up at the upstream toe of the embankment, 0.3 m upstream of the upstream toe, in the inlet tank, and in the outlet tank below the flume near the V-notch weir. With this setup, flow during the experiment could be measured by using both the gauge at the V-notch weir as well as a combination of the other 3 gauges which could yield a volume change relationship over the course of the test.

A total of four successful tests were conducted to determine the effects of compaction on breach characteristics. In addition to those four tests, there were numerous others which failed, either because they were part of the test series that used a non-ideal water content during compaction or because the breach occurred in the wrong location such as against a side wall rather than through the notch. Table 3.5 shows the complete series of tests, including the unsuccessful ones.

The scale of the embankments is 1:120 (the prototype size for all embankment testing being 30 m). The size of the reservoir behind the embankment was 1.4 m^3, which when scaled to the prototype becomes 1.68 million m^3. Reservoir impounding was conducted using the pump for the most part, though impounding when water level was near the dam crest was conducted with a hose alone with a flow of 0.45 L/s (71.0 m^3/s at prototype scale). Initial tests had kept the inflow for the entire duration of the breach failure. However, this procedure resulted in the reservoir elevation to rise higher than expected and for the embankment to be overtopped at locations other than the notch. As such, future tests shut off the inflow once it was certain that the breach would sustain itself. For the August 19 test, inflow was shut off too early a couple times which resulted only in overtopping failures and not breach failures (the overtopping water simply seeped into the downstream slope of the embankment). Generally, inflow was shut off once the flow through the breach channel had reached the downstream toe of the embankment.

Table 3.5: Sand Compaction Tests

Test Number	Test Date	Compaction	Notes
1	May 28, 2008	Unknown, low	Preliminary test
2	May 30, 2008	Unknown, medium	Preliminary test
3	July 31	5 blows, 50 mm high	Successful breaches but not usable due to unknown compacted density.
4	August 19, 2008	5 blows, 50 mm high	Successful test, however irregular inflow pattern.
5	August 20, 2008	10 blows, 50 mm high	Failure when breach occurred against side wall. Useful comparative video shots.
6	August 21, 2008	1 blow, 50 mm high	Failure when slope fails during impounding.
7	August 25, 2008	5 blows, 100 mm high	Successful test though wave gauge data incomplete.
8	August 27, 2008	10 blows, 100 mm high	Successful test.
9	August 28, 2008	20 blows, 100 mm high	Successful test.

3.4 Clay Embankment Tests

In addition to the sand embankment tests conducted in the tilting flume, two tests were also conducted with embankments constructed from clay on September 9th and September 14th, 2008. These tests were designed to be preliminary tests involving preparation of the clay in order to determine whether or not remolded clay would be required when further tests were conducted for varying compaction as with the sand embankment tests. The clay used for the tests is a Champlain Sea clay which was obtained from the area of Sandy Hill in Ottawa. The properties of the clay are shown in Table 3.6.

Table 3.6: Clay Properties for Embankment Tests

D_{50}	Clay Fraction	Liquid Limit	Plastic Limit	G_s
4.5 μm	95 %	32%	20%	2.76

The embankments were constructed 250 mm high with an 80 mm crest width with 2:1 upstream and downstream slopes. A schematic of the experimental setup is shown in Figure 3.9. The embankments were constructed with no clear scale in mind as no prototype embankment would realistically be constructed 100% out of clay. The reservoir behind the embankments was 1.4 m^3.

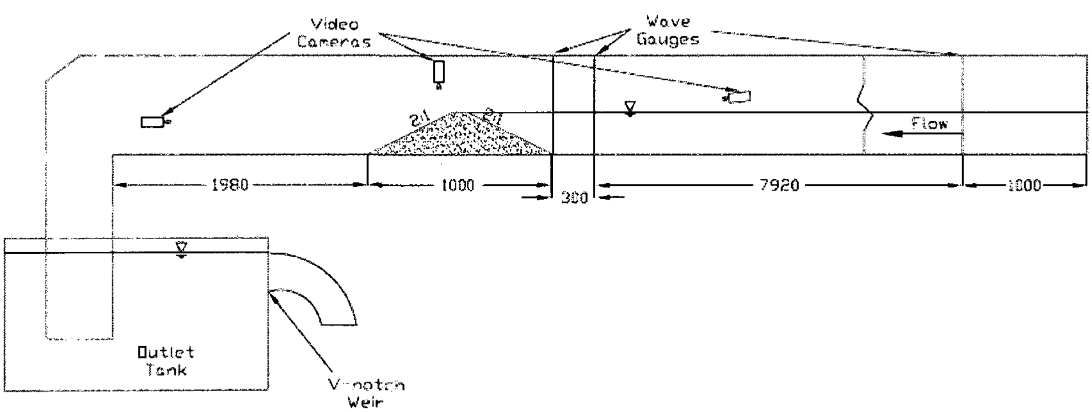

Figure 3.9: Clay Embankment Test Setup
(dimensions in mm)

The first test was conducted with natural clay which was compacted into place in the same manner as the sand embankments but without the aid of formwork. Prior to compaction of each lift, soil samples were taken to confirm the water content of each lift.

Shaping the embankment was done with a spirit level and a trowel, though it should be noted that shaping in this fashion shears the surface of the clay and changes some of the physical properties of the surface material. It is an unavoidable error, however. Due to the nature of the clay, chalk does not stick, so gridlines were painted on both the upstream and downstream slopes of the embankments.

It should be noted that the clay was sticky and difficult to work with. While compaction consisted of 5 blows from 100 mm high, often clay would stick to the bottom of the compactor after having been pulled up during the compaction process. So, while compaction did physically occur, the suction resulting from removing the tamper afterwards likely caused compaction effects to be minimized. Also, the natural clay, even after having water added to it to make it more malleable, is still rather chunky and stiff in many areas, resulting in numerous voids being present throughout the embankment even after compaction.

The second test used remolded clay which was dried, crushed, and then mixed to the desired water content which was very similar to that from the first test. However, remolded clay is much stickier and softer. In order to fill voids which were prevalent during the first clay embankment, preliminary consolidation was conducted by hand in order to fill the most obvious voids. This adjustment had the desired effect of making the embankment much more impervious.

Inflow was not set to a constant rate throughout the first test. Rather, it was adjusted in the beginning to see if a breach could be sustained with minimal flow. In the end, it could not be sustained and erosion was minimal so the inflow was set to 0.45 L/s for the rest of the first test and the entirety of the second.

Given that the erosion process for clay is much slower than it is for sand, video was only used for the first hour or so of the test. Upstream, downstream, top, and side views were shot with video cameras. Afterwards, photos were taken at regular time intervals. Four WG-50 capacitance wave gauges were used to measure water surface elevations at various points in the flume. They were set up at the upstream toe of the embankment, 0.3 m upstream of the upstream toe, in the inlet tank and below the flume in the outlet tank near the V-notch weir. Styrofoam beads were used as flow tracers to obtain surface velocity measurement. However, due to the length of the tests, these tracers were quickly used up and velocity measurements could only be obtained for the first 10 minutes or so of the tests.

3.5 Large Flume Tests

A series of tests were conducted to determine the effects of initial breach geometry on breach characteristics. These tests were conducted in the large flume at the University of Ottawa Hydraulics Laboratory. Three initial breach geometries were used in homogeneous, non-cohesive embankments: a V-notch cut into the embankment, a flat crest, tapered towards the centerline of the flume, and a profiled crater that simulates the effects of an explosion.

While many researchers have used trapezoidal breaches for pilot channels, the current experiments use two more realistic breach geometries (flat and crater), as well as a simple control notch which keeps the initial breach width small. All breaches were initiated at or near the centerline of the flume to mitigate the effects of the flume side walls. Further, the height of the embankment was designed such that the eventual breach width would not reach the side walls and not be influenced by wall effects to any notable extent. As the effects of the breach never reached the flume walls, their lack of erodibility can be ignored. Also, most breaches reached the test flume floor rather quickly, creating the necessary assumption that the embankment foundation is not erodible.

The embankments for these tests were constructed 300 mm high, with a 100 mm wide crest. Several early variants of the embankment construction were homogeneous but later tests included a gravel toe drain with a medium sand filter. The upstream slope was 2.5:1, the downstream slope was 3:1 and the embankment measured the full width of the flume. The dams were constructed in a 29.2 m long flume with a 1.5 m width and 0.77 m depth with a nil slope. The upstream toe of the embankment was placed at a distance of 25.35 m from the upstream end of the flume, yielding a maximum reservoir size of 11.6 m^3, prior to overtopping. At prototype scale, the embankment is 30 m high with a reservoir volume of 11.6 million m^3. Figure 3.10 shows a schematic of the experimental setup.

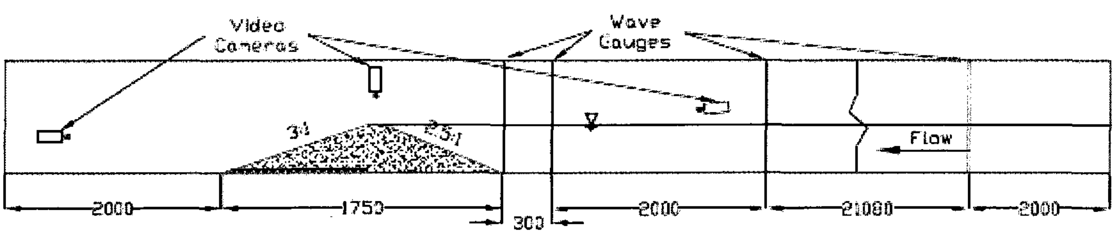

Figure 3.10: Experimental Setup of Large Flume Tests
(dimensions in mm)

The sand used for the construction had a D_{50} of 220μm, D_{10} of 110μm, and a D_{90} of 410μm, as presented in Table 3.7 and contains 3.4% fine material. The size and gradation of the toe drain material (both the filter and the drain mediums) were designed based on recommendations provided by the United States Bureau of Reclamation's Design of Small Dams Section 6.10(i) (1987). While materials used did not rigorously follow the recommended gradation, separate tests were conducted to determine the infiltration curve using this filter gradation and confirmed the mediums selected were adequate for the experiments.

Table 3.7: Sand Properties

Material	D_{10} (μm)	D_{50} (μm)	D_{90} (μm)
Embankment Sand (standard deviation)	110 (4)	220 (8)	410 (4)
Filter Medium	840	1200	1500
Drain Medium	2900	4500	8000

Compaction of the embankments was achieved by compacting by hand with an 8.7 kg metallic plate. Blows to each of the 5 lifts were made from 100 mm high and were evenly distributed to achieve uniformity. The sand was mixed with water to increase the water content to near optimum, as determined by Standard Proctor tests. The compaction energy applied to the embankment and the density were made deliberately low compared to the Standard Proctor density for the sand, as a method of compensating for the improper scaling of erodibility of sand material. The average density of the embankments was 1530 kg/m^3. Formwork composed of concrete blocks was used along the edges of each lift to hold the lift in place in order to ensure the embankment held its shape during the compaction process. As noted earlier, the specific gravity of the sand was measured to be 2.75 (versus the common value of 2.65), due to the large natural iron content in the local sand. The angle of internal friction was determined to be 36°. Figure 3.11 shows the various stages of embankment construction.

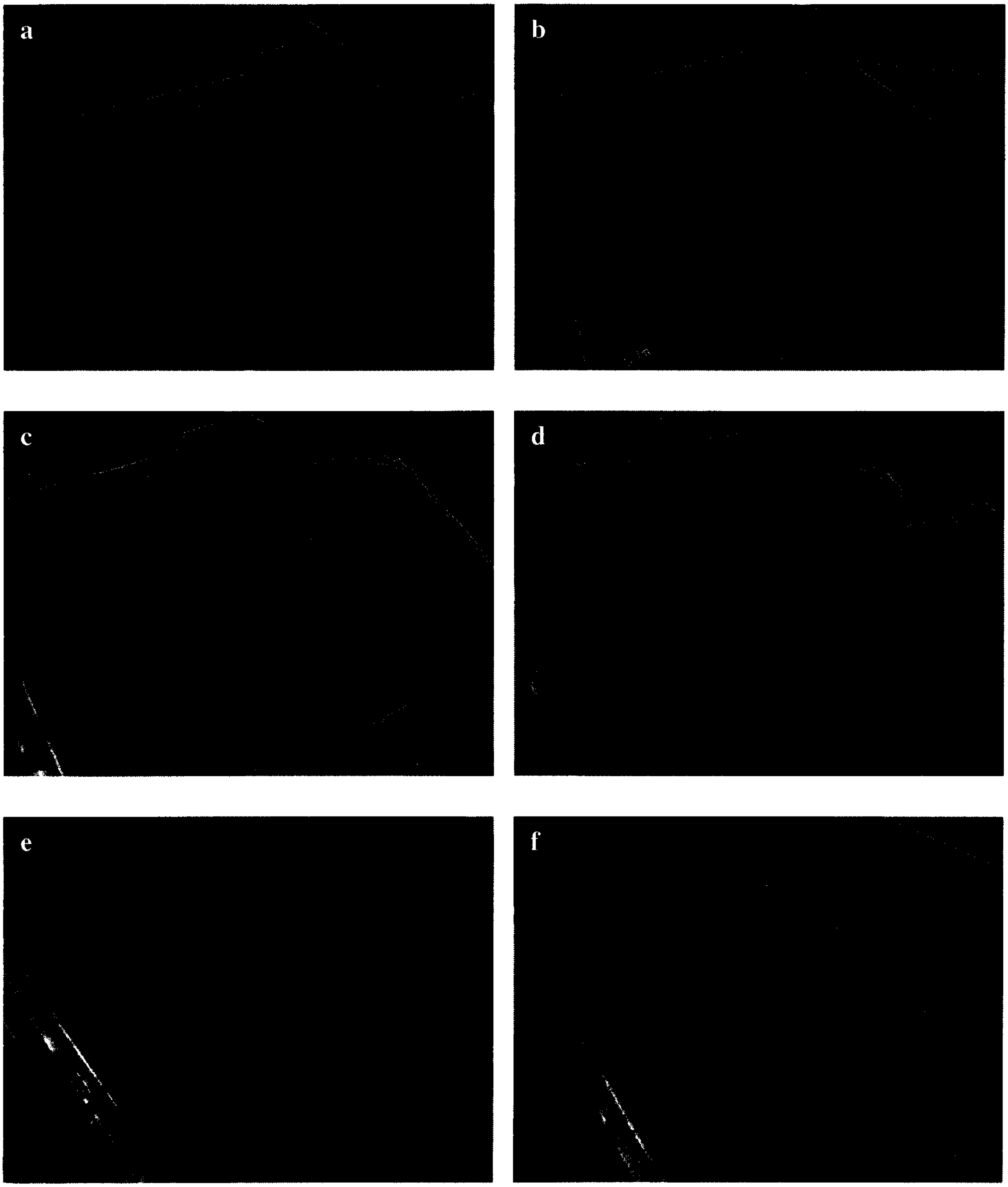

Figure 3.11: Large Flume Embankment Construction

Four WG-50 capacitance wave gauges were set at 0.0 m, 0.3 m, 2.3 m, and 23.4 m from the upstream toe of the dam to measure the water surface profile and to determine the volume remaining in the reservoir. By plotting the change in the volume-time relationship, flow through the breach could be determined. Three video cameras were used to record the breach events: one located downstream of the embankment, one located upstream, and one located above the crest looking down at the embankment. Flow tracers made of Styrofoam beads were also used to determine surface velocities in the reservoir and through the breach channel. Table 3.8 shows the complete series of tests conducted in the large flume. Gridlines were placed on the dam using a chalk line. The grid spacing was 50 mm x 50 mm relative to the face of the dam they were being applied.

Table 3.8: Large Flume Tests

Test Number	Test Date	Crest Type	Notes
1	September 23, 2008	Tapered	250 mm high, no toe drain used, gate was up 30 mm, and breach occurred away from the centerline and hit the side wall.
2	September 30, 2008	V-Notch	No toe drain used, top camera view not available, and conducted in 6 lifts rather than 5.
3	December 15, 2008	Crater	Successful test.
4	December 22nd, 2008	Tapered	Successful test.
5	January 13, 2009	V-Notch	Successful test.

For the initial tests (1 and 2), painted pieces of cork were placed in the dam between the lifts in an effort to use them as flow tracers. Once the embankment eroded to an elevation containing the tracers, they would pop up into the flow and be visible to the downstream camera, similar to the method used by Morris *et al.* (2007), though they use electronic sensors which would have been too large to use in this study. A time of entrainment could then be determined to pair with the location of the tracer and sub-aqueous breach geometry could then be estimated. However, after the first two tests, video analysis showed that it was virtually impossible to see any of the tracers so they were dropped from future tests.

For the crater initiated breach, the crater was sized as an explosive effect from 8,000 kg TNT, which is typical of a truck bomb, detonated from an elevation of 1.0 m above the crest of the dam (FEMA, 2003) and is meant to represent the effects of a terrorist attack on dam infrastructure. The crater diameter was sized according to Kinney and Graham (1985) as $D = 0.8W^{1/3}$, where W is the TNT equivalent charge weight in kg, and the crater depth was defined as $D/4$. The crater was thus estimated as being 12 m wide and 3 m deep (in the model this is 120 mm wide and 30 mm deep). The crater was simulated by excavating the crater material and then backfilling it in a cloth sack in the crater volume to be removed. This approach facilitated in maintaining the appropriate hydraulic conductivity of the embankment prior to initiating the breach. When the embankment was near overtopping, the breach was initiated by rapidly lifting the cloth sack by hand. For the V-notch initiated breach, the notch measured 20 mm deep and 40 mm wide at the top (with 1:1 lateral slopes). The breach over the flat crest had no special features except that the crest was tapered slightly towards the flume centerline. This tapering did not, in fact, prevent the breach from initiating away from the centerline, though it did help to contain the breach within the limits of the flume walls.

Impounding was conducted using the lab pump when possible for tests 1 and 2 using the water from the reservoir. Tests 3 through 5 used tap water from hoses instead, as the pump was not available during the time of those tests. Therefore, it must be noted that there is a potentially important difference in the water source used for tests 1 and 2 and 3 through 5. However, in all cases, inflow during the breach process was sourced from tap water at a rate of 0.45 L/s for the entire duration of the test.

3.5.1 Clay Core Test

A single test in the large flume was also conducted February 20th, 2009 with a sand embankment containing a clay core. The embankment shell had the same dimensions as the homogenous tests. The clay core was 120 mm wide and 250 mm high and was situated right beneath the crest of the dam. Figure 3.12 shows a profile of the clay core embankment. The experimental setup was also the same as per other large flume tests except that the wave gauges were placed at 0.0 m, 1.0 m, 2.3 m and 23.35 m from the upstream toe of the dam. The placement was changed in an effort to reduce the noise that had been observed in the wave gauge readings for previous tests.

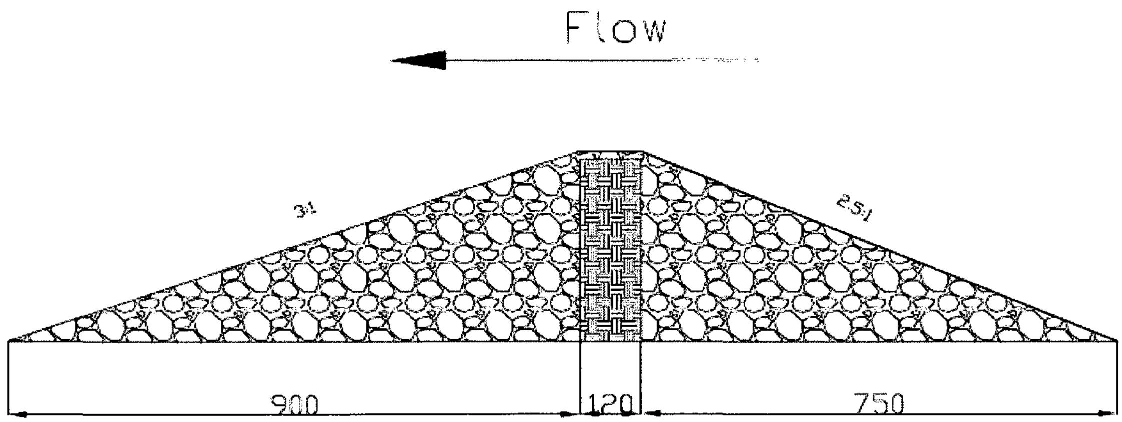

Figure 3.12: Clay Core Profile
(dimensions in mm)

Remolded clay was used for the core with the same preparation techniques and properties as discussed in Section 3.4. The clay core was constructed first, before the shell, to avoid the mixing of sand with the clay and do avoid potential errors during the process of consolidating the sand. No compaction was used for the clay apart from simply shaping the core and making sure it could stand upright under its own strength. It should be noted, however, that some compaction did take place as the sand which was placed above it required compaction. It is uncertain exactly how much compaction energy was transferred to the clay core. The edges of the core were smeared along edges at the bottom of the flume and the flume side walls in order to obtain a more impervious seal. The core was also sculpted in order to create the proper shape before the shell was constructed around it. Figure 3.13 shows the construction of the clay core and the shell.

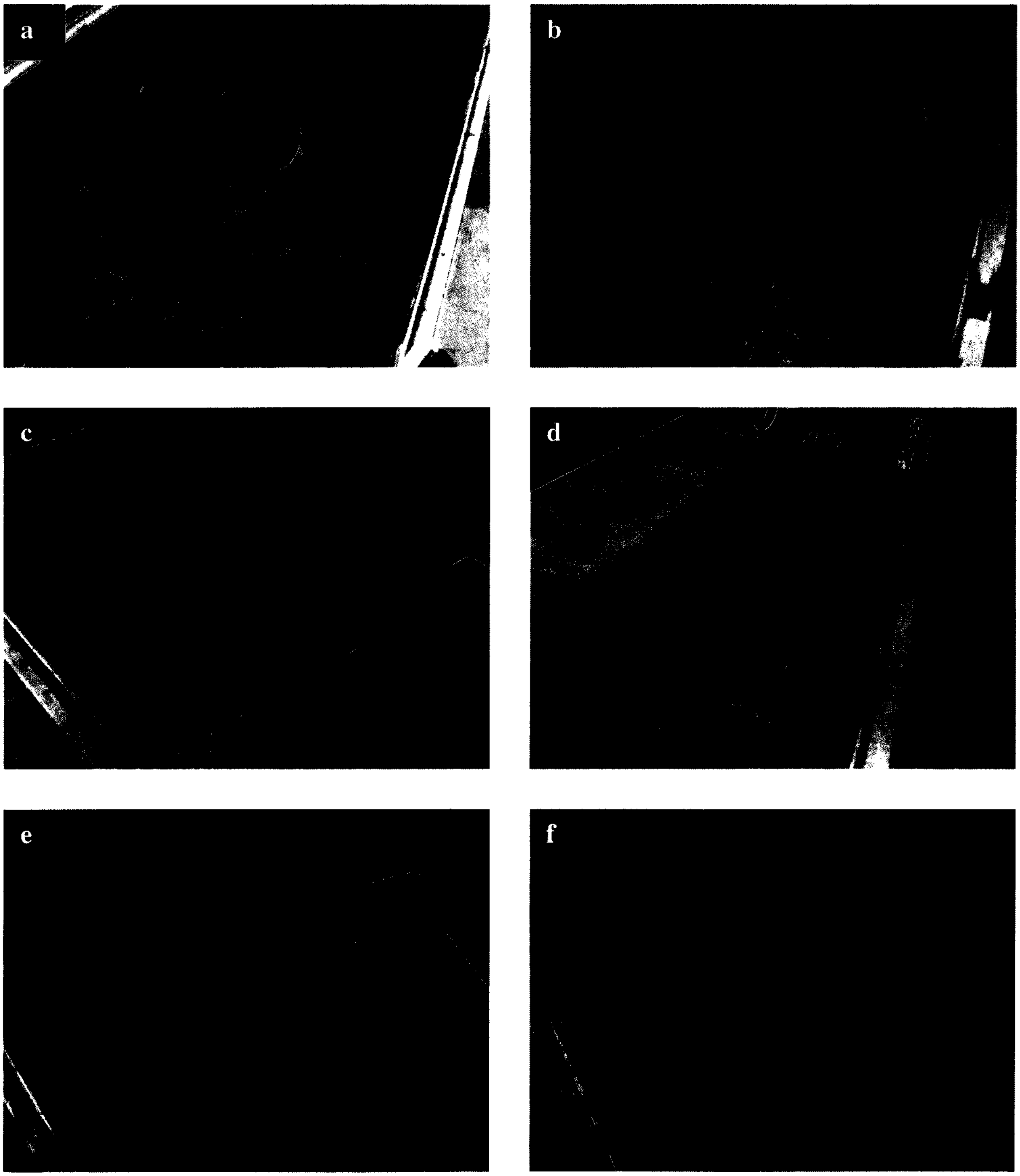

Figure 3.13: Clay Core Construction

The clay core embankment was breached using a crater initiation. The crater had the same measurements as for the sand embankments. The reservoir behind the dam was impounded using the lab pump. Gridlines were spaced 50 mm x 50 mm relative to the face of the dam to which they were being applied. Inflow was constant at 0.45 L/s.

4.0 ANALYTICAL METHODOLOGY

In the embankment breaching tests, two measurement tools were generally used: video cameras and wave gauges. For the erosion rate and critical shear tests, only an ADV and point gauges were used. This section outlines how video and wave gauge data were interpreted and analyzed to obtain the results presented in Section 5. Methods for determining shear stress using an ADV are presented in Section 5.2.2.

4.1 Hydrographs

The primary purpose of the wave gauges was to determine the breach outflow hydrograph. Each gauge shows a water surface elevation at each sample time. Sampling rates were generally 30 Hz. These elevations were then used to determine the volume in the reservoir at a given time. The rate of change of the volume of the reservoir (flow) were then determined for each sampled time step.

Hydrographs were generated using a three step numerical process. First, the raw data from the wave gauges were filtered using a Butterworth filter using a MatLab code. Next, the filtered data were processed using a FORTRAN hydrograph programming method to calculate the reservoir volume. Then the discharge was calculated based on the change in that computed volume for each time step.

It has been observed that actual noise in the lab influences the level of noise recorded by the wave gauges as the most quiet test times have given the best results while the most crowded and noisy tests have yielded the worst in terms of variability and filtering requirements.

4.2 Video and GIS Techniques

Each dam breach test was videotaped with at least three different camera sources not only as a means of record for each test but also for further detailed analysis. For the large flume tests (varying initial breach geometry), videos were taken for a downstream, a top, and an upstream view. For the tilting flume tests (varying compaction), a side view was added.

In order that all instruments were synchronized, time 0 in every video was cropped to be the moment when the overtopping failure begins. However, the time stamps for both the wave gauges and the cameras use a different source and in order to match them up, one of the cameras must record the wave gauge time stamp which is generated by the computer. This first step in synchronization involved downloading a screen saver to the laptop used to take the wave gauge readings which would show the time to $1/100^{th}$ of a second. This accuracy was required because the video records at 30 Hz and a frame by frame time stamp was desired with an accuracy of plus or minus one frame. The screen saver imparts the same time stamp to the screen as it reads from the internal clock of the computer (which is the same time stamp which is imprinted on the wave gauge data), meaning that one camera can thus be synchronized with the wave gauge files.

For synchronization between the cameras, a simple shot of a light being turned on or the flash of a camera which all video views can see was used. This procedure was normally accomplished by turning on the lights on the upstream and downstream rigs one by one and allowed for duplication of the synchronization between the cameras as there were four independent light sources to film.

Once the film had been synchronized and cropped, video snapshots were taken at regular intervals (generally 10 seconds) for each of the large flume tests to be used for analysis using the geographic information system (GIS) in the ArcGIS computer program. ArcGIS allows for a two-dimensional coordinate system to be generated for each imported picture. This coordinate system is generated by selecting points on an image and assigning them with a given value in the proposed coordinate system. The image can then be rectified, or stretched out, to fit the new coordinate system (by literally bending or stretching individual pixels within the image). Snapshots from the downstream view used the adjust function and the snapshots from the top view used the spline function.

For this study, the coordinate system used was a local coordinate system in mm with the origin being downstream toe of the embankment on the far wall of the flume (bottom left corner if looking upstream). This was an easy location to spot for both the downstream and top camera views. For the downstream view, the x-coordinate was the cross-stream component and the y-coordinate was the vertical component. For the top view, the x-coordinate was the streamwise component and the y-coordinate was the cross-stream component.

Determining the individual control points on an image by image basis, however, was not possible as many of the control points on the embankment erode away with time and cannot be used for later images. Also, glare from the lights reflecting off the water surface can cause points to be obscured. Instead, a template was generated using a snapshot from before the impounding of each embankment. Before impounding, the gridlines are more easily visible, there is no glare, and there are no potential slope failures in the embankment. The points in the template can then be saved in ArcGIS and the coordinate system generated can be imported to any new image. The drawback of this strategy is that the camera has to be assumed to be still for the entire duration of the test or some of the accuracy will be lost. While some movement was sometimes visible, mostly at the beginning of tests after the video cameras had been turned on and recording was initiated, the end result did not show too much variation between the images. Figures 4.1 and 4.2 show images before and after GIS modification.

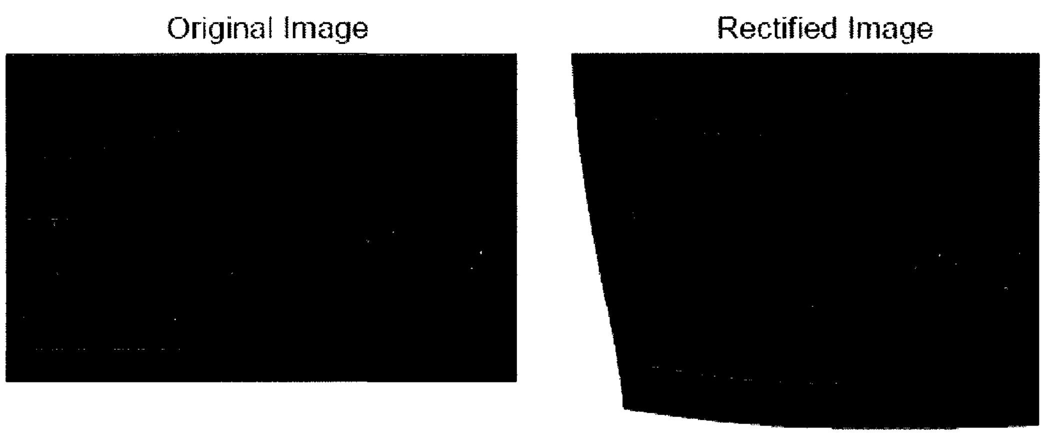

Figure 4.1: GIS Modification of Top View Images

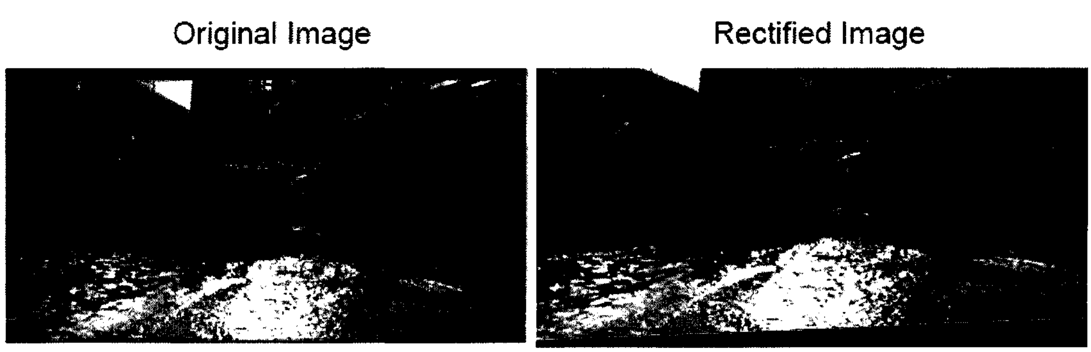

Figure 4.2: GIS Modification of Downstream View Images

It can be seen from Figure 4.1 that there are regions of the rectified image which are more suitable to use than others. For example, near the top of the image, the idealized modification would be to have a straight line at the flume wall rather than the curved line shown. This difference is due to the spline equation which was used to rectify the image as well as the locations of the known points. However, close to the centerline of the embankment, the gridline arrangement is much better. As most measurements were taken from the region around the centerline of the flume and not near the outside flume wall, the method appears to be effective. In one iteration of selecting known points, many more points were used which could better adjust the outer edges of the rectified image, but which sacrificed accuracy near the breach centerline as the gridlines appeared sinuous.

Breach characteristics, such as breach width, were then scaled off each image by drawing lines or curves in the proposed coordinate system. The characteristics could then be plotted over time or against each other if necessary. The characteristics examined were:

- Breach width at 300 mm elevation (the crest);
- Breach width at 150 mm elevation;
- Breach width at the toe of the embankment;
- Downstream face eroded surface area;
- Breach crest length*; and
- Top face eroded surface area*.

Characteristics with a "*" used the top view while the others used the downstream view. The upstream view was generally not used in the video analysis except at times as a check. It should also be noted that some measurements were not possible with the top view at every examined time step. Due to the positioning of the camera and the height of the flume side walls, some areas near the side wall were not visible. Once the breach progressed into those areas, no further video measurements could be taken.

It should be noted, however, that setting a particular coordinate system is not perfect. Not only is there still error within the rectifying process, but there is also error with respect to depth in the image. The template reference coordinates are all relative to the surface of the embankment and that surface erodes away with time, thus exposing something behind it (often a water surface) which has a different set of local coordinates. As such, when a camera angle is not perpendicular to the surface it is viewing, there can be some skew in the image. After all, stretching the image cannot show something that could not be seen in the original image, despite the fact that the proposed coordinate system may indicate that it is there or not. Figure 4.3 shows an image where this phenomenon takes place. In the red circle, it can be seen that there has been a slope failure. Judging from this image, it looks like there is a positive slope at about 1:2. However, shots from the downstream view show that this slope is much closer to vertical. Conversely, the overhang on the other side of the breach channel looks much greater than it truly is and there is more of the breach channel hidden from view than a truly overhead view would have seen.

Figure 4.3: Rectified Image

However, as the breach characteristics all use the existing dam surface as the primary measurement parameter, the depth effects are minimized.

4.2.1 Surface Velocity Distributions

The same GIS-based techniques described above were also used to track surface velocities through the breach channel and in the reservoir over time. Instead of images taken at regular time intervals, appropriate images were selected where the Styrofoam surface particles were easily visible at two time steps. Point coordinates were determined for each image and the distance between them was determined and averaged over the time step between the snapshots in order to obtain a velocity measurement. The location of the velocity measurement was determined to be the mean location between the two particle snapshots.

For measurements taken from the area upstream of the breach crest and downstream of the breach channel, only the top view was used as the water surface was assumed to be relatively flat. For measurements taken from the region around the breach crest, both the top view and the downstream view were used. In those cases, the cross-stream component of the rectified coordinate system was duplicated in both images. However, because of the position of each camera and their shooting angles, the downstream view was determined to be a more reliable indicator for cross-stream position of a surface tracer.

Surface velocities were converted to average velocities using the surface velocity method presented by Rantz (1982), where mean breach channel velocities can be estimated using a coefficient of 0.85 multiplied by the surface velocity.

The locations of the velocity measurements were made relative to a given location both for ease of comprehension and graphing and for relating velocities to the flow regime (subcritical, critical, or supercritical) in the breach channel. The coordinates of the flow regime changes are always moving throughout the breach process, so there must be an associated relative coordinate system to relate to them. Three relative distances were generated for use as positional tools for each velocity reference. Velocities can be relative to the static location of the centerline of the original upstream dam crest (X1), the nearest point on the curvilinear breach crest (X2), and the static location of the centerline of the downstream toe of the original embankment (X3). These relative distances are shown in Figure 4.4.

Figure 4.4: Relative Distances

Three dimensional plots were generated using the program Surfer in the form of contour maps where relative distance was plotted against time and the velocity measurements were used as the contour dimension. These plots are shown in Section 5.5. Given that only a series of points was plotted, the rest of the plot needed to be interpolated in order to fill in areas where no measurements had been taken. The interpolation was conducted using a kriging function which was fit to the experimental spherical variogram.

5.0 RESULTS AND ANALYSIS

The test program was comprised of geotechnical tests, erosion and critical shear tests, compaction tests, and large flume embankment tests. The geotechnical and erosion and critical shear tests were supporting tests used to bolster the results the various embankment tests. The compaction tests were designed to bolster the results of the large flume embankment tests which used varying initial breach geometries.

5.1 Geotechnical Tests

Two sands were used for the embankment tests. The compaction tests all used Sand I. The large flume tests initially used Sand I, but then changed to Sand II for the latter portion of the test series which included the crater, tapered, and V-notch with drain initializations. The gradation curves for Sand I can be seen in Figure 5.1. The gradation curves for Sand II can be seen in Figure 5.2.

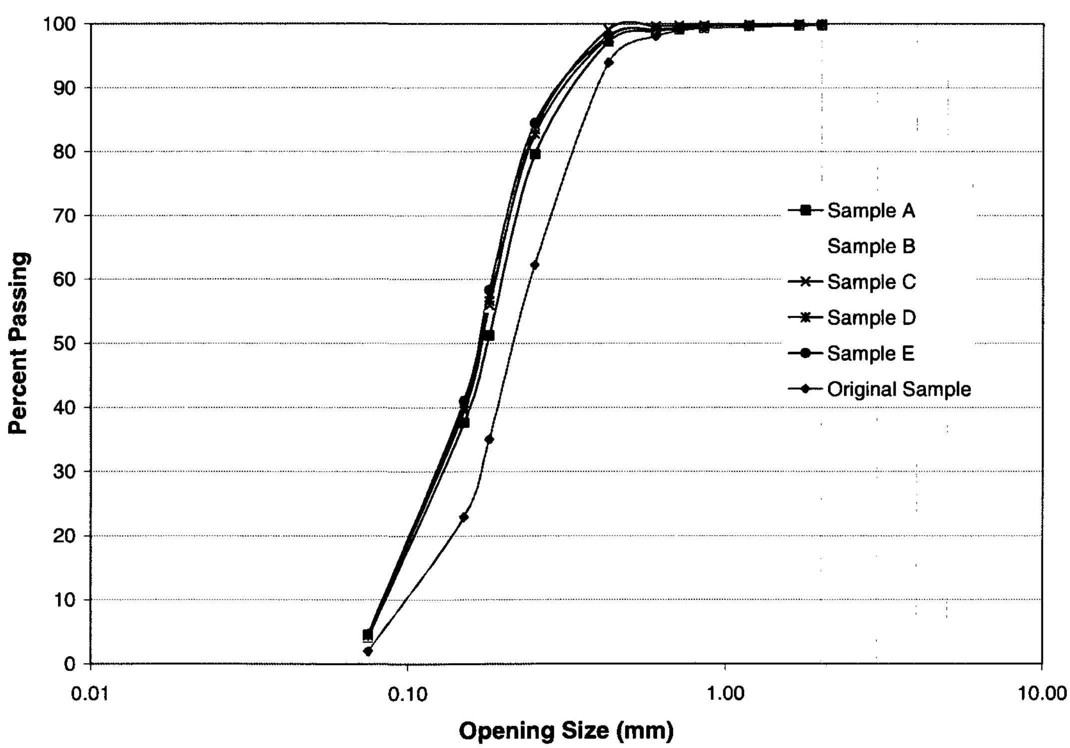

Figure 5.1: Sand I Distribution Curves

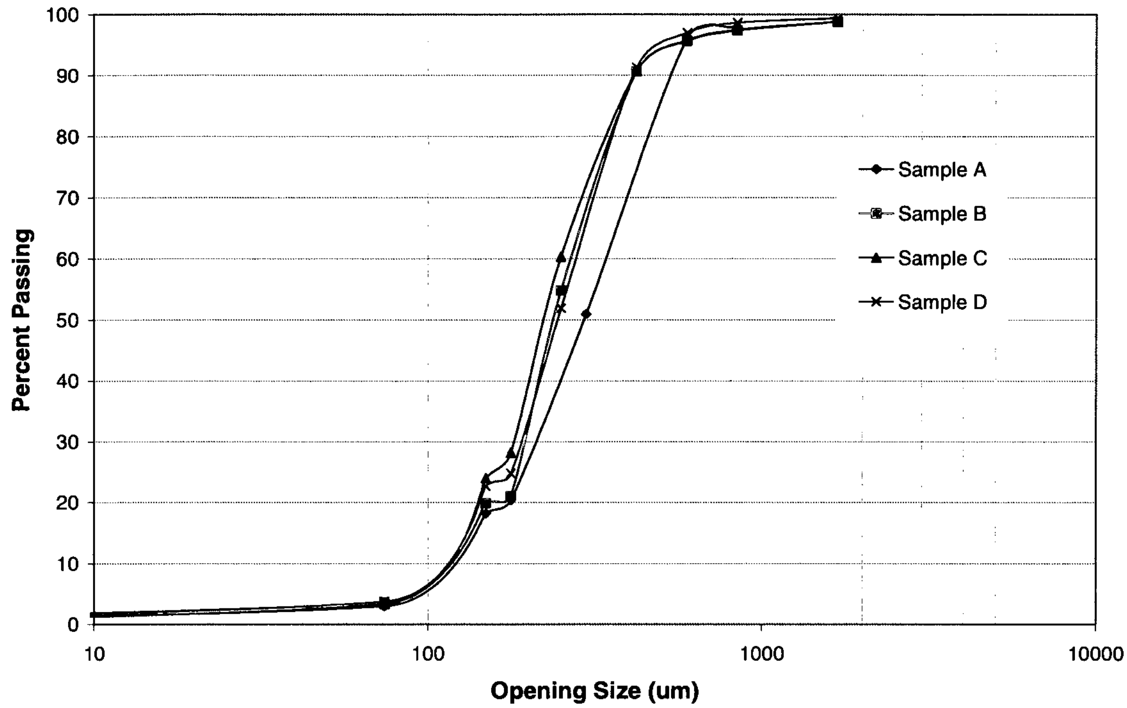

Figure 5.2: Sand II Distribution Curves

Samples were taken at random from various barrels used to hold the sand and from various locations within the barrels so as to obtain a more meaningful representative sample set. The original sample referred to in Figure 5.1 is the original sample of sand which was taken in the early stages of the project when a sand source was being examined. The difference between that sample and the other is attributed to the time between the samplings when new sand was put in the pile in the quarry which had a different gradation. It is the same reason there is a difference between Sand I and II. It can be seen that Sand I is finer than Sand II and that the median grain size for Sand II is about 50% larger than for Sand I. Also, Sand II has an unexplained gap in the grade. The gap is small and thought to be inconsequential. Sample A in Figure 5.2 is another original sample for Sand II which used a different set of sieves which is why it is thought to look like it has a different gradation. In both cases, however, all the gradation samples are very similar. Figure 5.3 shows the gradation curves for the drain and filter materials.

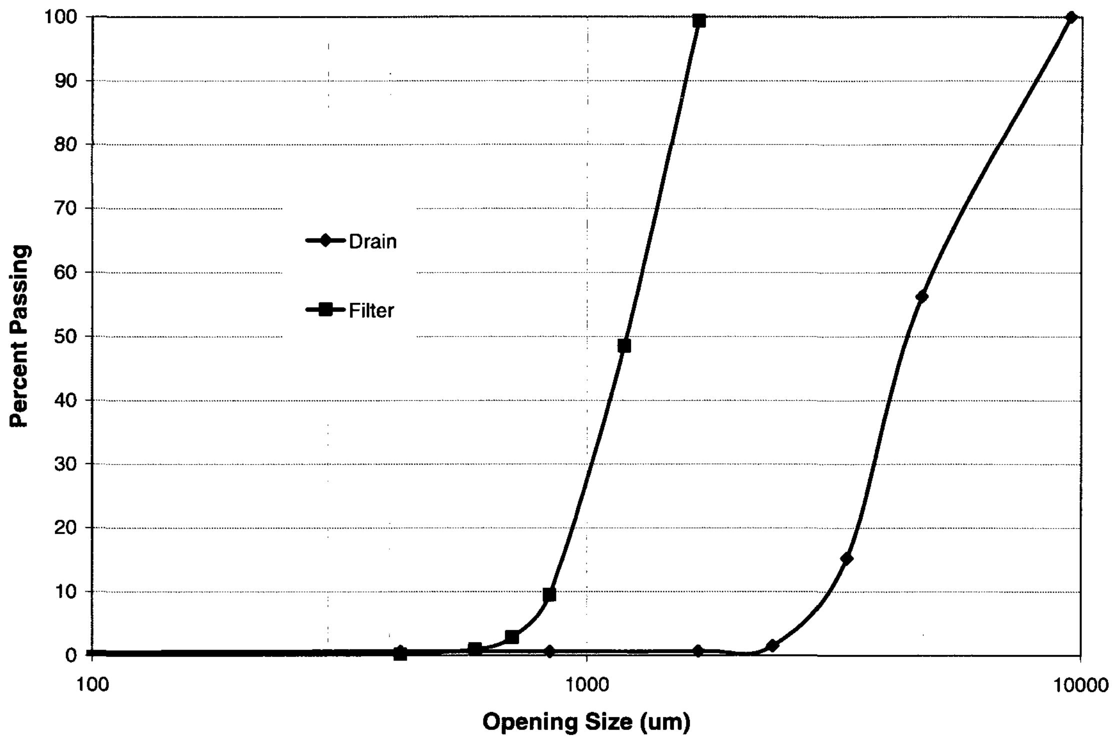

Figure 5.3: Drain and Filter Medium Distribution Curves

The compaction curves from the Proctor Tests are shown in Figure 5.4 along with the estimated curve for compaction with an effort equivalent to 5 blows from 100 mm high. While it may be desirable to have a curve with less compaction effort so as to interpolate the 5 blows from 100 mm high curve rather than extrapolate it, it is simply not possible to conduct a 1 blow Proctor test. A single blow does not provide the uniformity necessary to make the test reliable and any changes to the volume of the mold or the weight of the hammer or the drop height would require significant changes to the apparatus. Table 5.1 shows the predicted embankment densities relative to the compaction effort.

Table 5.1: Embankment Density

Compaction Effort	Density of the Compacted Lift (kg/m^3)
5 blows (5 mm)	1495
5 blows (10mm)	1530
10 blows (10 mm)	1560
20 blows (10 mm)	1600

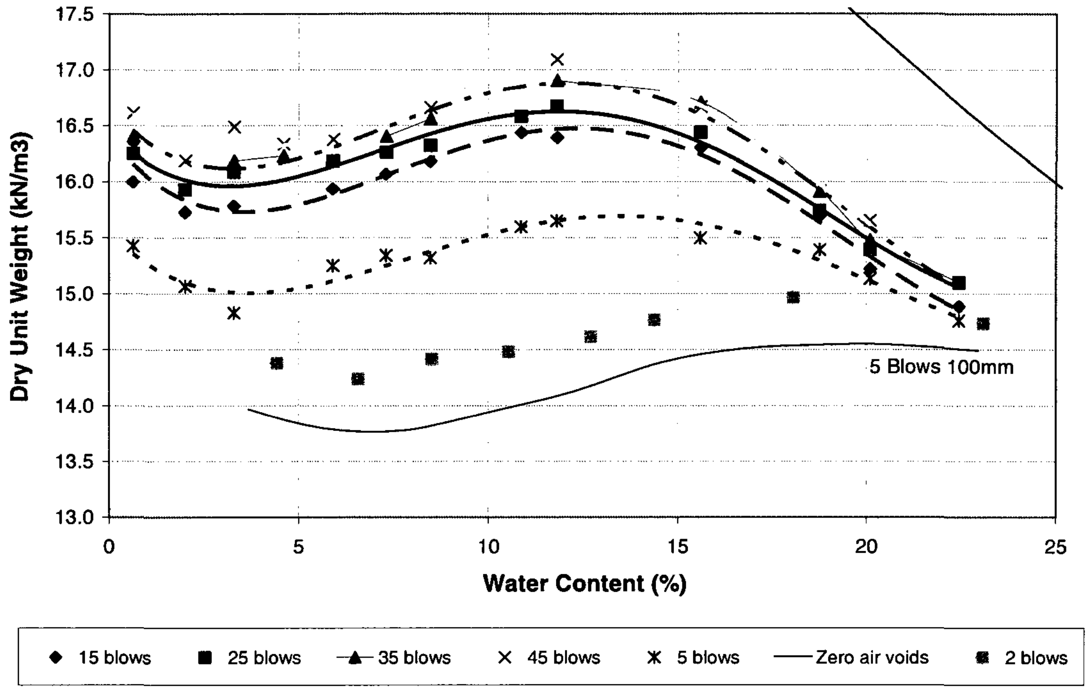

Figure 5.4: Standard Proctor Test Results

The permeability curve for Sand I is shown in Figure 5.5. The curve shows the coefficient of permeability compared with the void ratio to show the variation of permeability of the sand which has been varied by compaction. The result is a linear relationship with can be easily extrapolated to obtain the permeability of the soil at a variety of different compaction efforts.

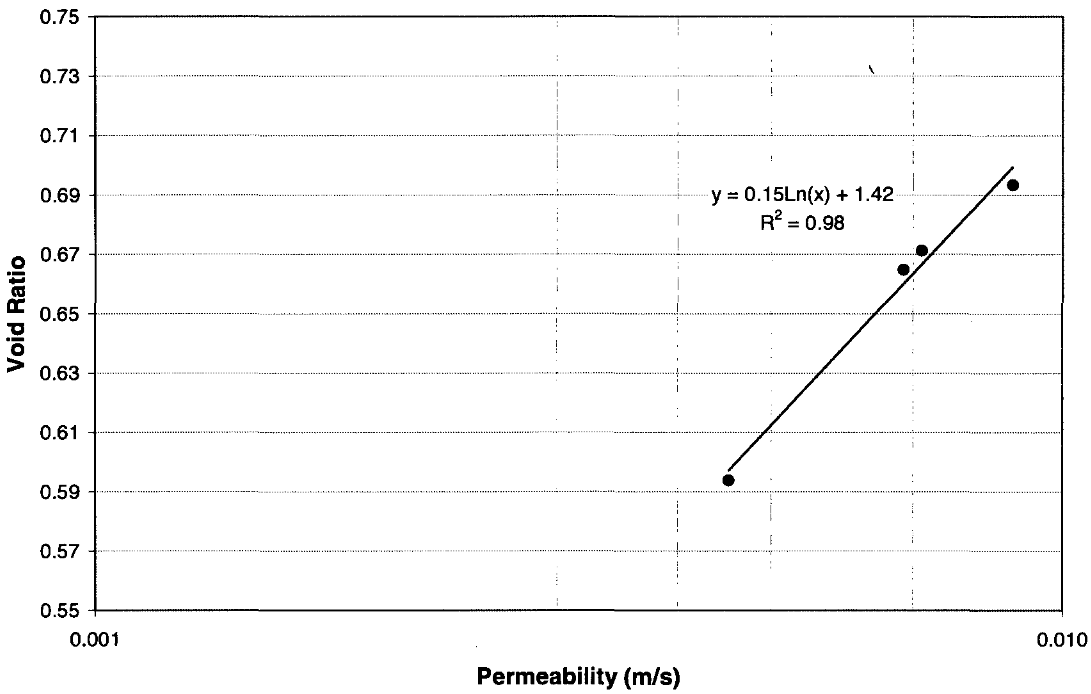

Figure 5.5: Sand I Permeability Analysis

Figure 5.6 shows the shear strength envelope for Sand I as determined using the direct shear test. The test was conducted slowly, so the values presented are the effective shear stress parameters. For the trend line, the intercept was set to 0 rather than using regression to determine the intercept. As the soil is coarse grained and the percentage of fines less than 2%, the soil can be assumed to be non-cohesive. The angle of internal friction, ϕ', was determined to be 36°.

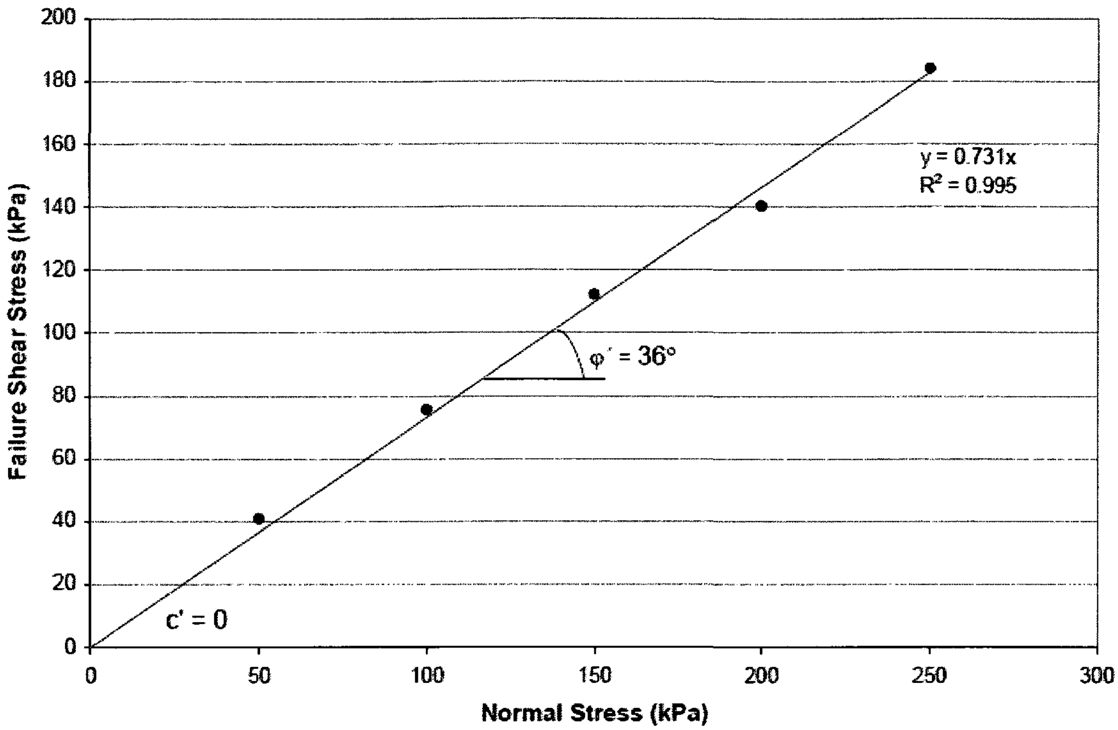

Figure 5.6: Shear Strength Envelope for Sand I

Figure 5.7 shows the hydrometer analysis for the clay. It should be noted that this method is only a guide to determine the gradation of the clay. It can be seen from the analysis that the percent fines is about 95%. It should be noted that the USCS classifies this soil as lean clay, but using the gradation curve from the hydrometer analysis places the soil as a silt. From physically handling the material, the soil felt more like clay than. Figure 5.8 shows the Standard Proctor compaction curve for the clay. Only a single test was conducted as, later, it was decided the clay would be placed at a very high water content, easily wet of optimum. As such, the standard compaction method would not be applied as it seemed to do more lifting due to the clay sticking to the compactor than it did compacting.

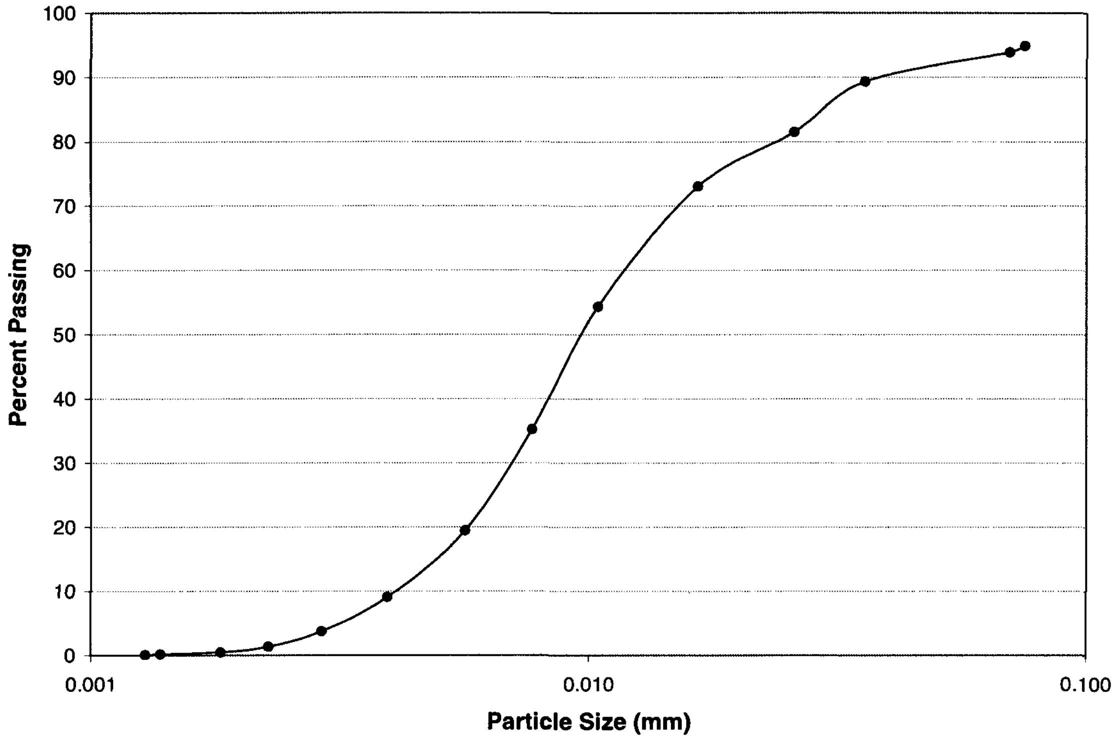

Figure 5.7: Hydrometer Results for Sandy Hill Clay

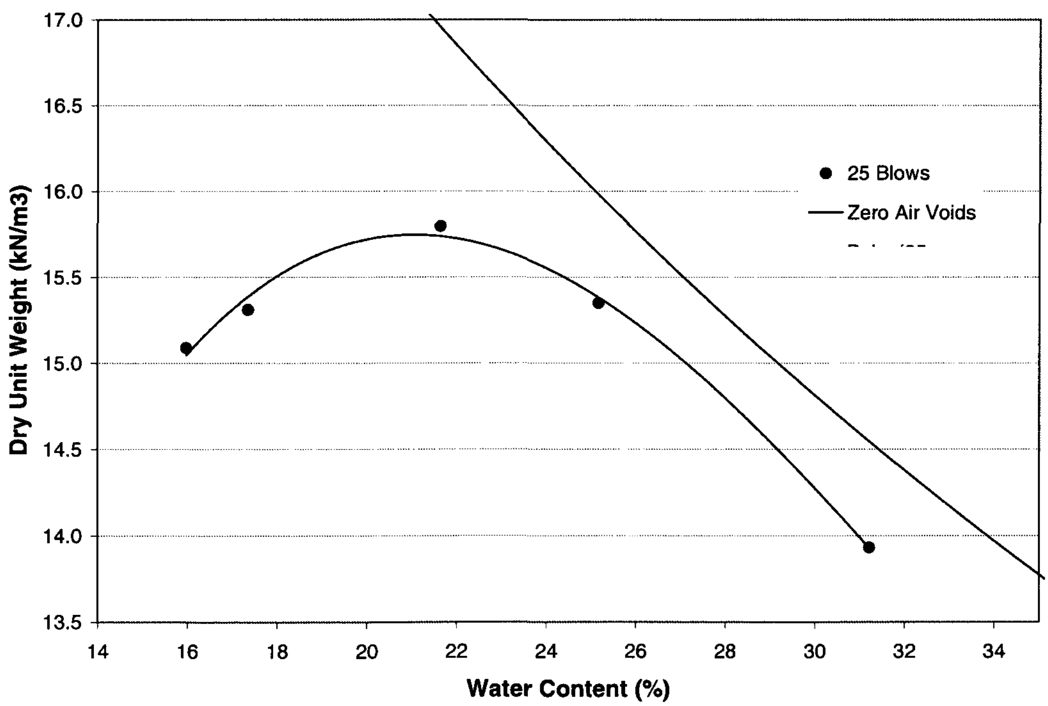

Figure 5.8: Proctor Test for Sandy Hill Clay

5.2 Erosion Rate and Critical Shear Tests

This section presents both the results from the critical shear tests for both the sand and clay sediment as well as results for the vertical and mass erosion rates which were determined through a series of six experiments for sand and six tests for clay. These rates have been plotted against the excess shear at the bed in accordance with the form shown in Equation 2.8.

5.2.1 Soil Sampling

Mass erosion for these experiments is simply the difference in total mass within the test section before and after the test. In order to find the initial mass in the test section, certain assumptions must be made. For the non-cohesive material, the assumption is the sand is at its loose, dry density. Therefore, the void ratio is known and all voids are filled with air, which is considered to have no mass. The initial mass, therefore, is simply the product of the volume of the test section and the loose dry density. After the test has been completed and the sand in the test section has been recovered, it is dried and weighed to determine the final dry weight from the test section.

For the cohesive sediment, the same assumption cannot be made as the clay is mixed with water. In order to determine the initial water content of the clay, a sample was taken for each test and a representative water content from the clay mixture was determined. Once the clay in the test section was recovered, the wet weight was determined before drying it to obtain the dry weight recovered from the test section, yielding what is assumed to be the saturated water content of the cohesive sediment. This difference is crucial as we cannot assume the initial clay placed in the test section is fully saturated. With both the initial and final water contents and knowing the specific weight of the clay solids, an estimate of the initial dry density can be made and the initial dry mass can be determined.

While sand samples were only left in the oven 24 hours to dry, the clay samples were left for at least 72 hours before being massed. Water contents for each of the clay samples are presented in Table 5.2. Both the initial and final water contents showed variability within about 5%, which is good.

Table 5.2: Initial and Final Water Contents for Clay

Run	Initial Water Content (%)	Final Water Content (%)
1	49.5	55.4
2	51.8	57.0
3	49.0	52.6
4	54.1	56.8
5	51.3	57.8
6	49.5	55.1

5.2.2 Shear Stress

An ADV was used to obtain velocity measurements at different elevations at the centerline of the flume approximately above the centre of the test bed. These velocity measurements were used in two ways to obtain the shear stress at the bed. Both a log-linear plot of streamwise velocity vs. depth and a plot of depth vs. principal Reynolds stress were used to estimate the bed shear. Figure 5.9 shows a log-linear velocity plot that was used to determine the critical shear value of the sand.

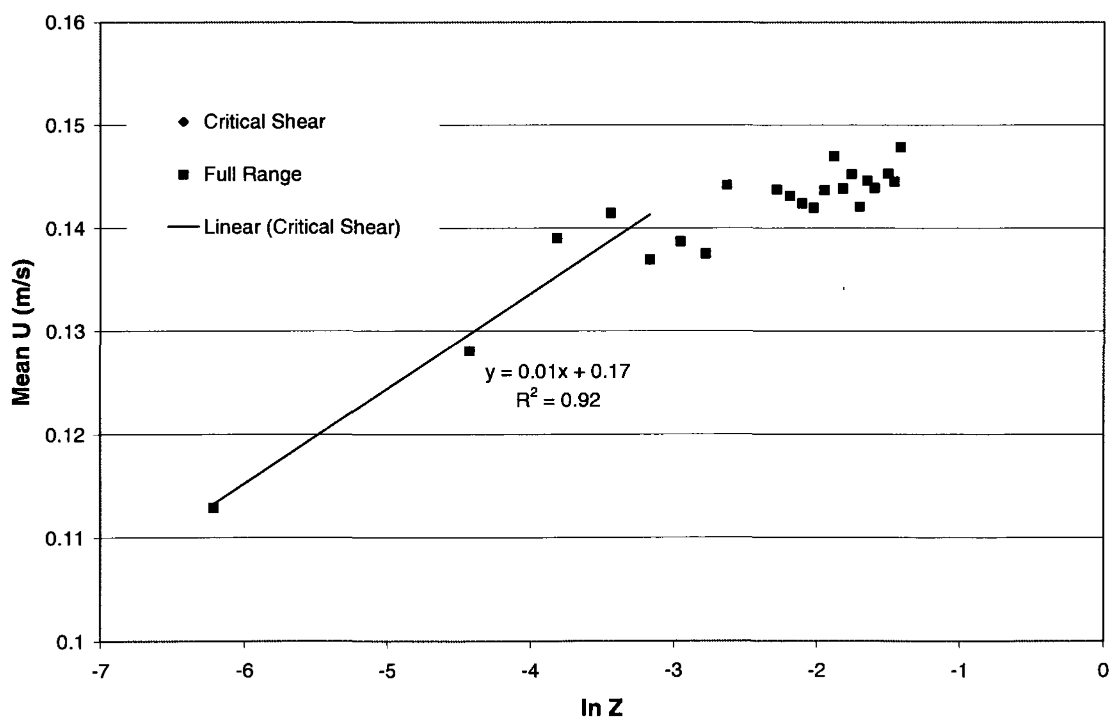

Figure 5.9: Critical Log-linear Velocity Plot for Sand

While many more data points are available, only the first few, nearest the bed, show a linear trend on the plot. Measurement at shallower depths show a different trend which indicates that the log boundary layer no longer exists at that depth and so those points would yield an underestimation of shear stress at the bed. The deviation from log-linearity in the upper portion of the water column was due to non-uniform flow over the test section. Shear stress is determined using Equation 5.1.

$$u^{+} = \frac{1}{\kappa} \ln y^{+} + C \qquad [5.1]$$

In the above equation, $u^{+} = \frac{u}{u_*}$ and $y^{+} = \frac{u_* y}{\nu}$. Therefore, the shear velocity u_* can be obtained by multiplying the slope of the plotted line by the von Karman constant (κ = 0.41). Shear stress at the bed can then be estimated as $\tau_{\circ} = \rho u_*^2$.

In the case of these experiments, the water temperature was approximately 25°C. Using this method, the critical shear stress for the loose sand was estimated to be 0.014 Pa.

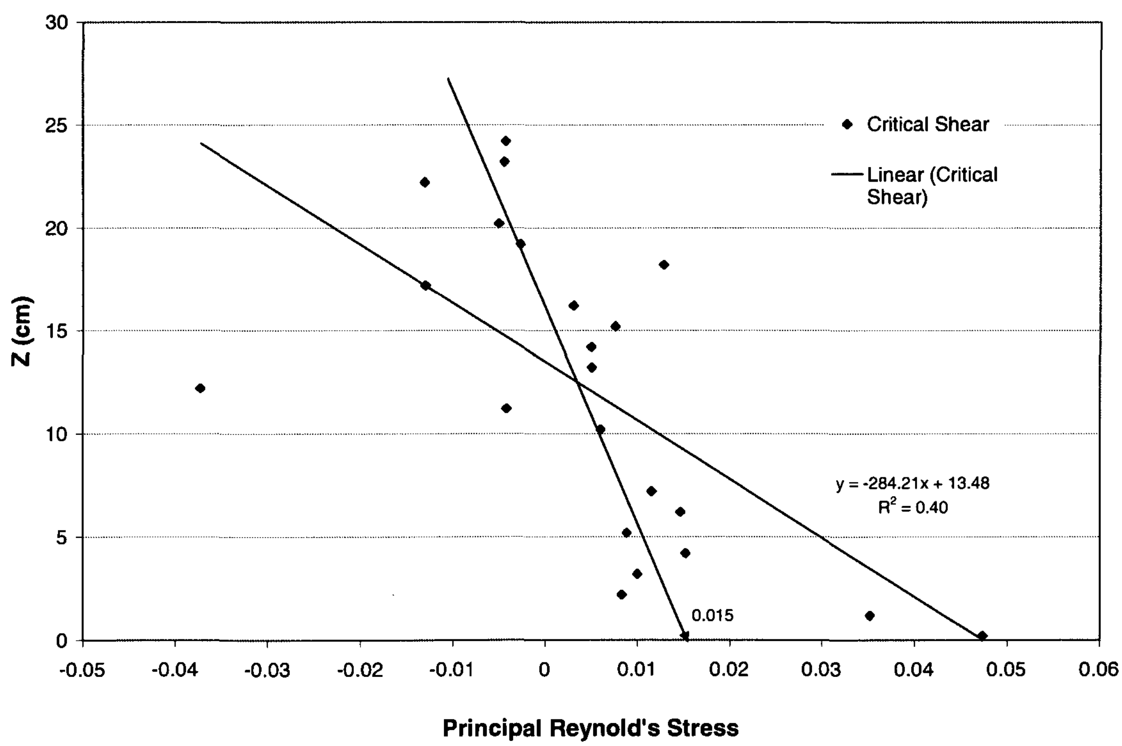

Figure 5.10: Critical Reynolds Stress Profile for Sand

Figure 5.10 shows a plot of the principal Reynolds stress vs. depth. Reynolds stresses represent the mean transport of fluctuating momentum due to turbulence. The principal Reynolds stress is the average of the product of the velocity fluctuations of the streamwise and cross-stream directions. Figure 5.11 shows a typical plot of principal Reynolds stress with depth for uniform flow. The relationship is roughly linear following the form $\frac{\tau}{\rho} \equiv -\overline{uv} + \nu \frac{\partial U}{\partial y}$ (Nezu and Nakagawa, 1993) until the viscous sub-layer is reached, after which it theoretically curves to 0. For shear stress at the bed, this linear relationship is extrapolated to y = 0. Figure 5.12 shows the influence of ridges and troughs on principal Reynolds stress.

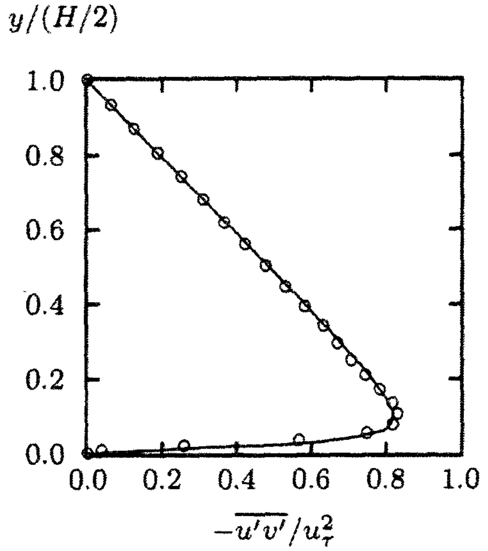

Figure 5.11: Principal Reynolds Stress Distribution for Uniform Flow (Wilcox, 1998)

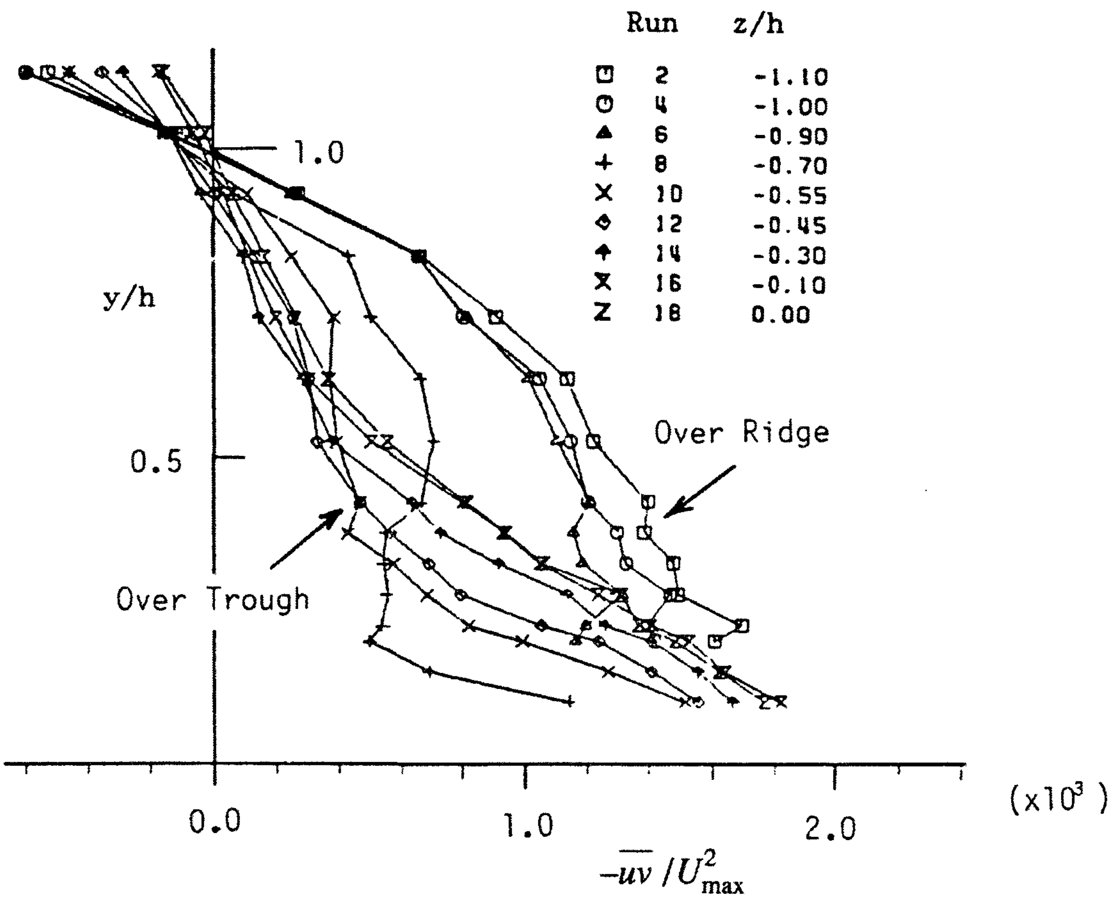

Figure 5.12: Distribution of Principal Reynolds Stress over Ridge and Trough (Nezu and Nakagawa, 1993)

It can be immediately seen in Figure 5.10, as the R^2 value for the trend line shows, that the trend is not a linear one. This non-linearity means the flow field is not uniform. A more visual trend line was drawn on the figure (shown in red) and this trend line yields a critical shear value of 0.015 Pa which corresponds well with the value determined using the previous method, as opposed to the trend line determined value of 0.047 Pa.

While normally this situation would indicate that the actual shear at the bed is lower than what the trend line would yield, the near-bed measurements of shear stress correspond very well with the trend line value. Therefore, the trend line value was used and the critical shear stress using this method was determined to be 0.047 Pa. The non-dimensional shear in this case for the critical shear state is therefore 0.023, which lies well below the threshold of motion on the Shields curve regardless of the Re_* value. This lower threshold is likely due to the very loose nature of the sediment.

The plots for the critical shear stress values for the clay are shown in Figures 5.13 and 5.14. It should be noted that two critical shear values were determined for the clay. This was discovered when, after determining the first critical shear value for the clay, the flow was increased and the test begun and then erosion stopped after a short time. Flow was then increased until "initial" motion re-initiated and new measurements for critical shear were established. After this second threshold of motion, erosion continued and did not stop a second time. While this phenomenon is supported by the observations of Aberle *et al.* (2003), it is doubtful this is the sort of depth criteria they meant. Rather, it seems that this phenomenon is due to loose surface particles generated from the formation of the bed (whether they dried out quickly or some other factor is at work).

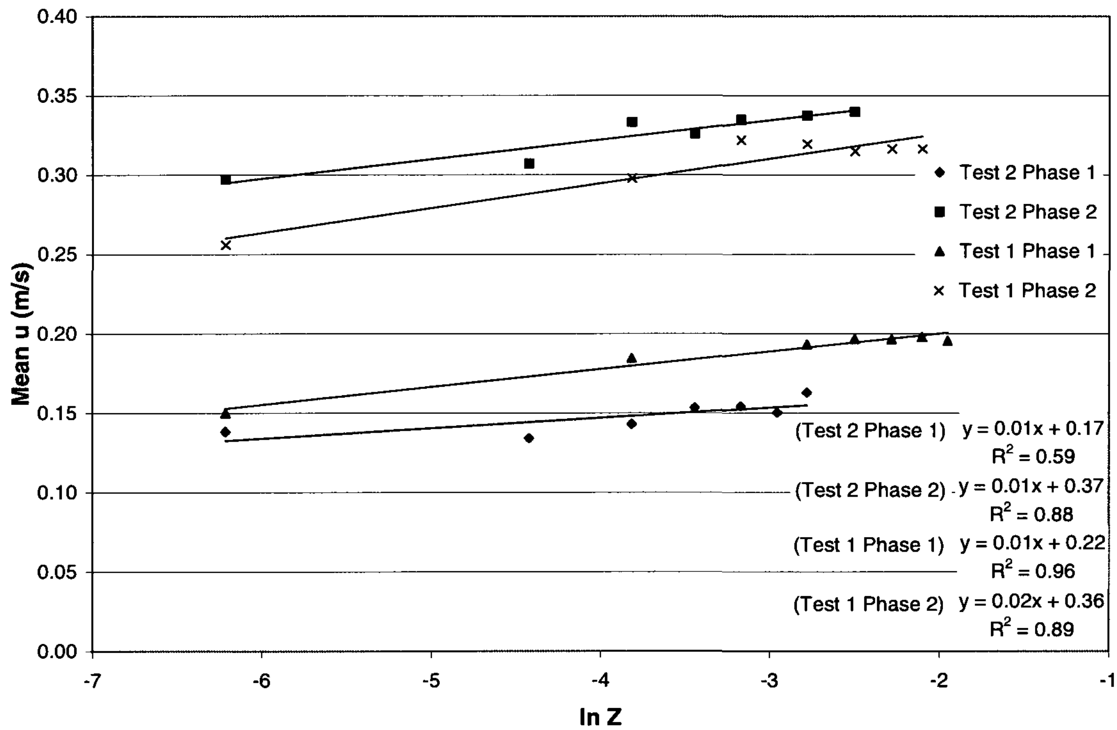

Figure 5.13: Critical Log-Linear Plot for Clay

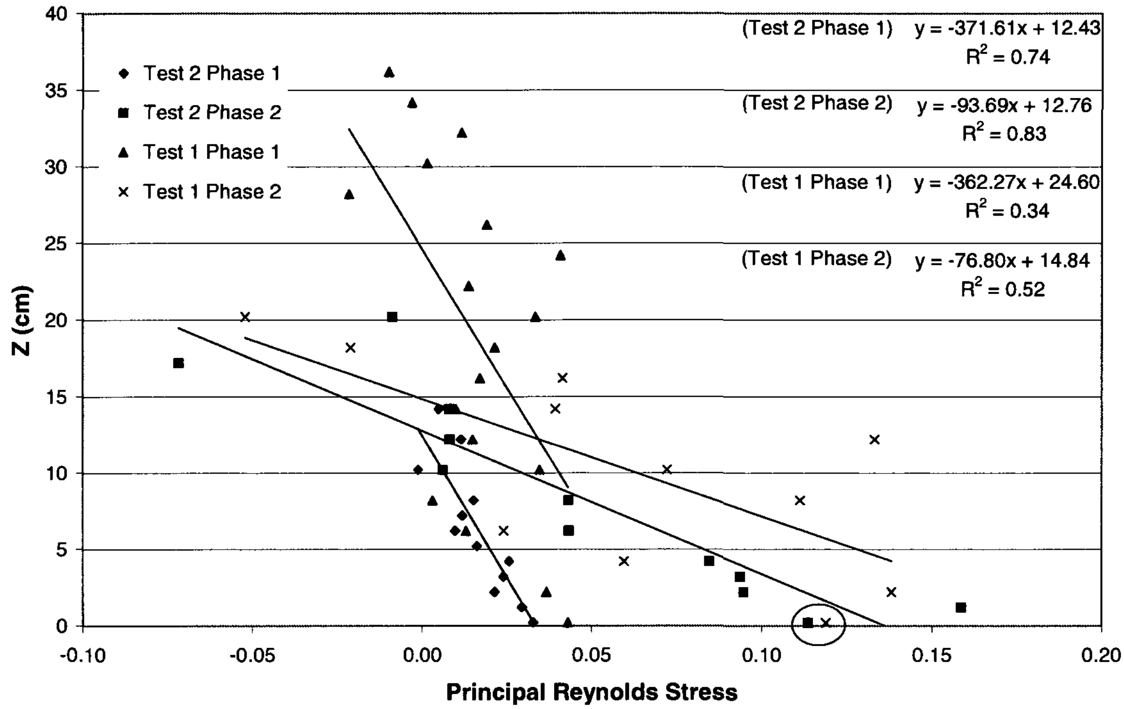

Figure 5.14: Critical Principal Reynolds Stress Plot for Clay

Two sets of critical shear tests (test 1 and test 2) were conducted on the clay due to a change in procedure for the erosion rate tests. This procedure changes apply only to steps which were conducted after critical shear was determine so, while these earlier erosion rate tests are not used to show erosion rate results, they did provide an excellent opportunity to check the critical shear results. The critical shear duality was observed for both sets of critical shear stress observations. The critical shear stress of the clay, for the purposes of the erosion rate formulae, was determined to be the average of the results for near-bed critical shear stress measurements for the second phase of motion which are circled in red in Figure 5.14.

5.2.3 Sand Tests

Six tests erosion rate tests were conducted for the sand bed at different shear stresses. The plots to determine the bed shear are shown in Figures 5.15 and 5.16. The tabular results are presented in Table 5.3. The differences between the two methods are quite pronounced. Given how the results compare so poorly to each other, they were compared to the measured near-bed principal Reynolds stress as well. The comparison is shown in Table 5.4.

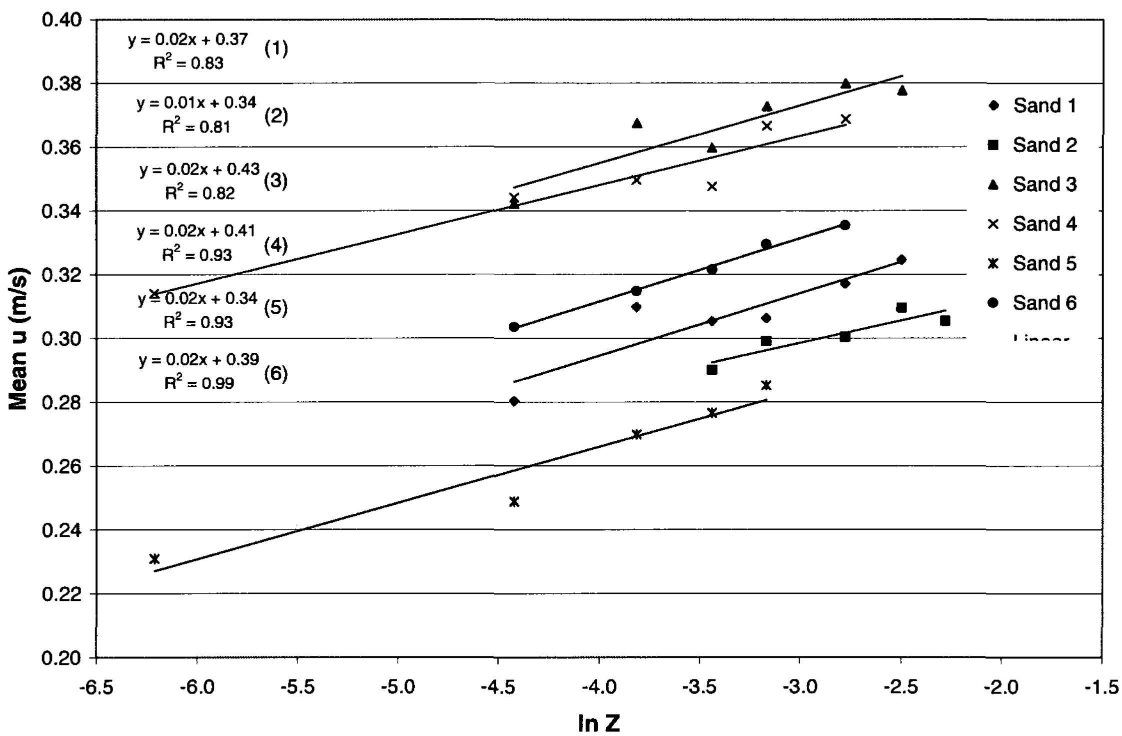

Figure 5.15: Log-Linear Velocity Plots for Sand Tests

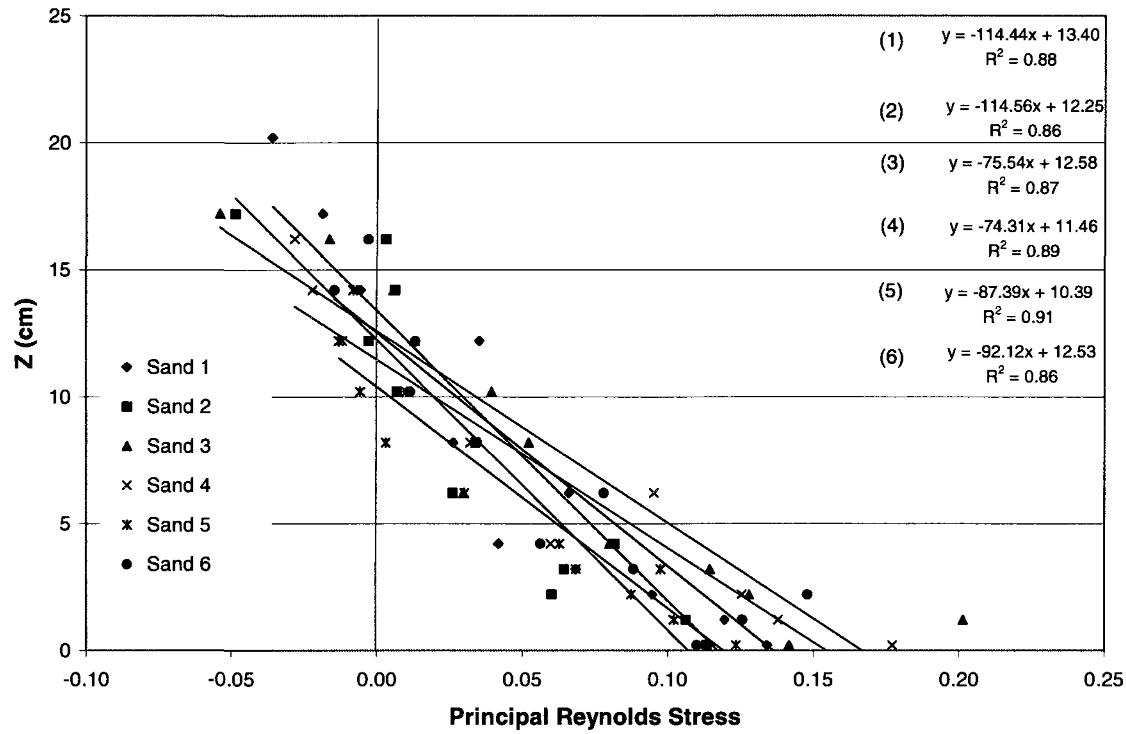

Figure 5.16: Principal Reynolds Stress Plots for Sand Tests

Table 5.3: Bed Shear Estimates for Sand

Run	Shear Stress from Velocity (Pa)	Shear Stress from Reynolds Profile (Pa)	Q (L/s)	Total Difference (Pa)	% Difference
1	0.064	0.117	27.2	0.053	45
2	0.032	0.107	24.1	0.075	70
3	0.055	0.166	29.6	0.112	67
4	0.040	0.154	27.2	0.114	74
5	0.052	0.119	19.0	0.067	56
6	0.066	0.136	23.2	0.070	52

Table 5.4: Comparison with Near Bed Measurements for Sand

Run	Shear Stress from Reynolds Profile (Pa)	Shear Stress from Near-Bed Measurements (Pa)	Total Difference (Pa)	% Difference
1	0.117	0.134	0.017	14
2	0.107	0.113	0.006	6
3	0.166	0.142	0.024	15
4	0.154	0.177	0.023	15
5	0.119	0.123	0.004	3
6	0.136	0.110	0.026	19

The estimates for shear stress in Table 5.4 compare much better. While it is difficult to say which source is more accurate, it is sufficient to say that the values obtained using the velocity method are unsuitable to be carried forward in the analysis. Erosion rate functions were carried out for both shear values obtained from measurements of principal Reynolds stress. Figure 5.17 shows the vertical erosion rate function for sand and Figure 5.18 shows the mass erosion rate for sand, both plotted using the shear stress from the Reynolds profile. Figures 5.19 and 5.20 show a comparison of erosion rate functions using the trend line values and the near-bed measurements.

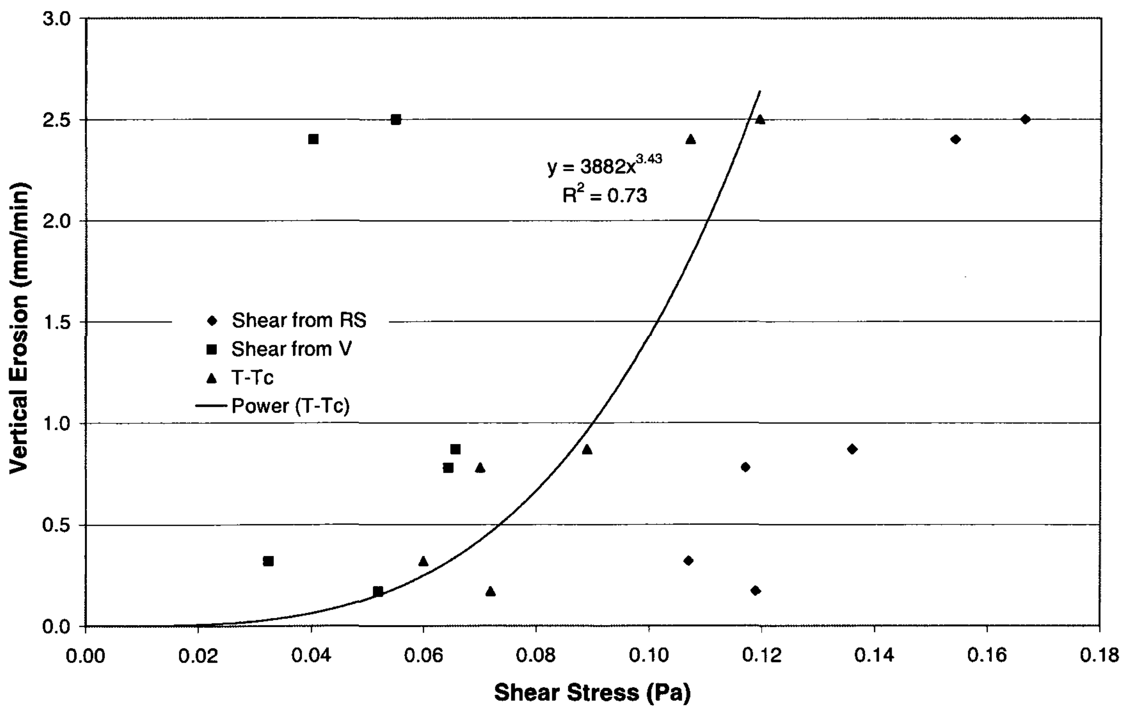

Figure 5.17: Vertical Erosion Rate of Sand

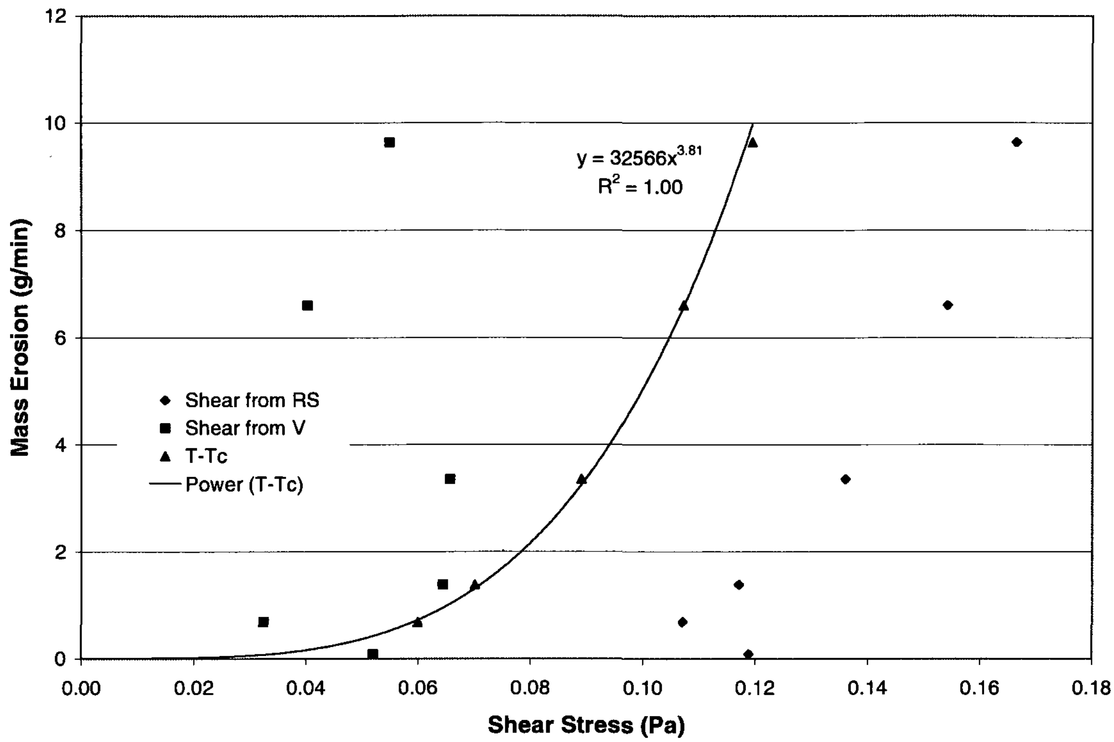

Figure 5.18: Mass Erosion Rate of Sand

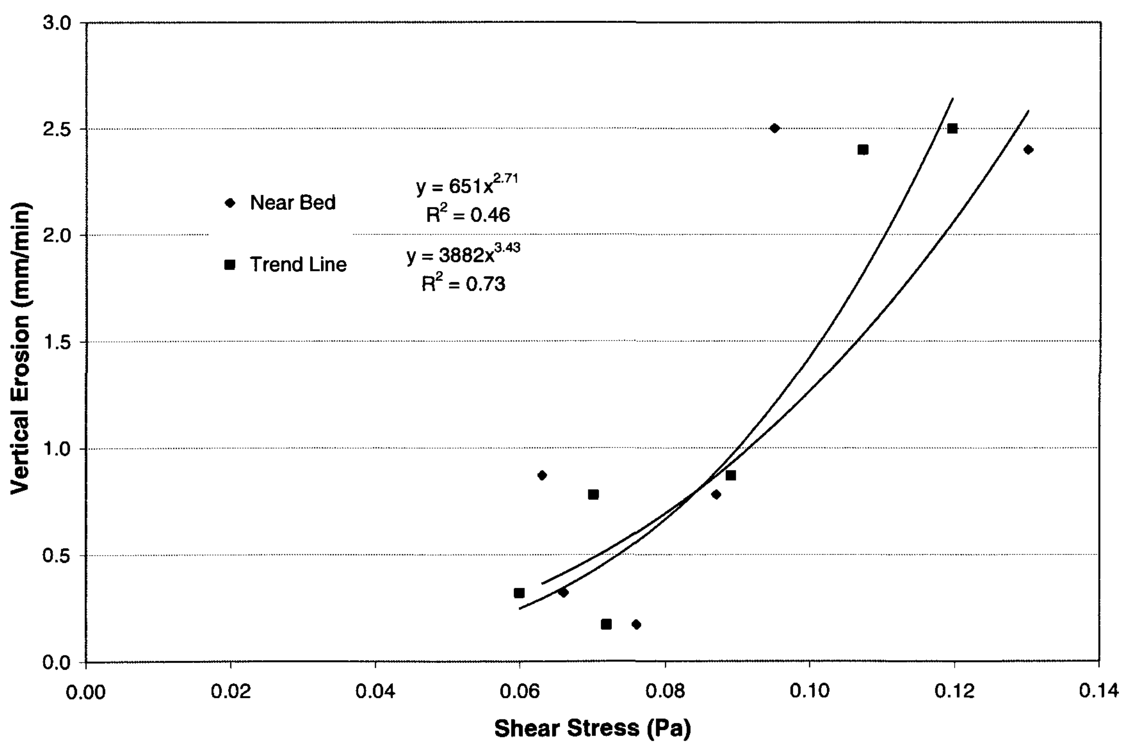

Figure 5.19: Vertical Erosion Rate Comparison for Sand

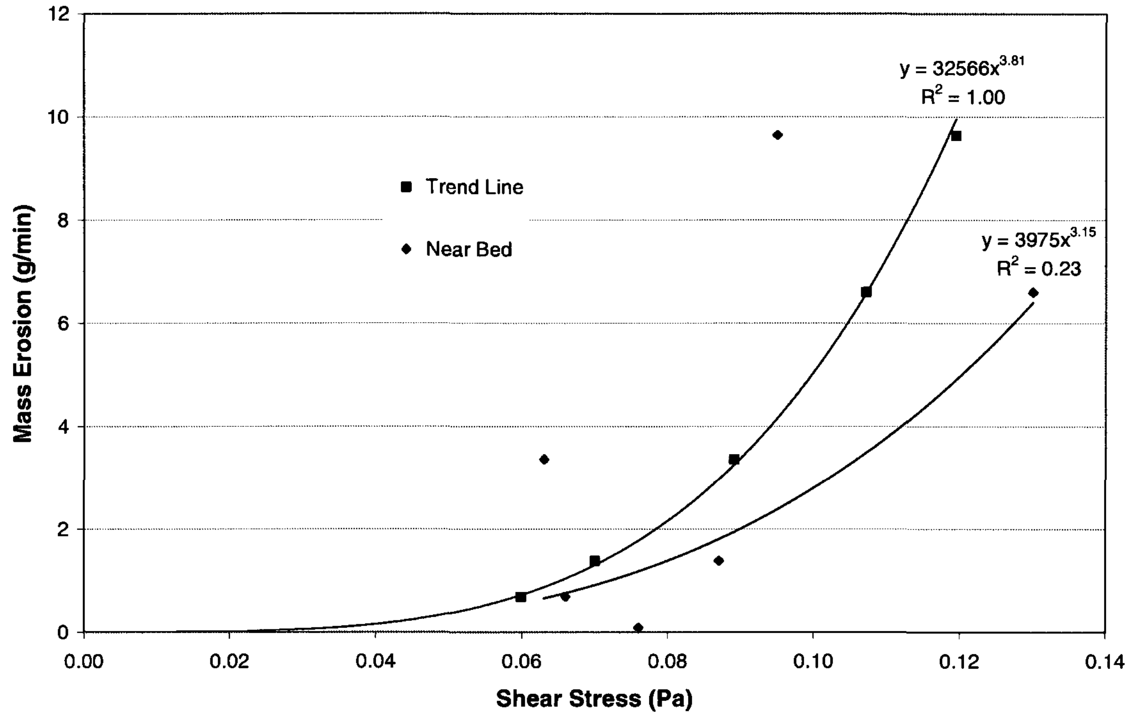

Figure 5.20: Mass Erosion Rate Comparison for Sand

It should be noted that in the case of the mass erosion rate in Figure 5.18, one of the data points was omitted as it appeared to be an outlier. Also, Figures 5.17 and 5.18 show again how the shear stresses obtained using the mean velocity measurements are not appropriate for this analysis given how they show an opposite erosion trend. Table 5.5 shows the comparison of the erosion rate values as determined using Equation 2.8.

Table 5.5: Comparison of Erosion Rates for Sand

Vertical Erosion				Mass Erosion			
Trend Line		Near Bed		Trend Line		Near Bed	
C_e	n	C_e	n	C_e	n	C_e	n
3882	3.43	651	2.71	32566	3.81	3975	3.15

The comparison shows dramatically different results, indicating that the parameters are extremely sensitive to the method with which the excess shear stress is determined. Moreover, the R^2 values from the trend line results are much better than those for which used the near bed shear.

5.2.4 Clay Tests

Six tests were conducted for the clay bed. The plots to determine the bed shear are shown in Figures 5.21 and 5.22. The tabular results are presented in Table 5.6. Once again, the differences between the two methods are great. Given how the results compare so poorly to each other, they were compared to the measured near-bed principal Reynolds stress. The comparison between the methods is shown in Table 5.7.

Table 5.6: Bed Shear Estimates for Clay

Run	Shear Stress from Velocity (Pa)	Shear Stress from Reynolds Profile (Pa)	Q (L/s)	Total Difference (Pa)	% Difference
1	0.047	0.266	33.1	0.220	82
2	0.090	0.410	19.5	0.320	78
3	0.056	0.658	29.2	0.601	91
4	0.088	0.572	23.5	0.484	85
5	0.072	0.529	25.6	0.457	86
6	0.088	0.772	38.5	0.684	89

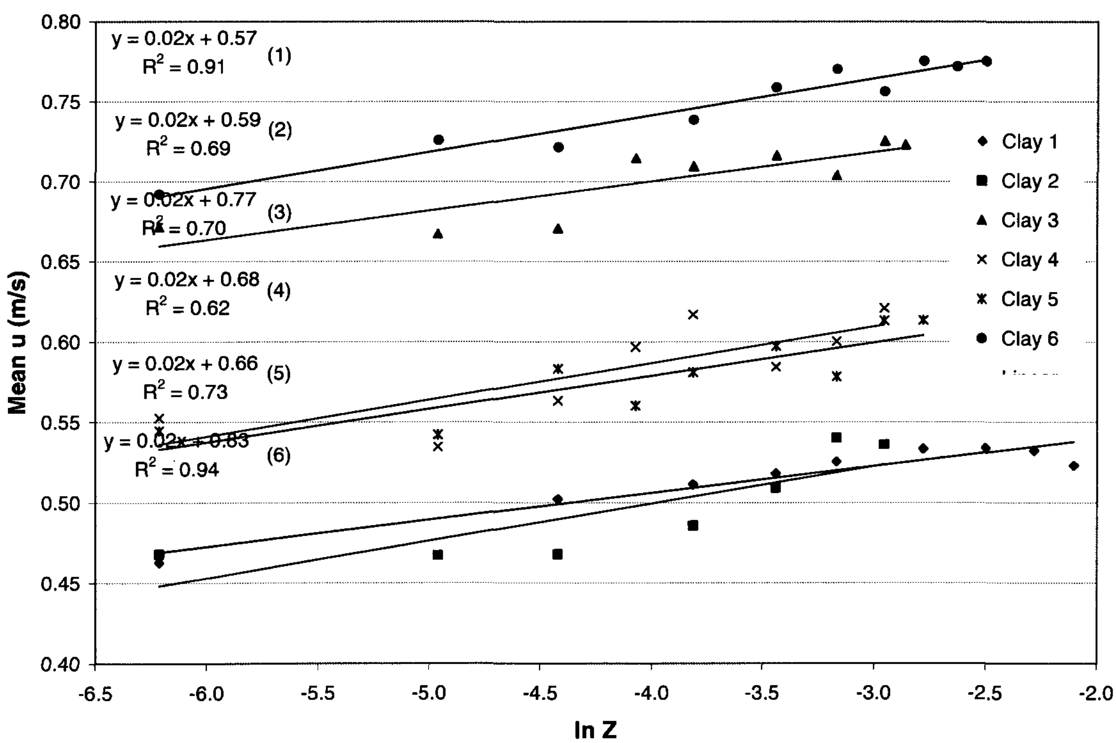

Figure 5.21: Log-Linear Velocity Plots for Clay Tests

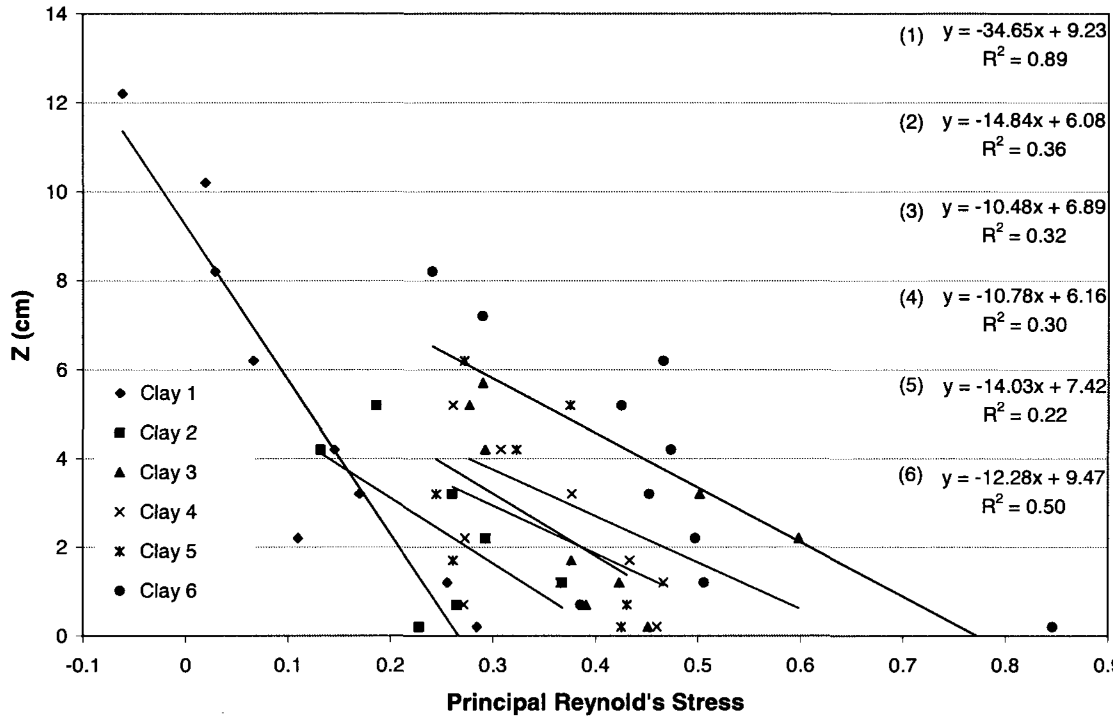

Figure 5.22: Principal Reynolds Stress Plots for Clay Tests

Table 5.7: Comparison with Near Bed Measurements for Clay

Run	Shear Stress from Reynolds Profile (Pa)	Shear Stress from Near-Bed Measurements (Pa)	Total Difference (Pa)	% Difference
1	0.266	0.284	0.018	7
2	0.410	0.228	0.182	44
3	0.658	0.451	0.207	31
4	0.572	0.460	0.112	20
5	0.529	0.425	0.104	20
6	0.772	0.846	0.074	10

Once again, when comparing against the near bed principal Reynolds stress, the results are much better. And once again, the shear values obtained using the mean velocities can be looked upon as unfavourable. Figure 5.23 shows the vertical erosion rate function for clay and Figure 5.24 shows the mass erosion rate for clay. The applied shear value used for both of these cases is the value obtained using the trend line. Figures 5.25 and 5.26 show the function obtained using the near bed principal Reynolds stress as compared to those determined using the trend line method.

The erosion rate parameters in Figures 5.25 and 5.26 are not as good as those that were obtained for the sand given the R^2 values for the trend lines. It should be noted that in both erosion rate cases, the outlier was deemed to be the point where the erosion rate was 4.0 g/min. Once again, the shear stress obtained using the mean velocities showed an opposite trend.

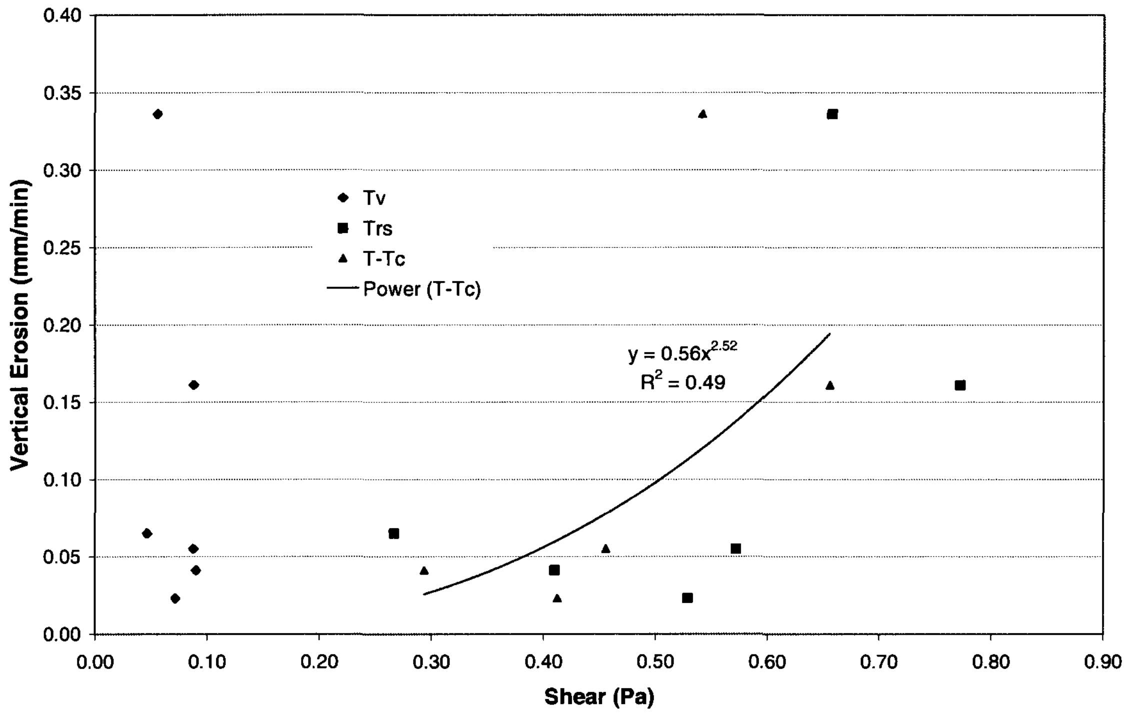

Figure 5.23: Vertical Erosion Rate for Clay

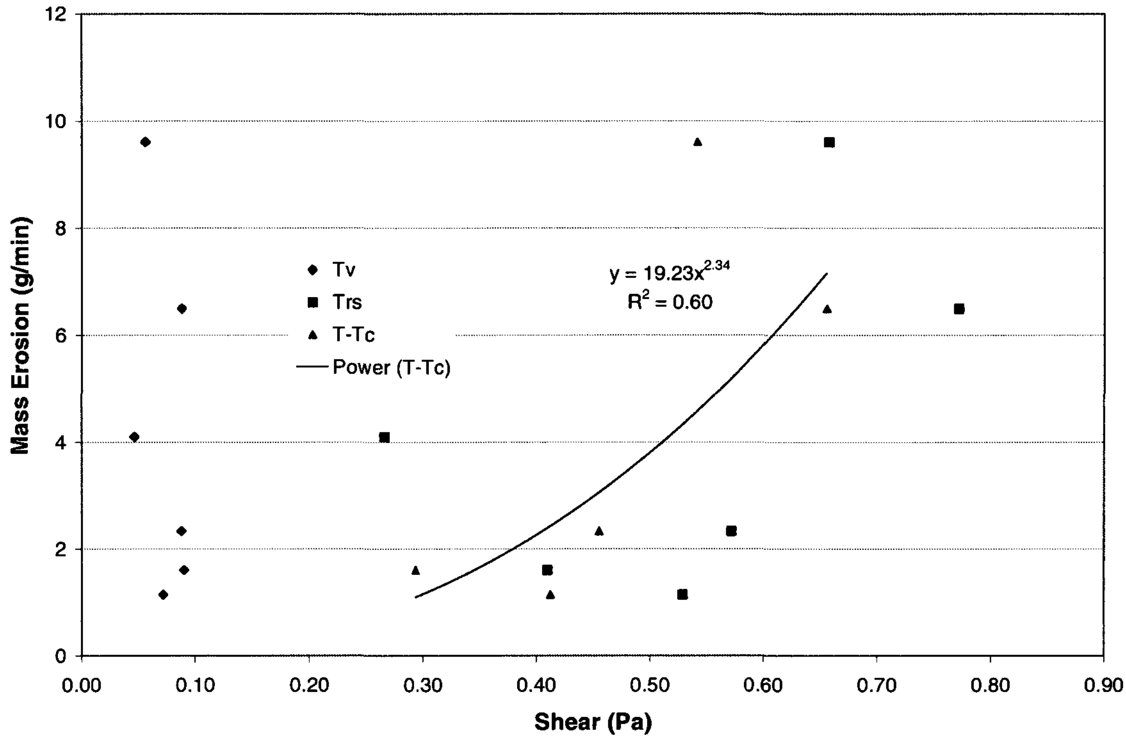

Figure 5.24: Mass Erosion Rate for Clay

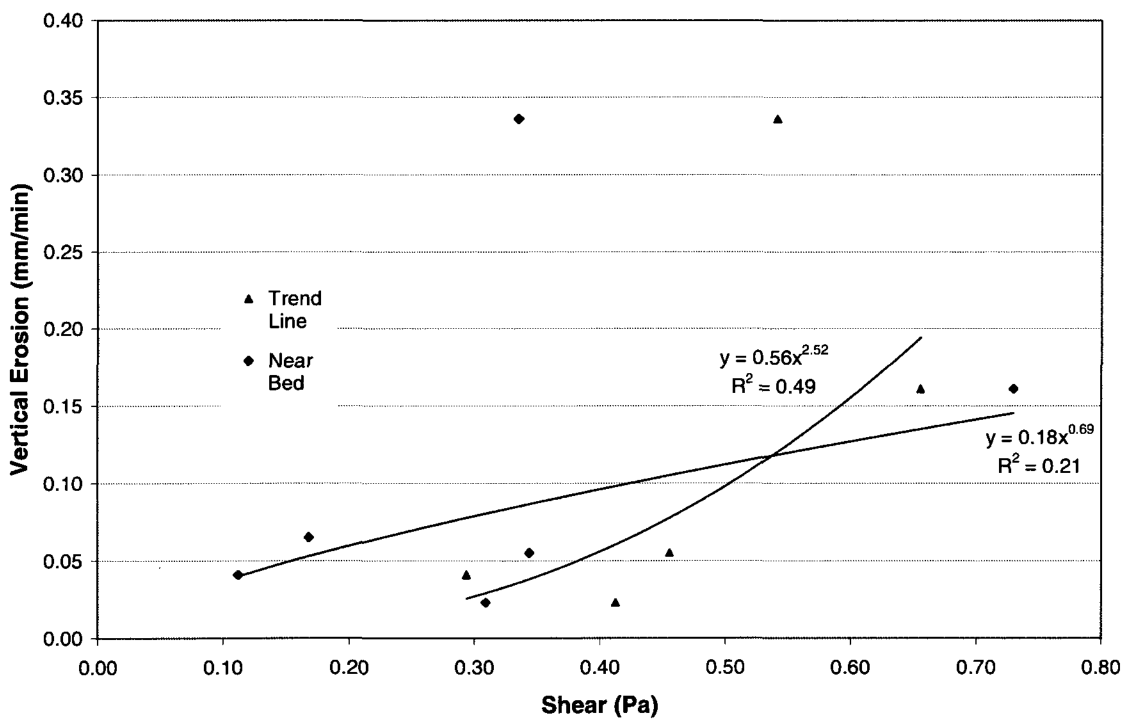

Figure 5.25: Vertical Erosion Rate Comparison for Clay

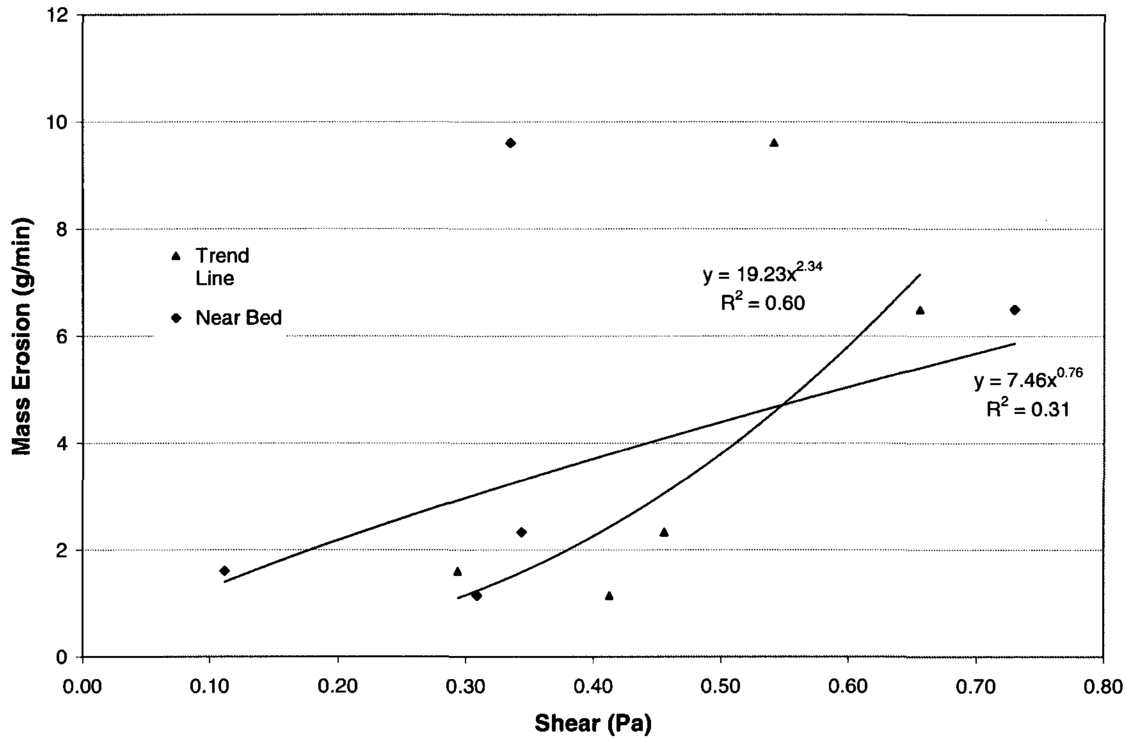

Figure 5.26: Mass Erosion Rate Comparison for Clay

Table 5.8 shows a comparison of the erosion rate parameters for the clay using the shear stresses obtained from the trend line of the principal Reynolds stresses vs. those obtained from plots which used the near-bed principal Reynolds stress. The dependence on the determination of the excess shear is even more pronounced with the clay tests, to the point where the exponential trend is somewhat debatable as the characteristics of the exponent are dramatically different. The R^2 values for the trend line method are superior, however.

Table 5.8: Comparison of Erosion Rates for Clay

Vertical Erosion				Mass Erosion			
Trend Line		Near Bed		Trend Line		Near Bed	
C_e	N	C_e	n	C_e	n	C_e	n
0.563	2.52	0.181	0.69	19.23	2.34	7.46	0.76

5.3 Compaction Tests

Four main tests were conducted to test the effects of compaction. Below are a number of photos taken during the tests. Figure 5.27 shows the downstream view of the embankment constructed using 10 blows from 10 mm high at regular time intervals which show the breach progression. It can clearly be seen at time 0 s (Figure 5.27 [a]) that the embankment's downstream slope is very wet due to seepage through the dam. The phreatic surface exits in this case at about ¼ of the dam height. This fraction is entirely dependent on the density of the dam such that dam with greater compaction experience a more depressed phreatic surface while those which are more loose are much more wet. The portion of the embankment in the phreatic zone feels almost like a liquid and so is assumed to be supersaturated. This portion of the embankment is also in a state of slope instability on the verge of failure. If touched, generally there is a small slide.

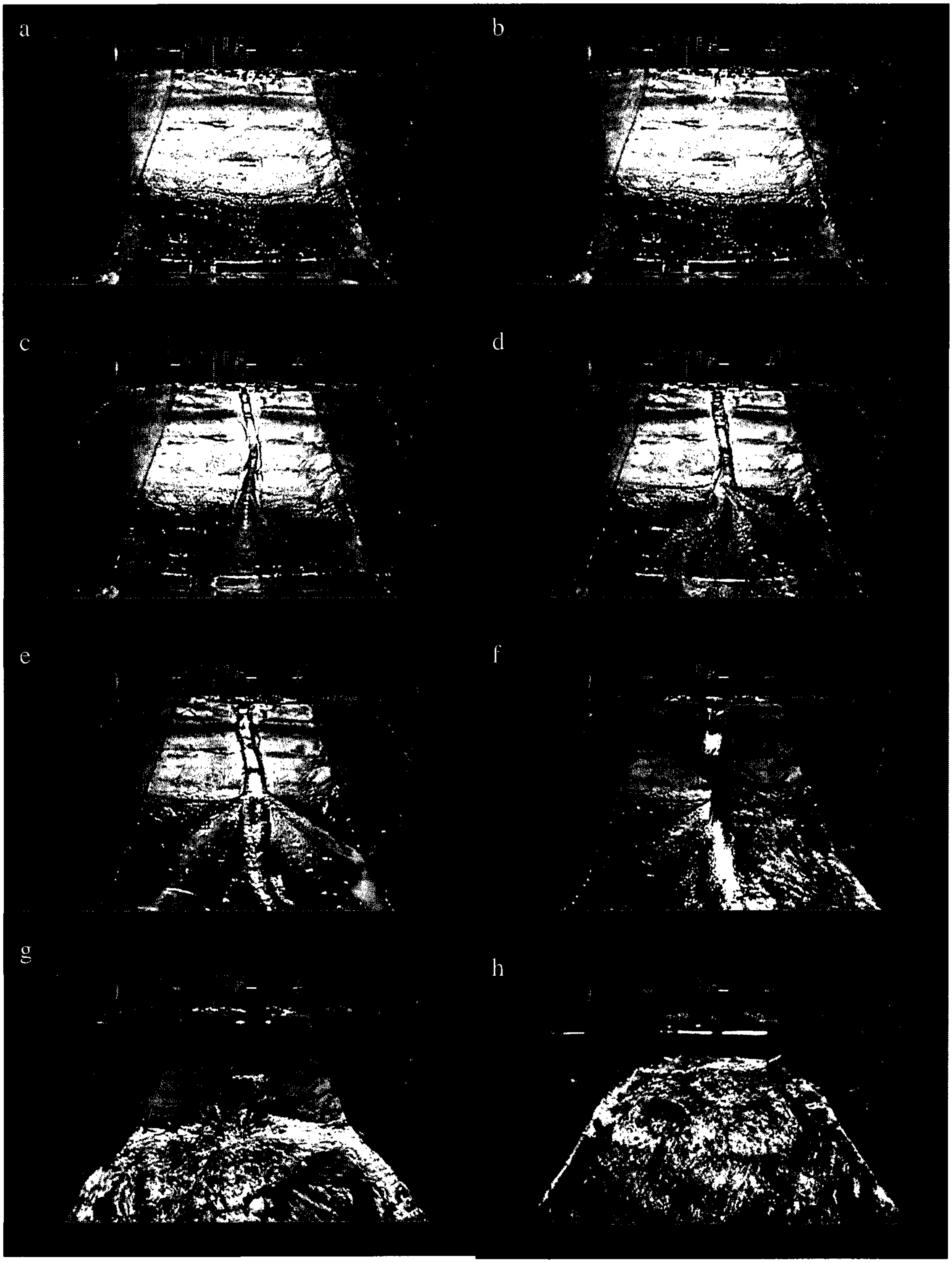

Figure 5.27: Breach Progression for 10 Blows Compaction Test for (a) t_0, (b) t_{30}, (c) t_{60}, (d) t_{90}, (e) t_{120}, (f) t_{150}, (g) t_{180}, (h) t_{210}

Generally, the overtopping failure begins slowly as much of the overtopping flow is consumed by infiltration on the upper portion of the slope. In fact in this case, flow only reaches the downstream toe of the embankment after about 60 seconds, following a somewhat meandering path which straightens over time. It should also be noted that as soon as the overtopping flow hits the phreatic surface on the downstream slope of the embankment it fans out as it no longer seems able to carve out a distinct channel.

Another note of interest is the rather high tailwater elevation once the breach has been firmly established after 150 seconds. It is anticipated that this notable elevation may be due to the constriction of the flume side walls as the flume floor is smooth and the downstream gate has been fully lowered such that there is a free overfall less than 2 m downstream. A side view of the tailwater condition for the embankment compacted with 5 blows from 10 mm high is shown in Figure 5.28.

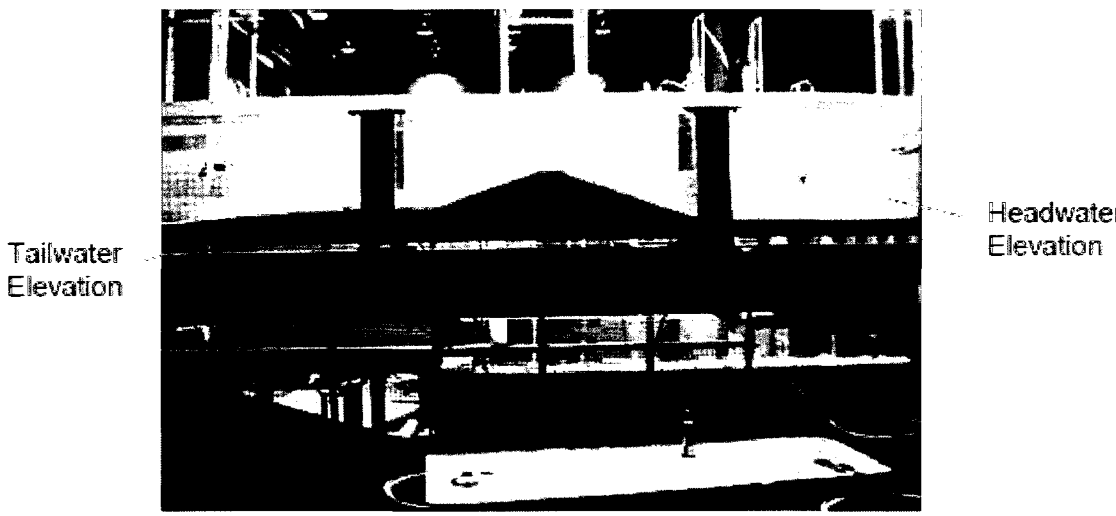

Figure 5.28: Side View of Tailwater Condition

The side walls not only have an effect on the tailwater condition, but they also have a direct effect during the test run by constricting the flow and breach geometry (specifically on the breach width progression) and adding roughness. Figure 5.29 shows the point at which the side walls begin to have an effect. At that point, the breach crest, and therefore the flow into the breach channel, is starting to be confined by the width of the flume, causing a potential diminishing of the peak outflow. Inevitably, the side walls begin to have an effect long before the peak flow is reach. In fact, peak flow often occurs once the entire embankment has been washed away as shown in Figure 5.27(h).

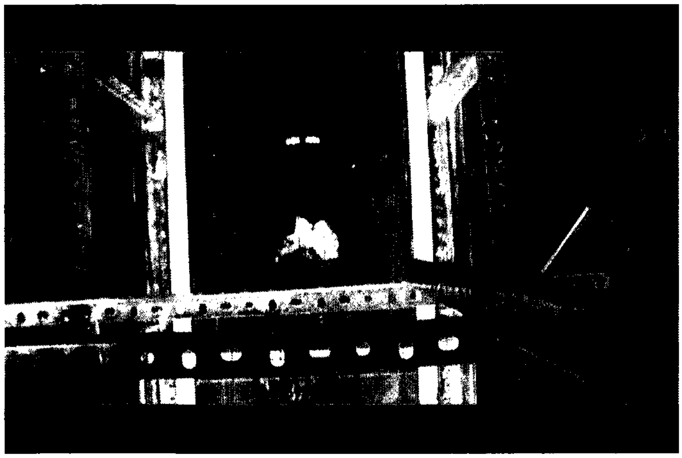

Figure 5.29: Beginning of Side Wall Effects

By varying the density of the embankment, difference in the slope failure mode can also be observed as shown in Figure 5.30. In the case with less applied compaction, the slopes fail predominantly be sliding. In fact, it almost looks like the slope is melting into the breach channel in some cases due to the high water content of the embankment. Conversely, the slopes of the denser embankments failed largely in blocks. This process occurs because the flow undercuts the slope and, rather than a shear based failure that induces sliding, there is a moment based tensile failure as a large chunk of the embankment can no longer support itself and falls into the breach channel. Even the large chunks of sand are rather quickly eroded away. This process is also discussed in the collaborative effort of Al-Riffai *et al* (2009).

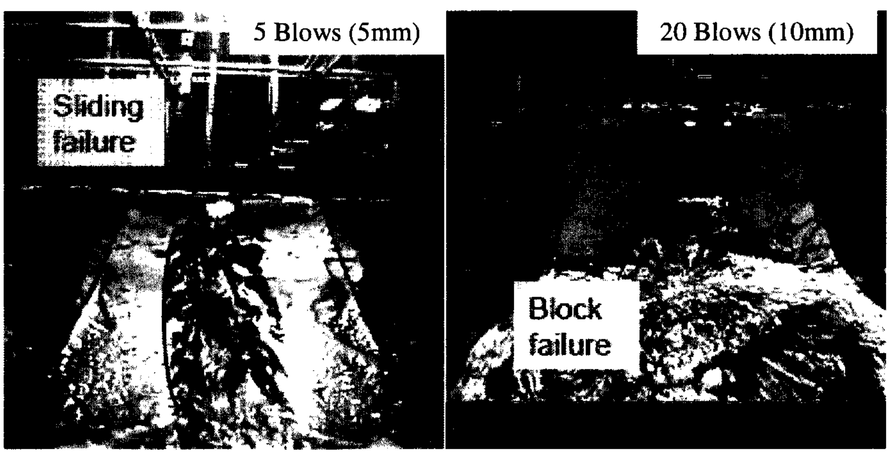

Figure 5.30: Side Slope Failure Comparison for Two Compaction Efforts

The denser the embankment, the larger the blocks become and the more tensile strength they have. This strength is due primarily to the suction forces prevalent in the unsaturated embankment. The more the saturation curve is depressed by greater density, the greater the negative pore water pressures and, therefore, the greater the binding force due to suction. This process is also discussed in the collaborative effort of Al-Riffai *et al* (2009). Figure 5.31 shows the upstream view for the embankment compacted using 20 blows at 10 mm. At that point, the side walls have been reached, yet the breach channel is quite thin and on the upstream side there is clearly much undercutting of the side slopes of the breach channel taking place, yet the side slopes are still marginally stable. As a consequence of the higher binding forces in the side slopes and greater undercutting required to destabilize them, the blocks which fall into the breach channel become larger as compaction increases.

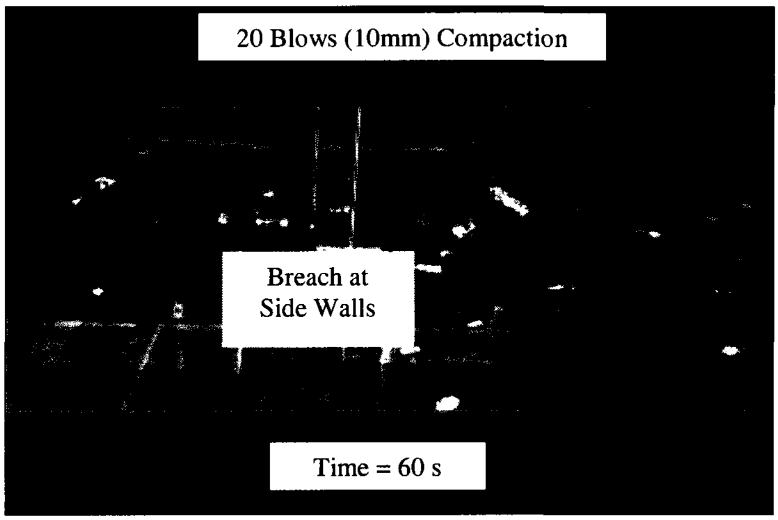

Figure 5.31: Upstream View of Embankment for Initial Side Wall Effects

Figure 5.32 shows a plot of volume in the reservoir vs. time. It should be immediately noted that the wave gauge data for the 5 blows (10 mm) test is incomplete due to the gauges not beginning their recording until about half way through the test. Nevertheless, the results are presented here. Time 0 in all cases is the time at which the overtopping failure begins. It can be clearly seen that there are initial differences in the volume of the reservoir between the different tests. This different is due in part to differential settlement during the impounding process (as is primarily the case for the 5 blows (5 mm) test) as well as poor quality control during construction. Embankments may not have all been constructed to exactly the same height and therefore the notch used to initiate the breach may not have had the same invert. The potential error in invert elevation is estimated to be ±5 mm.

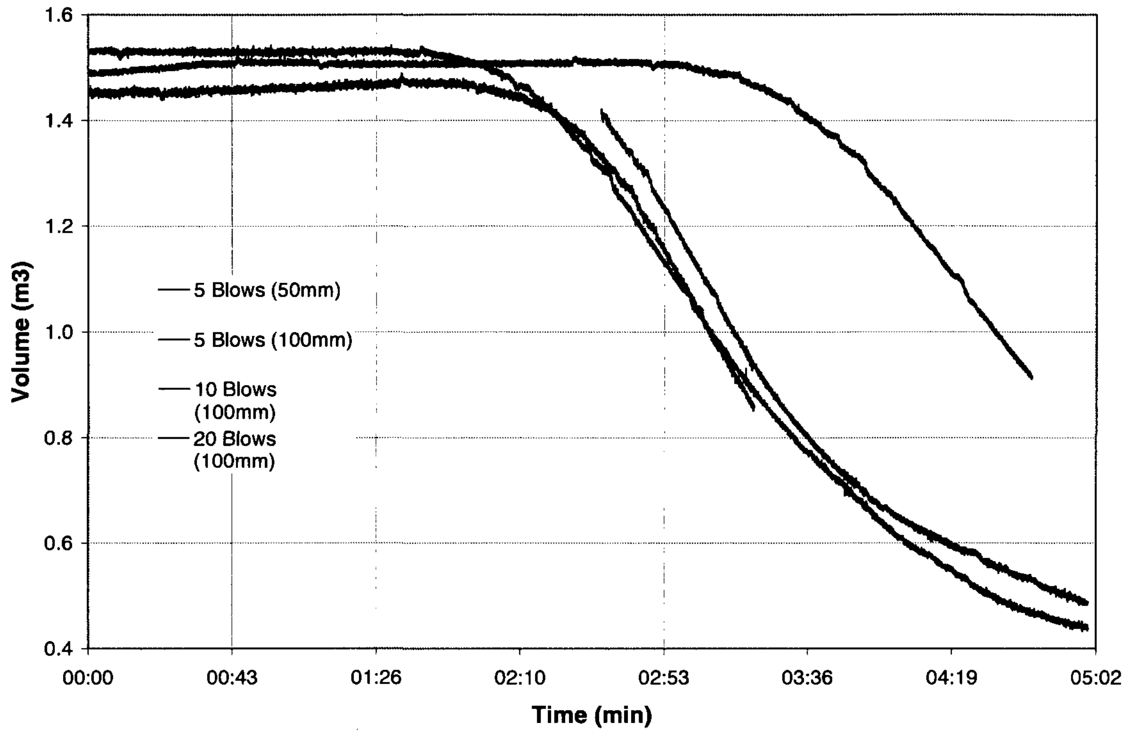

Figure 5.32: Volume-Time Relationship for Compaction Tests

In the case of Figure 5.32, the flow can be seen as the slope of the curve. It can clearly be seen then that the peak flow for the 5 blows (5 mm) embankment is greater than for the 10 blows (10 mm) embankment due to the greater maximum steepness of the slope. Also, it can be seen that the breach time for the 20 blows (10 mm) embankment is substantially longer than for other embankments.

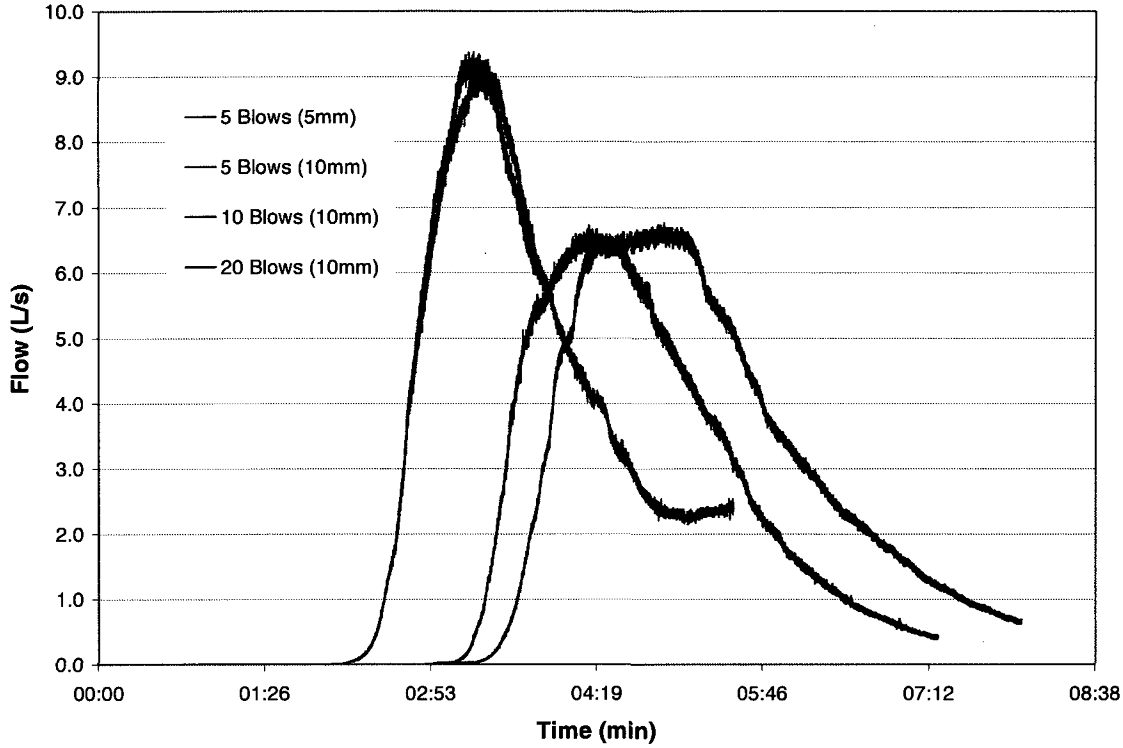

Figure 5.33: Compaction Test Outflow from V-Notch Weir

Figures 5.33 and 5.34 show the hydrographs generated for the compaction tests. Hydrographs were generated in two ways: using the V-notch weir and using the volumetric approach from the wave gauge analysis. In general, the two methods compare moderately well, as can be seen in Figure 5.35. The times to peak are very similar, but the peak flows are somewhat smaller using the V-notch method than for using the volumetric approach. This difference can be attributed to the configuration of outlet tank and the weir which, due to the tight confines of the space, may experience backwater effects which could diminish the peak flows and cause them to appear sustained as is the case for the 10 blows (10mm) run and 20 blows (20mm) run. However, while the results from the V-notch are somewhat noisy in places, they do not show the oscillations apparent using the volumetric approach because they have not been filtered. As such, we can assume that the oscillations do not in fact exist in reality and a smooth curve should be prevalent.

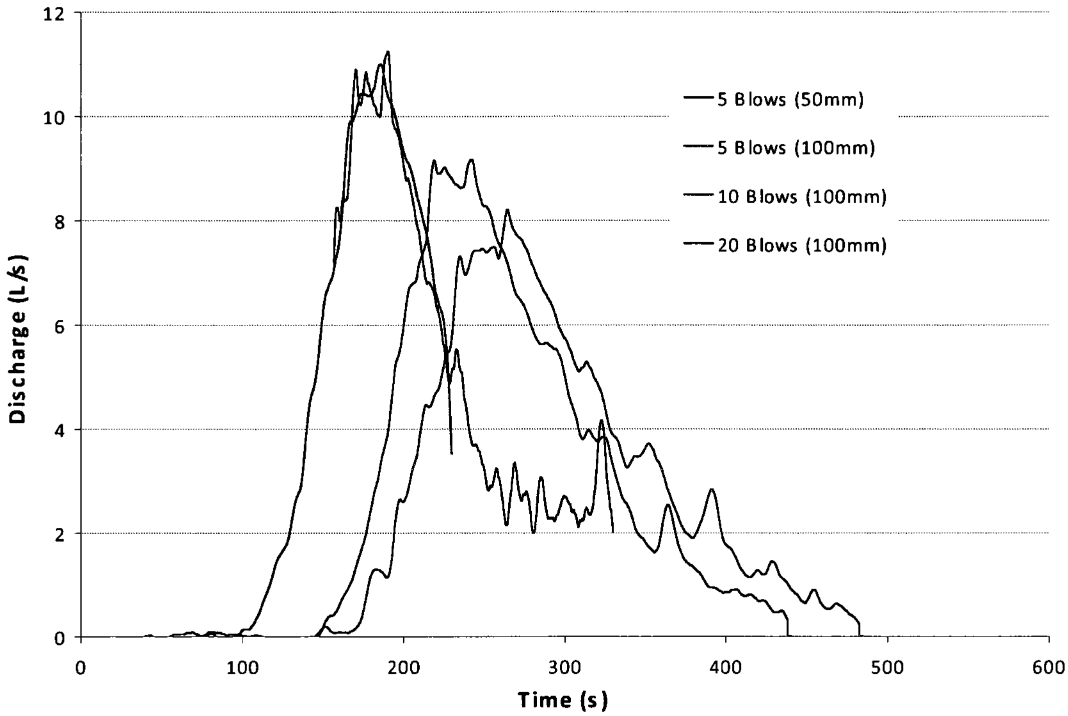

Figure 5.34: Compaction Test Outflow from Wave Gauge Analysis

It should be noted, however, that the peak outflows from the breaches occur well after the side walls of the flume have been reached. Figure 5.36 shows the cropped hydrographs which only consider data used between the beginning of the overtopping failure and when side wall effects are initiated. As it can be seen, there is little flow data which is not influenced by the side walls.

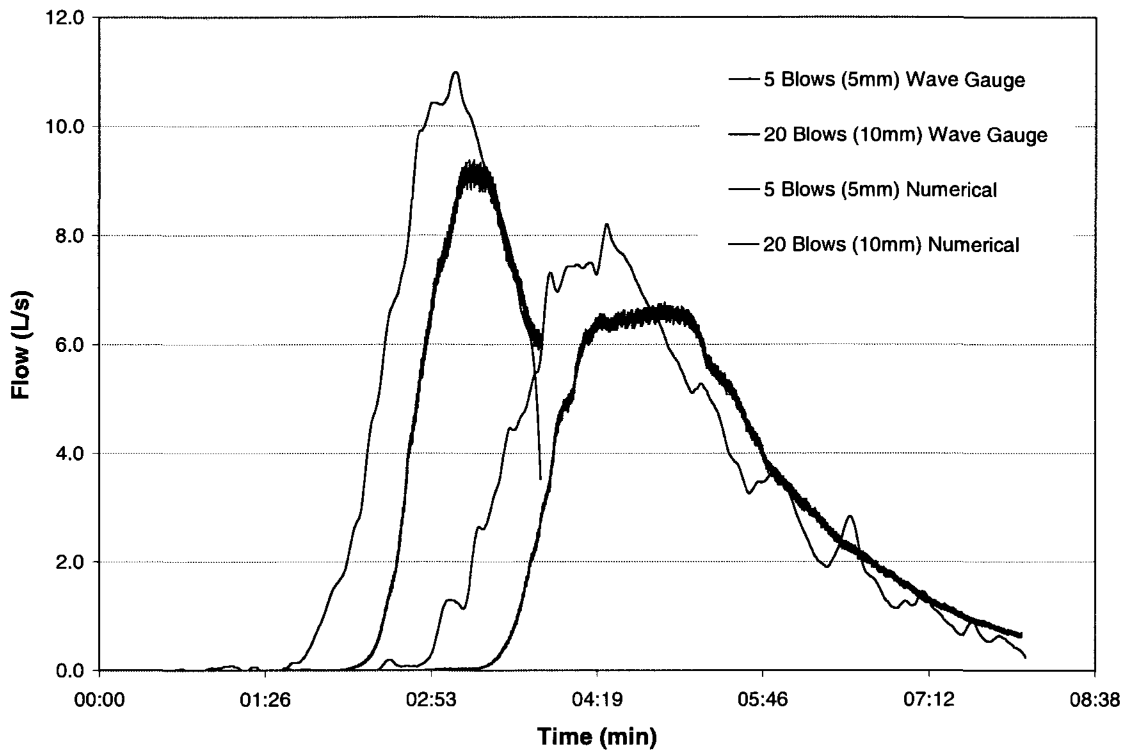

Figure 5.35: Output Comparison of Hydrograph Generation Techniques

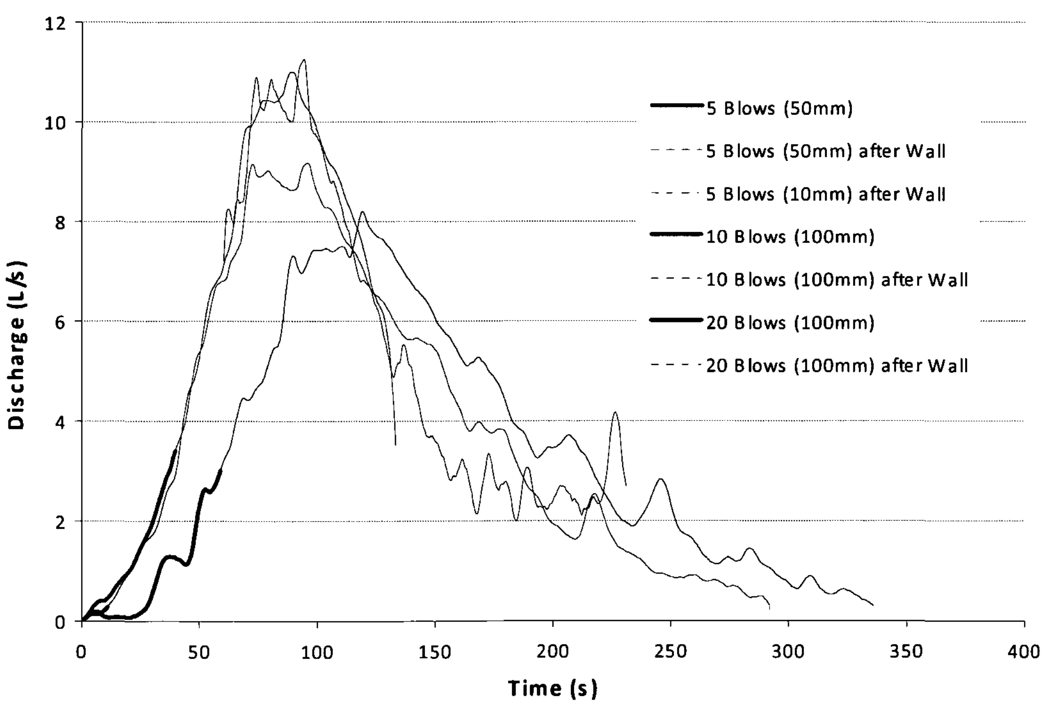

Figure 5.36: Compaction Test Outflow from Wave Gauge Analysis Cropped for Side Wall Effects

5.4 Clay Embankment Tests

The clay embankment tests were largely considered to be failures, owing to the extremely long length of time each embankment was subjected to the erosion process. As such, they are presented here as qualitative examinations of the erosion process rather than quantitative discussions. Both tests used 5 blows from 10 mm high compaction but the first test used the natural clay dug up from the ground and broken apart largely by hand, while the second test used remolded clay. The average water content for each test was very similar (38.9% and 38.7%, respectively). In both cases, video was used to record the first hour of each test, after which photos were used. For the first test, extra pictures were taken at 2.5, 3.0, 3.5, 4.0, 5.5, and 9.5 hours after the overtopping failure after which the test was ended. For the second test, extra pictures were taken at 1.5, 2.0, 2.5, 3.0, 3.5, and 17.75 hours after the overtopping failure after which the test was ended. In neither case did the test completely destroy the embankment. Figure 5.37 shows the different stages of erosion for the first test.

It can be seen from Figure 5.37 that the erosion process is quite slow and that much of the erosion takes place in the first 2.5 hours. The process is the same as that reported by Hahn *et al.* (2000). Figure 5.37 (f) shows 4 distinct headcut steps in the erosion process. These steps then migrate upstream at different rates and gradually merge together. After 9.5 hours, only 2 headcut steps can be seen.

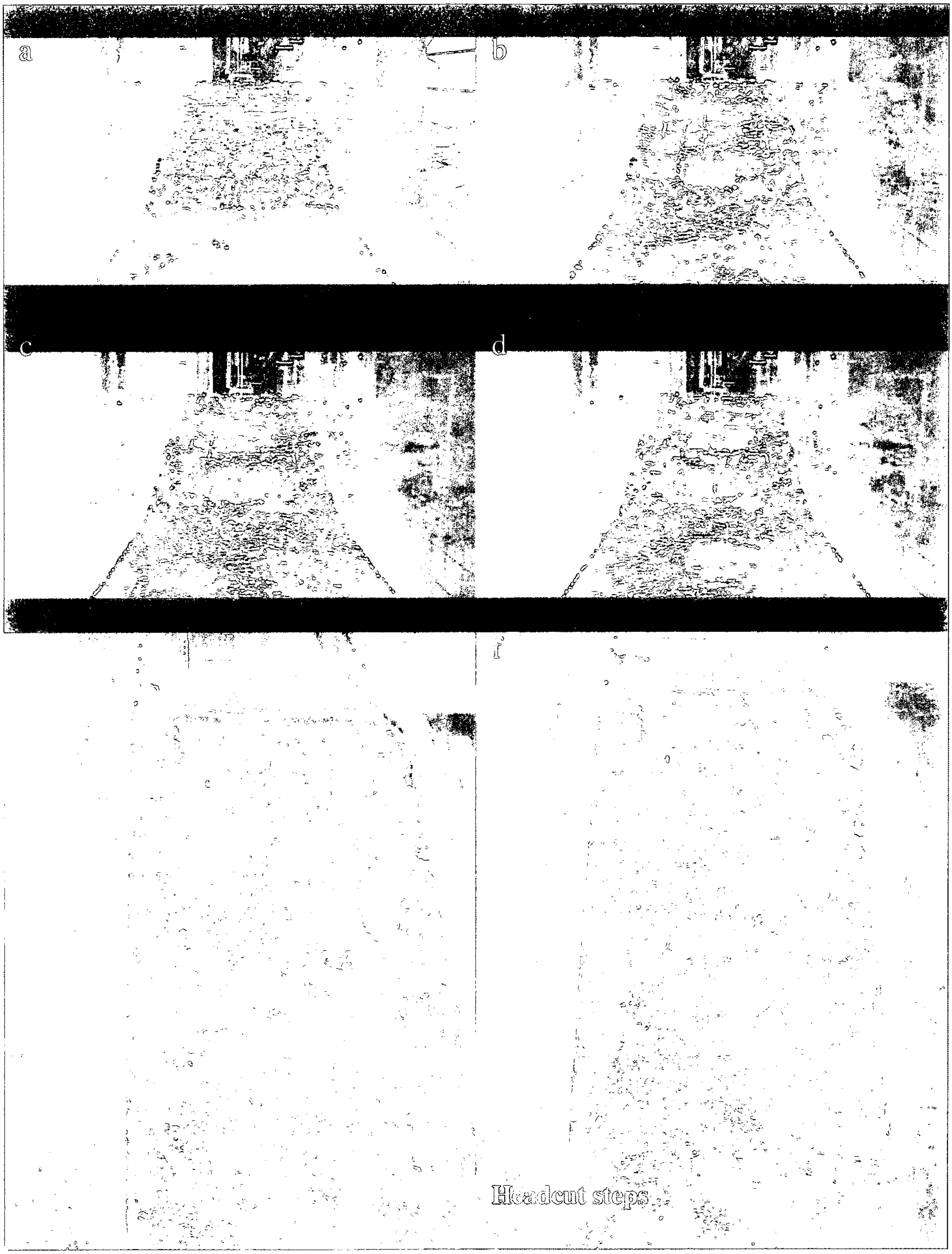
a
b
c
d
Headcut steps

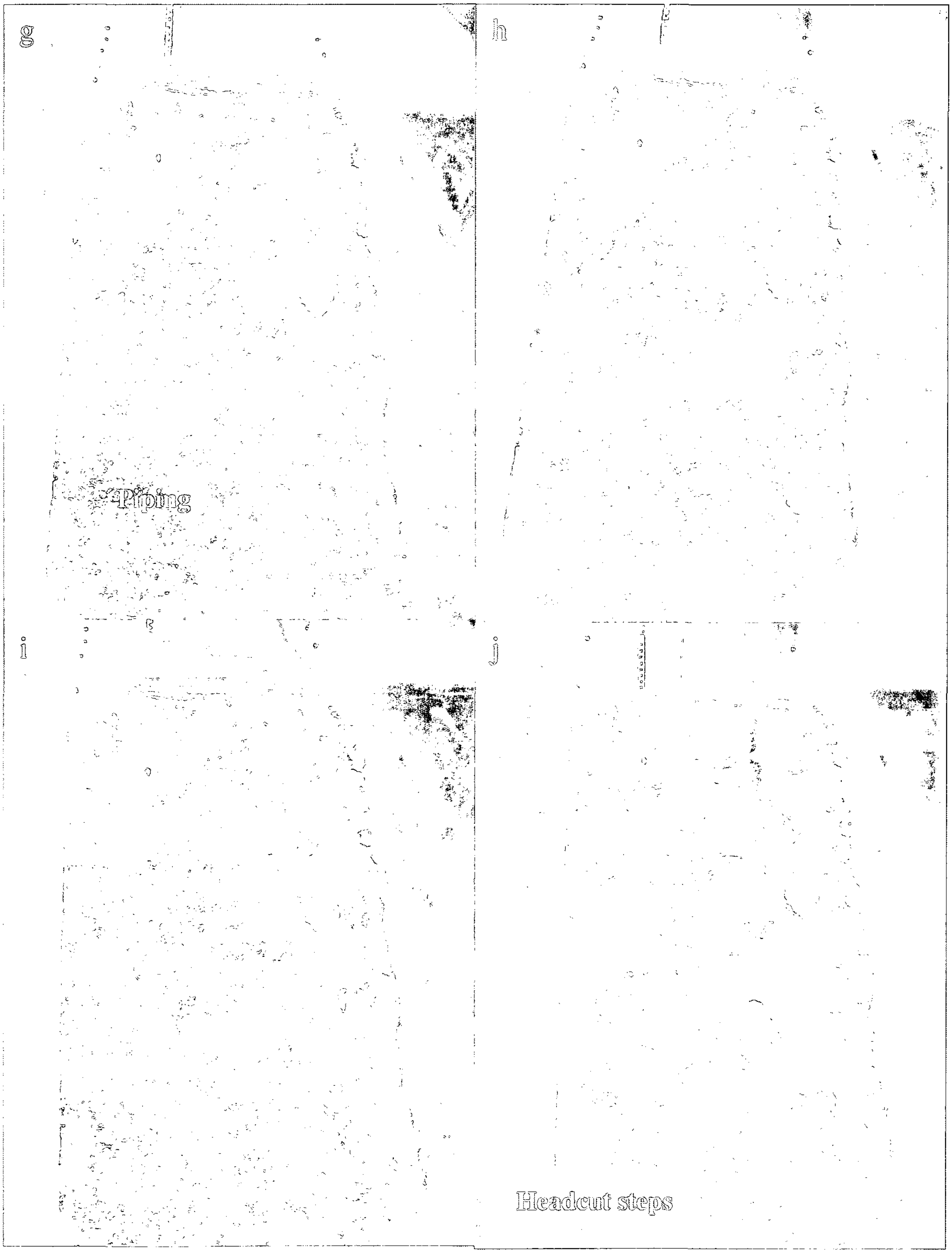

Figure 5.37: Clay Embankment Test 1 Erosion over Time
at (a) 0 min , (b) 10 min, (c) 20 min, (d) 30 min (e) 2.5 hrs , (f) 3.0 hrs, (g) 3.5 hrs, (h) 4.0 hrs, (i) 5.5 hrs, and (j) 9.5 hrs

It should also be noted that this embankment created from the original unworked clay was not very impervious. In fact, due to the natural broken composition of the clay, many internal voids were prevalent in the final construction and the embankment surface was very rough. These voids led to piping infiltration rather quickly forming in the embankment near the flume wall. While the piping erosion was eventually dominated by the erosion due to overtopping, it was still important in creating the final erosion pattern in the embankment.

It was also observed that the headcut steps were generally induced at locations where the clay was naturally weakest rather than at any prescribed location where hydraulic force may have been greater. In the case of these test embankments, these naturally weaker places were generally found to be between the different compaction lifts.

Generally, it was observed that once a step had formed, the erosion was most prevalent not on the edge of the step, but at the bottom. Flow pours over the step and the jet plunges into the upper part of the next step. This process creates a small scour hole which then undermines the step. Eventually, the step is so undermined that it fails in relatively large chunks and the headcut progresses upstream. The chunks, being rather large, also seem to fill in parts of the scour hole which was generated. Figure 5.38 shows the stages of erosion for the second test.

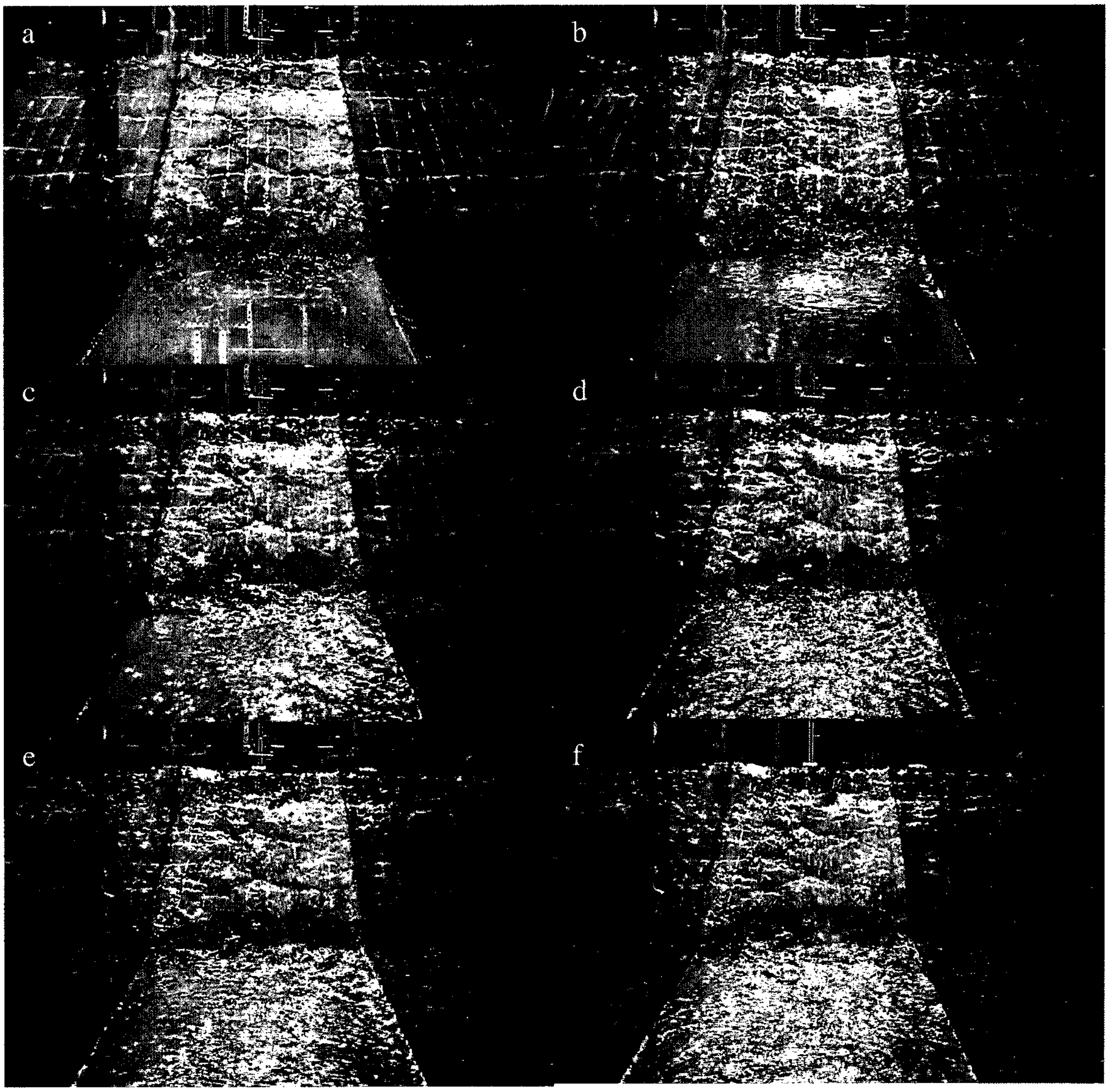

Figure 5.38: Clay Embankment Test 2 Erosion over Time at (a) 0 min , (b) 5 min, (c) 10 min, (d) 20 min (e) 30 min , (f) 60 min

As seen in Figure 5.38, the embankment is much more impervious, though there is significant leakage along the bottom of the flume. Most of the erosion takes place near the toe of the embankment and near the crest and in general erosion progressed more quickly than for the previous test. This difference is likely due to the remolded nature of the clay which, though it would not break off in chunks, was softer, more workable, and in seems more erodible.

5.5 Large Flume Tests

A number of tests were conducted in the large flume to determine the effects of varying the initial breach geometry on dam breach characteristics. Three main tests were conducted with a crater, tapered, and V-notch geometry variations. In addition to these tests, another V-notch embankment which did not have a toe drain as part of its construction was also breached. Snapshots of the breach stages for the crater initiated breach are shown in Figure 5.39.

As was the case for the compaction tests, the breach channel does not always start straight down the downstream slope. Rather, flow finds the natural recesses in the slope and carves a unique path with every test. For the tapered breach initiation, two breach channels very near to one another were initially formed before widening into a single channel. The breach channel becomes much straighter with time as the depth of the channel increases.

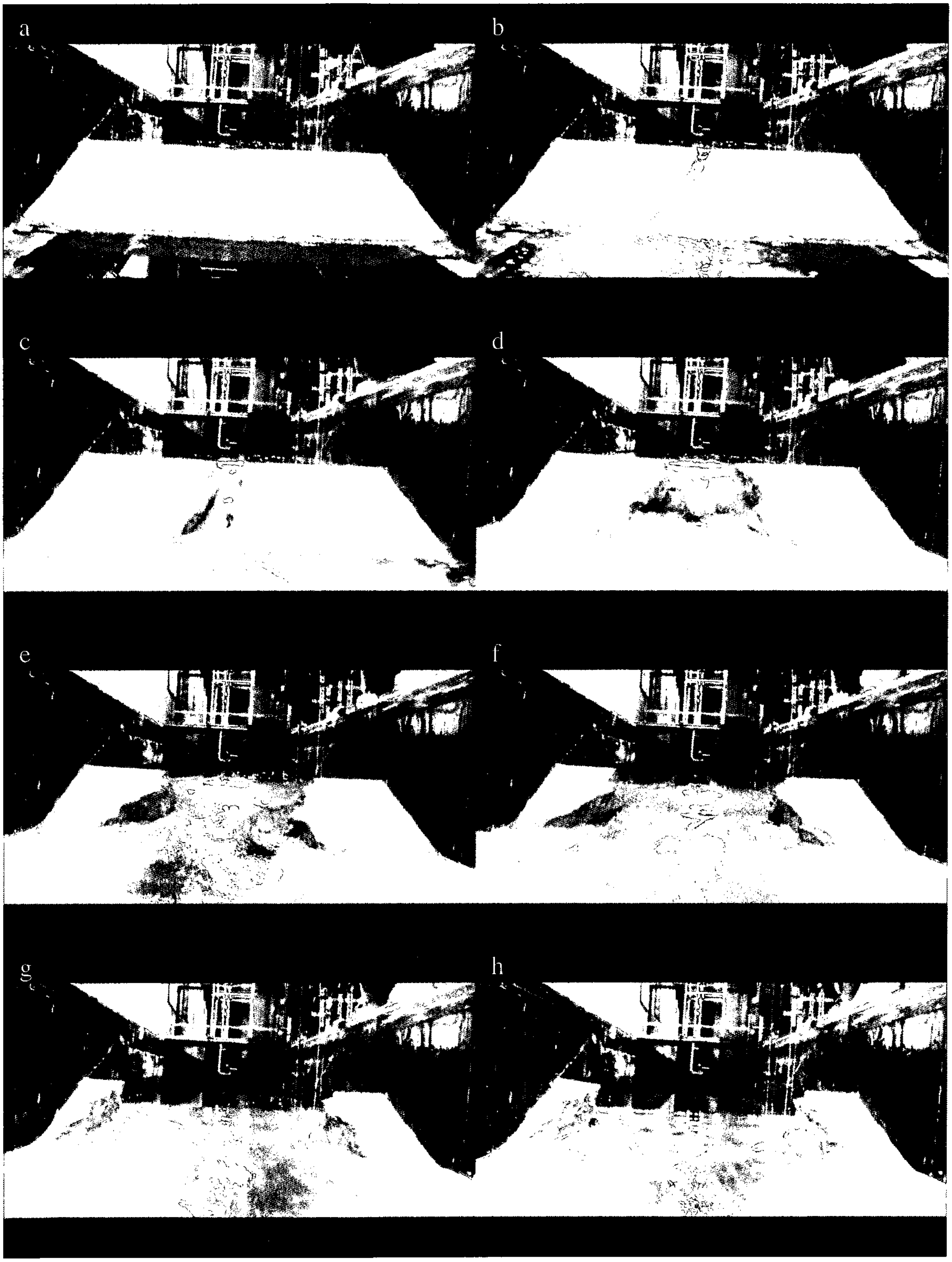

Figure 5.39: Sand Embankment Breach Progression for Crater Initiation at (a) t_0 (b) t_{30}, (c) t_{60}, (d) t_{90}, (e) t_{120}, (f) t_{150}, (g) t_{180}, (h) t_{210}

However, the water content in the embankment for these tests is different than for the compaction tests due to the use of the toe drain. Only near the drain is the dam surface wet to the touch. Consequently, there are substantial differences in the side slope resistance of the breach channel as suction becomes a consequential factor in slope stability. This difference is also discussed in the collaborative effort of Al-Riffai *et al* (2009).While some small amounts of material do slide or slump into the breach channel, the vast majority breaks off in often large clumps. Figure 5.39 (e) shows one of these large block failures after it has fallen into the breach channel and is subsequently eroded away.

There are also major difference between this test series and the compaction test series in inflow characteristics, the size of the reservoir, and the tailwater conditions. The inflow was kept constant at 0.45 L/s throughout the entire test and the size of the reservoir for each test can be seen in Figure 5.40. The tailwater condition is different in that there is no high tailwater condition which is generated for this test series, largely owing to the width of the channel with respect to the breach width and flow. By using a wider flume, the flow is less restricted and flows out of the system earlier. This change also has a major impact on sediment transport downstream of the embankment as very little material remains on the downstream side as velocities at the downstream side of the embankment can remain high and carry the sediment out of the system. This difference can clearly be seen in Figure 5.39 as the flume floor is visible after 120 seconds.

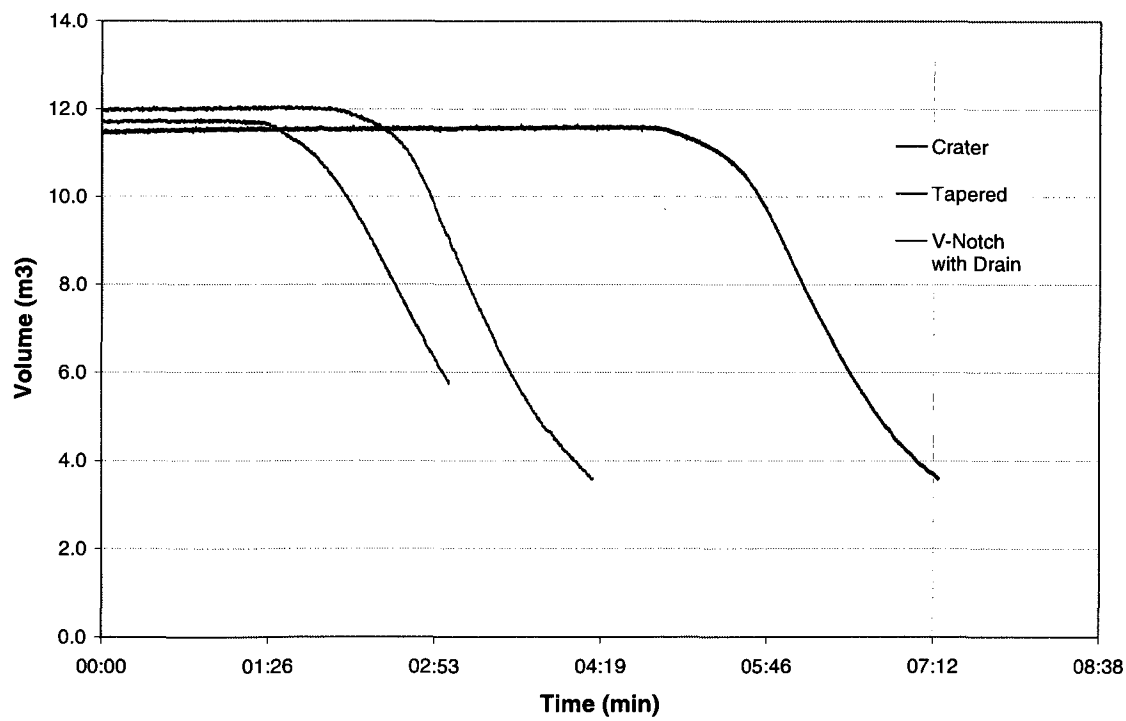

Figure 5.40: Large Flume Volume-Time Comparison

It can be seen in Figure 5.40 that the data for the crater initiation has been terminated earlier (for a higher volume) than the other two tests. This crop is due to placing the upstream wave gauge too high in the flow for that run, meaning that the minimum water surface elevation the gauge could record was about 120 mm. These data were corrected for the hydrograph calculations by modifying the volume equations and relying more heavily on the next most upstream gauge.

It is also apparent that there are different initial volumes between the tests. Unlike the results from the compaction tests, these differences in volume are expected due to the changes in the inverts of the initial breach channels. The tapered breach is initiated over the crest at 300 mm from the floor of the flume. The V-notch uses an invert 20 mm lower due to the depth of the notch. While the depth of the crater is lower and a lower initial volume might be expected, it should be noted that the crater is somewhat spherical in shape and the invert of the initial breach is not at the bottom of the crater, but rather at the lip where the crater meets the downstream embankment, which is approximately 10 mm lower than the dam crest. Hence, the initial volume is between that of the other two tests.

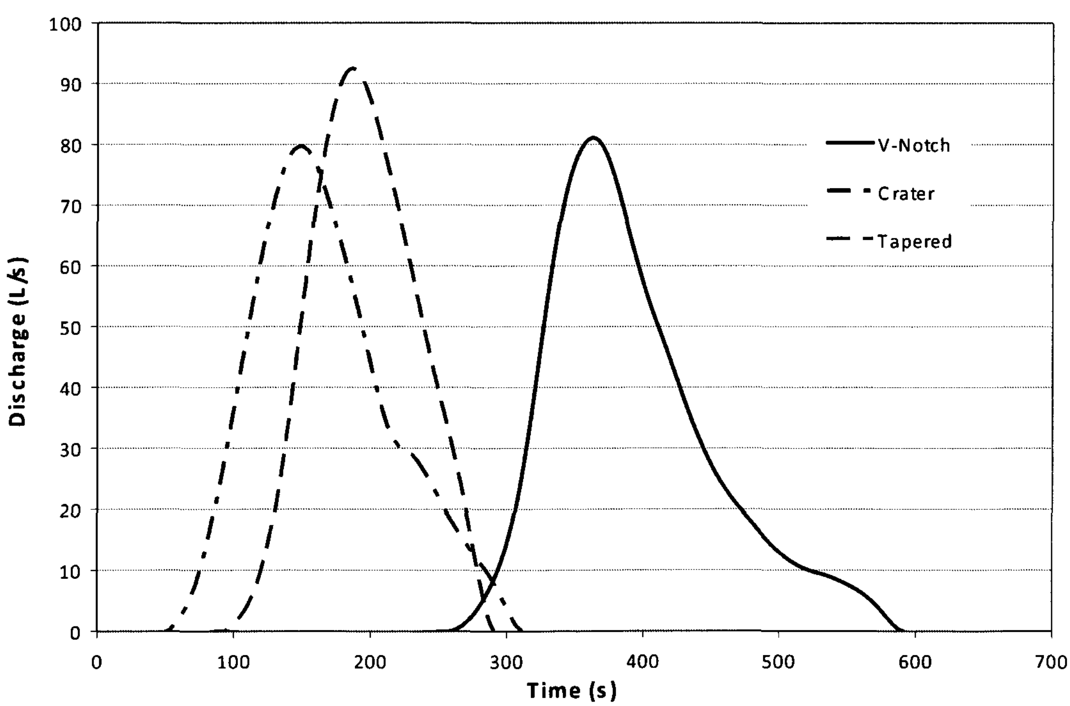

Figure 5.41: Hydrographs Comparing Initial Breach Geometries

Figure 5.41 shows the hydrograph generated from the volumetric data for the three main tests. Generally, it can be said that the hydrograph characteristics for each breach are fairly similar. The peak flow for the tapered breach is attributed to the larger reservoir volume during the failure. The most important difference between the three tests, however, is the time to peak, which varies by more than 100% when the crater and V-notch initiations are compared.

Figure 5.42 compares the hydrographs for the two tests that used the V-notch initiation but only one used a toe drain. Physically, this difference meant that embankment without the filter was much wetter and had less internal strength due to increased pore water pressure. The difference in peak flow between the two runs can be attributed to the slightly greater reservoir volume for the test using the filter. Because the embankment has more initial resistance to breach flow (from infiltration mostly), net flow into the reservoir continues to increase for a longer period of time. Once again, however, it is the time to peak that is the starkest difference between the two runs, as there is a difference between them of almost 150 seconds (almost 70%). At prototype scale, this difference becomes approximately 25 minutes, which is a significant value from the point of view of an early warning system for dam failure.

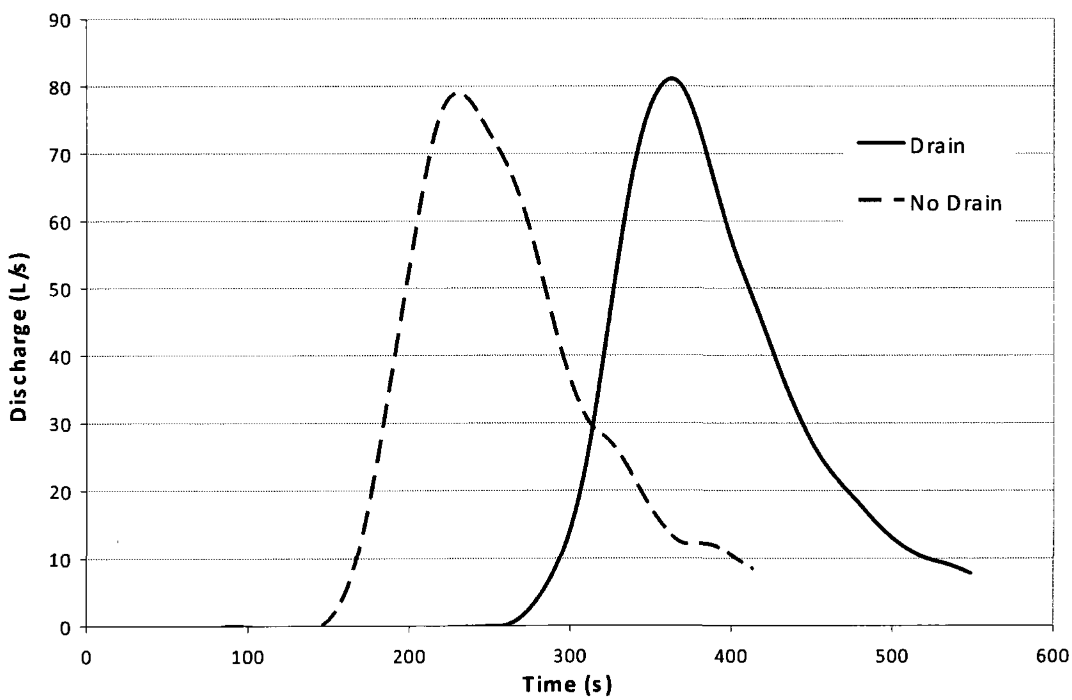

Figure 5.42: Hydrographs comparing Filter and No Filter V-Notch Embankments

Figure 5.43 compares the shape of each of the four hydrographs. The hydrographs have all been lagged so that they all begin roughly at the same time when the discharge value of the hydrograph begins to increase in a notable manner (called the hydrograph initiation time). From this initiation time, it can be seen that the time to peak for the various breaches is very similar. Other than the drained V-notch case, the rate of increase of breach flow is also very similar between the tests, though there are some differences on the falling limb.

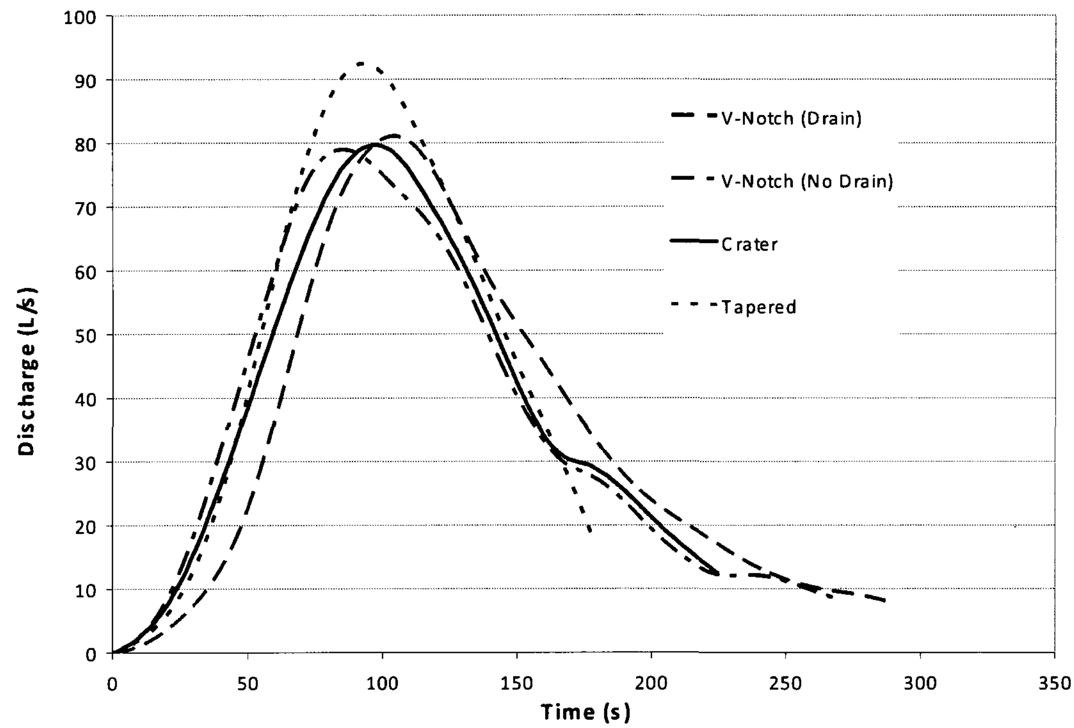

Figure 5.43: Comparison of Hydrograph Characteristics

Figures 5.44 and 5.45 show the progression of breach width between the three main tests at both the crest and the middle (elevation of 150 mm). The V-notch initiated test has been advanced 220 seconds to compare better the results. The curves are not smooth owing to the nature of the slope failures during the breach process. Often, large blocks break off in less than a second, meaning the resulting plot will show a somewhat stepped pattern. Generally, the three breaches show a similar pattern in increasing width, though the final crest breach width is larger for those breaches that began with larger initial breaches. The trend is the opposite, however, with regards to the middle breach width and there are fewer steps in the breach progression indicating that larger blocks fell from the crest than from the middle area of the breach side slopes.

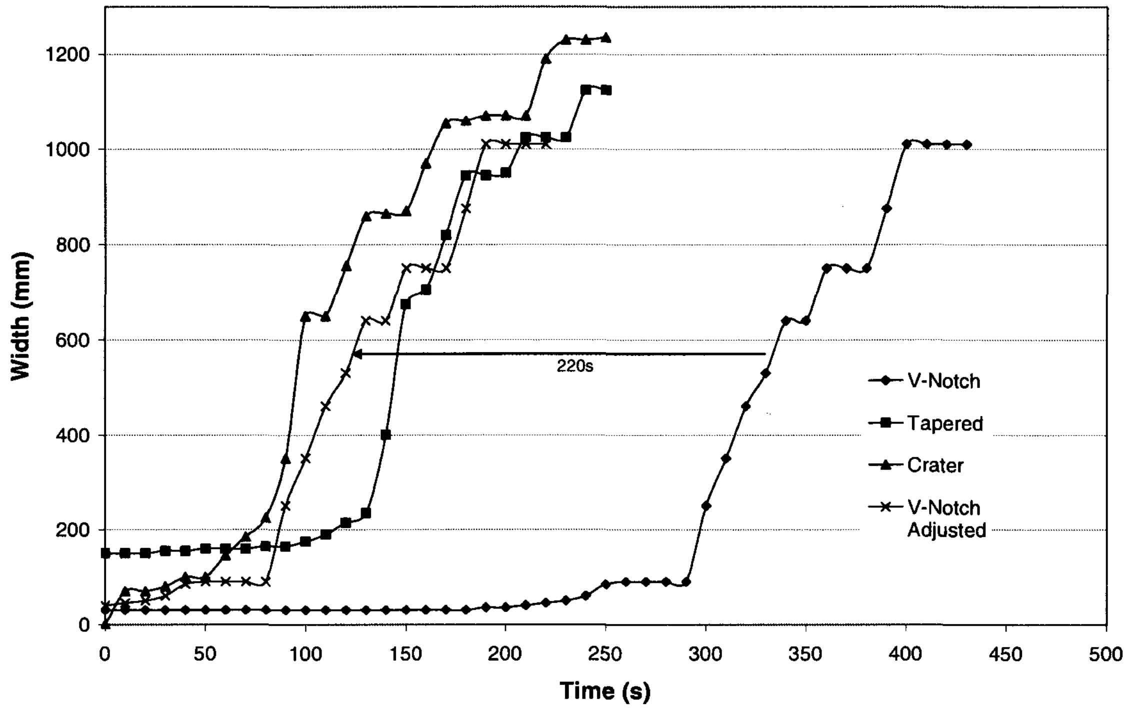

Figure 5.44: Crest Breach Width Comparison

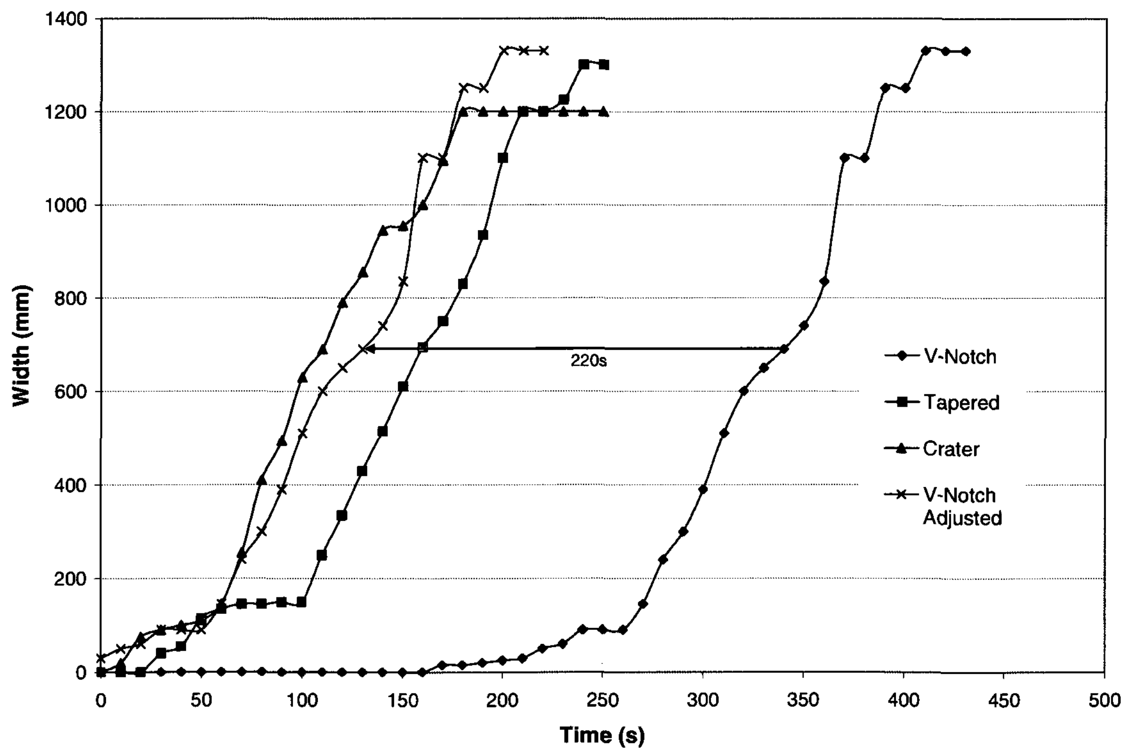

Figure 5.45: Middle Breach Width Comparison

Figures 5.46 through 5.48 compare the rates of change of breach width over time for the three main tests. Effectively, these plots give an idea of how large the block failures were and when they occurred. Once again, the V-notch initiated breach was advanced 220 seconds for ease of comparison. There is no particularly visible pattern to the rates of increase in breach width except to say that in all cases breach width changes start off smaller, get larger as peak flows are reached, and then get smaller once again.

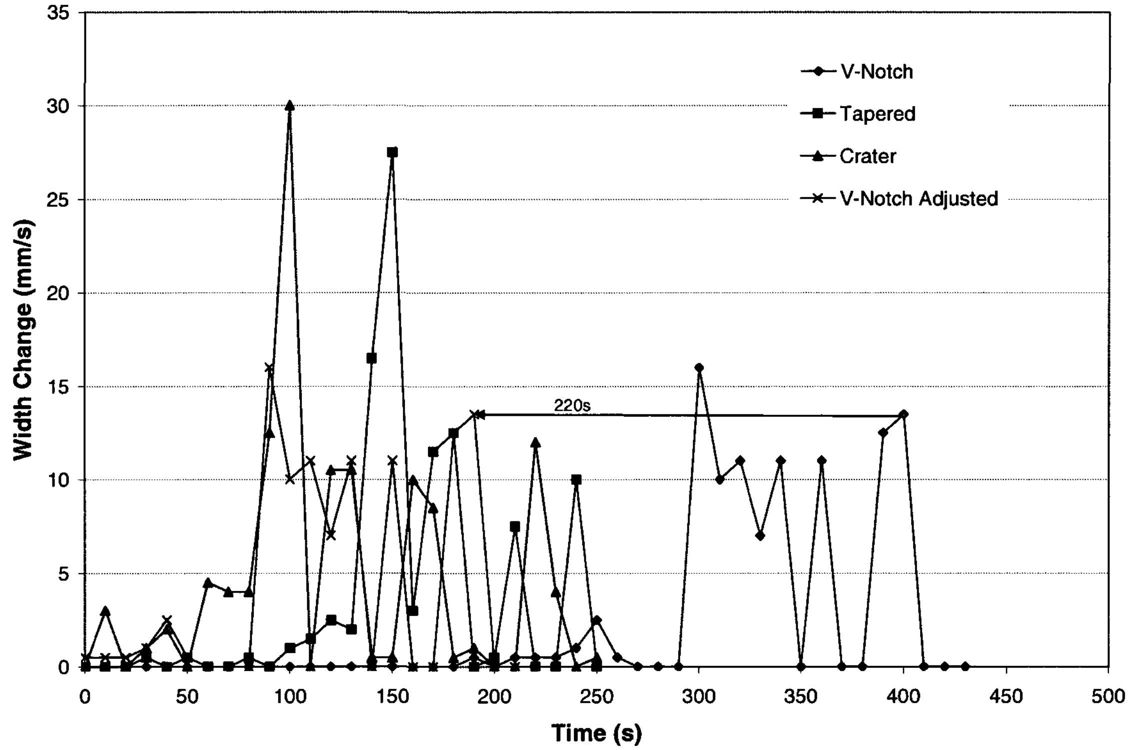

Figure 5.46: Change in Crest Breach Width Comparison

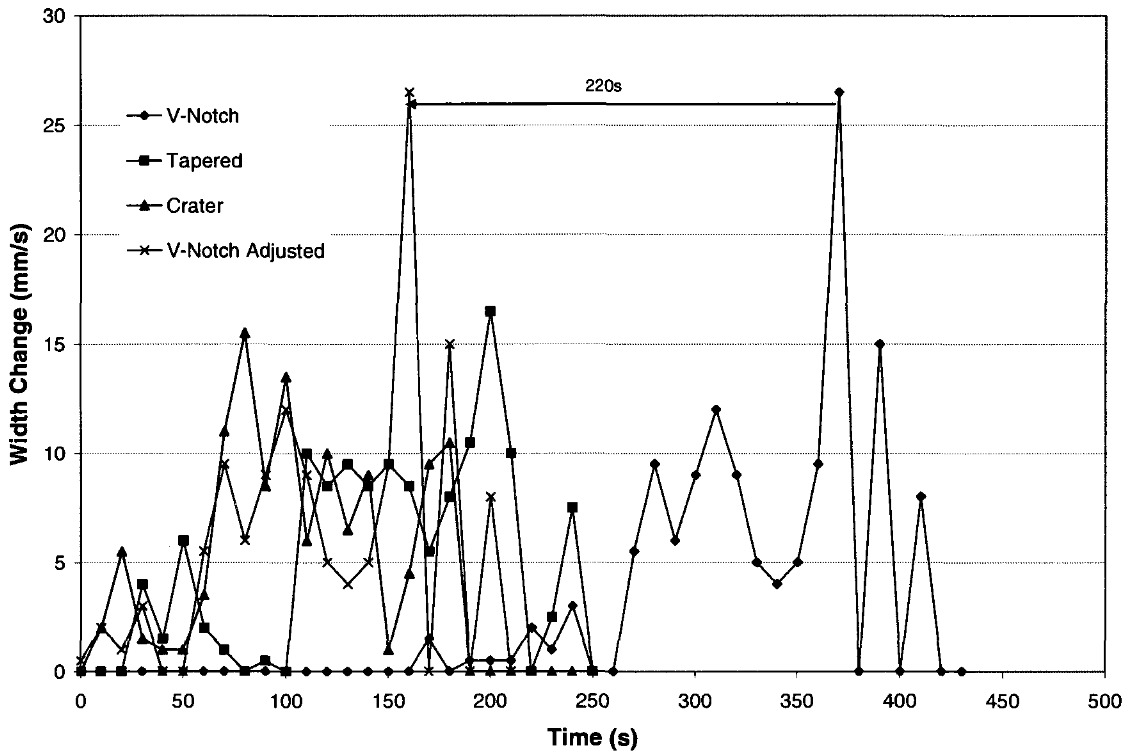

Figure 5.47: Change in Middle Breach Width

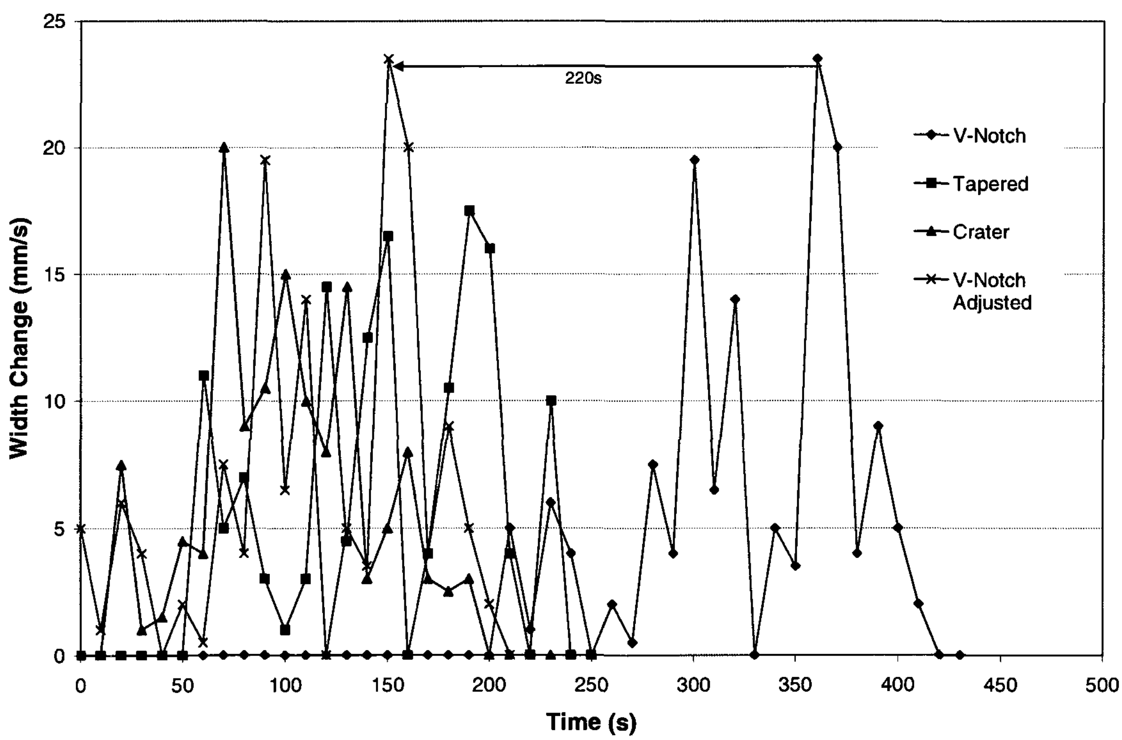

Figure 5.48: Change in Bottom Breach Width

Figure 5.49 shows a log-time plot comparing bottom breach width progression. With this type of plot, three distinct breach phases can be seen: an initiation phase, a roughly log-linear phase of steady increase, and then an ending phase in which breach progression trails off and becomes constant. Using this breakdown as a guide, breach data were cropped to isolate the semi-log portion, from which characteristics of the semi-log-linear portion of breach widening were determined (as shown in Figures 5.50 through 5.52). The relations in Figures 5.50 through 5.52 use linear relations for the middle section of the breach width progression, as they produced better fits than semi-log relations.

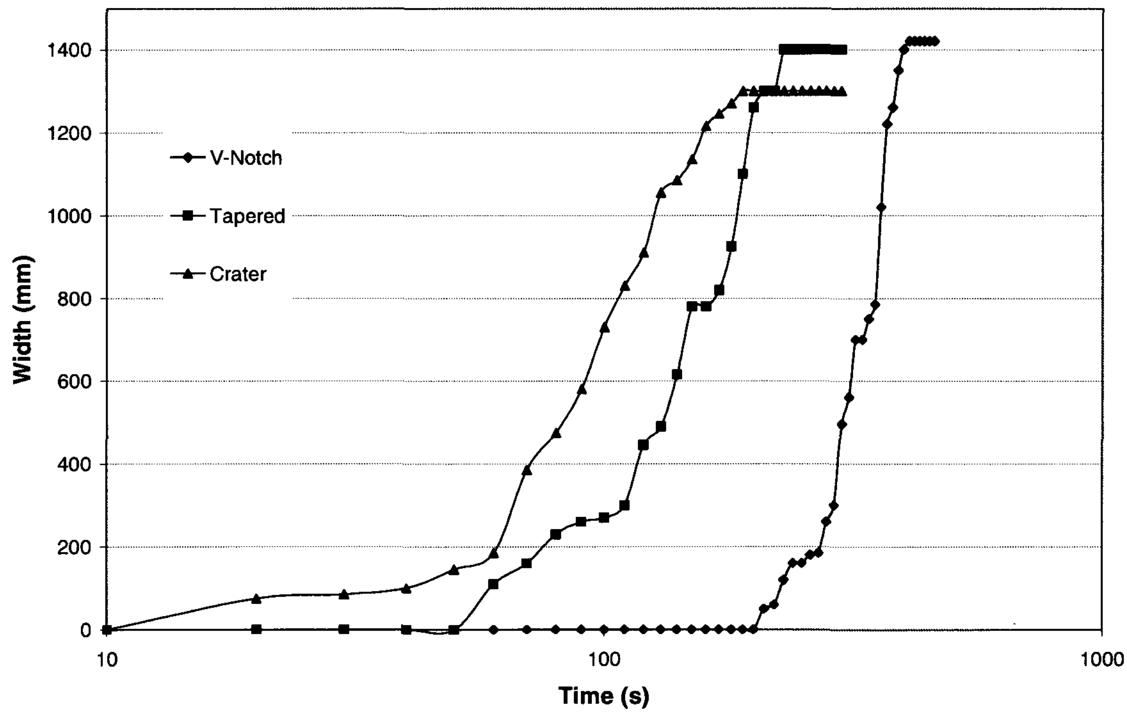

Figure 5.49: Bottom Breach Width Comparison (Log Scale)

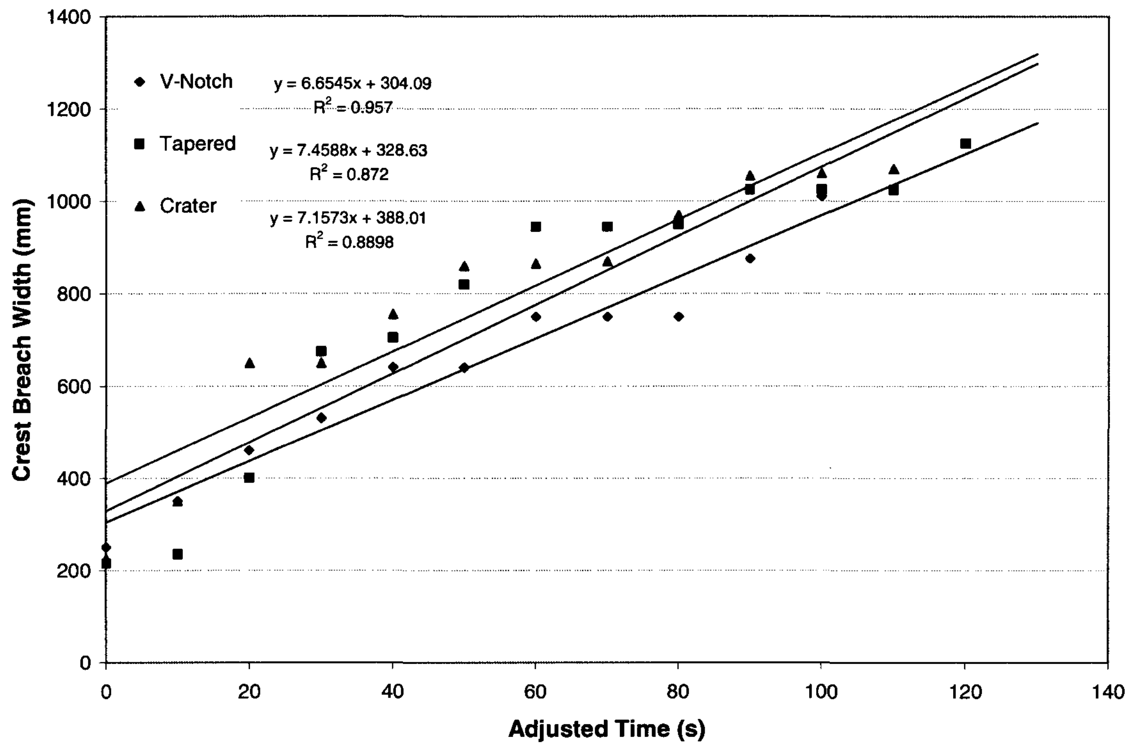

Figure 5.50: Adjusted Crest Width Comparison

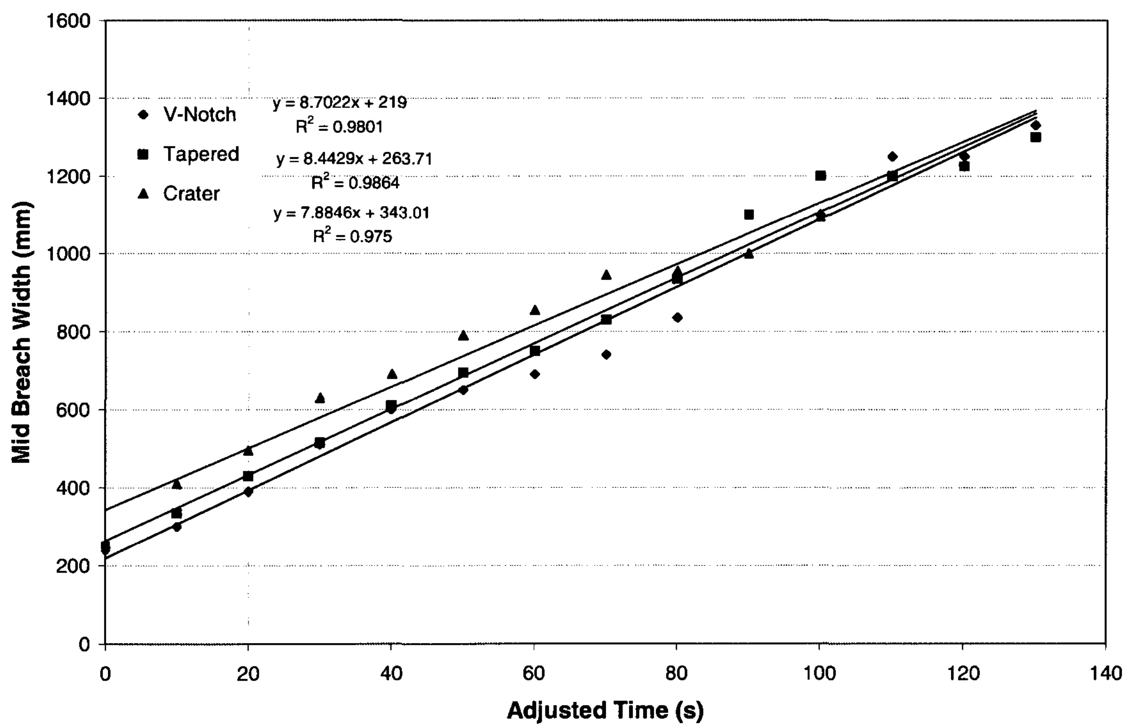

Figure 5.51: Adjusted Middle Width Comparison

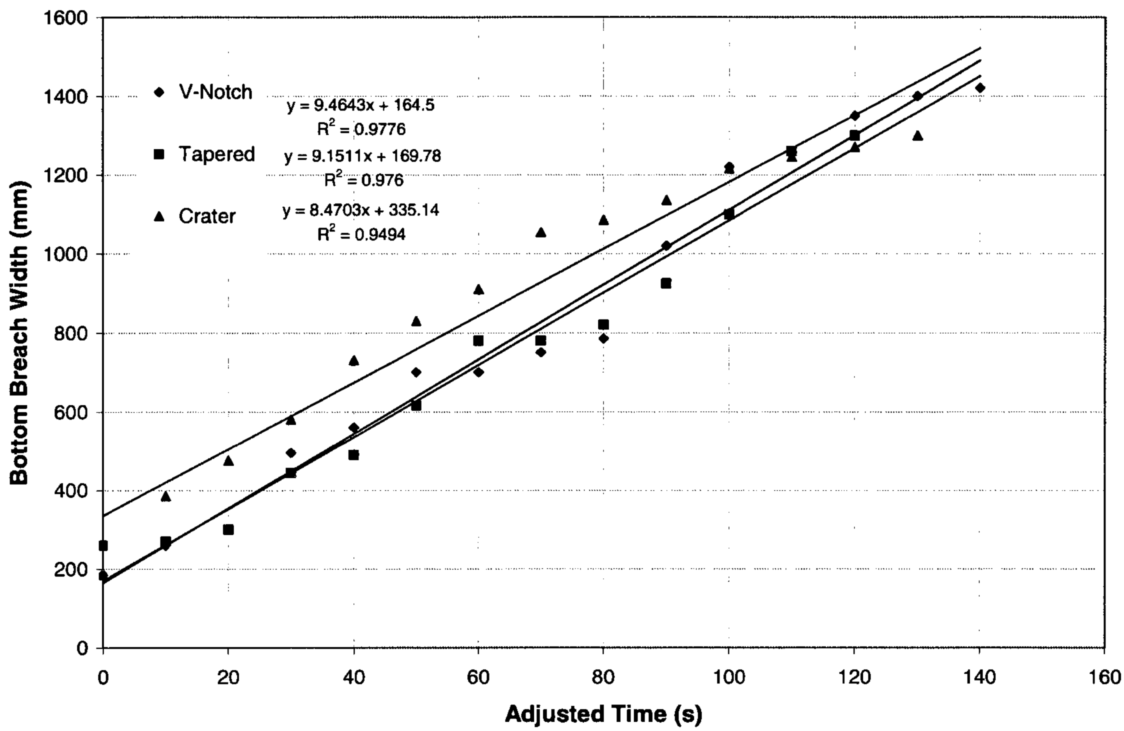

Figure 5.52: Adjusted Bottom Width Comparison

Table 5.9 shows the tabular results of these plots using a $y = ax + b$ format.

Table 5.9: Breach Width Comparison Characteristics

Width Location	Crater Initiation		Tapered Initiation		V-Notch Initiation	
	a	*b*	*a*	*b*	*a*	*b*
Crest	7.16	388	7.46	329	6.65	304
Middle	7.88	343	8.44	264	8.70	219
Bottom	8.47	355	9.15	170	9.46	165

Figures 5.53 through 5.55 show the velocity plots generated for each of the three main breaches using the surface tracer analysis method. Crosses indicate the actual sample times and locations and the dashed black line shows the location of the breach crest through time with respect to the relative distance. Relative distance in these cases is the distance of the particle relative to the downstream toe to the dam.

It should be noted that there is a space and time domain for which no velocity measurements could be taken or reliably extrapolated. In the early stages of the breach, the downstream portion of the breach channel is highly turbulent for the most part and also contains a hydraulic jump. These conditions make surface particle tracing impossible as the tracers are submerged in the breach flow.

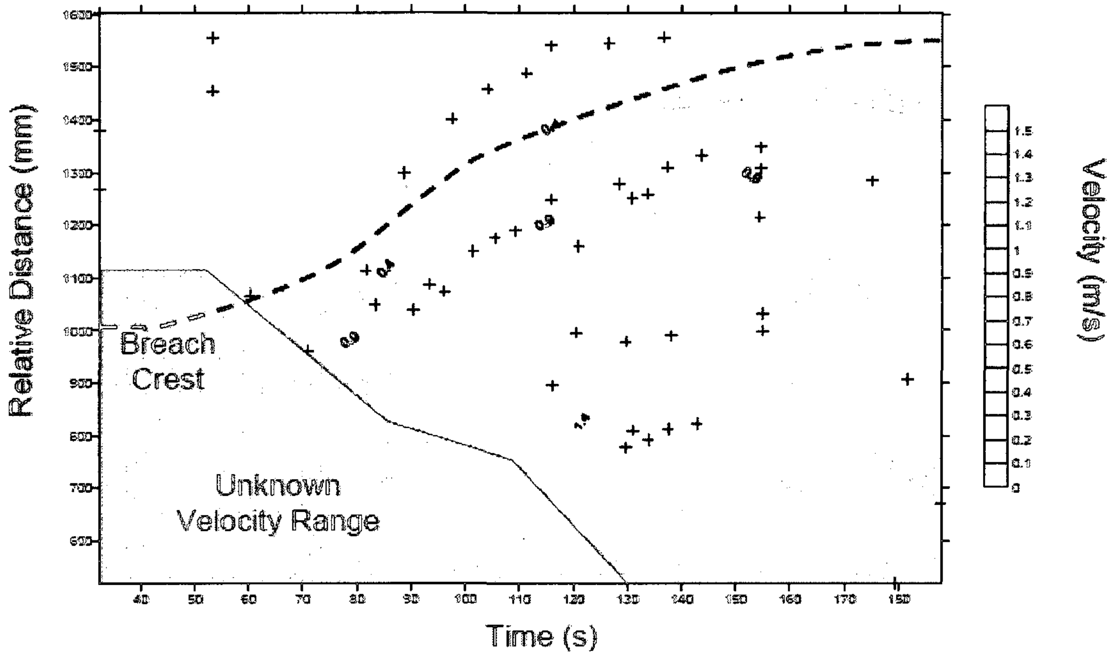

Figure 5.53: Crater Initiation Velocity Plot

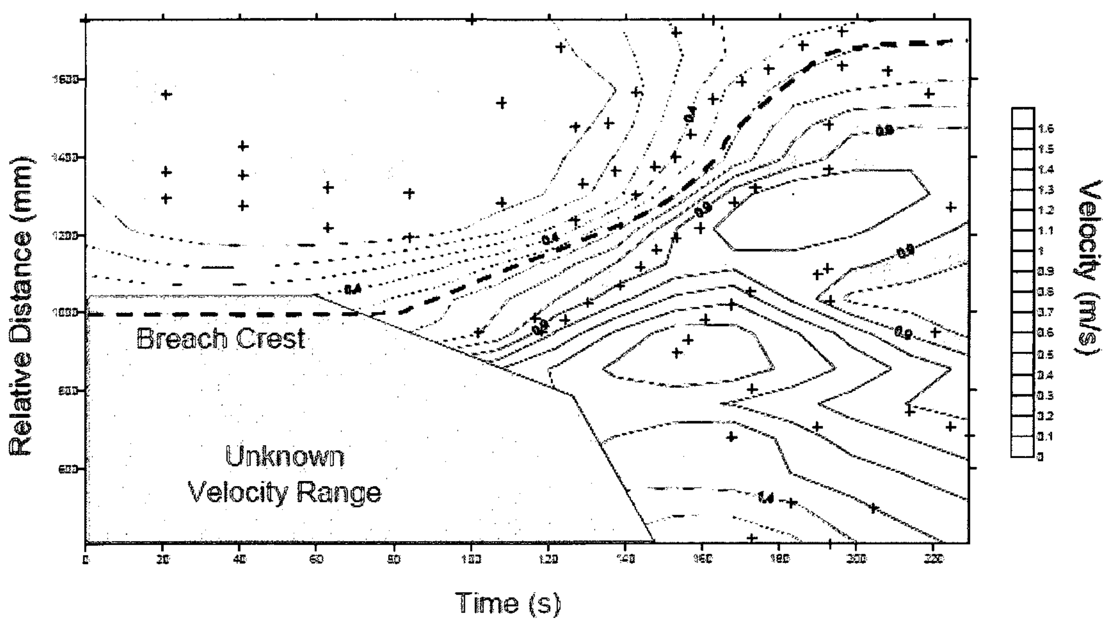

Figure 5.54: Tapered Initiation Velocity Plot

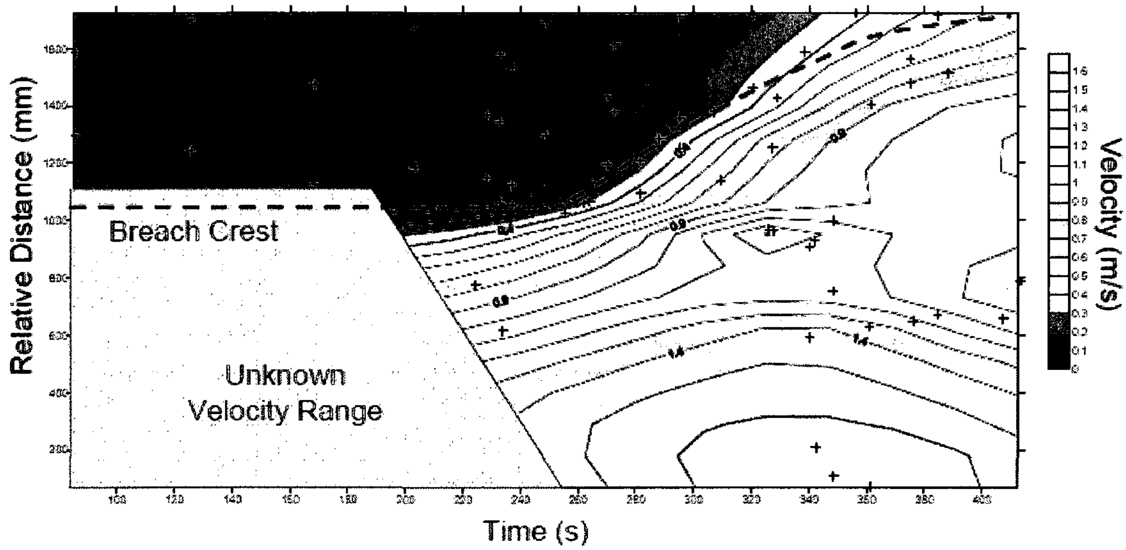

Figure 5.55: V-Notch Initiation Velocity Plot

Surface velocities downstream of the embankment in the supercritical flow zone exceeded 2.0 m/s for both the V-notch and the tapered initiation. At prototype scale, those velocities become 20 m/s, or 72 km/h. Using the Rantz (1982) method, these peak velocities translate into average stream velocities of over 60 km/h. The breach crest for the crater initiation begins to move upstream the earliest, which reflects the earlier time to peak for that run. Interestingly, the velocities for the crater initiation are lower than for the other two tests.

In each of the three cases, there is a spike in velocity located approximately 400 mm downstream of the breach crest over a period of approximately 60 s just prior to the breach reaching peak flow. In the case of the crater, this phenomenon occurs at around 130 s, compared with 160 s and 320 s for the tapered and V-notch breaches respectively. This spike occurs as flow reaches peak velocity right before the hydraulic jump downstream of the breach. It can only be seen during this 60 s window because prior to this point the jump is located at the very bottom of the spill crest and after this point the jump dissipates as the reservoir level draws down.

5.5.1 Clay Core Test

A single test in the large flume was conducted with a clay core. The breach was initiated by a crater and was the same dimensions as the other, homogeneous tests in the large flume. Figure 5.56 shows the breach progression at regular time intervals. It should be noted that the clay core embankment did not use a toe drain as it was thought the clay core would be sufficiently impervious that such an addition and potential construction complication would not be required. However, it can clearly be seen that the downstream slope of the embankment is quite wet. This water, however, is not likely coming through the core of the dam. Rather, it was observed to emerge mostly from below the surface of the flume. The flume is made impermeable by using long strips of impervious membrane material. However, this process leaves the flume susceptible to flow between the strips which is more than likely the case for this embankment. The phreatic surface is still more depressed that it would otherwise have been had the core not been there.

As seen in Figure 5.56, the breach process began in much the same way as for homogeneous embankments. After just over a minute, however, the top of the clay core was reached and the erosion process began to differ due to the lack of erodibility of the clay. Instead, flow plunged over the top of the clay core like a waterfall and scoured out the downstream slope. A substantial portion of material on the upstream side of the core around where the beach crest was located was also removed. The breach width progressively widened up to a limit after about 5 minutes, and then came to equilibrium with the hydraulic forces as water elevation in the reservoir dropped to a lower constant level.

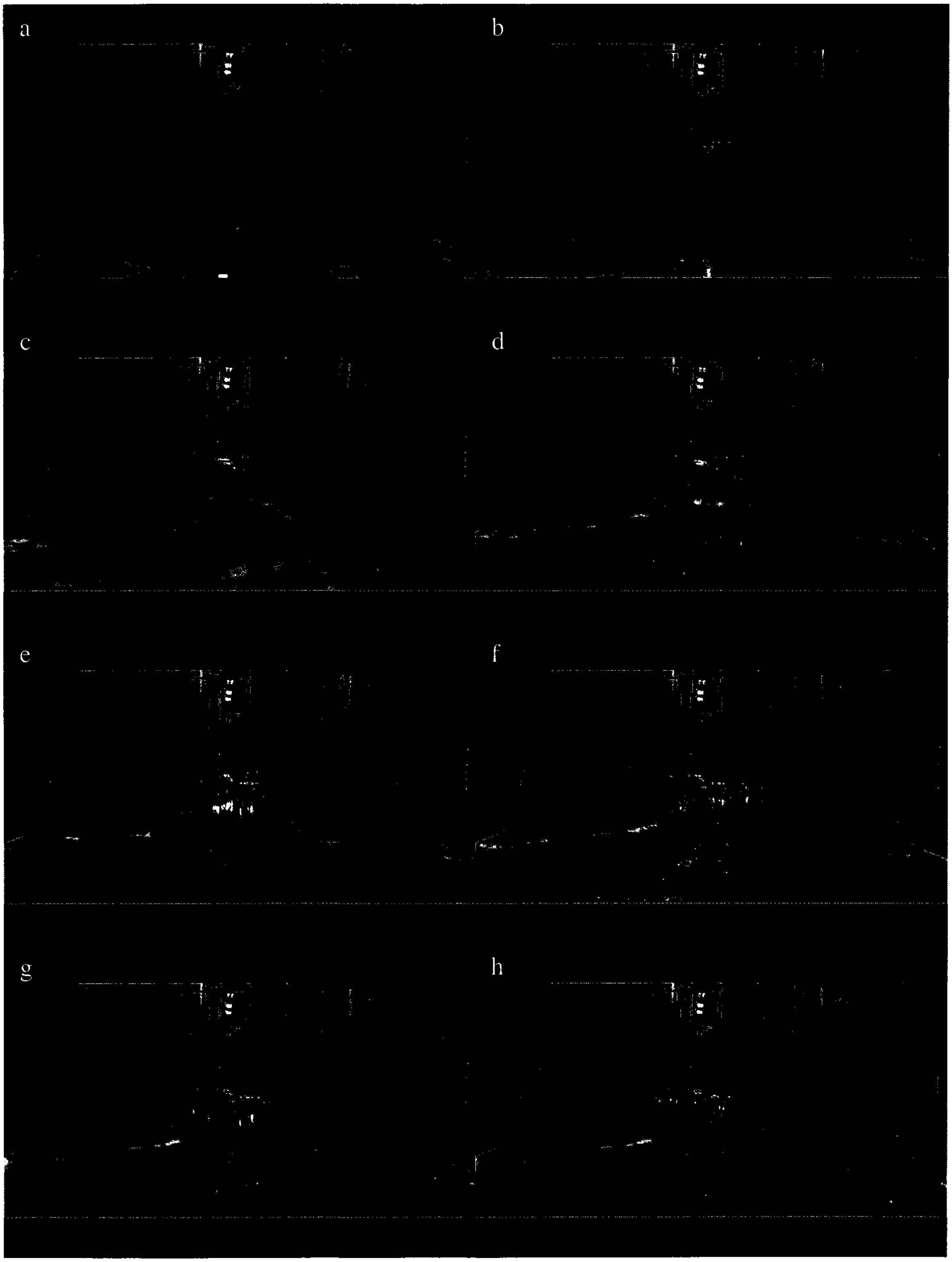

Figure 5.56: Clay Core Embankment Breach Progression at (a) t_0 (b) t_{60}, (c) t_{120}, (d) t_{180}, (e) t_{240}, (f) t_{300}, (g) t_{360}, (h) t_{420}

Figure 5.57 shows the volume-time relationship for the clay core test. In cyan are the raw results from the wave gauges which can be seen to be exceptionally noisy. A trend line through the approximate middle of the noise was drawn in by hand for representative purposes. It is postulated that the noise in the readings is not due to proximity of the instruments, which has been noted by the manufacturer as a potential source of noise, because they were kept well apart of 1.0 m of each other, but rather due to the actual noise and disturbance of the crowd which had gathered to watch the experiments.

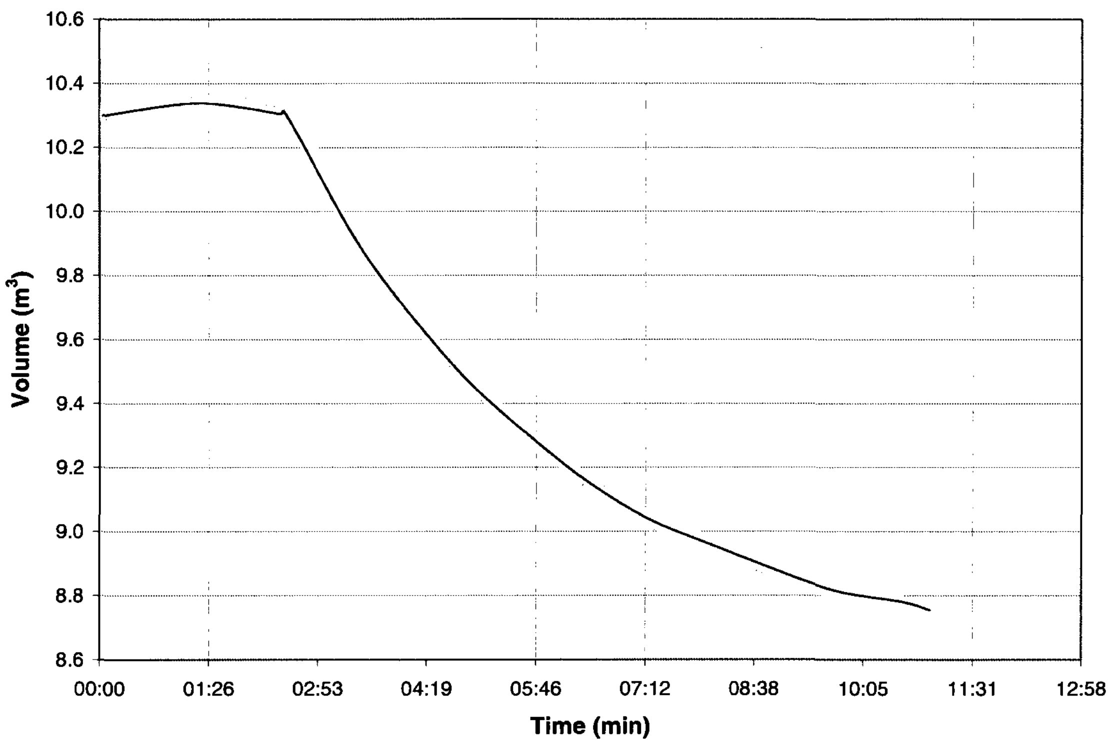

Figure 5.57: Volume Time Relationship for Clay Core Embankment

It should be noted that no breach measurements were made for this test as it was determined to be a mostly qualitative test given that the clay proved to be far more resistant to flow than previously estimated.

While the hydrograph terminates after 11 minutes of testing time, the test was continued longer in order to determine what type of flow condition would cause the clay core to fail. Flow was dramatically increased by using the pump to supply the inflow. This added inflow did not do much besides slightly increasing the width of the breach in the downstream sand slope. A notch was then cut into the breach using a claw hammer to better funnel the flow over the clay and thus increase the applied stress. However, even this change did not increase the rate of clay erosion. Rather, the hydraulic forces applied to the clay core caused it to undergo a bending and foundation shear failure as it opened up much like a set of doors and then drained the rest of the reservoir as shown in Figure 5.58.

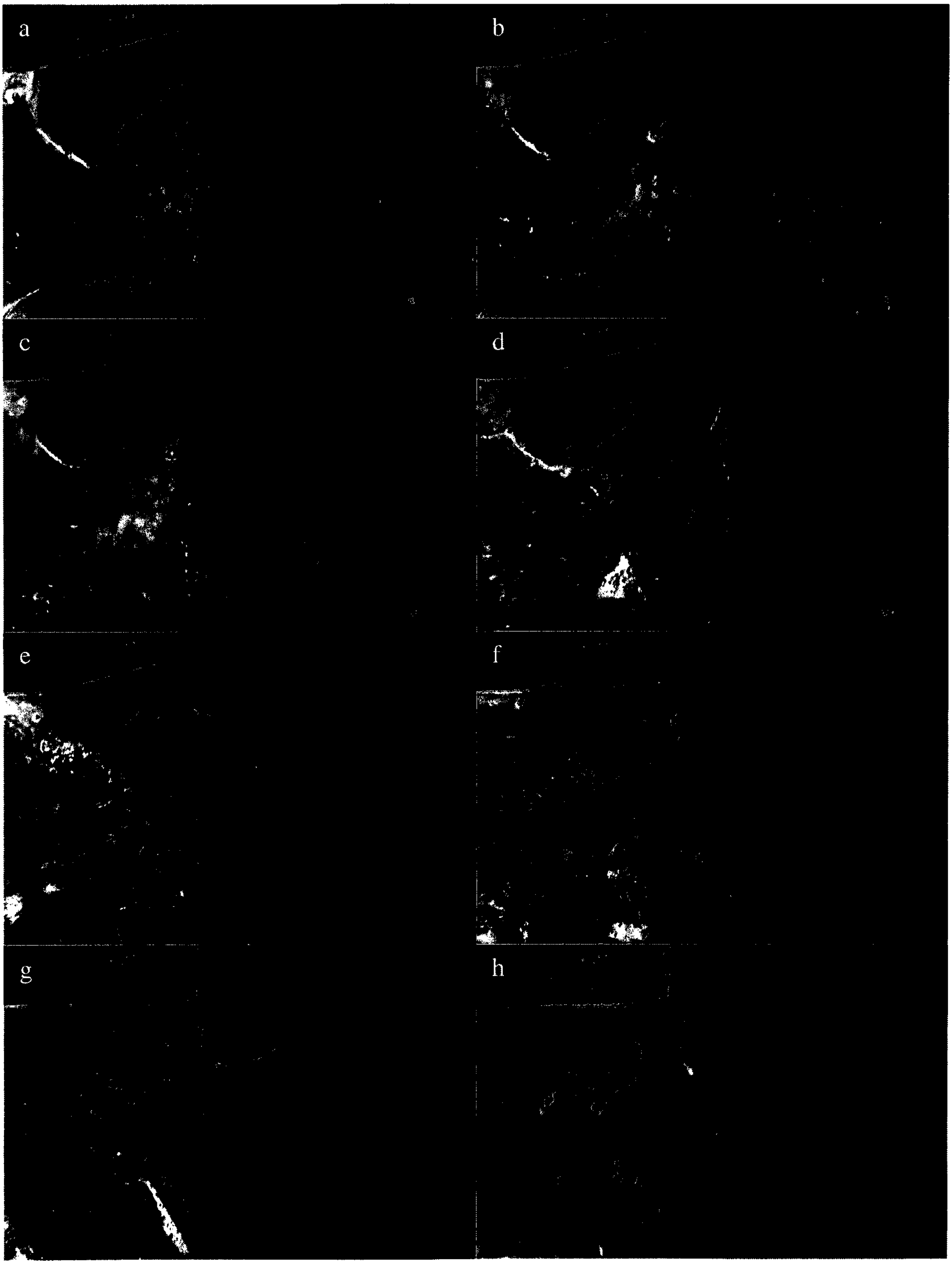

Figure 5.58: Clay Core Failure

6.0 DISCUSSION

While there has been strong focus on the geotechnical characteristics of the embankment dams in order to better understand the structural response of the embankment to the applied hydraulic forces, the study is still focused on the hydraulics of the breaching process. Therefore, while the study might use geotechnical concepts, no detailed analysis or discussion will take place with respect to those aspects. Rather, they will be applied as a means of analysis and discussion for the field of embankment dam breaching.

6.1 Erosion Rate and Critical Shear Tests

Six tests for clay and six tests for sand were conducted to determine the vertical and mass erosion rate characteristics for each sediment type. Three methods were used to determine the shear stress being applied on the bed: using a log-linear plot of mean velocity, using a linear plot of principal Reynolds stress, and using the near-bed principal Reynolds stress measurements. However, there was exceptional variability in the results depending on the method used. The variability was so great that the trend lines generated using a power relationship had completely different general trends (i.e. exponents that were both greater and less than 1).

The best method for determining bed shear stress, as shown by using the R^2 value of each of the trend lines generated to determine the erosion rates, were the results obtained by extrapolating the principal Reynolds stress profile to the bed. While the R^2 values were still not very good for the clay tests, they were excellent with respect to the sand tests.

It should be noted, however, that the coefficients are likely only valid for the range of shear stresses which were observed experimentally, which is to say generally low bed shear stresses. The maximum applied shear stress on the bed was approximately 0.8 Pa. This limitation is unfortunate as the overall goal of this portion of the study was to try and find an equation that could be extrapolated to more realistic shear stresses in a dam breach channel. High shear stresses simply were not able to be generated using the flume in its current configuration. It is currently limited by its slope as well as the configuration and volume of the outlet tank which, for these tests, was put at its limit. While changing the slope could yield higher shear stresses, they will not likely exceed 2.0 Pa. It seems as though only a pressurized flume like a High Shear Stress Sediment Erosion Flume

(Roberts *et al*, 2001), which is a modified SEDflume, can be used to generate the sort of high bed shear stress near 10 Pa which are required to simulate dam breaching.

With respect to the sand tests, it should be noted that the end time for the tests is extremely important given the erosion characteristics exhibited. Unlike the clay, which erodes piece by piece and leaves the system quickly, the sand was pushed forward by the flow from the pump and formed dunes. Rather than vertical erosion, it is vertical dune formation that was measured. Moreover, as the dunes progress forward out of the test section, the vast proportion of their overall mass lies at the front of the dune due to the arched shape (in the cross-stream direction) the dune takes in the flume as shown in Figure 6.1. As such, the mass "eroded" in the early stages of the dune migrating beyond the test section is different than in the latter stages, which influences the erosion rate measurements. For example, between planes 1 and 2 in Figure 6.1 is a smaller amount of sand than between planes 2 and 3. The mass between planes 2 and 3 is greater than the mass just upstream of plane 3 which is near the dune trough. During these experiments, while this parameter could not be completely controlled, an effort was made to let tests go on longer such that the migration of the dune at the completion of each test was similar.

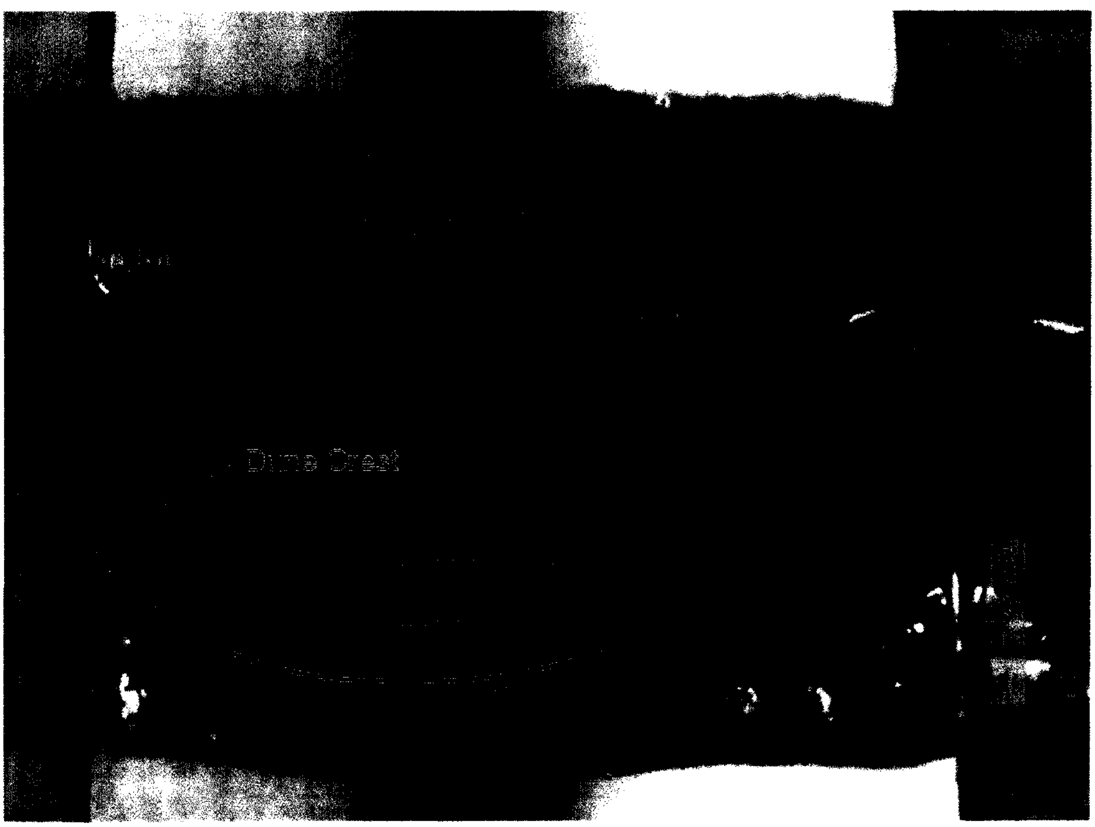

Figure 6.1: Dune Migration past Erosion Plane

It is difficult to compare the erosion rate constant C_e to the previous literature sources as different authors have different final units for erosion rate. While the form g/min is used for mass erosion in this study, some authors use cm^3/cm^2/hour or g/m^2/min, etc. While volumetric measures are simple test section surface area conversions, mass measures require knowledge of the density of the eroded material. In any event, the scaling parameters to obtain the surface area or the volume of eroded material are all generally constant and so will only impact C_e and not the exponent, n, which is theoretically the more important of the two parameters as it better describes the erosion mechanism (depth limited erosion, exponentially increasing erosion, or linear erosion, for example).

Utley and Wynn (2008) show there have been highly variable reports of the exponent, n, in previous research, from values of 1.0 (linear relationships) to 6.8. While the values reported here do in fact fall within that range, it is small comfort given all the parameter variations there are between tests. Therefore, it is difficult to conclude anything with solid, concrete reasoning, given the multitude of factors which make up the different rates. Suffice it to say that, for low shear values, the tests do seem to work, though they do show variability.

An improvement to the technique employed in this study would be to extend the upstream ramp so as to achieve more uniform flow depth after the flow separation resulting from the ramp. This flow separation and flow non-uniformity have caused difficulties in estimating the shear stress at the bed because the principal Reynolds stress profiles were slightly nonlinear.

The limitation of this study with respect to low applied bed shear cannot be readily resolved with the current laboratory equipment. While an increase in the slope of the existing flume would increase the shear stress, it would not approach the 10 Pa shear stress which can be applied using a High Shear Stress Sediment Erosion Flume (Roberts *et al.*, 2001). It is this higher range of shear stresses that are of greater interest with respect to the field of dam breaching. In fact, it has been suggested that the erosion rate trend differs from a strictly exponential relationship at high shear stresses. This theory is supported by Aberle *et al.* (2003) who advocate depth limited erosion.

6.2 Compaction Tests

Four successful dam breach tests were conducted to determine the effects of compaction on breach characteristics. It was seen clearly that compaction had a significant effect since the peak flow for the highest compaction of 20 blows from 10 mm was 8 L/s and the peak flow from the lowest compaction of 5 blows from 5 mm was 11 L/s. Moreover, the hydrograph of the denser embankment was more drawn out and the time to peak was delayed compared to less dense embankments.

Also, the manner of failure was dramatically different for the denser embankments. Due to the depression of the phreatic surface, suction plays a more dominant role in the soil mechanics of the denser embankments. This process is also discussed in the collaborative effort of Al-Riffai *et al* (2009). However, it was determined in the large flume tests of the V-notch initiations with and without a toe drain that the decrease in pore water pressures in the embankment has no clear effects on the shape of the hydrograph, whether it is the base width or the peak flow. While the length of the overtopping failure was more drawn out for the case with the toe drain, when the hydrographs were lagged so they both began at the hydrograph initiation time, the shape was very similar as shown in Figure 5.43. This similarity does not exist for the compaction tests as shown in Figure 5.34.

It can be surmised, therefore, that the degree of saturation of a soil is not what is causing the major changes in breach characteristics for the compaction tests. Similarly, it can be surmised that the manner in which the side slopes fail, whether by sliding or by breaking off in blocks, is also not a primary cause of the difference. The only other parameter which was varied was the density of the embankment.

Sediment transport and shear stress equations often use density of the sediment as an equation parameter, normally to define τ_*. However, the density of an individual soil particle (such as a grain of sand) is normally the density to be considered. As such, the density of sand is normally assumed to be approximately 2650 kg/m^3, which is the density for quartz. Any practical amount of compaction will never cause that density to change, as compaction changes the density of the soil matrix rather than any individual particles. Yet, it is some aspect of either τ_c or τ_* which is affecting the breach hydrograph as it is certainly some increase in resistance from the embankment which is causing the peaks to be lower and the hydrograph to become more drawn out for denser embankments. Moreover, τ_* uses the submerged density of the sediment ($\rho_s - \rho_w$) for its calculation and this assumption does not necessarily apply to the quickly eroding characteristics of an embankment breach scenario where the saturation of the eroding slope may not be 100%.

Therefore, it should be considered that sediment transport equations, such as the Smart Method, use the density of the soil matrix rather than of individual particles for the purposes of dam breach applications or else include a porosity or a void ratio term to describe the compaction effort. It is also possible that it should be used for more conventional sediment transport applications as well.

It is unfortunate, however, that these tests are somewhat shrouded by a great portion of the breach time being potentially influenced by wall effects from the flume side walls as well as inconsistencies in the control of inflow. Without such controls in place, it is difficult with any degree of certainty to put forward any empirical relationship between compaction or embankment density and breach characteristics, but it is an area which can be improved upon in the future.

6.3 Large Flume Tests

Visser (1998) proposes a 5 stage process to describe breach morphology, based on qualitative observations of the breach process. The Visser process conflicts with the failure mechanism proposed by Coleman *et al.* (2002), as it describes the breach as widening in the middle area and having an almost hexagonal shape rather than widening at the crest and having an hourglass shape. The results from this study, however, conflict with both of those sources. As shown in Figures 6.2 through 6.4, the breach width is wider at the base of the embankment and is the narrowest at the crest in all cases for almost all of the time steps which is consistent with Mohamed *et al.* (1999).

The difference for Visser (1998) can possibly be attributed to the side wall effects from the experimental setup as well as the different flow direction which was used to simulate a dike failure (the dike crest initially being parallel to the flow rather than perpendicular as in most dam breaching cases). The variation from Coleman *et al.* (2002) can almost certainly be attributed to the free overfall tailwater condition as well as to effects from the side wall. With a free overall, tailwater elevations cannot back up and cause turbulence in the downstream zone of the breach which would lend to undermining of the side slopes in that region and a wider breach channel. In addition, initiating the breach along a smoother side wall would encourage flow to be funneled quickly through the breach channel.

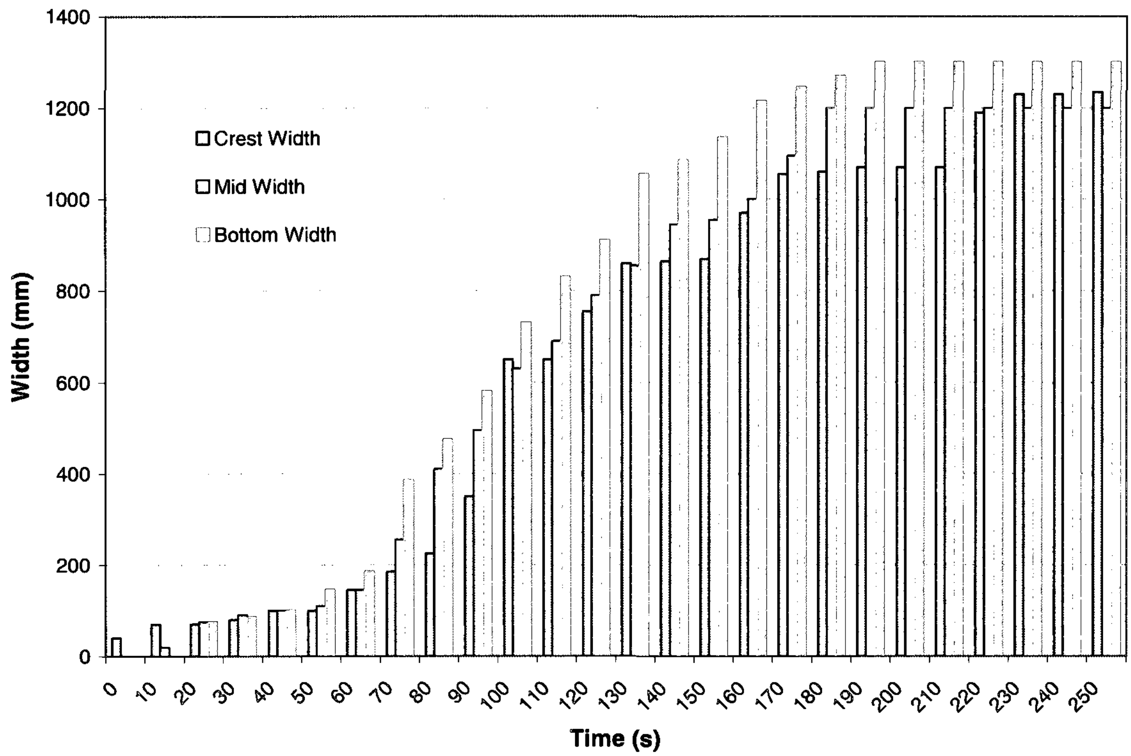

Figure 6.2: Crater Initiation Breach Widths

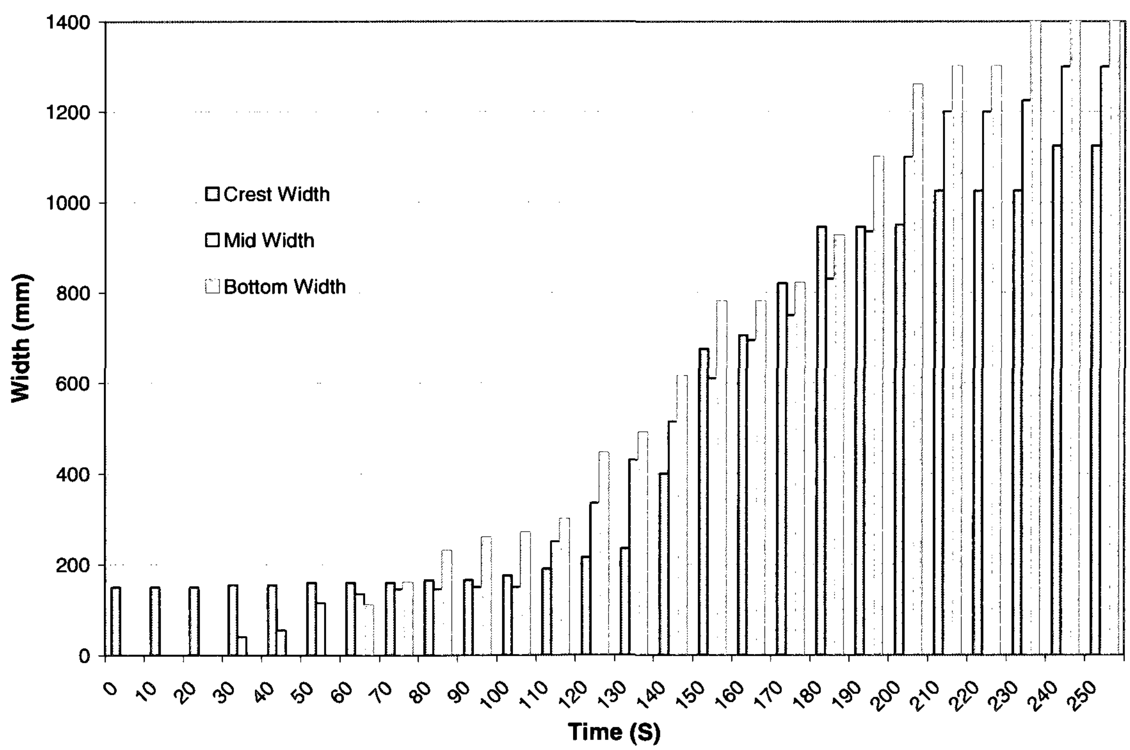

Figure 6.3: Tapered Initiation Breach Widths

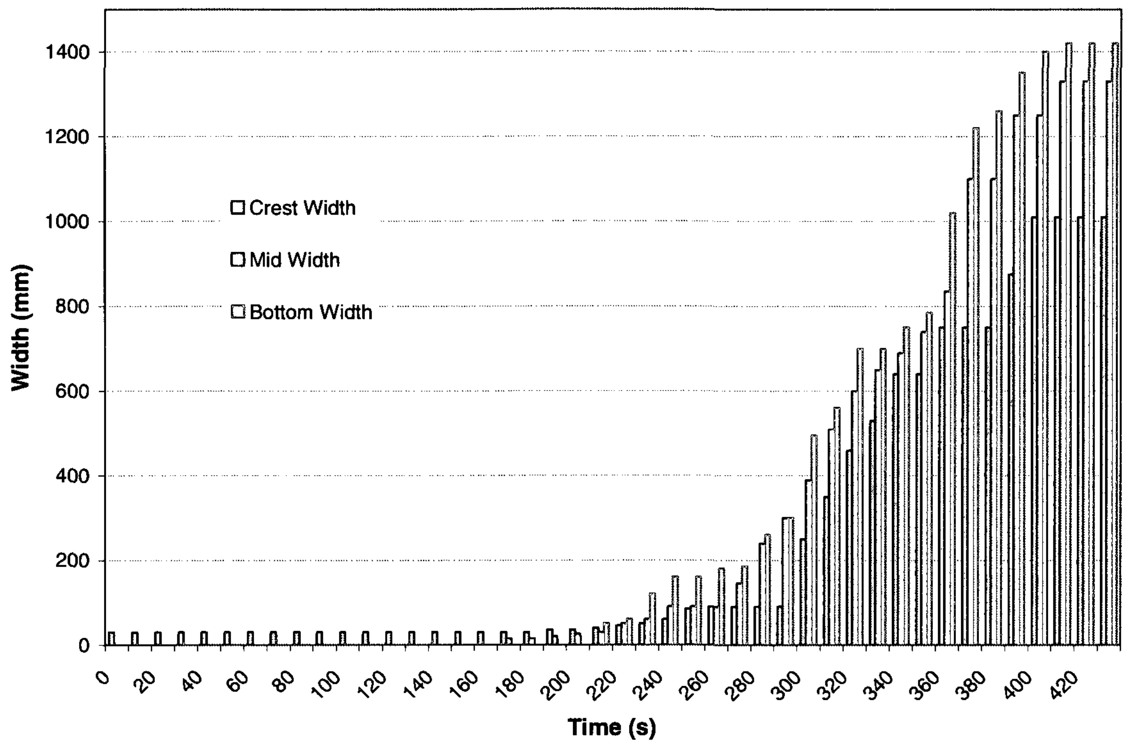

Figure 6.4: V-notch Initiation Breach Widths

One of the compaction tests which resulted in failure was the result of the breach having formed against the side wall. This result was considered a failure because the side wall would be an obviously interfering factor. However, breach widths in the earlier stages of breach development show a striking similarity to those in Coleman *et al.* (2002); namely that there is greater evidence of an hourglass shape as shown in Figure 6.5. In the later stages of breach development, this shape ceases to exist as tailwater conditions undermine the downstream slope.

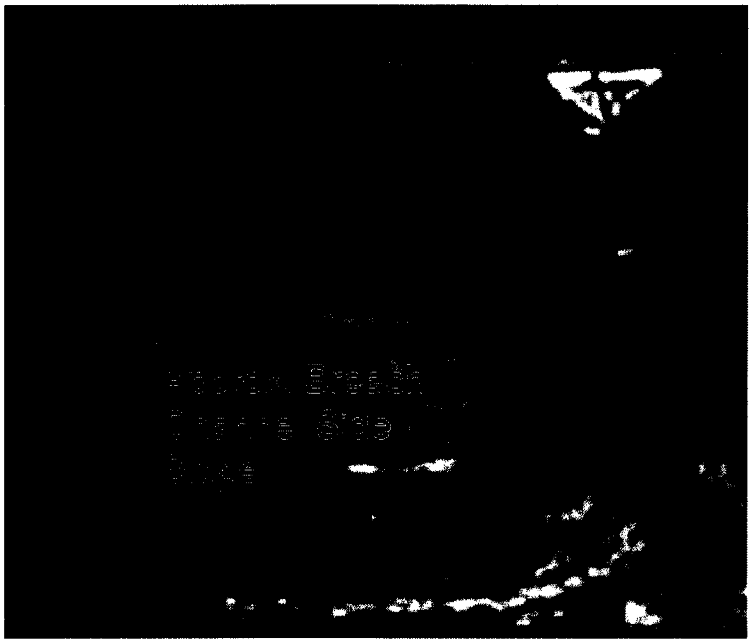

Figure 6.5: Breach Channel with Side Wall Interference

Given that the results from Visser (1998) do not seem to conform directly to the observed breach morphology phenomena, the breach staging he proposed has been modified to fit the results of this study. The stages are shown in Figure 6.6. It should also be noted that the shape of the breach width vs. time curve is very similar to those presented by Visser which are shown in Figure 2.4.

Stage 0: Freeboard failure as reservoir level rises.
Stage 1 (Initiation): Overtopping failure begins. Water pours onto the downstream slope and is largely infiltrated into the downstream slope of the embankment. The breach channel is shallow and poorly defined, often winding down the slope or drifting off to one side.
Stage 2 (Exponential): Channel deepens and straightens and becomes truly defined. There is not a great progression of breach width.
Stage 3 (Linear): Breach depth has nearly bottomed out and large amount of undercutting of the side slopes begins as the breach widens at a steady rate.
Stage 4 (End): The volume in the reservoir has decreased substantially and flow has tapered off leading to a decrease in breach enlargement and soon after a complete halt.

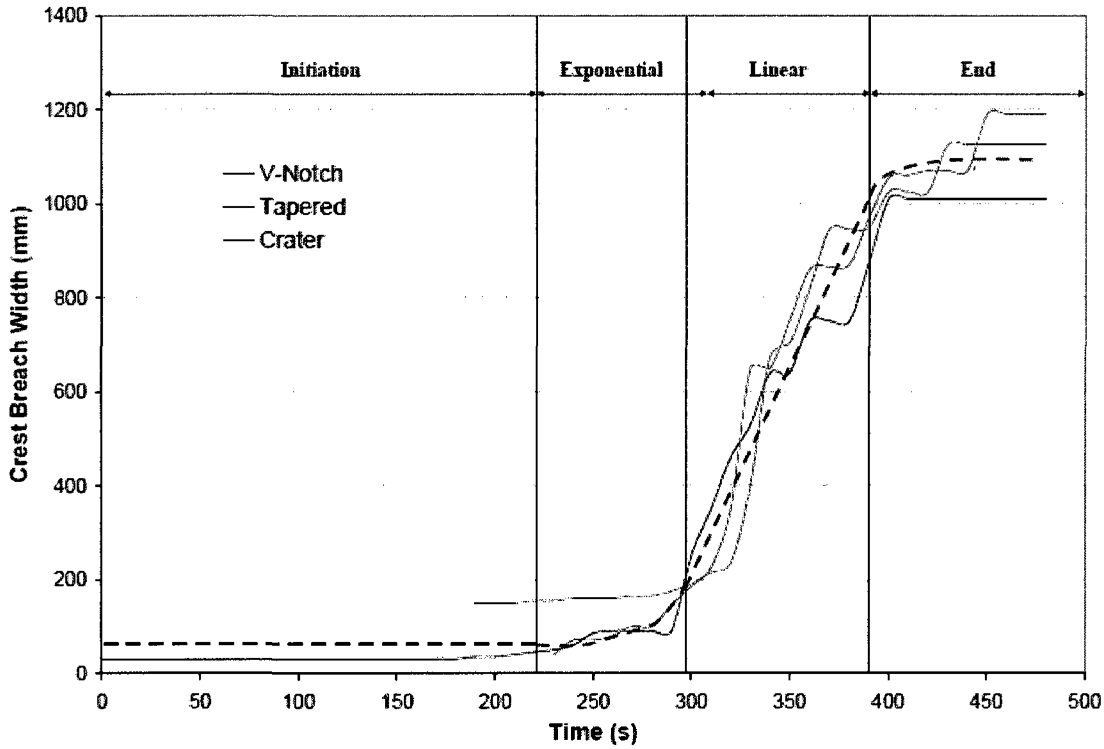

Figure 6.6: Proposed Breach Phasing

The breach staging is perhaps more clearly defined when showing the breach outflow and breach with together as shown in Figure 6.7. When plotted in this manner, the Initiation Phase (Stage 1) starts at the beginning of overtopping failure. The Exponential Phase (Stage 2) begins once there has been a noticeable change in breach width. It is also during the beginning of the exponential phase that the overtopping failure progresses to a breach failure as even with no further inflow to the reservoir, the embankment will still fail. The Linear Phase (Stage 3) begins once there has been a measurable increase in flow in the breach. This time also corresponds to the hydrograph start time using the numerical method for computing the breach outflow hydrograph presented in this study. The End Phase (Stage 4) begins right after peak flow has been reached.

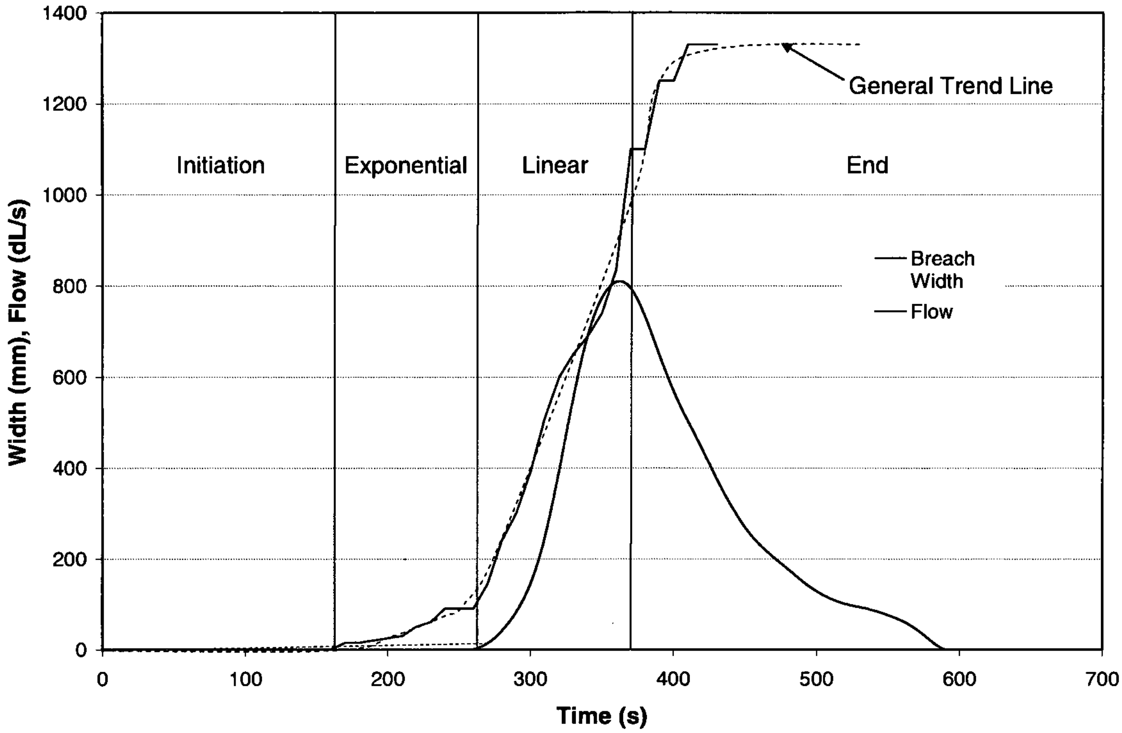

Figure 6.7: Comparison of Breach Width and Outflow for V-notch Initiation

Figure 6.8 shows a comparison plot of the change in breach width and the outflow hydrograph for the V-notch initiation. In this case, the two plots follow the same general trend with the largest increase in breach width occurring near the peak flow through the breach channel. The largest difference is the change in breach width begins a bit earlier and trails off earlier.

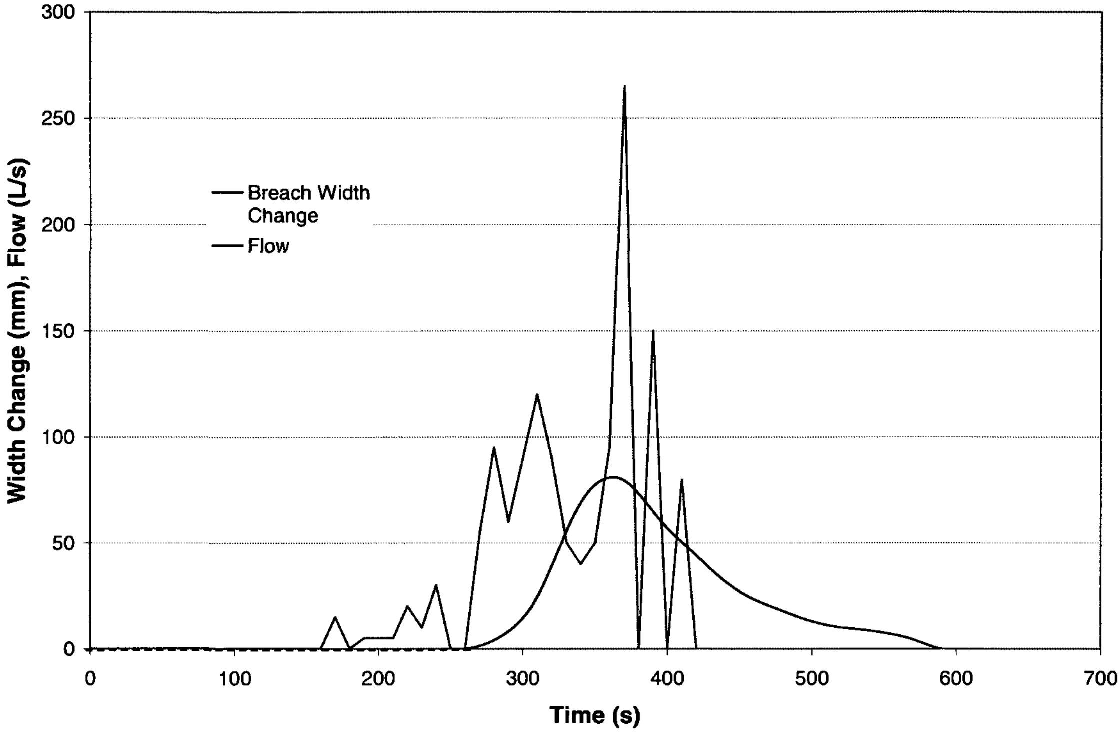

Figure 6.8: Comparison of Breach Width Change and Outflow for V-notch Initiation

The peak flow of large flume tests seems to be directly linked to the reservoir size at the time of breach failure (as opposed to overtopping failure), as shown in Table 6.1. Reservoir volumes were taken as the maximum reservoir volume as computed using the wave gauges. The time at which there is a maximum reservoir corresponds roughly with the hydrograph initiation time. Peak volume is considered to be a more appropriate indicator as the volume at the time of initial overtopping failure for the V-notch test with the drain is less than that of the V-notch test without the drain, though the peak flow is higher.

Table 6.1: Breach Flows and Reservoir Volumes

Initiation Method	Peak Volume (m^3)	Peak Flow (L/s)
Crater	11.58	79.7
Tapered	12.07	92.4
V-notch (no drain)	11.47	78.9
V-notch (drain)	11.65	81.0

If presented in the form Peak Flow = β x Peak Volume, where β is an empirical constant, the values for β ranges from 6.88 to 7.66 (difference of 11% maximum). If presented in the form Peak Flow = β x (Peak Volume)^2, the values for β range from 0.59 to 0.63 (difference of less than 7%). This trend of increasing the power to which the peak volume is presented can continue to take place, but all it serves to do is artificially reduce the measurable difference between the peak volumes and thus artificially reduce the error.

By using a graphing means and modifying the equation to include the addition of a constant, Figure 6.9 shows an excellent correlation between the two variables, though the β value changes dramatically. Clearly, peak flow is related to the peak volume of the reservoir. While embankment density is a likely resisting factor, in this case it is kept constant between the tests and would not be a factor in influencing the differences between the values proposed for β.

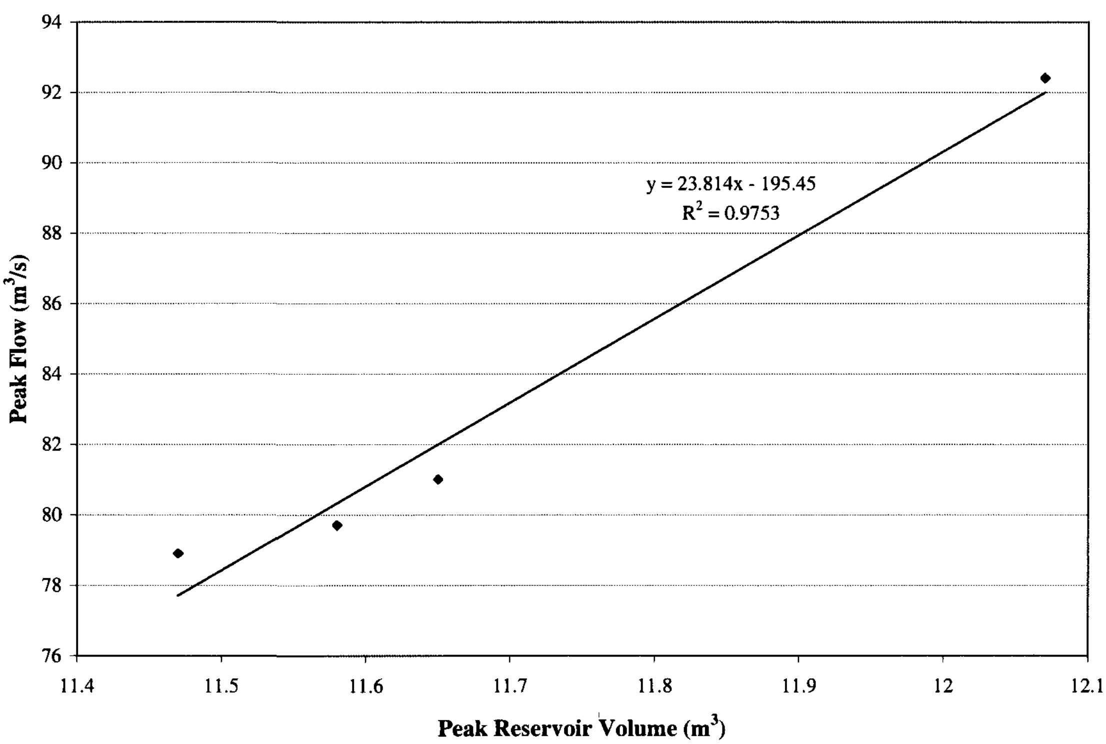

Figure 6.9: Comparison of Peak Outflow vs. Peak Reservoir Volume

It is worth noting, however, that the V-notch test with no drain used different sand than the test for the V-notch filter with the drain. The undrained V-notch test used the same sand as was used for the compaction tests, which was finer sand (D_{50} = 140 μm vs. D_{50} = 220 μm). Given the use of a larger sediment size, it would be expected that the V-notch initiated test with the drain would be more resistant to the breach flows and, like the compaction test which used higher compaction efforts, would have a lower peak flow and a more drawn out breach time. However, as the shape of the breach hydrographs are very similar and the peak flow is likely more heavily influenced by reservoir volume, it can be surmised that the grain size used for the construction of the embankment has much less bearing on the breach outflow characteristics than previously thought. As such, many sediment transport equations which have been used to perform breach analysis, such as the method proposed by Smart (1984), may need to be examined in greater detail to ascertain the depth of their applicability.

It is interesting to note that this phenomenon of erosion not being heavily related to the sediment size is also found with respect to pier scour (Melville and Coleman, 2000). Both dam breach morphology and pier scour are more a function of erosion depth and breadth rather than sediment transport which makes them similar concepts.

Initial breach geometry does not seem to impact the rapid changes in breach channel width which occur in the Linear Phase. There is, however, a notable impact during the Initiation Phase as smaller initial breach width (due to the initial geometry) leads to a greater portion of the overtopping flow being infiltrated into the downstream slope of the embankment, as observed for the case of the V-notch initiation. In the case of the V-notch initiation with drain, the Initiation Phase lasts for about 50% of the total breach time and represents an important increase in the warning time available to downstream inhabitants. This dramatic increase in the length of the Initiation Phase corresponds to a 40 minutes difference between the V-notch and crater initiated breaches at the prototype scale.

Sediment deposition downstream of the embankment was a focus of the study by Franca and Almeida (2004). In that study, they found that the length of rockfill deposition measured 1.5 times the dam height. This relation of deposition to the height of the dam seems impractical, to say the least, as the height of the dam has no proven bearing on the forces acting on the breach channel (which would be entraining and deposition embankment material).

This study had two different tailwater conditions between the compaction tests and the large flume tests. While the distance to the outfall was approximately the same for both cases, the tailwater elevation in the tilting flume for the compaction tests was very high relative to the height of the tailwater for the large flume tests. Tailwater elevation has already been established in this study as important when observing the bottom breach width, but it also has an effect on deposition. Due to the narrower confines of the tilting flume, the tailwater elevation was higher. This greater dissipation of energy caused a greater amount of sediment to deposit immediately downstream of the embankment. During two tilting flume tests, sediment appeared to be largely uniformly distributed across the flume and held a slope which tapered from the remains of the embankment steadily to the outfall looking somewhat like a wedge. Such a case was not observed at all in the large flume. Instead, supercritical flow was observed for longer periods of time as the sediment at the flume floor was washed away and could not induce a hydraulic jump.

A separate, qualitative, supplementary test was conducted in the large flume to test a few theories. The test was conducted with a coarser sand to see if the side slopes would hold vertical as had been observed in other tests. Also, the reservoir was made smaller by moving the embankment much further upstream. The tailwater condition was different in that while the width of the flume remained the same, there were many meters of dry flume downstream of the embankment which could be filled with the breach outflow before backwater effects would become significant. Photos taken after the completion of the test are shown in Figure 6.10.

It was determined that the width of the sediment deposition was approximately three times the width of the breach and the length of the deposition was 3.4 m (17 times the height of the dam). The depth of the deposition at its deepest point was approximately 25 mm. The embankment was constructed to 200 mm high and had an approximate reservoir volume of 2.2 m^3.

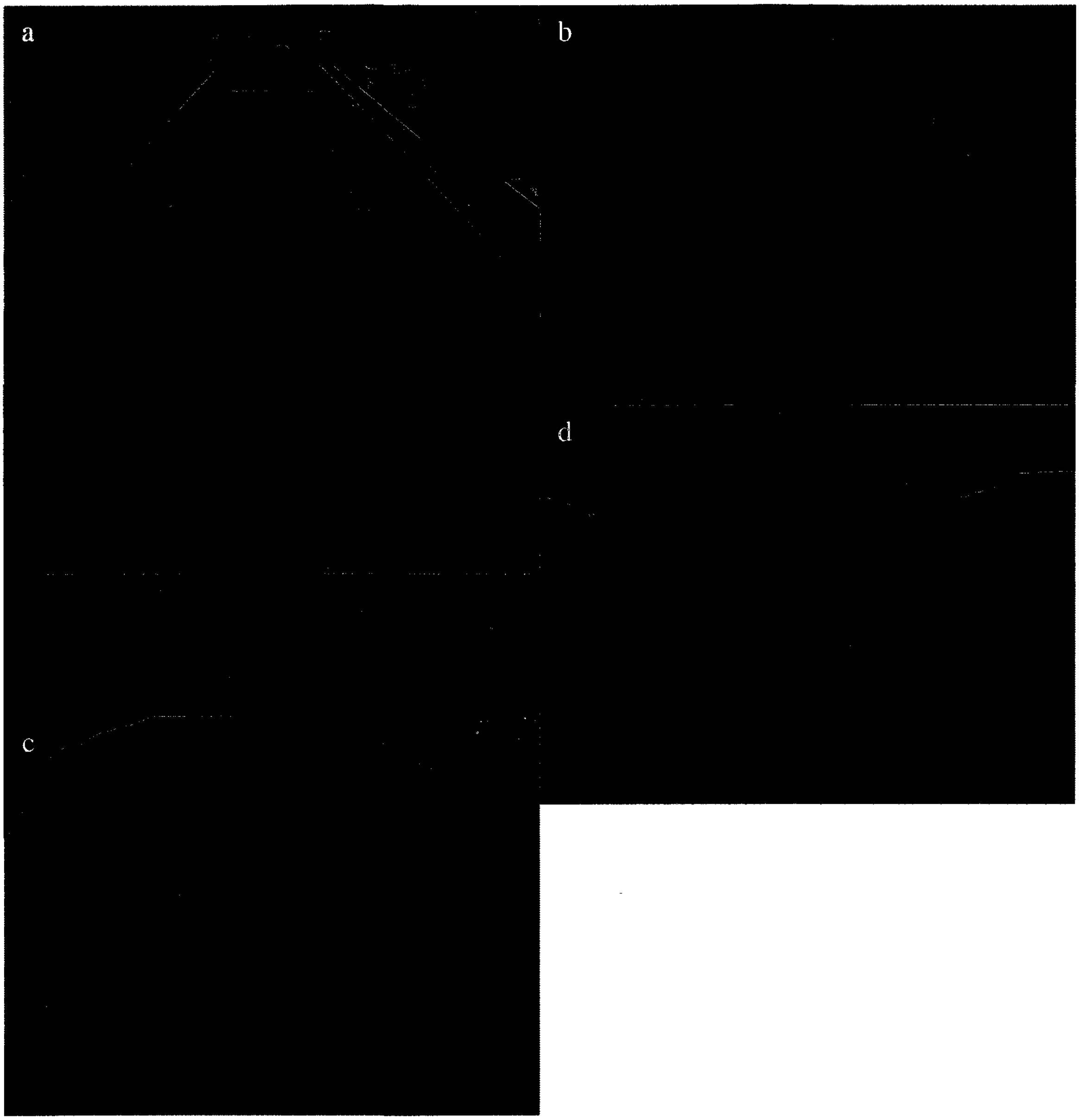

Figure 6.10: Large Flume Qualitative Test
(a) Sediment Plume, (b) Channel Wall, (c) Top View of Breach Channel,
(d) Upstream View of Breach Channel

6.4 Scaling

As shown in Section 2.1, scaling is an important parameter for any laboratory experiment. In this study, the scale was mostly designed to be 1:100 for the embankment tests. However, Froude scaling the embankment tests was effectively impossible to implement because using an appropriate Froude scaled grain size for the material in the embankment would have forced the embankment to use silt rather than sand for construction. Silts generally exhibit cohesive forces which dramatically change the manner in which erosion takes place.

Generally, it can be considered that the embankments constructed in this study were more resistant to shear stress than they would have been at the prototype scale due to the larger sediment grain size. This change would indicate that the embankments constructed at prototype scale would likely have hydrographs with higher peak flows with a shorter time to peak, making the estimates in this study potentially not conservative. However, this study uses embankment material that is generally finer than that reported in literature sources, as shown in Table 2.2. Moreover, the degree of compaction is also far less than that used for those same studies, where reported. The estimates in those other studies are likely to have been less conservative than the estimates in this study.

Sediment similitude is considered satisfied when τ_* of the model is the same as τ_* of the prototype (Prasuhn, 1992). Given that sediment size cannot be used to scale the embankment material in this case, compaction was used instead to modify the density of the embankment. While strictly using the equation for τ_*, such a method should not be possible. However, as shown in Section 6.2, the compacted density of the embankment has a direct effect on its resistance to shear and therefore on τ_*.

The degree to which proper scaling has been achieved is not known. A proper embankment is generally compacted to a much higher degree than any of the degrees of compaction which were attempted during this study, mostly because this study used manual compaction methods, whereas full scale embankments use mechanical means. A more detailed project dedicated to the study of compaction with respect to shear resistance in non-cohesive materials would be a beneficial next step to determine alternate methods to scale laboratory models without changing the grain size.

7.0 CONCLUSIONS

The core of this study is comprised primarily of three embankment tests which were conducted in the large flume at the University of Ottawa Hydraulics Laboratory. These tests were designed to examine the effects of varying the initial breach geometry on breach morphology and outflow characteristics. This portion of the study addresses a key need in the field of experimental dam breaching as no two existing studies used the same initial breach geometry for overtopping tests as shown in Table 2.5. Often there is also variance found in the manner of breach initialization and this lack of consistency and experimental standards must be addressed.

As direct Froude scaling was not possible, a separate series of tests were developed to determine if modifying the compaction effort and density of the embankment would be a sufficient means for compensating for a larger grain size. Four successful tests were conducted in the tilting flume using varying degrees of compaction below the standard Proctor density. These compaction tests were supplemented with a series of geotechnical tests to determine the full array of geotechnical properties of the materials used.

In addition, a test that used a clay core was conducted in the large flume. The embankment used the same outer dimensions as for the other large flume tests, but used a vertical wall of clay as the impervious core of the embankment. The clay proved to be highly resistant to the breach flow and the test was determined to be an unrealistic model for a composite embankment.

To supplement the clay core test, erosion rate tests were conducted in the tilting flume to determine the possibility of scaling the erosion results for high shear stresses resulting from dam breaching.

From this study, the following conclusions have been drawn:

i. A four phase breach process is proposed based on quantitative analysis of breach morphology which also describes the differences between overtopping failure and breach failure as shown in Figure 6.6.
ii. While initial breach geometry does not appear to have any effect on the peak breach outflow, it does have an effect on the length of the Initiation Phase of the breach as shown in Figure 5.41.

iii. The density of the embankment plays an important role in determining the shape of the outflow hydrograph as well as the peak flow. As such, compaction can be an effective means of scaling homogeneous non-cohesive embankments in order to achieve similar dimensionless shear stress for the model and the prototype.
iv. Breach shape follows an hourglass shape, though not as proposed by Coleman *et al.* (2002). The breach is widest at the downstream toe of the embankment and smallest at the crest, but widens again upstream of the crest due to the effects of the curved weir.
v. The slope failure mode (sliding, block failures, etc) does not appear to have any impact on breach characteristics as the breach channel below the water surface dominates breach characteristics.
vi. Tailwater conditions have a notable effect on breach morphology near the toe of the embankment and on downstream sediment deposition characteristics. Reservoir volume also appears to have an important effect on sediment deposition characteristics.
vii. Clay in scaled embankment dams is highly resistant to shear stress from hydraulic sources. A clay core is more likely to fail due to bending and sliding.

It should be noted that these conclusions have not been drawn for the purposes of improving dam construction techniques. Rather, they are proposed for the purposes of developing a more advanced numerical breach model in the hope of improving the accuracy of risk assessments in downstream flood zones. A new set of criteria could then be developed to define the new flood elevations and improve warning times for people who may be at risk. In addition to the above, the following observations have been made:

i. Peak outflow from the breach appears to have a direct relationship to the maximum volume in the reservoir during the breach process as shown in Figure 6.9.
ii. Suction in the unsaturated embankment does not appear to have a direct relationship to breach characteristic, with the exception that the level of suction is related to the amount of infiltration that is possible on the downstream slope, which has a consequential impact on the length of the Initiation Phase.
iii. Sediment grain size might have a minimal effect on breach characteristics for homogeneous non-cohesive embankments, similar to the phenomena observed with pier scour. Moreover, the equations to determine dimensionless shear stress should use the density of the soil matrix, as opposed to individual soil particles for embankment erosion purposes.

8.0 OPPORTUNITIES FOR FUTURE WORK

This study is part of a larger, ongoing study on dam breaching at the University of Ottawa. This study addresses part of the experimental portion of that study and it is expected that during the completion of the full study most of the opportunities listed below will be examined. Nevertheless, they represent the questions and concerns still to be resolved from an experimental standpoint in the field of earth dam breaching.

i. One of the key conclusions of this study is the link between reservoir volume and peak outflow. This conclusion is based on a small sample set of tests. It would be wise, therefore, to compare this specific and previously unreported breach characteristic with other studies as well as to conduct a separate study which specifically examines the effects of a change in reservoir volume. This change should not be accomplished by varying the height of the embankment, but it should rather be accomplished by moving the location of the embankment within the flume. It should be noted that the proposed experiment may be complicated due to a varying tailwater condition, which should be kept constant where possible, though this would possibly impractically require varying the length of the flume. It should also be noted that the rate of change in the reservoir rating curve should also be kept as constant as possible (i.e. keeping the same cross-stream cross-section for each test).

ii. This study examined the effects of compaction (i.e. density change) on breach characteristics, but ran afoul of side wall effects during the early stages of the breach. Similar tests to the compaction tests should be conducted again in a larger flume location where side walls will not be a potential source of error in the analysis. This future study should also use higher degrees of compaction than were used in this study in an attempt to reach the degrees of compaction achieved by previous researchers for their models (such as 95% Standard Proctor density) in order to develop a more complete range of densities with which to work from.

iii. The effect of tailwater conditions on dam breaching should be examined in greater detail as part of a flood routing study rather than a dam breach study. The deposition of sediment from a breach is a critical parameter when considering the environmental damage of both standard embankment dams and tailings dams. As such, this proposed study should endeavor to use realistic tailwater cross-section based on actual rivers, etc, as was attempted by Davies *et al.* (2007). While the outflow hydrograph remains a very important parameter in assessing risk, proper flood routing of that hydrograph is just as important, if not more so.

iv. A uniform set of testing techniques ought to be developed as a means of integrating future research in this field of study. There are too many parameters which can be varied and for which there is limited understanding (for example, the effects of changing inflow rates, or inflow rates relative to the reservoir rating curve, etc). It was unfortunate during this study that similarity to previous studies could not be achieved and more direct comparisons could not be made with much of the previous work conducted in the field.

v. Much work has been done by researchers on the erodibility of clays. This highly complex field of study is still evolving and effort should be made to continue this research with an eye to use it as a potential input into developing computer models for clay-core embankments, as it seems to be nearly impossible to create a realistic experimental model. These tests should focus on high shear stresses using material similar to that which is used in dam construction rather than the *in-situ* sampling which is presently favoured by many researchers, as *in-situ* conditions from a creek bed simply do not accurately reflect dam breach conditions.

vi. Sediment transport and shear stress equations should be revisited for supercritical flow conditions. Most have been developed for subcritical flow regimes and it is not known exactly what sort of practical differences may exist between the two regimes with respect to modeling the dam breaching process.

vii. All of the successful breach tests conducted in this study used a breach initiated down the centerline of the test flume. However, this is not necessarily the regular location for the occurrence of a breach. For example, the Teton Dam failure occurred near to a rock wall at the side of the canyon. This study has shown there are differences when side wall effects are considered but it was not within the scope of this study to determine what the full effects might be. This knowledge is required in order to properly determine a worst case scenario for dam breaching risk assessments.

viii. A full scale test really needs to be conducted with the aim of aiding to determine the effects of scaling on embankment dam testing. The present study is limited in that it is unclear if the resistance of the test embankments was too little or too much, and clearly it could be seen that varying this resistance (i.e. the degree of compaction) has a significant effect on breach characteristics. An embankment need not even be constructed, as there are numerous existing dams which have been slated for decommissioning.

It is the hope of this author that at least some of these opportunities will be pursued as they represent key pieces to the greater puzzle of assessing risk from embankment dam breaching.

9.0 REFERENCES

Aberle, J., Nikora, V., and Walters, R. (2003). "Straight Benthic Flow-through Flume for in situ Measurement of Cohesive Sediment Dynamics." *Journal of Hydraulic Engineering*, 129(1), 63-67.

Al-Riffai, M., Nistor, I., Vanapalli, S., and Orendorff, B. (2007). "Overtopping of Earth Embankments: Sensitivity Analysis of Dam Breaching using Two Numerical Models." *60th Canadian Geotechnical Conference*, Ottawa, Canada.

Al-Riffai, M., Orendorff, B., Nistor, I., Rennie, C., and St-Germain, P. (2009). "Influences of Compaction and Toe Drains on the Formation of Breach Channels of Overtopped Earth Embankments – an Experimental Study." 33rd IAHR Biennial Congress, Vancouver, Canada.

Al Qaser, G. N. (1991). "Progressive Failure of an Overtopped Embankment." Colorado State University, Fort Collins, Colorado.

Ambrosini, R. D., Luccioni, B. M., Danesi, R. F., Riera, J. D., and Rocha, M. M. (2002). "Size of Craters Produced by Explosive Charges on or above the Ground Surface." 69-78.

Ambrosini, R. D., Luccioni, B. M., and Danesi, R. (2006). "Craters Produced by Explosions on the Soil Surface." *Journal of Applied Mechanics*, 73.

Ambrosini, R. D., and Luccioni, B. M. (2007). "Craters Produced by Explosions above the Soil Surface.".

Baker, W. E., Cox, P. A., Westine, P. S., Kulesz, J. J., and Strehlow, R. A. (1983). *Explosion Hazards and Evaluation.*, Elsevier, Amsterdam.

Banasiak, R., and Verhoeven, R. (2006). "Quantification of the Erosion Resistance of Undisturbed and Remolded Cohesive Sediments." *Water, Air, and Soil Pollution: Focus*, 6, 17-27.

BBC. (2009). "Indonesia Dam Burst Kills Dozens." http://news.bbc.co.uk/2/hi/asia-pacific/7967205.stm.

Berlamont, J. E., Ockenden, M. C., Toorman, E. A., and Winterwerp, J. C. (1993). "The Characterisation of Cohesive Sediment Properties." *Coastal Engineering*, 21, 105-128.

Braimah, A. (2007). "Lecture Notes." Department of Civil Engineering, Carleton University, Ottawa.

Briaud, J. L., Ting, F. C. K., Chen, H. C., Cao, Y., Han, S. W., and Kwak, K. W. (2001). "Erosion Function Apparatus for Scour Rate Predictions." *Journal of Geotechnical and Geoenvironmental Engineering*, 127(2), 105-113.

Brown, C. A., and Graham, W. J. (1988). "Assessing the Threat of Loss of Life from Dam Failure." *Water Resources Bulletin*, 24(6).

Bui, T. (2000). "Cohesive Sediment Transport in Natural Streams: State of Knowledge." *Proceeding from the Water Resources 2000 Conference.*

Bull, J. W., and Woodford, C. H. (1998). "Camouflets and their Effects on Runway Supports." *Computer and Structures*, 69(6), 695-706.

Caldwell, L. W. (2009). "Rehabilitating our Nation's Aging Small Watershed Projects." *Proceedings of the Annual Conference of the Association of State Dam Safety Officials.*

Chapuis, R. P., and Gatien, T. (1986). "An Improved Rotating Cylinder Technique for Quantitative Measurements of the Scour Resistance of Clays." *Canadian Geotechnical Journal*, 23, 83-87.

Chen, Y. H., and Anderson, B. A. (1987). "Development of a Methodology for Estimating Embankment Damage due to Flow Overtopping." Federal Highway Administration and Forestry Service.

Coleman, S., Andrews, D., and Webby, M. G. (2002). "Overtopping Breaching of Noncohesive Homogeneous Embankments." *Journal of Hydraulic Engineering*, 128(9), 829-838.

Costa, J. (1985). "Floods from Dam Failures." United States Geological Survey, Denver, Colorado.

Das, B. M. (2002). *Principles of Geotechnical Engineering.*, Brooks/Cole, Sacramento, California.

Davies, T. R., Manville, V., Kunz, M., and Donadini, L. (2007). "Modelling Landslide Dambreak Flood Magnitudes: Case Study." *Journal of Hydraulic Engineering*, 133(7), 713-720.

Debnath, K., Nikora, V., Aberle, J., Westrich, B., and Muste, M. (2007). "Erosion of Cohesive Sediments: Resuspension, Bed Load, and Erosion Patterns from Field Experiments." *Journal of Hydraulic Engineering*, 133(5), 508-520.

DeKay, M., and McClelland, G. (1993). "Predicting Loss of Life in Cases of Dam Failure and Flash Flood." *Risk Analysis*, 13(2), 193-205.

Federal Emergency Management Agency (2003). "Reference Manual to Mitigate Potential Terrorist Attacks against Buildings." United States Department of Homeland Security, Washington, D.C.

Fell, R., Wan, C. F., Cyganiewicz, J., and Foster, M. (2003). "Time for Development of Internal Erosion and Piping in Embankment Dams." *Journal of Geotechnical and Geoenvironmental Engineering*, 129(4), 307-314.

Foster, M., Fell, R., and Spannagle, M. (1998). "Analysis of Embankment Dam Incidents." UNICIV Rep. No. R-374, Univeristy of New South Wales, Sydney, Australia.

Foster, M., Fell, R., and Spannagle, M. (2000). "The Statistics of Embankment Dam Failures and Accidents." *Canadian Geotechnical Journal*, 37, 1000-1024.

Franca, M. J., and Almeida, A. B. (2002). "Experimental Tests on Rockfill Dam Breaching Process." *International Symposium on Hydraulic and Hydrological Aspects of Reliability and Safety Assessment of Hydraulic Structures*.

Franca, M. J., and Almeida, A. B. (2004). "A Computational Model of Rockfill Dam Breaching cause by Overtopping." *Journal of Hydraulic Research*, 42(2), 197-206.

Fread, D. L. (1988). "BREACH: An Erosion Model for Earthen Dam Failures." National Weather Service, Office of Hydrology, Silver Spring, Maryland.

Fread, D. L. (1998). "NWS FLDWAV Model." Hydrologic Research Laboratory, National Weather Service Office of Hydrology, Silver Spring, Maryland.

Fredlund, D. and Morgenstern, N. (1977). “Stress State Variables for Unsaturated Soils.” *Journal of the Geotechnical Engineering Division*, 103, 447-466.

Froehlich, D. (1995). "Peak Outflow from Breached Embankment Dam." *Journal of Water Resources, Planning and Management*, 121(1), 90-97.

Gibbs, H. J. (1962). "A Study of Erosion and Tractive Force Characteristics in Relation to Soil Mechanics Properties." United States Department of the Interior, Bureau of Reclamation, Denver, Colorado.

Graham, W. J. (1998). "Estimation of Loss of Life Due to Dam Failure." United States Bureau of Reclamation, Washington, D.C..

Hahn, W., Hanson, G., and Cook, K. (2000). "Breach Morphology Observations of Embankment Overtopping Tests." *Proceedings of the Joint Conference on Water Resources Engineering and Water Resources Planning & Management, Minneapolis, Minnesota, July 30-August 2, 2000.*

Hamilton, D., and Meehan, R. (1971). "Ground Rupture in the Baldwin Hills." *Science*, 172, 333-344.

Hanson, G., and Simon, A. (2001). "Erodibility of Cohesive Streambeds in the Loess Area of the Midwestern USA." *Hydrological Processes*, 15, 23-38.

Hanson, G., and Hunt, S. L. (2007). "Lessons Learned using Laboratory JET Method to Measure Soil Erodibility of Compacted Soils." *Applied Engineering in Agriculture*, 23(3), 305-312.

Heinzen, R. T. (1976). "Erodibility Criteria for Soil." University of California.

Helley, E. J., and Smith, W. (1971). "Development and Calibration of a Pressure-difference Bedload Sampler." United States Geological Survey, Menlo Park, California.

Henrych, J. (1979). "The Dynamics of Explosion and its Use." Elsevier, Amsterdam.

Jakarta Post. (2009). "Learning our Lesson from Another Dam Failure." http://www.thejakartapost.com/news/2009/04/01/learning-our-lesson-another-dam-failure.html.

Kandiah, A., and Arulanandan, K. (1974). "Hydraulic Erosion of Cohesive Soils." *Transportation Research Record 497.*

Kelly, W. E., and Gularte, R. C. (1981). "Erosion Resistance of Cohesive Soils." *Journal of Hydraulics Division*, 107(10), 1211-1224.

Kinney, G., and Graham, K. (1985). *Explosive Shocks in Air*, Springer Verlag, New York.

Lane, E. W. (1934). "Security from Under-seepage Masonry Dams on Earth Foundations." *Transactions of the ASCE*, 60(4), 929-966.

Lecointe, G. (1998). "Breaching Mechanisms of Embankments." University of Birmingham.

Melville, B. W., and Coleman, S. (2000). "Bridge Scour." Water Resource Publications, Littleton, Colorado.

Meyer-Peter, E., and Muller, R. (1948). "Formulas for Bed-load Transport." *Proceedings of the 2nd meeting of the IAHR*, 39-64.

Mohammed, M., Samuels, P. G., Ghataora, G. S., and Morris, M. W. (1999). "A New Methodology to Model the Breaching of Non-cohesive Homogeneous Embankments." *Proceedings of the Zaragoza Meeting-CADAM*, 289-308.

Mohammed, M., Samuels, P. G., Morris, M. W., and Ghataora, G. S. (2002). "Improving the Accuracy of Prediction of Breach Formation through Embankment Dams and Flood Embankments." *International Conference on Fluvial Hydraulics*.

Morris, M. W. (2000). "CADAM Concerted Action on Dambreak Modelling Final Report." HR Wallingford, Wallingford, UK.

Morris, M. W., and Hassan, M. (2002). "Breach Formation through Embankment Dams and Flood Defence Embankments: A State of the Art Review." HR Wallingford, Wallingford, UK.

Morris, M. W. (2005). "Investigation of Extreme Flood Processes and Uncertainty (IMPACT) Final Technical Report.".

Morris, M. W., Hassan, M., and Vaskin, K. A. (2007). "Breach Formation: Field Test and Laboratory Experiments." *Journal of Hydraulic Research*, 45 Extra Issue, 9-17.

Mostafa, T. S., Imran, J., Chaudhry, M. H., and Khan, I. B. (2008). "Erosion Resistance of Cohesive Soils." *Journal of Hydraulic Research*, 46(6), 777-787.

Munson, B., Young, D., and Okiishi, T. (1990). "Fundamentals of Fluid Mechanics." Wiley, John & Sons, Toronto.

Naval Facilities Engineering Command (NAVFAC) (1986). "Blast Resistant Structures, Design Manual 2.08." United States Navy, Alexandria, Virginia.

Nezu, I., and Nakagawa, H. (1993). "Turbulence in Open Channel Flows." IAHR, Rotterdam, Netherlands.

Nistor, I., and Rennie, C. (2005). "Earth Fill Breach Failure due to Explosive Blast.".

Petrascheck, A. W., and Sydler, P. A. (1984). "Routing of Dam Break Floods." *International Water Power and Dam Construction*, 36, 29-32.

Pokrovskyi, G. I., and Tshernygovskyi, A. A. (1967). "Explosions [in Russian]." Nedra, Moscow.

Powledge, G., Ralston, D., Miller, P., Chen, Y. H., Clopper, P., and Temple, D. (1989). "Mechanics of Overflow Erosion on Embankments Part II. Hydraulic and Design Considerations." *Journal of Hydraulic Engineering*, 115(8), 1056-1075.

Prasuhn, A. L. (1992). *Fundamentals of Hydraulic Engineering.*, Oxford University Press, New York.

Rantz, S. E. (1982). "Measurement and Computation of Streamflow: Volume 1 Measurement of Stage and Discharge." United States Geological Survey, Washington, D. C..

Reid, I., Layman, J. T., and Frostick, L. E. (1980). "The Continuous Measurement of Bedload Discharge." *Journal of Hydraulic Research*, 18, 243-249.

Rennie, C., and Hay, A. (2009). "Reynolds Stress Estimates in a Tidal Channel from Phase-wrapped ADV Data." *Journal of Coastal Research*, 25(in press).

Richards, K., and Reddy, K. (2007). "Critical Appraisal of Piping Phenomena in Earth Dams." *Bulletin of Engineering Geology and the Environment*, 66(4), 381-402.

Roberts, J., Jespen, R., and Gailani, J. (2001). "Measurements of Bedload and Suspended Load in Cohesive and Non-cohesive Sediments." *Proc. from the World Water Congress.*

Sekine, M., and Iizuka, N. (2000). "Erosion Rate of Cohesive Sediment." *The Fourth International Conference on Hydroscience and Engineering*.

Shields, A. (1936). "Anwendung der Ahnlichkeitsmechanik und Turbulenzforschung auf die Geschiebebewegung." Mitt Preuss Versuchsanstalt fur Wasserbau und Schiffbau, Berlin.

Singh, K., and Snorrason, A. (1984). "Sensitivity of Outflow Peaks and Flood Stages to the Selection of Dam Breach Parameters and Simulation Models." *Journal of Hydrology*, 68, 295-310.

Smart, G. M. (1984). "Sediment Transport Formula for Steep Channels." *Journal of Hydraulic Engineering*, 110(3), 267-276.

Solava, S., and Delatte, N. (2003). "Lesson of the Failure of the Teton Dam." *Proceedings of the Third Congress, Oct. 19-21, 2003, San Diego, CA*, 178-189.

Terzaghi, K. (1939). "Soil Mechanics: a New Chapter in Engineering Science." *Journal of the Institution of Civil Engineering* , 12, 106-141.

Tingsanchali, T., and Chinnarasri, C. (2001). "Numerical Modelling of Dam Failure due to Flow Overtopping." *Hydrological Sciences Journal*, 46(1), 113-130.

United States Bureau of Reclamation. (1987). *Design of Small Dams.*, United States Department of the Interior, Washington, D.C.

United States Bureau of Reclamation(1999). "A Procedure for Estimating Loss of Life caused by Dam Failure." United States Bureau of Reclamation, Denver, Colorado.

USCOLD (1975). "Lesson from Dam Incidents, USA. Committee on Failures and Accidents to Large Dams of the United States Committee on Large Dams (USCOLD)." American Society of Civil Engineers, New York.

USGS (2005). "Natural Debris Dams and Debris-Dam Lakes."

Utley, B. C., and Wynn, T. M. (2008). "Cohesive Sediment Erosion: Theory and Practice." *World Environmental and Water Resources Congress*.

Van Rijn, L. C. (1993). "Manual Sediment Transport Measurements." Delft Hydraulics, Delft, Netherlands.

Vanapalli, S. K. (20008). "Mechanics of Unsaturated Soils: Class Notes." Univeristy of Ottawa Department of Civil Engineering, Ottawa.

Vanapalli, S. K. (2006). "Soil Mechanics Laboratory Manual." University of Ottawa, Ottawa.

Visser, P. (1998). "Breach Growth in Sand Dikes." Delft Technical University, Delft, The Netherlands.

Voulgaris, G., and Trowbridge, J. (1998). "Evaluation of the Acoustic Doppler Velocimeter (ADV) for Turbulence Measurements." *Journal of Atmospheric and Oceanic Tehcnology*, 15, 272-289.

Wahl, T. (1998). "Prediction of Embankment Breach Parameters: A literature Review and Needs Assessment." US Department of the Interior, Denver, Colorado.

Wahl, T. (2004). "Uncertainty of Predictions of Embankment Dam Breach Parameters." *Journal of Hydraulic Engineering*, 130(5), 389-397.

Wahl, T. (2007). "Laboratory Investigations of Embankment Dam Erosion and Breach Processes." CEA Technologies, Inc..

Wahl, T., Hanson, G., Courivaud, J.-R., Morris, M. W., Kahawita, R., McClenathan, J., and Gee, D. M. (2007). "Development of next-generation embankment dam breach models." *Proceedings of the 2008 U. S. Society on Dams Annual Meeting and Conference.*

Wan, C. F., and Fell, R. (2004). "Investigation of Rate of Erosion of Soils in Embankment Dams." *Journal of Geotechnical and Geoenvironmental Engineering*, 130(4), 373-380.

Wan, C. F., and Fell, R. (2009). "Investigation of Internal Erosion and Piping of Soils in Embankment Dams by the Slot Erosion Test and the Hole Erosion Test." University of New South Wales, Sydney, Australia.

Wang, Z., and Bowles, D. (2006). "Dam Brach Simulations with Multiple Breach Locations under Wind and Wave Actions." *Advances in Water Resources*, 29, 1222-1237.

Webby, M. G., and Jennings, D. N. (1994). "Analysis of Dam Break Flood caused by Failure of Tunawaea Lanslide Dam." *Proceedings of the International Conference on Hydraulics of Civil Engineering*, 163-168.

Wikipedia. (2009). "Buffalo Creek Flood." http://en.wikipedia.org/wiki/Buffalo_Creek_Flood.

Wilcox, D. (1998). "Turbulence Modeling for CFD." DCW Industries, La Canada, California.

Wong, M., and Parker, G. (2006). "Re-Analysis and Correction of Bedload Relation of Meyer-Peter and Muller using their own Database." *Journal of Hydraulic Engineering*, 132(11), 1159-1168.

Zhu, Y., Lu, J., Liao, H., Wang, J., Fan, B., and Yao, S. (2008). "Research on Cohesive Sediment Erosion by Flow: An Overview." *Science in China Series E: Technological Sciences*, 51(11), 2001-2012.